ARCHAEOGEOPHYSICAL INVESTIGATION OF A SAMNITE SITE, MONTE

PALLANO, ITALY

by

KELLY BRIAN GRAGG

(Under the Direction of Ervan Garrison)

ABSTRACT

This study conducted an archaeogeophysical investigation of a Samnite site on Monte Pallano, Italy. The geophysical techniques of total field and vertical gradient magnetometry and ground penetrating radar were employed to locate buried stonewalls and other anthropogenic features at Monte Pallano in the area of Trench 8000. The application of the statistical technique of cross-correlation for processing magnetic data was developed.

Cross-correlation tests were conducted on synthetic magnetic data computed for a uniformly magnetized sphere. Seven parameters were tested to determine their effect on the ability of cross-correlation to resolve the position and depth of an anomaly source.

The locations of sixteen anomalies were corroborated with both the magnetic and ground penetrating radar techniques, four of which were the locations of known walls. Multi-technique geophysical prospection with magnetometry and ground penetrating radar with the statistical technique of cross-correlation, were effective at locating buried stonewalls at Monte Pallano.

INDEX WORDS: Geophysics, Magnetics, Ground Penetrating Radar, Cross correlation, Samnite Archaeology, Monte Pallano

ARCHAEOGEOPHYSICAL INVESTIGATION OF A SAMNITE SITE, MONTE

PALLANO, ITALY

by

KELLY BRIAN GRAGG

B.S., Virginia Polytechnic Institute and State University, 1997

A Thesis Submitted to the Graduate Faculty of The University of Georgia in Partial

Fulfillment of the Requirements for the Degree

MASTER OF SCIENCE

ATHENS, GEORGIA

2003

ARCHAEOGEOPHYSICAL INVESTIGATION OF A SAMNITE SITE, MONTE

PALLANO, ITALY

by

KELLY BRIAN GRAGG

Major Professor:	Ervan Garrison	
Committee:	Robert Hawman	
	Naomi Norman	

Electronic Version Approved:

Maureen Grasso
Dean of the Graduate School
The University of Georgia
December 2003

DEDICATION

To my family, and my family to be

Bello non abstinebant: adeo ne infeliciter quidem defensae libertatis taedebat et vinci quam non tempare victoriam malebant (10.31.14) Livy

"They shrank not from war and so far were they from wearying of even an unsuccessful defense for their freedom that they preferred to be conquered rather than make not the effort to win." (A quote from Livy concerning the Samnites)

ACKNOWLEDGEMENTS

I am thankful for all my friends near and far who helped make graduate school so great. Nina Serman for her constant encouragement, advice and friendship throughout my time here. Morris, Ben, Cliff, Mark, Steve, Kevin, and Erin for all the great gaming. Vanese Flood for being a great friend and office-mate throughout the struggles of grad school and allowing me stay at the 'Hotel Nantahala" while I finished up writing my thesis. Laura for being a great running partner and teaching me to knit.

I am deeply grateful to the love of my life, Brandi, for her unfailing love and support throughout graduate school. And for her patience these last few months as I completed my thesis writing. I am grateful to my family for their support encouragement and love. Thanks to Casey and Toni for allowing me to spend a month with them so that I could work on my thesis.

Lastly I am grateful to Cups Café Coffee shop for a great place to study, where I spent countless hours and drank countless cups of coffee.

TABLE OF CONTENTS

LIST OF TABLES

LIST OF FIGURES

xv

CHAPTER I

INTRODUCTION

The three objectives of this thesis were to:

1) Locate the positions of buried stonewalls by using magnetometry (total field and vertical gradient) and ground penetrating radar (GPR) within an archaeological site on Monte Pallano, Italy, in order to assist archaeologists with an excavation plan.

2) Compare the magnetic and GPR interpretations to determine the effectiveness of the combined methods at Monte Pallano.

3) Evaluate the use of cross-correlation as a processing technique data for locating the horizontal and vertical positions of anomaly sources in magnetic data.

Rarely is it possible to excavate an entire archaeological site because of limited time, funding, manpower, knowledge of the extent of the buried material, or a desire to preserve a site intact (Tite, 1972). Often only small portions of a site can be investigated during a field season, sometimes with archaeologists discovering very little. Shallow geophysical surveys are quick methods for non-destructively locating buried anthropogenic features (Vaughan, 1986).

An archaeogeophysical investigation was conducted in the Sangro River Valley, on Monte Pallano, Italy, in the area referred to as Trench 8000 from May 7 – 14, 2002. The investigation was conducted by a research team from the University of Georgia (UGA), - Kelly Gragg, the United States Department of Agriculture (USDA) – Forest Service - Kent Schneider,

and Oberlin College – Susan Kane in cooperation with the Superintendency of Abruzzo (Soprintendanza Archeologica di Abruzzo) (Superintendency, hereafter) as part of the Sangro Valley Project. Monte Pallano is the location of several Iron Age Samnite archaeological sites at which excavations have been conducted since 1994.

The background material on the physical setting and geology of Monte Pallano, and a brief history of the Samnites is presented in Chapter II. A literature review of the archaeological work conducted about Monte Pallano and a description of the excavations in the area of Trench 8000 are also included. In addition, literature reviews on the applications of cross-correlation to geophysics, magnetics, and ground penetrating radar are presented.

Chapter III explains the methodology used to conduct cross-correlation tests on synthetic magnetic data in order to identify anomalies, and determine their horizontal and vertical positions. A discussion is presented of the methodology used for data collection and analysis of both the Monte Pallano magnetic and GPR data.

Chapter IV presents the analyses of the Monte Pallano magnetic and GPR data. In addition, a comparison of the magnetic and GPR interpretations is presented.

Chapter V summarizes the conclusions and findings of this thesis and presents suggestions for future work with cross-correlation analysis and geophysical investigations at Monte Pallano.

Appendices A and B provides additional discussion about the cross-correlation analyses of the Monte Pallano Magnetic data, magnetic profiles, and Monte Pallano GPR radargrams and amplitude time slices.

CHAPTER II

BACKGROUND

Physical Setting

Site Description/Geography

The Sangro River Valley, located in eastern central Italy approximately 110 km east of Rome, has been inhabited since at least the early Iron Age (Figures 2.1 and 2.2) (Lloyd et al., 1997). The Sangro Valley Project has been a cooperative effort since 1994, between the Superintendency, the School of Archaeology of the University of Leicester, Oberlin College, and the University of Oxford, for investigating archaeological sites throughout the valley (Sangro Valley Project, 1999). The emphasis of the Sangro Valley Project is on the Samnite, Roman, and early medieval periods (c. 500 B.C.E. – 1000 C.E.) (Sangro Valley Project, 1996).

Geology/Topography

The Sangro River Valley is a combination of relatively level floodplains and terraces adjacent to piedmont and alpine areas and is approximately 120 km in length. The Sangro River originates on the slopes of Mount Turchio of the central Apennines in the mountainous heart of the National Park of the Abruzzo. The river runs due south out of the park, before changing to a northeasterly course to the Adriatic Sea, where it flows into the sea between Ortona and Vasto (Lloyd et al., 1997).

The geology of the Sangro River Valley (Figures 2.3 and 2.4) consists of five basic geomorphological units: (Figures 2.3 and 2.4, 1 and 3 (H) – Oligocene to Messinian (Miocene) age pelitic turbidites of the Molise Basin and allocthonous pelagic units consisting of clays,

Figure 2.1 The location of the Sangro River Valley.
(Squyres, 1975, p. 342-343)
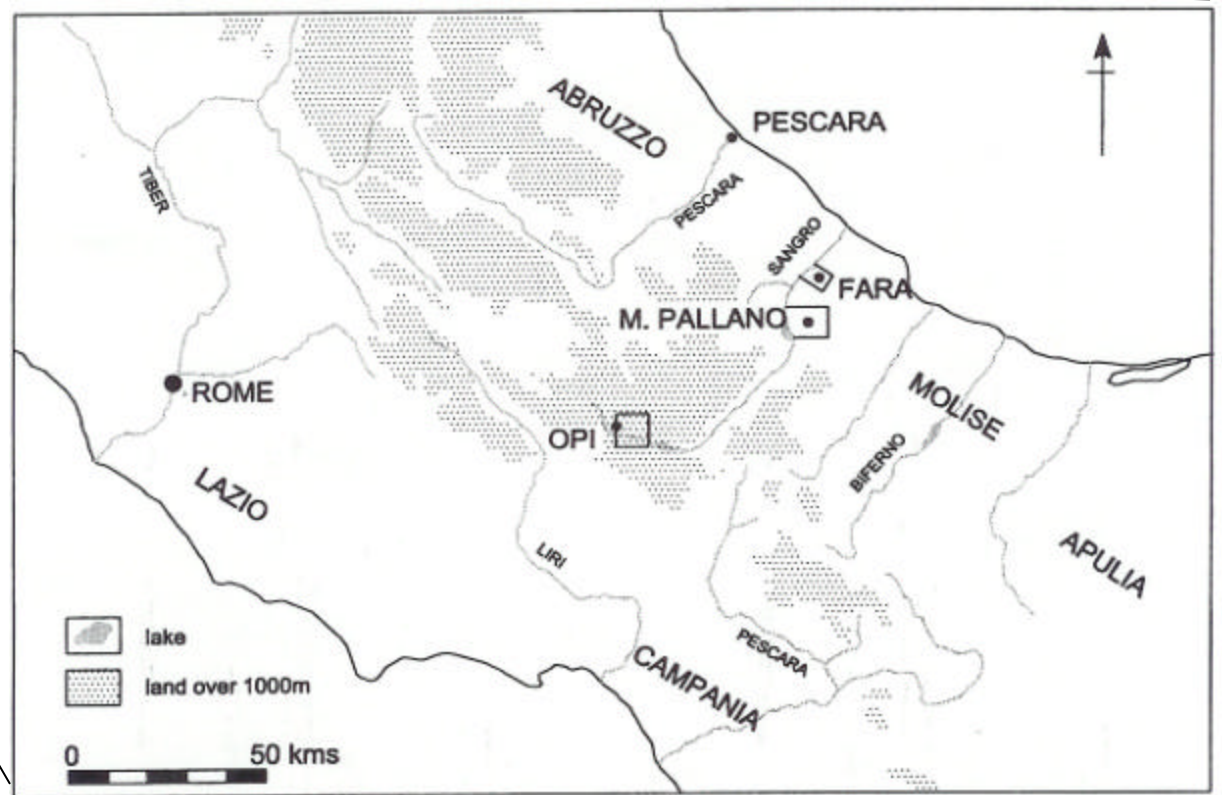
Figure 2.2 The location of Monte Pallano within the
Sangro River Valley. (Lloyd et al., 1997, fig. 1)
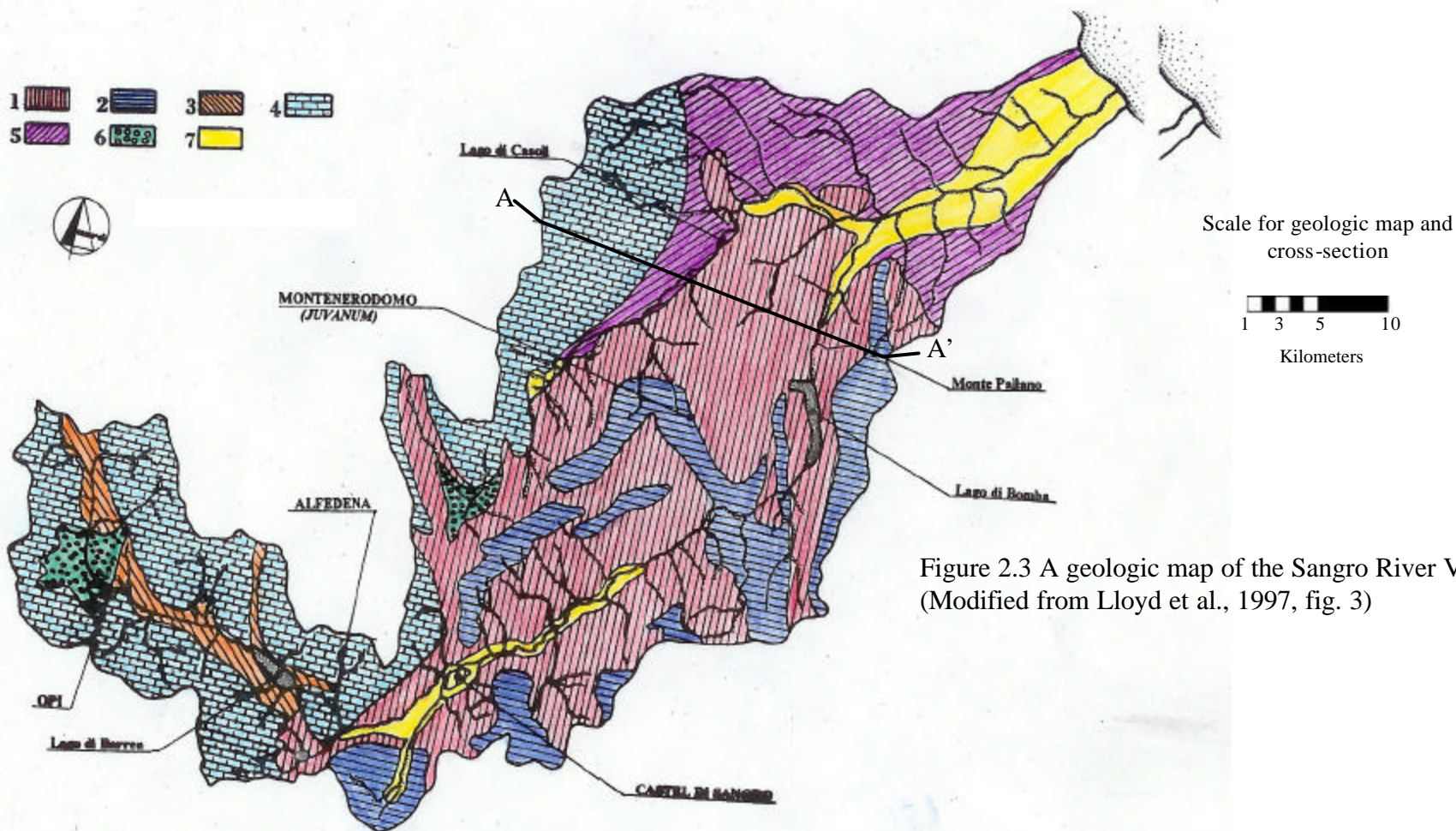
Figure 2.3 A geologic map of the Sangro River Valley. (Modified from Lloyd et al., 1997, fig. 3)

1) H - Pelitic turbidites of Molise basin and 'allocthonus' pelagic units. (Oligocene – Messinian (Miocene))

2) G - Units of Molise basin, isolated limestone peaks (Paleocene – Tortonian)

3) H - Sandy turbidites of carbonate platforms (Tortonian – Messinian)

4) G - Units of carbonate platforms: Latium – Abruzzi, Morrone, and Maiella mountains (Upper Triassic – Tortonian)

5) E & F - Clays sands and conglomerates of syn- and post orogenic sequences (Pliocene – Lower Pleistocene)

6) Q - Alluvial and lacustrine deposits, taluses and talus fan and slope breccias (Lower Pleistocene – Holocene)

7) B - Old and recent alluvial terraces (Middle Pleistocene – Holocene)

Vertical Exaggeration = 2.12 X
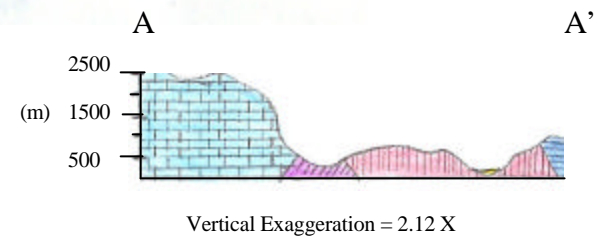
Figure 2.4 A geologic cross-section across Monte Pallano, trending northwest - southeast. (Modified from Lloyd et al., 1997, fig. 2)

sands, and marls; (Figures 2.3 and 2.4, 2 and 4 (G) - Paleocene to Tortonian age limestone peaks that make up Monte Pallano and the Upper Triassic to Tortonian age carbonate platforms of Mount Maiella; (Figures 2.3 and 2.4, 5 (E/F) - Pliocene to Lower Pleistocene age sands clays and conglomerates; (Figures 2.3 and 2.4, 6 (Q) – Lower Pleistocene to Holocene age alluvial terrace, lacustrine, and slope deposits; and (Figures 2.3 and 2.4, 7 (B)- Middle Pleistocene to Holocene age ancient and modern alluvial terraces (Lloyd et al., 1997). Monte Pallano is a north-northeast trending limestone peak with a maximum elevation of 1020 m. An exposed outcrop of the limestone bedrock that makes up Monte Pallano is presented in Figure 2.5.

Many of the archaeological sites within the Sangro River Valley are obscured by colluvial deposits, frost heaving, tectonism, and debris flows (Sangro Valley Project, 1996; 1999). The central Apennines is a seismically active zone with on-going uplift. These dynamic geomorphic surfaces create broad-scale slope erosion and failure, which are commonly seen in the Sangro River Valley. For this reason, archaeological sites in the Sangro River Valley are difficult to locate using the conventional archaeological methods such as surface collection. Non-invasive geophysical techniques can be used to locate buried archaeological features beneath sedimentary deposits.

Archaeological and Historical Background

The Sangro Valley Project is investigating the archaeological remains of cultures that existed in the Sangro River Valley between 500 B.C.E. and 1000 C.E. (Sangro Valley Project, 1996). Monte Pallano was inhabited by a variety of cultures from the early Bronze Age until the High Roman Empire and possibly during the Middle Ages (Cicchitti et al., 1996). Current excavations have revealed artifacts attributed to Bronze Age cultures, Samnites, the

6
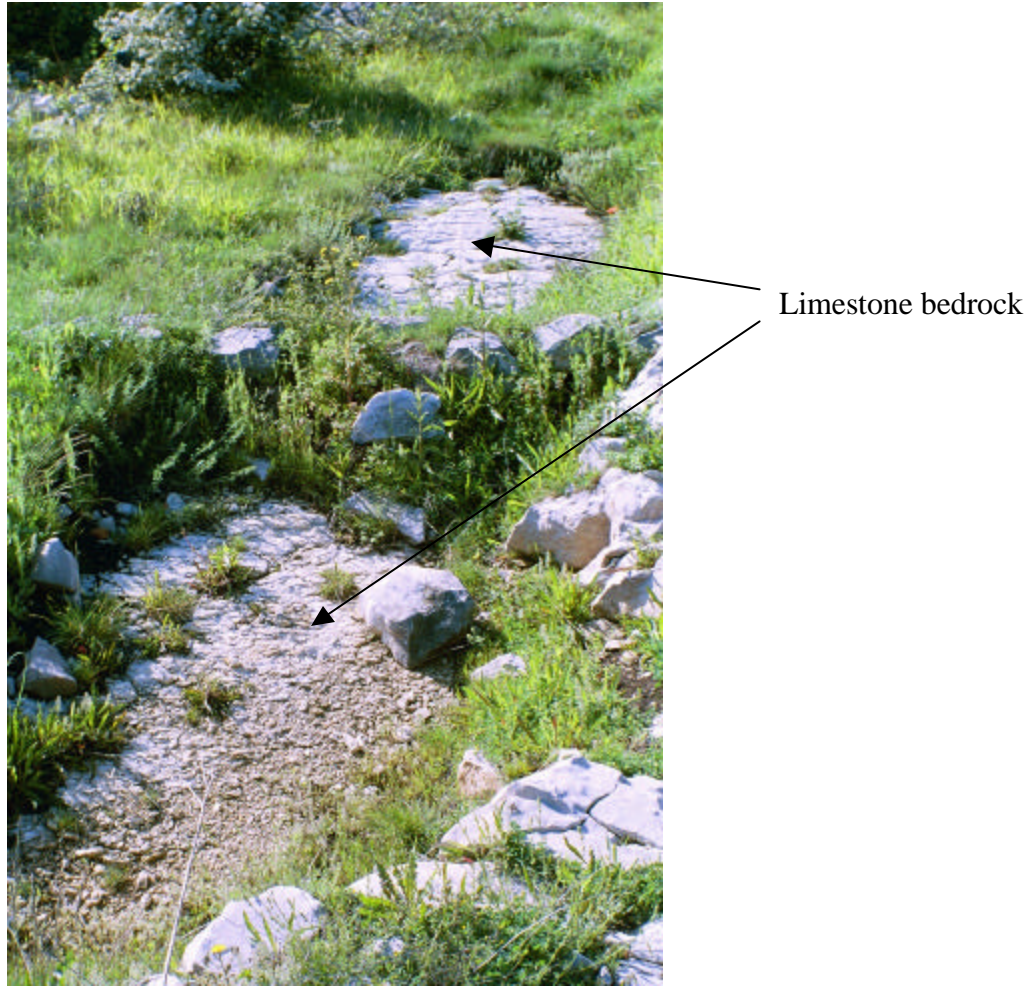
Limestone bedrock

Figure 2.5 The limestone bedrock exposed just north of Grid 1 on Monte Pallano. This photograph looks toward the north.

Roman Republic and Imperial periods, as well as the Middle Ages (Sangro Valley Project, 1999).

The main occupation period being investigated at Monte Pallano was that of the Iron Age culture of the Samnites. In peninsular Italy, Iron Age culture appeared to have begun during the 9th century B.C.E. and by the 8th century B.C.E. it had spread to the region of Samnium (Pallottino, 1955). By 500 B.C.E., the Samnites had migrated into the area we know as Samnium, which was inhabited by the Opici peoples. The origin of the Samnites prior to their occupation of Samnium is disputed. Strabo relates the story of the Sacred Spring in which the Samnites migrated from the country of the Sabines, while it is also believed that the Samnites may have instead been Indo-European immigrants (Salmon, 1967; Dench, 1995). By the 4th century B.C.E., Samnium was bounded on the north by the Sangrus (Sangro) River, on the east by the Plain of Apulia, on the west by the Plain of Campagnia, and on the south by the Aufidus (Oscan) River, covering at least 6000 square miles (Salmon, 1967).

During the 4th century, the Samnites expanded out of their mountainous country because of overpopulation and the need for more grazing land for their herds. They took over Lucania and parts of Etruscan Campania, including the city of Capua, at a time when these areas were weakened from extensive conflict. The Oscan language spread and its use increased as the Samnites extended the territory they controlled. They finally came into contact with the Roman peoples near the Liris Valley (Salmon, 1967).

The three Samnite Wars (343 – 290 B.C.E.) were a struggle between the Samnites and Romans for the control of Campania and ultimately of Italy. The Samnites were eventually defeated in 290 B.C.E. and signed a peace treaty becoming allies of Rome. The Samnites rebelled against Rome during the Pyrrhic War (280 – 272 B.C.E.) during Hannibal's invasion of

Italy in the late 3rd century B.C.E., and again during the Social War (91 - 82 B.C.E.) (Salmon, 1967). The Social War ended for the Samnites on November 1, 82 B.C.E. at the battle of the Colline Gate (Bennett, 1998). After the Social War, the Roman consul Cornelius Sulla attempted to exterminate the Samnites. The genocide was unsuccessful though the Samnites never again had the strength to contest Rome. The geographic name for Samnium remained long after the Samnites ceased being an independent people (Salmon, 1967).

On Monte Pallano was the most easterly of the six or so Archaic Age (590 – 490 B.C.E) hill-forts in the Sangro River Valley. It was near the areas inhabited by the Samnite Carricini, Pentri and Frentani. Colonna (1955) wrote the first archaeological discussion about Monte Pallano and investigated the polygonal stone fortification walls on the northeastern side of the summit. Salmon (1967; 1982) and Dench (1995) present comprehensive works on the history, culture, and identity of the Samnites. Barker (1977) presents a survey of the settlement patterns at Samnite farmsteads in the Biferno Valley in Molise and a geomorphological study of soils in order to better understand their agricultural practices. It has been proposed by La Regina (1989) that Monte Pallano was "the 'capital' of a small tribe of Samnite stock identifiable with the (northern) Lucani" (Faustoferri A. and J. Lloyd, 1998). Faustoferri and Lloyd (1998) discussed the hilltop stone fortifications on Monte Pallano and their role in pre-Imperial settlement patterns. Oakley (1995) compiled a monograph of the hill-forts of the Samnites and identified numerous new sites. Bispham et al. (2000) briefly investigated Monte Pallano's megalithic walls and the message they were intended to convey to observers.

Archaeological Investigations at Monte Pallano under the direction of the Superintendency of Abruzzo (1994 – 2001)

Excavations have been conducted at Monte Pallano since 1994 under the direction of the Superintendency, in cooperation with Oxford University and Oberlin College. Several stonewalls have been discovered in and around Trench 8000 on Monte Pallano (Figures 2.6 – 2.8). Two parallel stonewalls, trending northwest to southeast, have been discovered in Trench 8000, walls 8010/8024 and 8017. Wall 8010/8024 is a polygonal limestone terrace wall at least 2 m in height, though possibly higher in antiquity, and was between 1 and 1.7 m thick. This wall was unmortared and had partially collapsed prior to the middle of the 1st century B.C.E., possibly by either an earthquake or enemy activity (Sangro Valley Project, 2000). The terrace created just to the north of wall 8010/8024 contained architectural terracottas dated to the 2nd century B.C.E. and religious debris dated to the 2nd and 3rd centuries B.C.E. and was thought to be the location of one or more ancient buildings (Sangro Valley Project, 2001). The original construction of Wall 8010/8024 was dated to the middle of the 2nd century B.C.E. Wall 8203, discovered in Trench 8200, was thought to be constructed during an alteration of Wall 8010/8024 during the Augustan period (Figures 2.7 and 2.8). Wall 8203 trends north south and is perpendicular to wall 8010/8024 (Sangro Valley Project, 2001).

Wall 8017 is a smaller limestone wall with yellow mortar, which would have originally stood about 1.5 m high. The lower courses of this wall extend east into Trench 8300 as Wall 8306 while the upper courses of the wall in this trench have collapsed. This wall is thought to date after the Social War, between (70 and 50 B.C.E.) (Sangro Valley Project, 2000; 2001). Two mortared walls, 8006 and 8007, were discovered in the southeast corner of Trench 8000. These
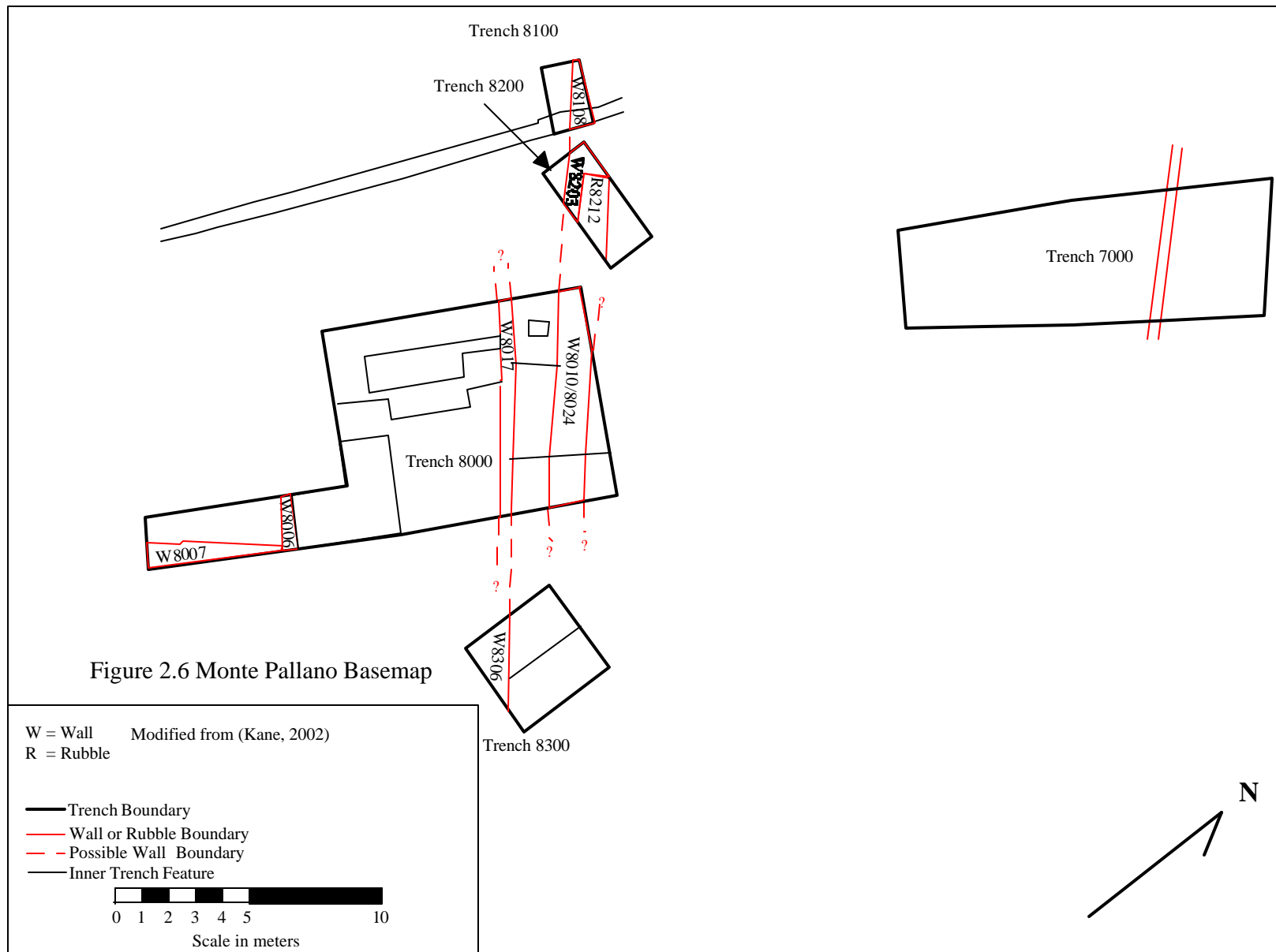
Figure 2.6 Monte Pallano Basemap

Trench 8100

Trench 8200

Trench 7000

W8108

R8212

W8203

W8017

W8010/8024

Trench 8000

W8006

W8007

W8306

Trench 8300

W = Wall   Modified from (Kane, 2002)
R = Rubble

Trench Boundary
Wall or Rubble Boundary
Possible Wall Boundary
Inner Trench Feature

0 1 2 3 4 5   10
Scale in meters

N

Figure 2.7 The stonewall 8010/8024 in Trench 8000 and an enlarged portion of the wall showing its polygonal construction. This photograph.looks toward the south.

Trench 8000

Wall 8010/8024

Figure 2.8 The parallel stonewalls 8010/8024 and 8017 in Trench 8000. This photograph looks toward the north.

Trench 8000

Wall 8017   Wall 8010/8024

walls lie at right angles to one another and probably formed the corner of a building referred to as the "Roman House." This structure is thought either to have been in use by the early 1st century B.C.E. or to have been built in the middle to late 1st century B.C.E. A charcoal layer was present on the inside of the walls which may suggest evidence that this building was destroyed by fire (Sangro Valley Project, 2000; 2001).

Archaeological Excavations Summer 2002

Two small trenches, 8800 and 8850, were excavated by the summer field school led by Oxford University and Oberlin College to "ground-truth" or field test the preliminary results of the geophysical data collected for this thesis (Figure 2.9). One course of large stones was discovered in Trenches 8800 and 8850 forming the corner of a small building with its western wall extending south. These walls were buried just beneath the surface vegetation. The construction technique used for these walls was similar to walls of the 3rd or 2nd century B.C.E. from the site to the west excavated by the Superintendency (S. Kane, personal communication, 2003). This construction technique involved building a wall with natural blocks of limestone stacked on their sides so that the horizontal bedding faced out. In the area excavated by the Superintendency these stones were quarried from the limestone bedrock upslope and not from a distant quarry (Sangro Valley Project, 1996).

Magnetic Prospection in Archaeology

Magnetic prospecting has been used for geologic surveys since early in the 20th century; the only geophysical technique with a longer history is resistivity. Magnetometry is a passive geophysical technique, which measures the magnetic field of the earth and locates anomalies, which diverge from the expected field values. The first use of a magnetometer for

Trench 8100

Trench 8250

Trench 8200

W8202

Trench 8700

Trench 8900

Trench 7000

W8108

W8203

R8212

W8017

W8010/8024

?

?

Trench 8000

W8006

W8007

?

?

?

?

W8800

W8850

Trench 8850

?

W8306
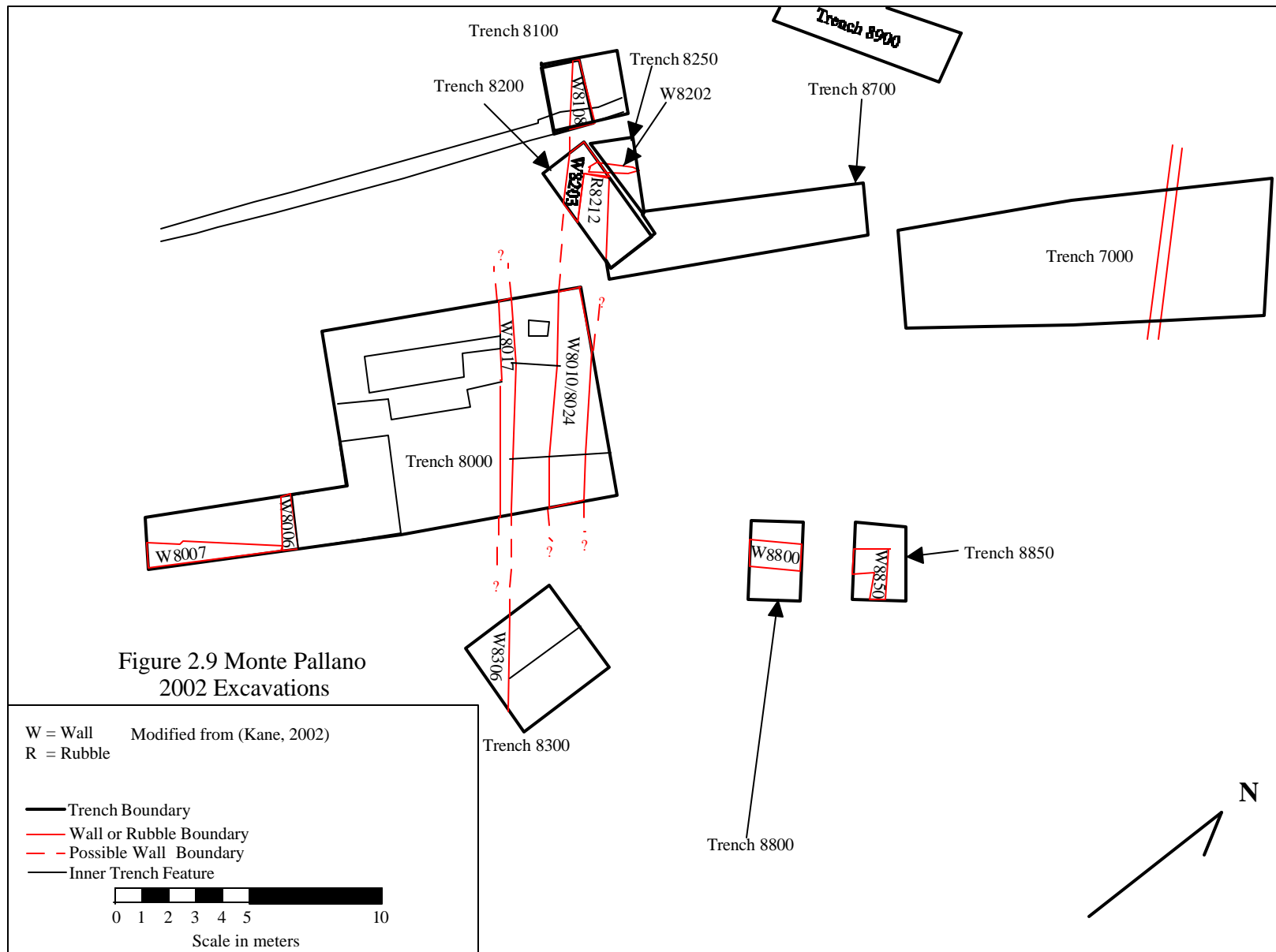
Figure 2.9 Monte Pallano
2002 Excavations

Trench 8300

Trench 8800

W = Wall   Modified from (Kane, 2002)
R = Rubble

N

Trench Boundary
Wall or Rubble Boundary
Possible Wall Boundary
Inner Trench Feature

0 1 2 3 4 5   10
Scale in meters

archaeological prospection was in September 1957 in the area of Kirstall Abbey near Leeds

where anomalies were detected, which were believed to be caused by a buried forge (Scollar et

al., 1990). Shortly thereafter in 1958, Aitken and Hall created a proton precession magnetometer

and conducted an archaeogeophysical survey near Petersborough in search of Romano-British

pottery kilns (Aitken et al., 1958).

The physics of magnetism and the earth's magnetic field, which underlie the technique of

magnetic prospection, have been understood for sometime (Tite, 1972; Aitken, 1974; Scollar et

al., 1990; Burger, 1992; Milsom, 1996) The design of an archaeological magnetic survey is

based on the site specific conditions, desired data density and type of instrument. The survey

design needs to address possible magnetic interferences including anthropogenic objects, nearby

rocks or soil with high susceptibilities, and diurnal variations in the magnetic field (Tite, 1972;

Aitken, 1974; Weymouth, 1986; Burger, 1992; Milsom, 1996).

The magnetic susceptibility of a site's soil is important for determining the success of a

magnetic survey. In order to detect anomaly sources a sufficient contrast must exist between the

soil and the anomaly source(s). Variations in the magnetic susceptibility between topsoil and the

underlying sub-soil or rock can allow for features such as pits and ditches to be located (Tite,

1972; Aitken, 1974; Weymouth, 1986). This difference can be caused by the production of

maghemite from the decay of organic materials in the soil (Le Borgne, 1955, 1960; Breiner,

1973; Aitken, 1974; von Frese, 1984) or by the action of burning (Tite, 1972; Aitken, 1974; von

Frese, 1984). Maghemite is a mineral with the same structure as magnetite, Fe_3O_4, but with one

ninth of the iron atoms replaced by another ion, such as sodium or magnesium (Scollar, et al.,

1990). Buried stonewalls often exhibited similar linear magnetic signatures to ditches when they

were constructed of materials with low magnetic susceptibility, such as limestone (Scollar et al., 1990; Aitken, 1974).

Thermoremanent magnetism, the acquisition of permanent magnetization when an object cools below Curie or blocking temperature, is central to locating buried pottery kilns, iron artifacts, and iron slag deposits (Tite, 1972; Aitken, 1974; von Frese, 1984; von Frese and Noble, 1984; Pattantyus, 1986; Scollar et al., 1990). Pottery also often possesses thermoremnant magnetism and large clusters of pots of pottery sherds can be located using magnetics (Aitken, 1974).

The ability to locate air-filled cavities or voids such as burials or tunnels is based on the void's size and the magnetic susceptibility contrast between the air filled void and the surrounding matrix (Aitken, 1974). There are numerous examples of voids being detected with magnetic prospection including locating Iron Age cremations near Kaliz, Poland (Dabrowski and Linington, 1967), cut rock burial chambers at the Etruscan necrepoleis of Tarquinia and Cerveteri, Italy (Linington, 1961) and tunnels cut from volcanic tuff beneath the Pyramid of the Sun, Teotihuacan, Mexico (Arzate et al., 1990; Chavez et al., 2001).

Archeological magnetic prospection requires instruments with greater sensitivities of resolution of the magnetic signal, 1 nT which is approximately 1 part in 50,000 for example, than those used for mineral and geologic surveys, because the strengths of the induced fields of the archaeological features are much smaller (Tite, 1972; Aitken, 1974). Several high-resolution magnetometers have been developed since 1958. The first was the proton precession magnetometer that measured the earth's magnetic field based on the frequency of precession of protons in a fluid (Tite, 1972; Aitken, 1974; Weymouth, 1986; Scollar et al., 1990). Another was the optically pumped cesium magnetometer that optically measured the frequency of precession

of an atomic magnetic moment. Optically pumped magnetometers were also created for the elements rubidium and helium in place of the cesium. This type of magnetometer provided greater sensitivity for weak anomalies in soils with low noise as well as providing a continuous signal/data output (Tite, 1972; Aitken, 1974; Scollar et al., 1990).

The magnetic gradiometer measured the differential magnetic field by computing the difference between the two readings collected simultaneously from the same location but from two sensors at different heights (Aitken, 1974). The gradiometer is insensitive to the effects of diurnal variation. The dual sensor proton precession gradiometer was developed by Scollar (Mundie, 1962; Scollar, 1965). The fluxgate gradiometer is a device that computes the differential magnetic field based on the magnetic behavior of a metallic alloy in the instrument. This continuous reading instrument could operate in strong magnetic gradients unlike the proton precession instruments (Tite, 1961; Alldred and Aitken, 1966; Tite, 1972; Aitken, 1974; Scollar et al., 1990). It also measures a single component, vertical or horizontal, of the total magnetic field (Milsom, 1996).

The induced magnetic fields generated by numerous geometries, both regular and irregular, have been computed and modeled (Pentz, 1940; Talwani, 1965; Linington, 1972; Breiner, 1973; Scollar et al., 1990;). These computed fields were compared with magnetic data in order to identify anomalies with similar forms (Burns, 1981; Burns et al., 1983) or were used as part of matched filter or cross-correlation analyses as noted above. The magnetic curves of irregular shapes were modeled by collecting data across scaled down archaeological features, such as ditches or walls, with a scaled down version of a magnetometer (Aiken and Alldred, 1964; Aspinall and Lynam; 1968; Tite and Mullins, 1970).

There are numerous filtering techniques available for magnetic analysis, including reduction to the pole, upward or downward continuation, deconvolution, and Fourier Transform methods. Reduction to the pole is a technique that transforms a magnetic profile into what it would look like if the anomaly source were located at the earth's north magnetic pole. This brings the anomaly peak directly over the anomaly location (Baranov, 1957; Baranov and Naudy, 1964; von Frese, 1984; Silva, 1986; Scollar et al., 1990; Blakely, 1995). Upward and downward continuation transforms a profile to appear as it would if collected from a different height above the anomaly source. Downward continuation is often used with aeromagnetic data to visualize the data as if it were collected at the ground surface (Scollar, 1970; Burger, 1992). Convolution filtering can also be used to remove background trends that obscure anomalies (Weymouth and Huggins, 1981). Magnetic data has also been analyzed with a variety of Fourier Transform methods (Bhattacharyya, 1965; Bhattacharyya and Navolio, 1970; Scollar, 1970; Bhattacharyya, 1978).

A number of inversion methods have been developed for estimating the depth of an anomaly source based on an assumption of the source's geometry. One of the most predominant is Peters half slope method (Peters, 1949; Robinson and Coruh, 1988). Other inversion methods include a series of reference maps for rectangular prisms of various dimensions (Vacquier et al., 1951) and the Werner deconvolution developed by S. Werner in 1953, and further adapted by Hartman, Tesky, and Friedberg (1971) (Robinson and Coruh, 1988).

Numerous data display methods have been applied to magnetic data to help visualize anomalies including contour maps, symbols representing specific anomaly strengths, dot density maps, isometric line traces, and 3-D wire frames surfaces (Scollar, 1965; Scollar and Kruecheburg, 1966; Linington, 1970; Tite, 1972; Scollar et al., 1986). The creation of these

visual displays is a form of low-pass filtering as it removes small-scale features (Tite, 1972; Scollar et al., 1990).

Magnetic prospecting has been successfully applied to a wide variety of archaeological sites including hill-forts, urban sites, production sites and ancient roadways. Aitken and Tite (1962) surveyed several hill-forts in England and Tite (1967) conducted a survey at a hill-fort in Rainsborough, Northants, England and delineated the outer ditch defenses, a guardhouse and the inner fort area. The search for the Greek city of Sybaris was an excellent example of the use of magnetometry to locate buried walls (Rainey and Lerici, 1967). May (1970) identified numerous linear ditches, roads, and walls at Dragonby, an Iron Age settlement near Scanthorpe, Lincolnshire. Linington (1967) surveyed a large scale Etruscan town at Tarquinia, Italy. Tite (1966) located several iron smelting furnaces near Targua, Nigeria. The first archaeomagnetic survey conducted in the western hemisphere was at Angel Mounds, Indiana, at the Fairfield Village Middle Mississippian site (Black and Johnston, 1962; Johnston, 1961, 1964). The first application of magnetics to monumental architecture in the New World was at the Olmec site in Veracruz Mexico (Breiner and Coe, 1972; Morrison et al., 1970). Eppelbaum et al. (2001) investigated the structure of ancient roads in Israel and Young and Droege (1986) surveyed building foundations at Fort Wilkins, State Park, Michigan.

Magnetic surveys have also been conducted underwater to locate shipwrecks (Hall, 1966, Green et al., 1967; Green and Martin, 1970, 1970a). The magnetometer would either be towed behind a boat or carried by a diver.

Ground Penetrating Radar

Ground penetrating radar or "GPR" as it is commonly called, has been used for archaeological prospection since 1975 when Vickers et al. (1976) investigated buried walls

20

within Chaco Canyon, New Mexico. GPR is an active geophysical technique which emits radar

waves from an antenna into the ground that are reflected off subsurface objects and features

based on their electromagnetic properties. GPR is useful for creating approximate subsurface

profiles of archaeological features ranging from depths of a few tens of centimeters to greater

than five meters (Conyers and Goodman, 1997). GPR was shown to delineate the locations of

buried walls and architectural features at Monte Pallano (Garrison and Schneider, 2001) as well

as burials, hearths and trenches (Conyers and Goodman, 1997).

The desired depth penetration and anomaly source size resolution affects the antenna

frequency choice as presented by Sternberg and McGill (1995) who investigated differences in

GPR penetration with various antenna frequencies, and located numerous buried plaster, adobe,

and rock walls in high clay soils at various sites in Arizona.

Estimates for the velocity of radar waves passing through the subsurface are necessary

for the depth determination of buried features. Numerous techniques for determining radar

velocities have been developed (Tillard and Dubois, 1995; Reppert et al., 2000)

The success of GPR surveying is dependant on soil mineralogy, clay content and ground

moisture (Conyers and Goodman, 1997). Soils with high water contents greatly attenuate the

radar propagation reducing the depth penetration of the signal (Topp et al., 1980).

There are numerous methods for GPR data processing explained by Olhoeft (2000) for

determining anomaly position, orientation and soil properties from GPR data. Fisher et al.

(1992) presents analysis of wide-aperture GPR data, and Sun and Young (1995) explain the

removal of surface scatter or radar waves using migration. The use of amplitude time slices is a

useful method for creating 2-D and 3-D visualizations of a site (Conyers and Goodman, 1997;

Leucci, 2002). Hildebrand et al. (2002) presents the comparability of seismic reflection and

GPR data, and Goodman (1994) models radargrams for the reflected radar waves of different subsurface geometries.

Successful GPR surveys have been used to locate a wide variety of subsurface targets, including buried walls from the Stenton Mansion in Stenton Park Philadelphia by Bevan and Kenyon (1975), royal burial chambers in Kazakhstan by Pipan et al. (2001), and the detection of old stonewalls beneath a Japanese castle by Zhou and Sato (2001).

Multi-Sensor Technique Prospection

Magnetic and GPR prospection has been combined in order to provide greater confidence to determine the nature of anomaly sources and to locate archaeological features with different physical properties. Heese (1999) presents considerations for use of either single or multiple geophysical techniques at an archaeological site. These two geophysical techniques have been successfully combined in numerous instances, e.g., locating archaeological features of Washington's camp at Valley Forge National Historical Park, Pennsylvania (Parrington, 1979), the investigation of the Deer Creek site in Oklahoma (Weymouth and Huggins, 1981; Weymouth and Bevan, 1983), in determining the location of a stone edifice of a medieval church Olonium (Arlsan et al., 1999), tunnels in basalt beneath the Pyramid of the Sun (Chavez et al., 2001), and architectural features in an ancient amphora workshop (Sarris et al., 2002).

This thesis builds on this previous geophysical research by expanding the understanding of cross-correlation's application to magnetic analysis for locating anomaly sources and the capabilities of the combined techniques of GPR and magnetometry at Monte Pallano, Italy.

CHAPTER III

METHODOLOGY

Synthetic Modeling of Magnetic Data with Cross-Correlation

Introduction

Cross-correlation is a statistical technique commonly used to analyze time series data but it has also been used as a tool for processing both total field magnetic data and seismic data. Cross-correlation has been used to process seismic reflection data, both as a general filtering operation by Jones et al. (1954) and as a method of optimizing common depth point (CDP) stacking filters (Schneider et al., 1968). In addition Yilmaz (1987) discusses the uses of cross-correlation to compute the static shifts for common midpoint data, for creating a Wiener filter, and for vibroseis correlation between a frequency modulated source signal and the recorded signal. Naudy (1971) used cross-correlation to determine the depths to magnetic anomaly sources from aeromagnetic data by varying the depth and dimensions of the vertical dike theoretical sources. Cross-correlation has also been used to identify tectonic trends in aeromagnetic data from Northern Saskatchewan (Agarwal and Kanasewich, 1971) and to estimate stacking velocities for seismic data (Tieman, 1993).

Alder (1988) presented an example of the viability of cross-correlation in archaeological prospection for determining the depths of buried kilns by modeling them for several synthetic cross-correlation tests. The synthetic cross-correlation tests conducted by Alder were for single anomaly sources at three separate depths using pilot signals with seven samples in the absence of noise. These tests provided a starting point for this thesis for the use and, hopefully, continued

development of a cross-correlation technique for analyzing magnetic data. In this thesis I have

evaluated the effects of seven parameters: (1) the depth of a spherical anomaly source, (2) the

number of samples in the pilot signals, (3) the radii of a spherical anomaly source, (4) the

magnetic susceptibility contrast between an anomaly source and the surrounding soil, (5) the

addition of varying levels of random noise to the synthetic data profiles, (6) the number of

anomaly sources, and (7) the spacing between the anomaly sources.

This project has investigated the usefulness of cross-correlation on magnetic data for

increasing signal to noise ratio (S/N) and identifying the horizontal and vertical positions of

anomaly sources by expanding on the work of Alder (1988). Cross-correlation comparisons

were conducted between magnetic data profiles and computed total field anomaly and vertical

gradient anomaly pilot signals. Cross-correlation is a commonly used statistical test which

computes the amount of similarity between two data sets, at each match point as the pilot signal

move across the data profile, thereby comparing each point of the pilot signal with each point on

the profile. The pilot signal is a synthetic signal with a computed or an arbitrarily defined shape,

which is being searched for within the data profile. The cross-correlation is the covariance

(COV) of the sections of the two profiles divided by the product of the standard deviation(s) of

the compared portions of each profile. The normalized correlation coefficient (r_m) was computed

for each match position using the following cross-correlation equation provided in Davis (1986):

$$r_m = \frac{n * \sum Y_1 Y_2 - \sum Y_1 \sum Y_2}{\sqrt{[n * \sum Y_1^{2} - (\sum Y_1)^2][n * \sum Y_2^{2} - (\sum Y_2)^2]}} \tag{1}$$

or equivalently,

$$r_m = \frac{COV_{1,2}}{S_1 \bullet S_2} \tag{2}$$

24

In equation (1), n* is the number of match positions compared on each profile, Y_1 is the magnetic field value of the magnetic data profile, Y_2 is the magnetic field value of the pilot signal. The value r_m is the correlation coefficient with values ranging from (1 to –1). Values of r_m of (1 or –1) denote perfect positive or negative correlation, while a value of (0) denotes no correlation. In equation (2), $COV_{1,2}$ is the covariance of the sections of profiles, which are compared at a specific match position, and S_1 and S_2 are the standard deviations of these same sections of the profiles. The r_m values were plotted on correlograms against the (x) positions.

Modeling Synthetic Magnetic Data

Cross-correlation tests were conducted with synthetic magnetic data to determine the sensitivity of position and depth estimates of anomaly sources as a possible means of locating anomaly sources in magnetic data. These tests investigated which of the seven parameters affected the cross-correlation of magnetic data and the optimal range of values for those parameters. Linear synthetic magnetic profiles were computed for transects crossing over one or more buried anomaly sources. These anomaly sources were homogeneous spheres buried at several depths (Linington, 1964; Tite, 1966). The magnetic profile for a sphere was used because it simplifies the geometries of many common archaeological features, because of its ease of computation, and because it avoids the problems of anomaly source orientation (Linington, 1964; 1966). The profiles and pilot signals were created using the following equations for computing the magnetic total field anomaly (F_{AT}) of a buried sphere (Burger, 1992):

$$Z_A = \frac{(\frac{4}{3}pR^3kF_E)\sin i}{(x^2+z^2)^{3/2}}[\frac{3z^2}{(x^2+z^2)} - (\frac{3xz}{(x^2+z^2)}\cot i) - 1] \qquad (3)$$

$$H_A = \frac{(\frac{4}{3}pR^3kF_E)\cos i}{(x^2+z^2)^{3/2}}[(\frac{3x^2}{(x^2+z^2)} - 1) - (\frac{3xz}{(x^2+z^2)}\tan i)] \qquad (4)$$

$$F_{AT} = Z_A \sin i + H_A \cos a \cos i \tag{5}$$

The vertical gradient profiles and pilot signals were computed from two sets of F_{at} values:

$$VG = \frac{(F_{atLowerprobe} - F_{atUpperprobe})}{(h_{upperprobe} - h_{lowerprobe})} \tag{6}$$

In equations (3, 4, 5, and 6), **R** is the radius of the spherical anomaly source (m) (Figure 3.1), **k** is the magnetic susceptibility contrast between the anomaly sphere and the surrounding soil (cgs emu), $\mathbf{F_E}$ is the undisturbed earth's magnetic field (nT), **x** is the horizontal distance from the center of the sphere (m), **z** is the depth of the center of the sphere below ground surface (m), **i** is the inclination of the earth's magnetic field (degrees), and **a** is the angle between magnetic north and $\mathbf{H_A}$ (degrees). $\mathbf{F_{AT}}$ is the portion of the anomalous field F_A in the direction of the earth's undisturbed main field. $\mathbf{F_{AT}}$ was computed from $\mathbf{Z_A}$, the vertical induced magnetic field of the anomaly, and $\mathbf{H_A}$, the horizontal induced magnetic field of the anomaly. **VG** is the vertical gradient value (nT/m), $\mathbf{F_{AT\ Lowerprobe}}$ is the $\mathbf{F_{AT}}$ value recorded for the lower gradiometer probe, $\mathbf{F_{AT\ Upperprobe}}$ is the $\mathbf{F_{AT}}$ value recorded for the upper gradiometer probe, $h_{\mathbf{Lowerprobe}}$ is the height of the lower gradiometer probe above the ground surface, and $h_{\mathbf{Upperprobe}}$ is the height of the upper gradiometer probe above the ground surface. All synthetic profiles and pilot signals used for the synthetic tests were computed for transects trending south to true north, having a value for **a** of 0 degrees.

Three parameters held constant for all tests were: the strength of the earth's magnetic field, ($\mathbf{F_E} = 46038$ nT); its inclination ($\mathbf{i} = 58$ degrees 15 minutes); and its declination ($\mathbf{d} = 1$ degree, 37 minutes). These parameters were derived from the 2000 International Geographic Reference Field (IGRF) with the Geomag v 4.0 software created by National Oceanic and Atmospheric Administration (NOAA). The earth's magnetic field was computed for Monte

Cross-Sectional View

Plan View
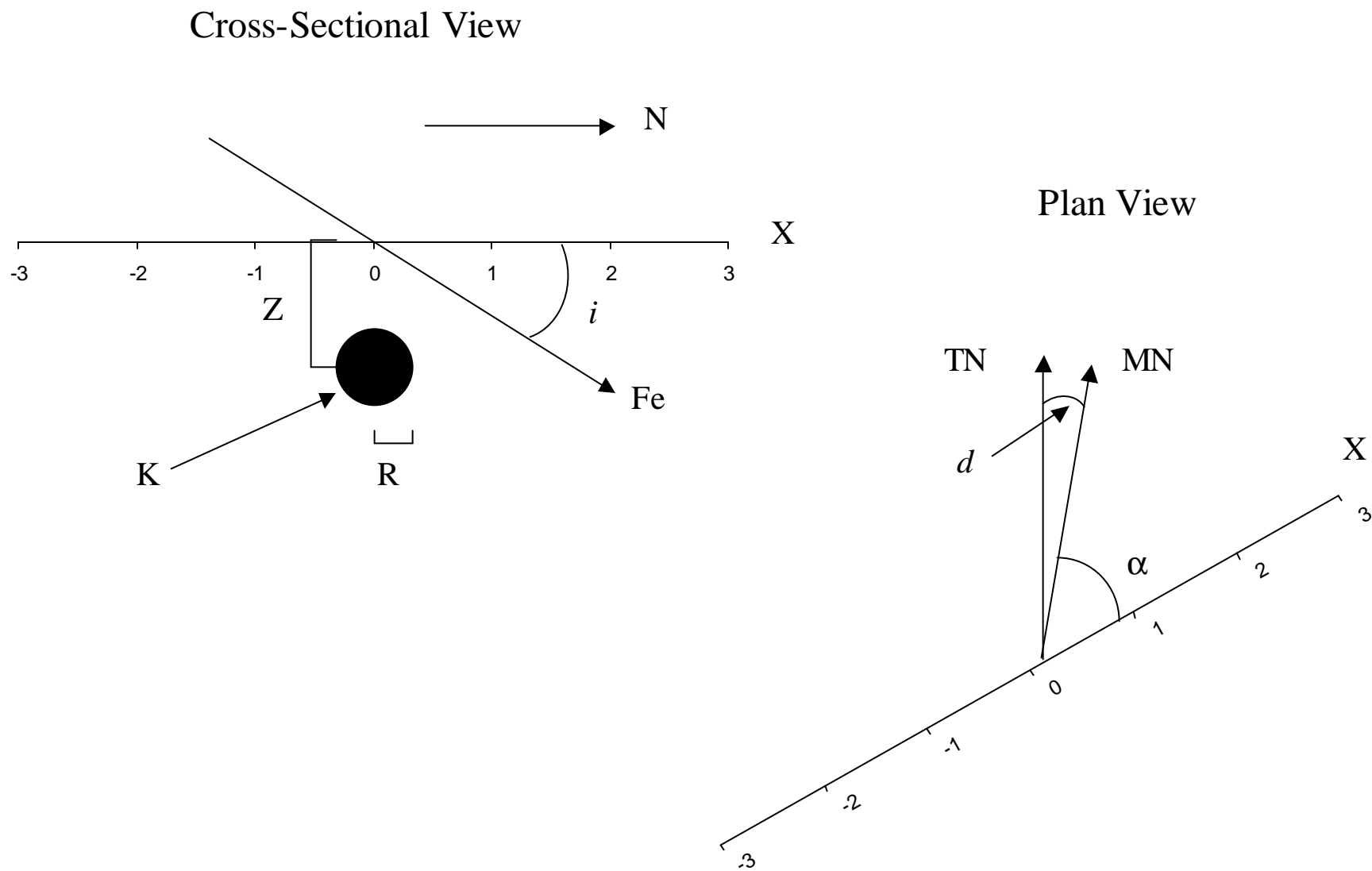
Figure 3.1 - The orientation of parameters for the computation of the magnetic field of a spherical anomaly source.

Pallano, Italy (latitude: 42 degrees, 1 minute, 20 seconds; longitude: 13 degrees, 42 minutes, 18 seconds; elevation: 1.02 kilometers) for May 12, 2002.

The value of **k** of 0.00004 cgs emu was computed for a limestone wall, 0.00005 cgs emu, buried in clay sediment, 0.00009 cgs emu (Burger, 1992). The ancient stonewalls on Monte Pallano were built from the limestone bedrock which makes up much of Monte Pallano. Limestone commonly contains little to no magnetite and therefore has a very low magnetic susceptibility. Topsoil tends to have higher magnetic susceptibilities than its parent rock because of the formation of maghemite by organic action (Le Borgne, 1955, 1960; Breiner, 1973; Aitken, 1974; von Frese, 1984) or by the action of burning (Tite, 1972; Aitken, 1974; von Frese, 1984). In addition magnetite is commonly concentrated in sediments as it is a very resistant mineral that forms from goethite or hydrated iron oxide forms.

Parameters

Seven different parameters were varied for experimentation with the synthetic total field and vertical gradient data. These parameters were again: (1) depth of the anomaly sphere, (2) length of the pilot signals, (3) radii of the anomaly sphere, (4) magnetic susceptibility contrast of the anomaly sphere, (5) addition of varying levels of random noise, (6) number of anomaly sources, and (7) spacing of anomaly sources. What is presented now is a discussion of the effect of each parameter on the efficacy of cross-correlation to identify the presence of anomalies and to resolve the position and depth of both test and archaeological anomaly sources. In addition a comparison between the total field and vertical gradient cross-correlations is presented.

Total Field Single Anomaly Profiles

Six magnetic total-field anomalies were computed, each with a single anomaly with (z) values of 0.5, 1, 2, 3, 4, or 5 m located at the (x) position of 0 m. These are presented

individually in (Figure 3.2), and together at the same scale in (Figure 3.3). These six profiles were the basis for the majority of my experiments. The profiles for these buried spheres had high positive amplitudes and narrow peak widths as one would expect. The maximum positive amplitude decreased and the signal width increased as (z) increased. The maximum positive amplitudes ranged from 9.02 nT for (z) = 0.5 m to 0.009 nT for (z) = 5 m. This is indicative of a "fall-off" factor that follows the cube power (Breiner, 1973). In the profiles for the anomaly sources at depths greater than 1 m, the position of the positive peaks are offset by 0.5 to 1 m south of the actual anomaly source, (x) position of 0 m.

Synthetic Vertical Gradient Single Anomaly Profiles

Synthetic vertical gradient anomaly source profiles (Figures 3.4 and 3.5) were created for the same spherical anomaly source depths as the total field anomaly source profiles and signals, 0.5, 1,2, 3, 4, and 5 m. These profiles were computed with a lower probe height of 0.5 m above ground surface and an upper probe height of 1.94 m above the ground surface, producing a gradiometer probe separation of 1.44 m. These probe heights were used so as to mimic the values used for the magnetic data collected at Monte Pallano. The vertical gradient single component profiles followed the same general trend as the total field anomaly profiles with decreasing maximum positive amplitude and increasing signal width as (z) increased. The maximum positive amplitudes ranged from 0.729 nT/m for (z) = 0.5 m to 0.003 nT/m for (z) = 5 m. In the profiles for the anomaly sources at depths greater than 0.5 m, the position of the positive peaks are offset by 0.5 to 1 m south of the actual anomaly source, (x) position of 0 m.

Figure 3.2 Synthetic F_{at}, single-source magnetic anomalies computed for uniformly magnetized spheres buried at various depths.
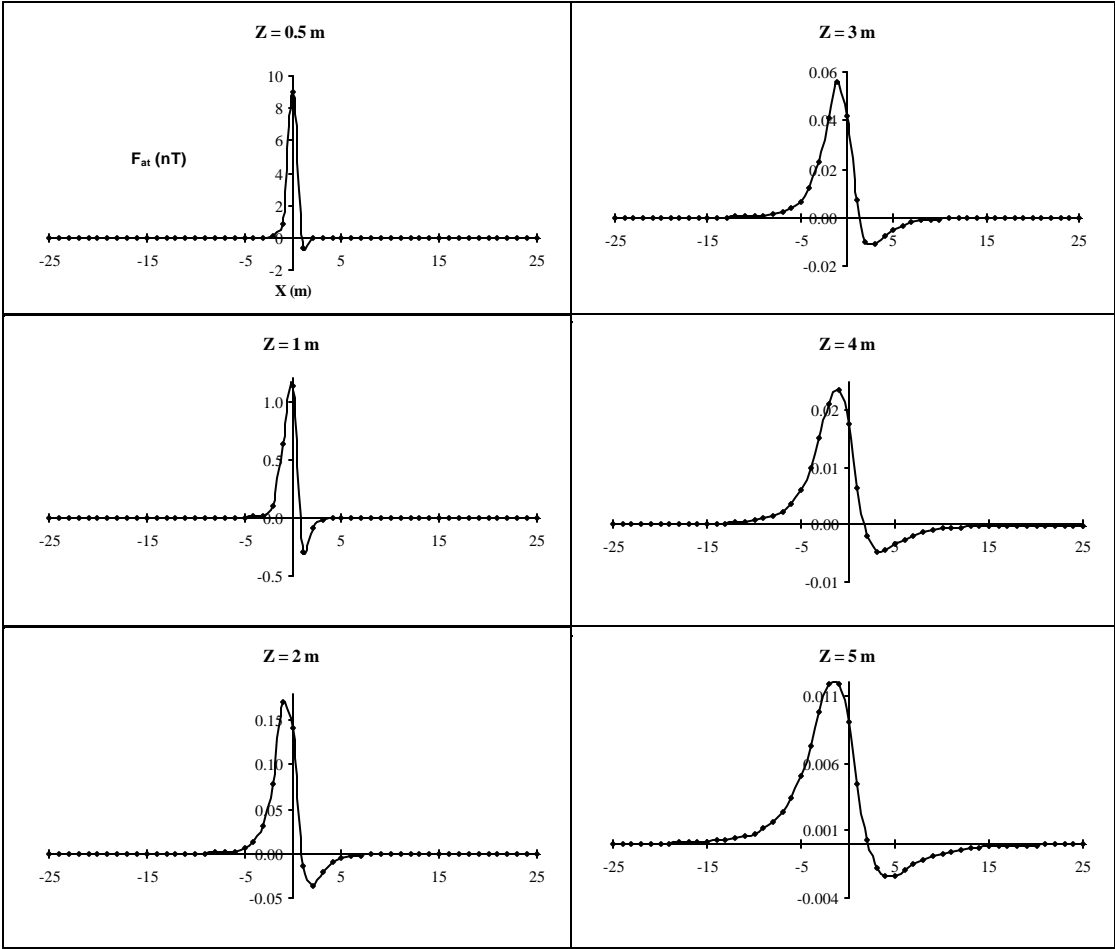
Figure 3.3 Synthetic F$_{at}$, single-source magnetic anomalies computed for uniformly magnetized spheres buried at various depths replotted to a common scale.
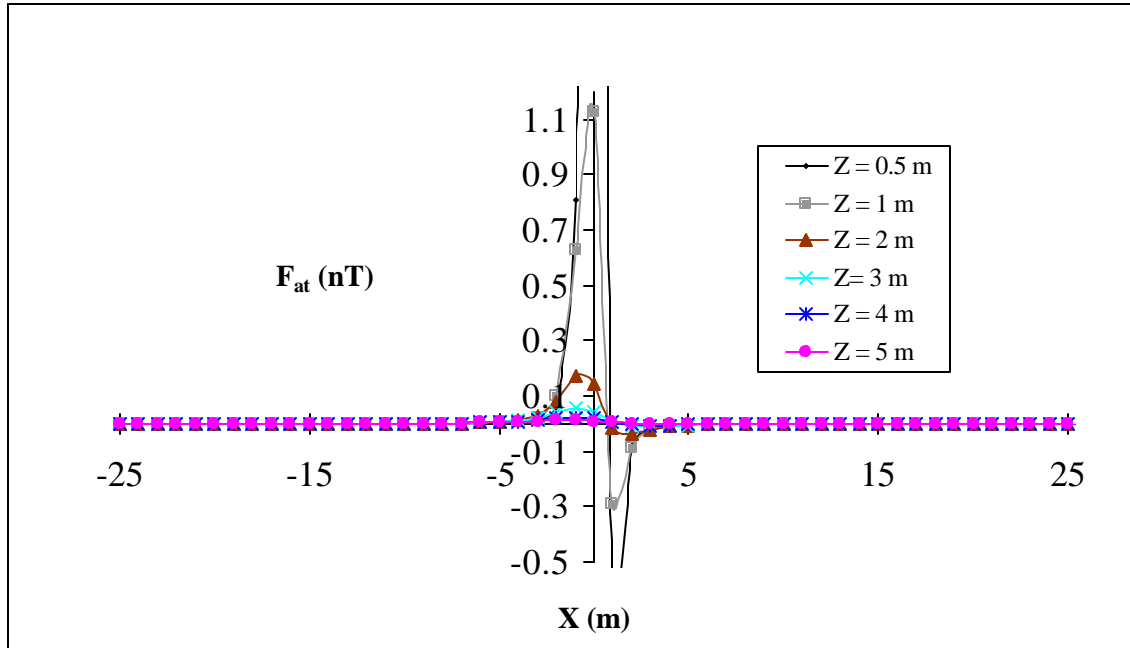
Figure 3.4 Synthetic vertical gradient, single-source magnetic anomalies computed for uniformly magnetized spheres buried at various depths.
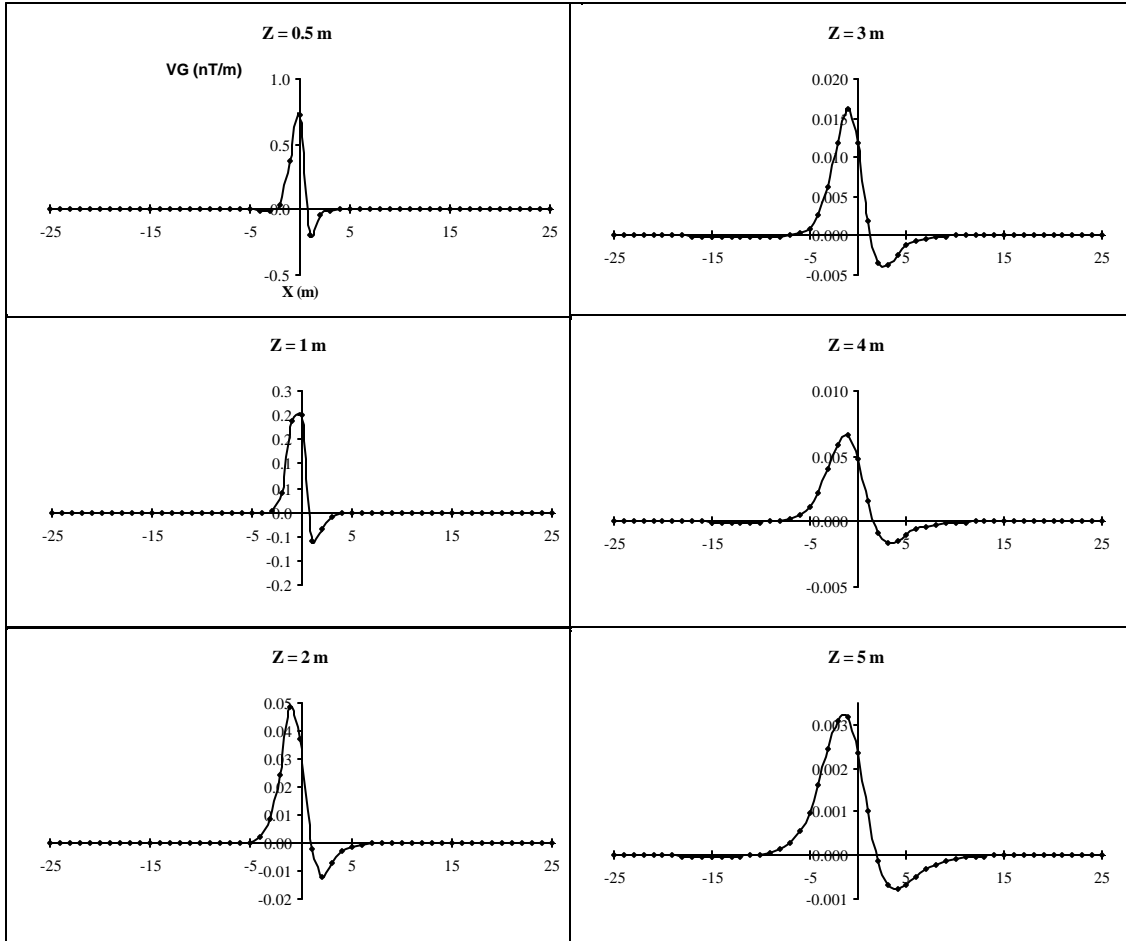
Figure 3.5 Synthetic vertical gradient single-source magnetic anomalies computed for uniformly magnetized spheres buried at various depths replotted to a common scale.
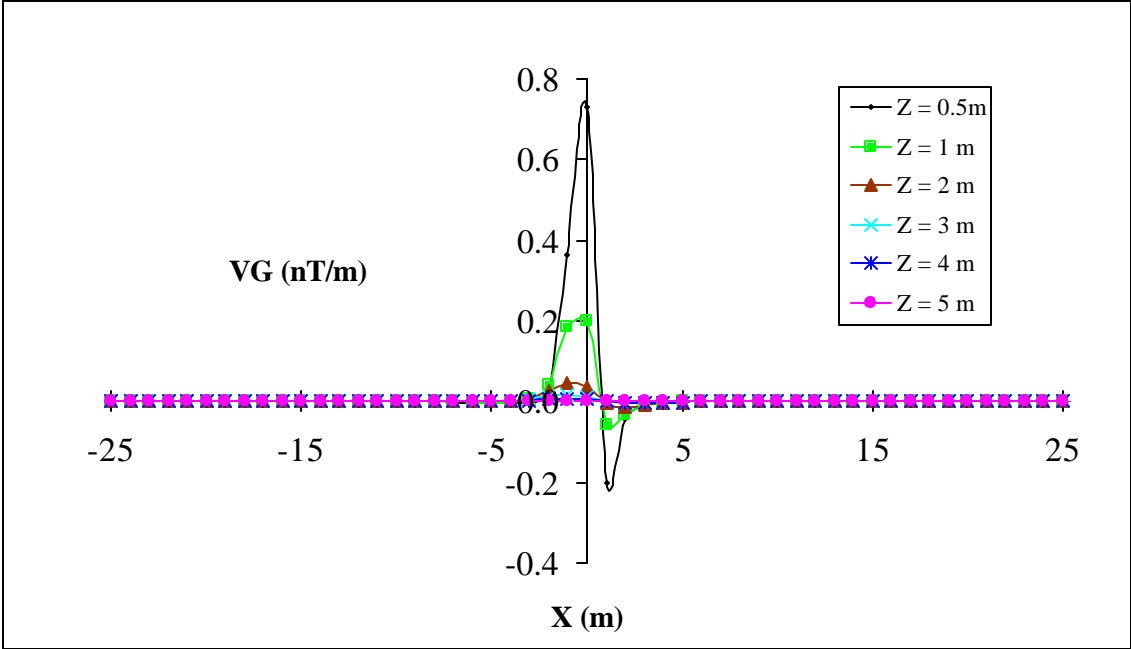
Multiple Anomaly Profiles

Some of the tests with synthetics used profiles with either three or six anomalies. These were created for the total field and vertical gradient by superimposing multiple single anomaly profiles with varying offsets between the positions of anomaly centers (Linington, 1964).

Pilot Signals

The pilot signals computed for several anomaly sources were cross-correlated with each profile. The pilot signals were derived from the single profiles, and were a subset of the single profiles extending a certain number of samples on either side of the anomaly source position. For example, a total field anomaly pilot signal with 19 samples for $(z) = 0.5$ m with samples spaced at 1 m intervals was composed of the F_{AT} values from the $(z) = 0.5$ m single profile for the (x) positions from +9 m to –9 m with the anomaly source located at 0 m. This produced a pilot signal encompassing 19 match positions (Figure 3.6). Likewise, vertical gradient pilot signals were derived from vertical gradient anomaly source profiles. Increasing the number of samples in a pilot signal allowed for a more definitive and selective cross-correlation, but decreasing the number of complete comparisons (the number of match positions) that could be made for a data profile.

Parameter 1: The Effect of the Addition of Random Noise Levels

Increasing levels of random noise were added to the profiles for each experiment to determine the efficacy of cross-correlation for identifying anomaly locations and depths in the presence of noise, and to determine at what point the cross-correlation peaks of the anomaly signals were indistinguishable from spurious peaks created by the added noise. The added random noise was a fractional scalar of the maximum amplitude for each profile multiplied by a random number (–1 to +1) using Microsoft Excel's random number generator (Weymouth,

Figure 3.6 Synthetic 19 sample pilot signals computed for uniformly magnetized spheres buried at various depths.
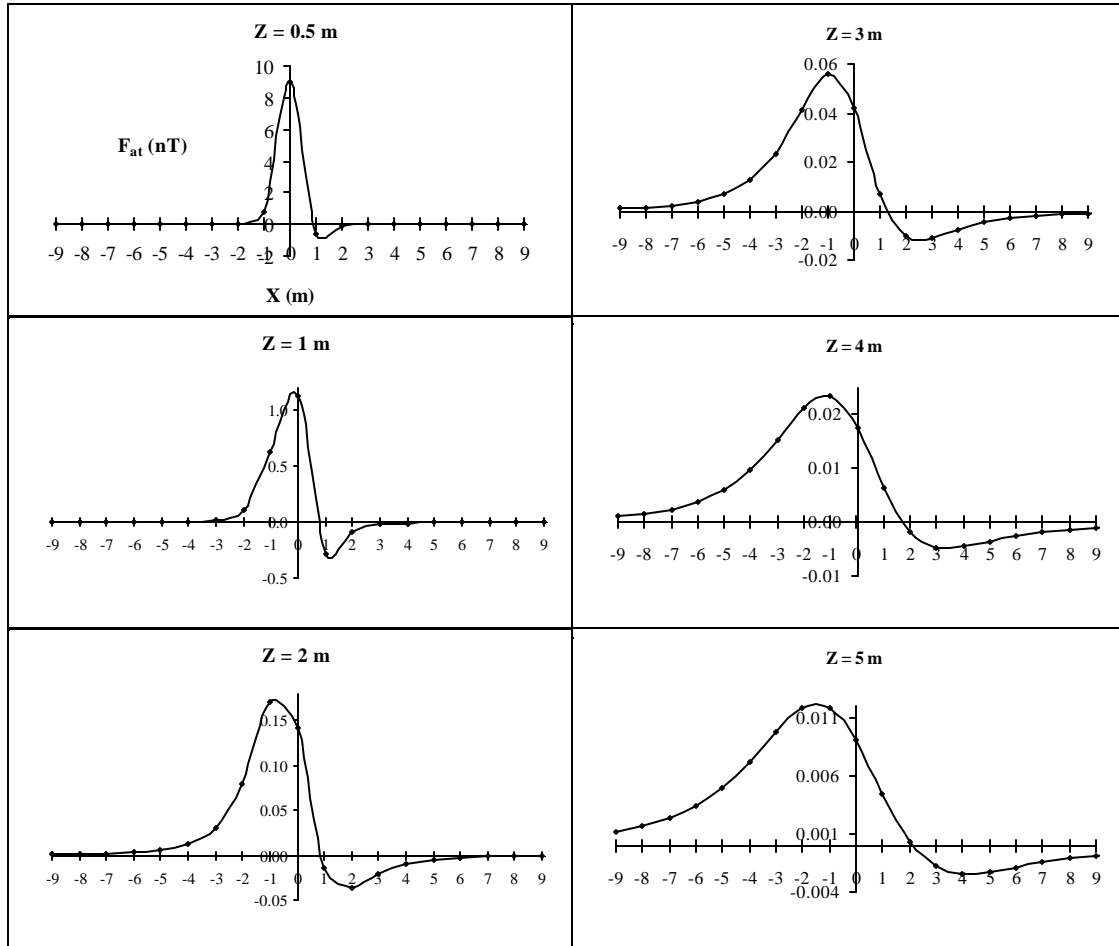
1986). This was done to allow comparability of cross-correlations because profiles of spheres with different (z) values had different maximum r_m peak values. The added noise ratio ranged from 1/100 of the maximum amplitude to the maximum amplitude for each profile. The noise ratio was held constant for all cross-correlations within the same test. Cross-correlations with variations in the added random noise levels were conducted simultaneously with all other parameters. The effects of noise are discussed in each section. Figure 3.7 presents a profile of random noise and a synthetic data profile with progressively greater amounts of random noise added.

Parameter 2: The Effect of Anomaly Source Depth

Purpose

To determine the effect of varying the source depths for the pilot signals on the ability of the cross-correlation technique to identify the position and depth of an anomaly source.

Method

Cross-correlations were conducted between six profiles and six pilot signals, each with anomaly sources at depths of (0.5, 1, 2, 3, 4, & 5 m) producing a total of 36 correlograms. All tests were conducted with pilot signals containing variable numbers of samples (5, 11, 15, 19, and 31). The cross-correlations were also conducted for profiles with varying amounts of added random noise, as described in the previous section.

Observations

Figure 3.8 presents six correlograms produced for a (z) = 2 m single source profile cross-correlated with pilot signals for anomaly sources at six different depths. In the absence of noise the positions of the anomaly sources were detectable in all 36 correlograms. Cross-correlations between profiles and pilot signals for anomaly sources at the same depth produced the greatest r_m

Figure 3.7 A comparison of random noise levels. A) An example of random noise computed for a noise factor of (1/1). B - F) A synthetic single-source magnetic anomaly computed for a 2-m deep anomaly with B) no added random noise. C) added random noise with a signal to noise ratio (S/N) of 100. D) added random noise with a signal to noise ratio (S/N) of 20. E) added random noise with a signal to noise ratio (S/N) of 4. F) added random noise with a signal to noise ratio (S/N) of 1.

Figure 3.8 A comparison of correlograms for the cross-correlation between a synthetic F_{at} single-source magnetic anomaly computed for a uniformly magnetized sphere at a depth of 2 m and pilot signals each with 11 samples computed for six different source depths.
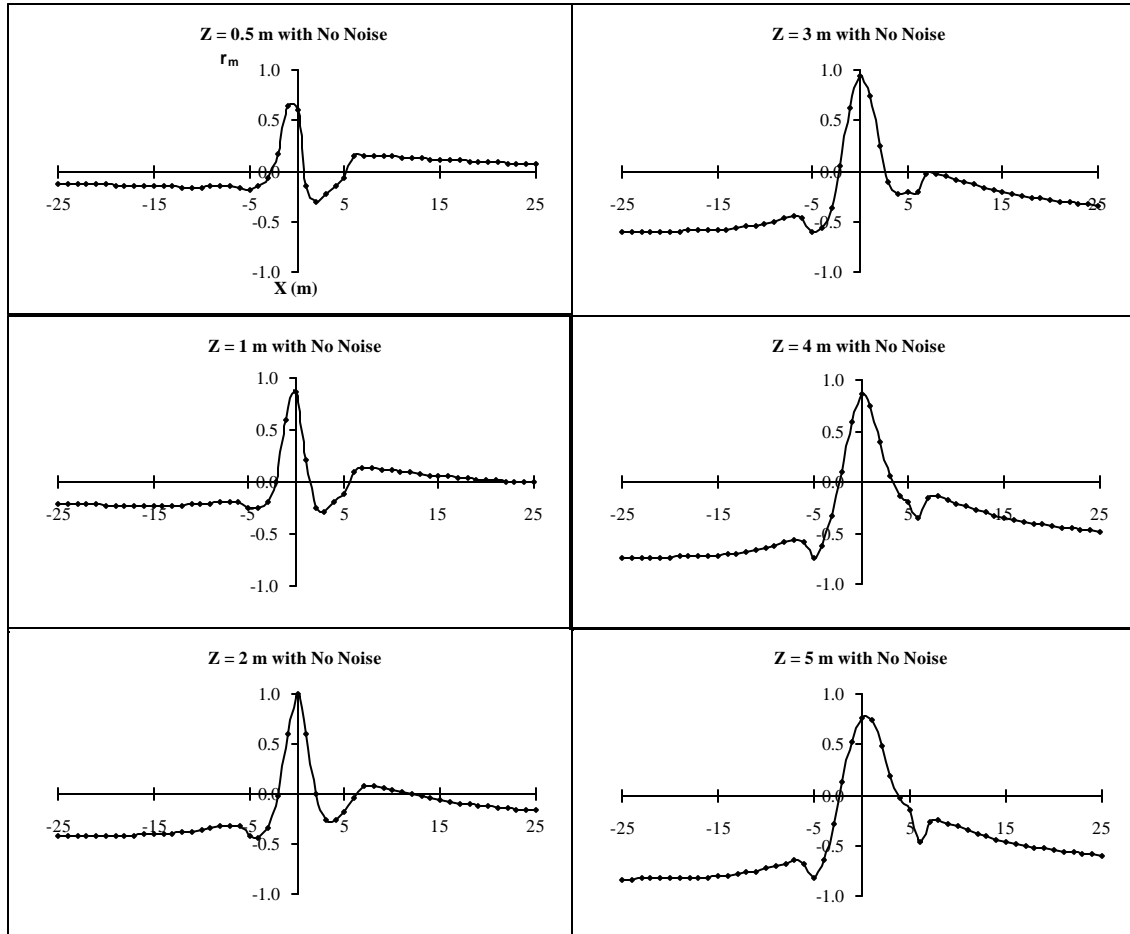
values. The anomaly peaks for the shallower depth pilot signals cross-correlated with the

shallower depth profiles produced anomaly peaks on the correlograms which were narrower and

more symmetrical than those for the deeper depth pilot signals cross-correlated with the deeper

profiles, which produced broader and more asymmetrical anomaly peaks on the correlograms.

For the 36 tests conducted the cross-correlations with the 3 m deep anomaly source pilot signal

produced the greatest mean r_m values for comparisons with all profiles. This was because the 3

m deep anomaly source pilot signal was in the middle of the range of source depths investigated

and therefore was most similar to all the profiles than any other pilot signal.

Figures 3.9 – 3.11 presents five correlograms for five (z) = 2 m single source magnetic

anomalies with different levels of added noise each cross-correlated with a noise-free pilot signal

computed for a 2 m deep anomaly source with 11 samples. Spurious peaks occurred first in the

correlograms of the shallower anomaly source pilot signals and then increased progressively in

the correlograms of the medium and deeper anomaly source pilot signals as the added random

noise factor increased. Some of the spurious peaks could be mistaken for possible anomaly

sources, though the peaks located at the anomaly source positions were discernable and had the

greatest amplitudes. Spurious peaks occurred in correlograms for all added noise factors and

increased in amplitude with increasing added noise. Scollar (1970) refers to the introduction of

spurious signals as "white noise." The amplitudes of the anomaly source peaks decreased with

increasing added noise though only minimally for all correlograms except those for profiles with

1/1 S/N added noise.

Conclusions

The depths of both the profile and pilot signal anomaly sources were important to the

outcome of the cross-correlations. The more similar the profile and pilot signal anomaly source

Figure 3.9 A comparison of correlograms for the cross-correlation between a synthetic single-source magnetic anomaly computed for a uniformly magnetized sphere at a depth of 2 m with five different levels of added random noise and a noise free pilot signal computed for a 0.5 m deep source with 11 samples.
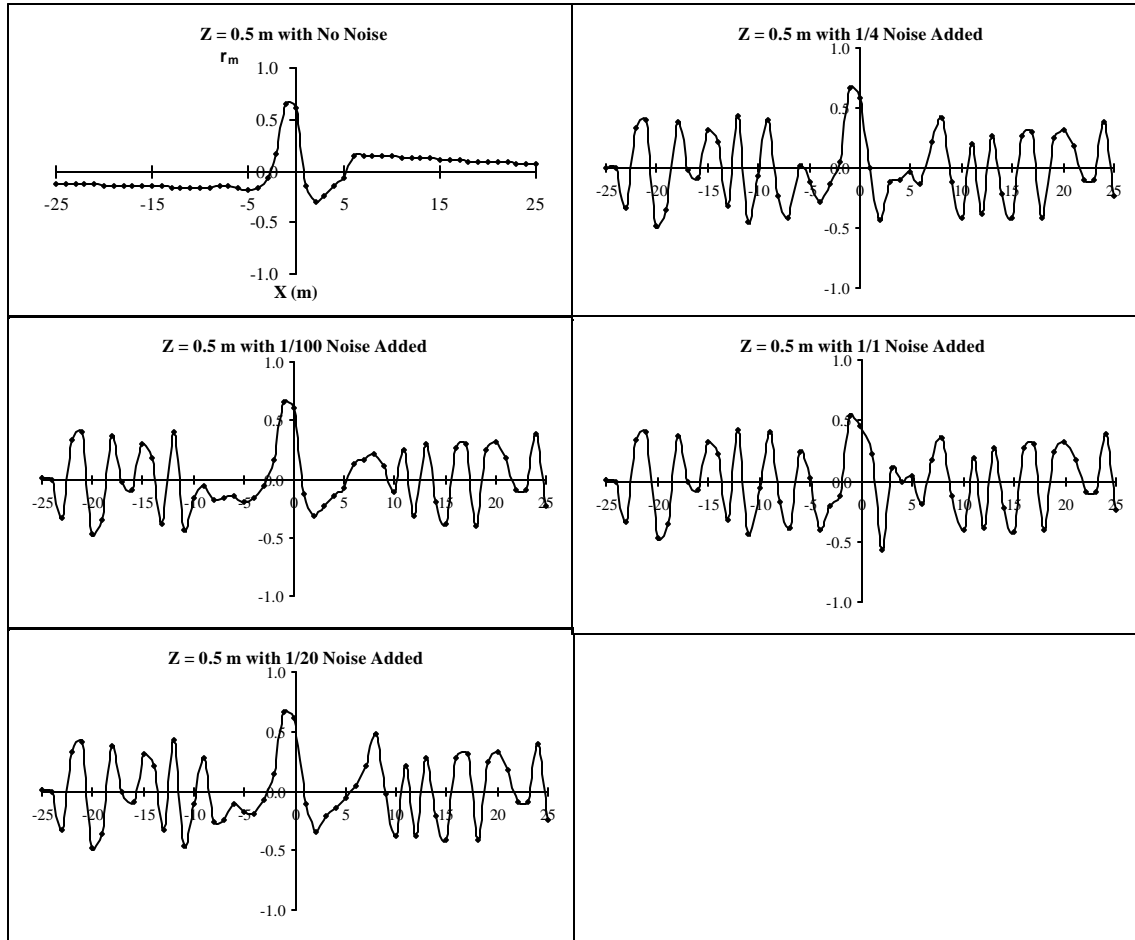
Figure 3.10 A comparison of correlograms for the cross-correlation between a synthetic single-source magnetic anomaly computed for a uniformly magnetized sphere at a depth of 2 m with five different levels of added random noise and a noise free pilot signal computed for a 2 m deep source with 11 samples.
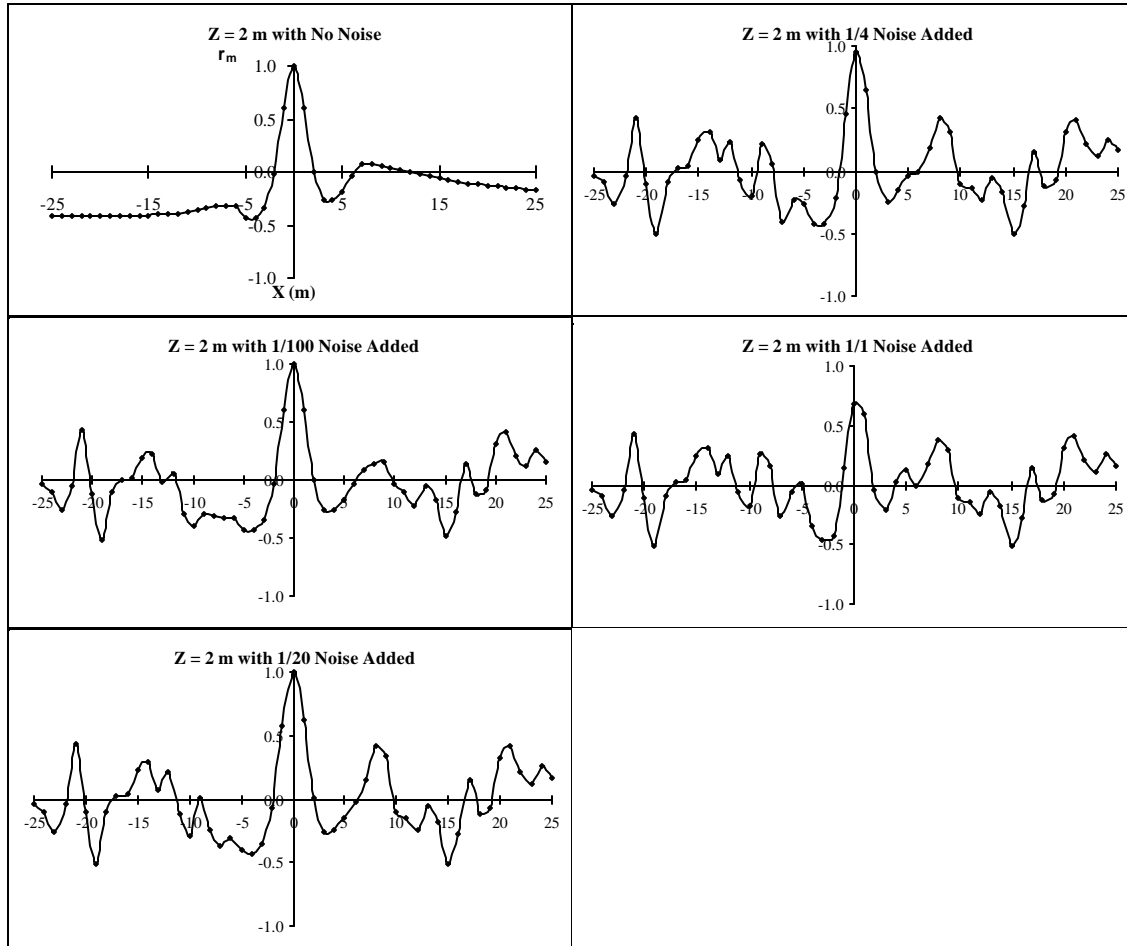
Figure 3.11 A comparison of correlograms for the cross-correlation between a synthetic single-source magnetic anomaly computed for a uniformly magnetized sphere at a depth of 2 m with five different levels of added random noise and a noise free pilot signal computed for a 4 m deep source with 11 samples.
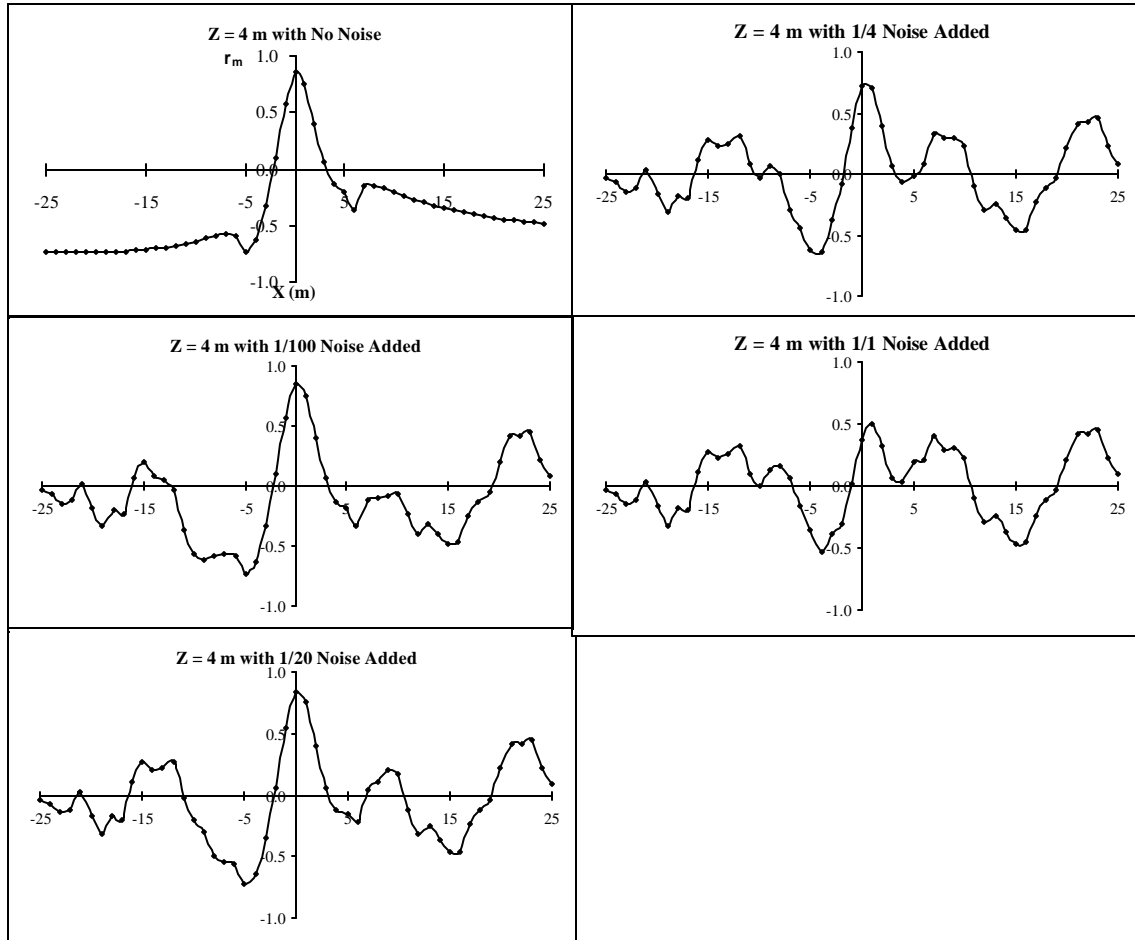
depths the greater the correlation coefficient, and therefore, the greater confidence in assessing the anomaly depth. The position of an anomaly source was best determined by the comparison of correlograms for pilot signals with different target depths. The depth to the center of an anomaly source was estimated to be equal to the depth of the pilot signal's anomaly source for the correlograms with the highest r_m value at the anomaly source (x) position, (Naudy, 1971). This depth estimate will always be greater than the actual source depth because it estimates the depth to the center of the object and not the outer edge of the object. These tests demonstrated that cross-correlation was sensitive to the depth of magnetic anomaly sources.

The process of cross-correlation eliminated the asymmetry in the shape of the magnetic anomalies due to magnetic latitude. This helped in the determination of the horizontal position of the buried source. Therefore the anomaly source was estimated to be located at the (x) position beneath the apex of the peak on the correlogram. This is similar to the reduction to the pole method (von Frese, 1984). The estimated horizontal position of anomaly sources was correct within on or two sample points in the correlograms regardless of the source depth of the pilot signal used in the cross-correlation. These tests demonstrated that the estimated horizontal position of magnetic anomaly sources is not sensitive to changes in the anomaly source depth.

Parameter 3: The Effect of the Number of Samples in the Pilot Signal

Purpose

To determine the effect of varying the number sample points in the pilot signals on the ability of the cross-correlation technique to identify the position and depth of an anomaly source.

Method

Cross-correlations conducted between six magnetic anomaly profiles and five sets of six pilot signals, each with anomaly sources at depths of (0.5, 1, 2, 3, 4, or 5 m), produced a total of

180 correlograms. Each of the five sets of pilot signals either had 4, 11, 15, 19, or 31 sample points. The cross-correlations were also conducted for profiles with added random noise factors of 1/20 and 1/1, as described in a previous section.

Observations

Figure 3.12 presents the correlograms of a (z) = 2 m single anomaly source profile cross-correlated with five different (z) = 2 m anomaly source pilot signals having either 4, 11, 15, 19, or 31 sample points. All five correlograms showed high r_m values though those with fewer samples had large plateau areas of negative r_m values on either side of the anomaly peak. The amplitudes of these plateaus approached zero with an increasing number of sample points.

Figures 3.13 and 3.14 present correlograms for similar cross-correlations except that random noise (S/N of 20/1, and 1/1, respectively) were added to the synthetic profiles before cross-correlation. Cross-correlation with the pilot signals with 11- 31 samples produced good results in the presence of noise with gradually increasing improvement as the length of the pilot signal increased. The cross-correlations with the pilot signal with 5 sample points were adversely affected by any amount of noise. The smaller the number of sample points the more likely a pilot signal was to show the higher correlation with noise. Spurious peaks occurred first and had greater amplitudes in the correlograms for pilot signals with smaller numbers of sample points as the amount of added random noise was increased. Although the S/N = 1 was a worst case but the correlograms showed that cross-correlation with pilot signals with a sufficiently large number of sample points could resolve anomalies out of the noise. The correlograms for pilot signals with fewer sample points produced greater amplitudes for both the anomaly source and spurious peaks.

Figure 3.12 A comparison of correlograms for the cross-correlation between a synthetic single-source magnetic anomaly computed for a 2 m deep anomaly source with no added noise (Figure 3.7B) and five pilot signals computed for a 2 m deep source with varying numbers of samples.
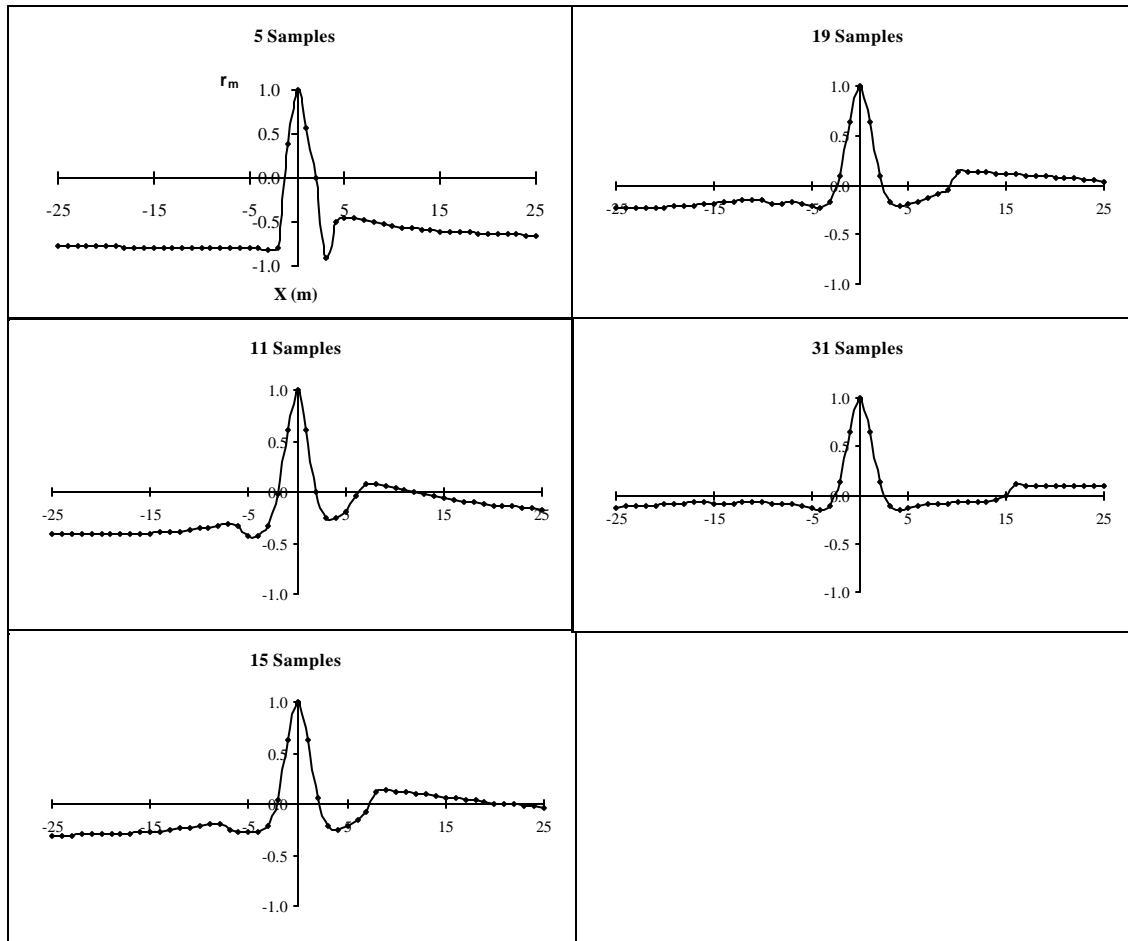
Figure 3.13 A comparison of correlograms for the cross-correlation between a synthetic single-source magnetic anomaly computed for a 2 m deep anomaly source with added random noise with a signal to noise ratio (S/N) of 20 (Figure 3.7D) and five pilot signals computed for a 2 m deep source with varying numbers of samples.
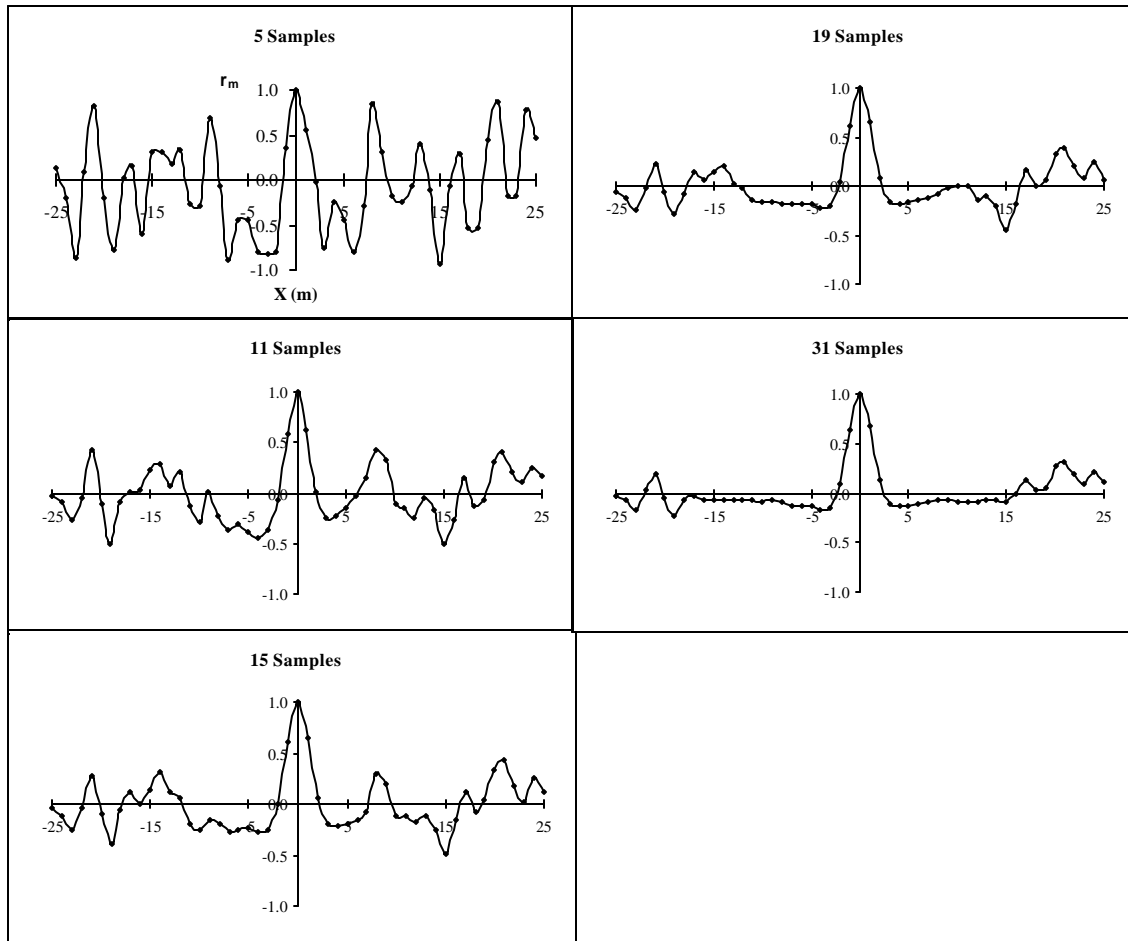
Figure 3.14 A comparison of correlograms for the cross-correlation between a synthetic single-source magnetic anomaly computed for a 2 m deep anomaly source with added random noise with a signal to noise ratio (S/N) of 1 (Figure 3.7F) and five pilot signals computed for a 2 m deep source with varying numbers of samples.
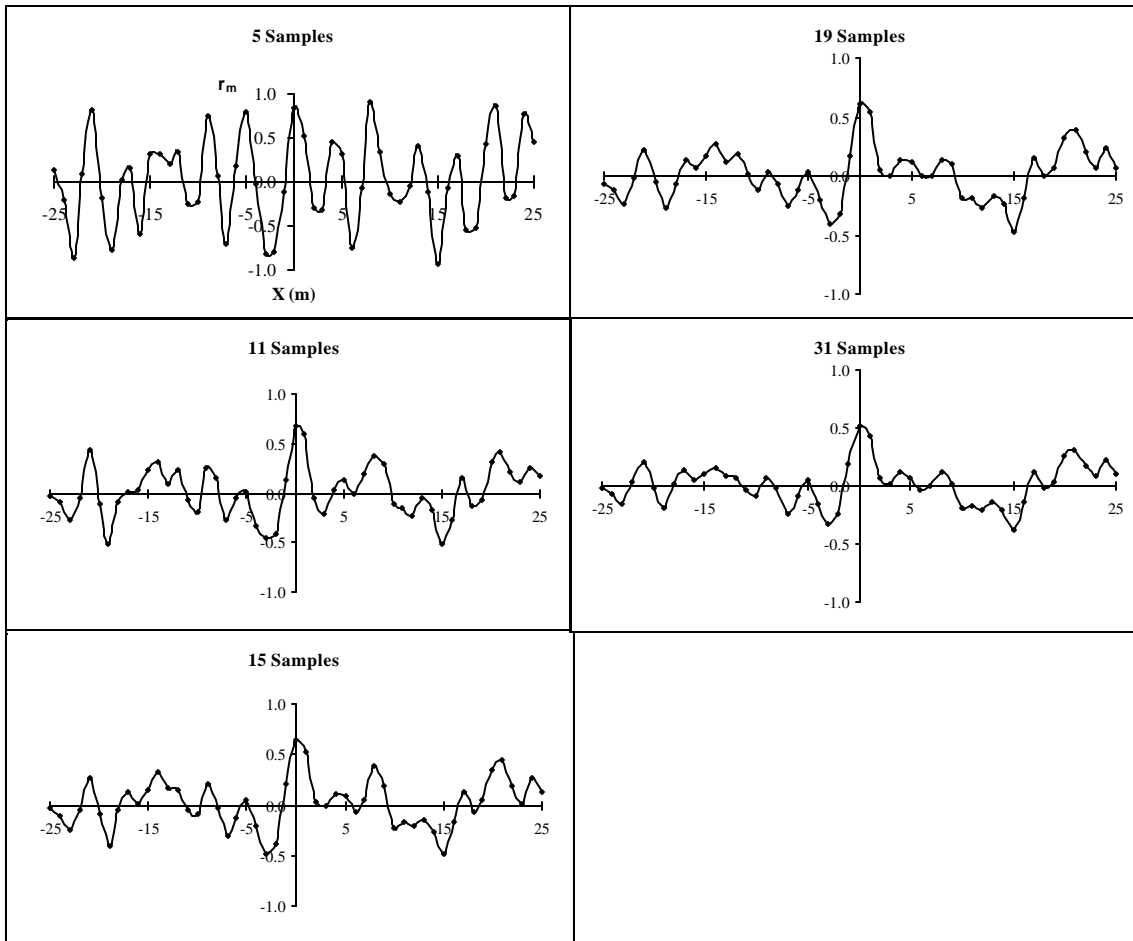
Conclusions

The number of samples in the pilot signal affected the outcome of the cross-correlation. The greater the number of samples in a pilot signal the more selective the cross-correlation because it required a greater number of matching positions between the profile and pilot signal, which produced correlograms with lower amplitudes but fewer number of spurious peaks. If the cross-correlation technique is intended to be used for an experiment, then data should be collected within a grid large enough to allow cross-correlation with pilot signals with a sufficient number of sample points. It would be best to cross-correlate data using pilot signals of various lengths in order to compare the outputs.

Parameter 4: The Effect of Varying the Radii of the Spherical Anomaly Source

Purpose

To determine the effect of the radii of the profile and pilot signal anomaly source spheres on the ability of cross-correlation to identify the position and depth of an anomaly source.

Method

Six profiles were created for homogenous spheres of radii, (0.1, 0.25, 0.5, 0.75, 1, and 2 m) buried at a depth of 2 m with magnetic susceptibility of 0.00004 emu cgs. These profiles were each 100 m in length and were cross-correlated with six pilot signals with 19 sample points, computed for each of the six different sphere radii. Random noise with S/N ratios of 20/1 and 1/1 were added and the same cross-correlations were computed again. Thirty-six profiles were produced for each noise factor.

Observations

All 36 of the correlograms were identical for a given source depth and added noise level regardless of depth of the pilot signal anomaly source or the sphere radii (Figure 3.15).
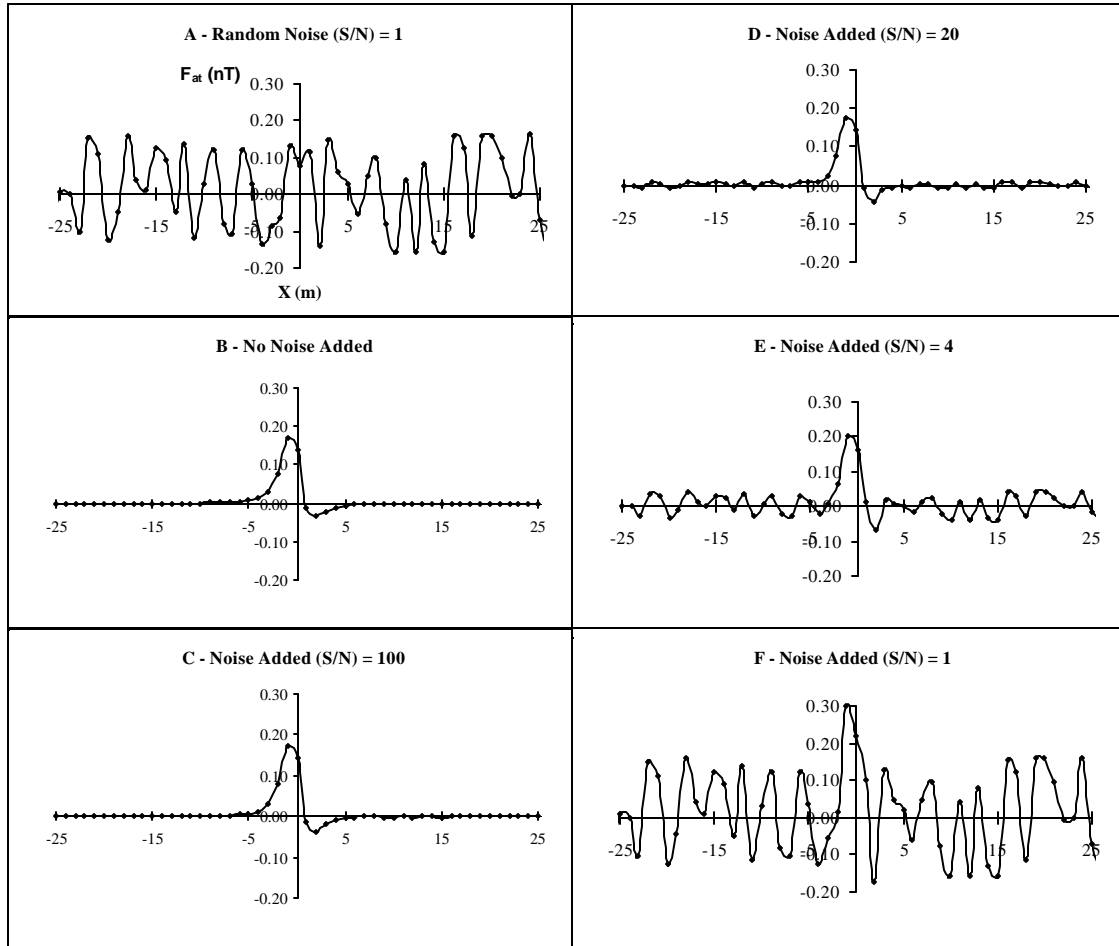
Figure 3.15 A comparison of correlograms for the cross-correlation between a synthetic single-source magnetic anomaly computed for uniformly magnetized spheres buried at 2 m with no noise added and pilot signals with 19 samples computed for a 2 m deep source with six different spherical source radii.
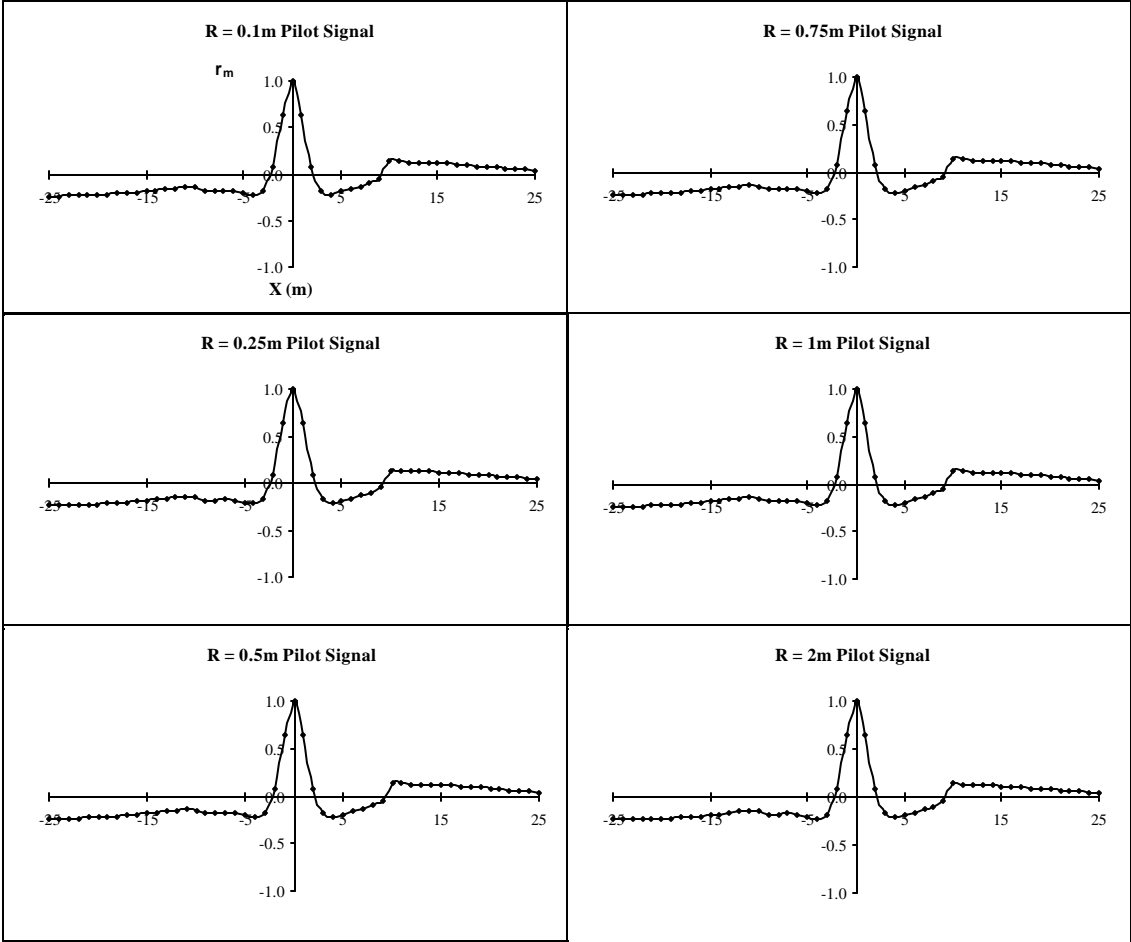
Conclusions

The variation of the radii of the anomaly sphere for a given source depth had no effect on the cross-correlations. This was because the sphere radii only scaled the anomaly values of the correlograms by either increasing or decreasing the anomaly amplitudes by a constant value. This did not affect the relative amplitude ratios of points along the correlograms.

The scalar factor was equal to the ratio of the profile and pilot signal anomaly sphere radii raised to the third power, which was a factor in equations (3 and 4) used to compute the magnetic field of an object, in which the radii was cubed.

Parameter 5: The Effect of Variable Magnetic Susceptibility Contrast of the Anomaly Source

Purpose

To determine if varying the magnetic susceptibility contrast (k) of either the profile or pilot signal anomaly sphere would affect the ability of cross-correlation to identify the horizontal and or vertical position of an anomaly source.

Method

Profiles and pilot signals were created for six different magnetic susceptibilities contrasts (k) and cross-correlated with each other while the anomaly source depth, spherical radii and pilot signal sample number were held constant.

Observations

The correlograms were identical for cross-correlations of all combinations of profile and pilot signal with positive (k).

Conclusions

The value of (k) was unimportant in either the profiles or pilot signals as the cross-correlations were independent of scalars. The sign (+/-) of (k) used for the pilot signal was important in terms of the type of material being investigated. The reason (k) did not affect the cross-correlation was because it was a constant scalar quantity in the same way as the radii of the anomaly sphere.

Parameter 6: The Effect of Multiple Anomaly Sources

Purpose

To determine the ability of cross-correlation to identify the position and depth of anomaly sources when multiple adjacent anomaly sources are present in a profile.

Method

Anomalies for multiple sources were added together to simulate the signal from multiple adjacent anomaly sources or a single continuous anomaly source, creating a composite profile. Six triple anomaly profiles were created each with three identical spherical anomaly sources at the same depth (0.5, 1, 2, 3, 4, and 5 m) whose centers were spaced 1m apart (Figures 3.16 and 3.17). These profiles were each cross-correlated with the same six pilot signals computed for single anomaly sources at depths of (0.5, 1, 2, 3, 4, and 5 m), as were used with the single anomaly source profiles. The tests with the triple anomaly source profiles mimicked those of the single anomaly source profiles and used all the same parameters, noise levels and pilot signals.

Observations

The cross-correlations of the triple anomaly profiles with single anomaly pilot signals produced the same patterns as for the single anomaly correlograms except that the shallow pilot signals did not correlate as well with the shallow anomaly triple profiles (Figure 3.18). This was

Figure 3.16 Synthetic triple-source magnetic anomaly computed for three equal radii uniformly magnetized spheres at equal depths spaced 1 m apart for various depths.
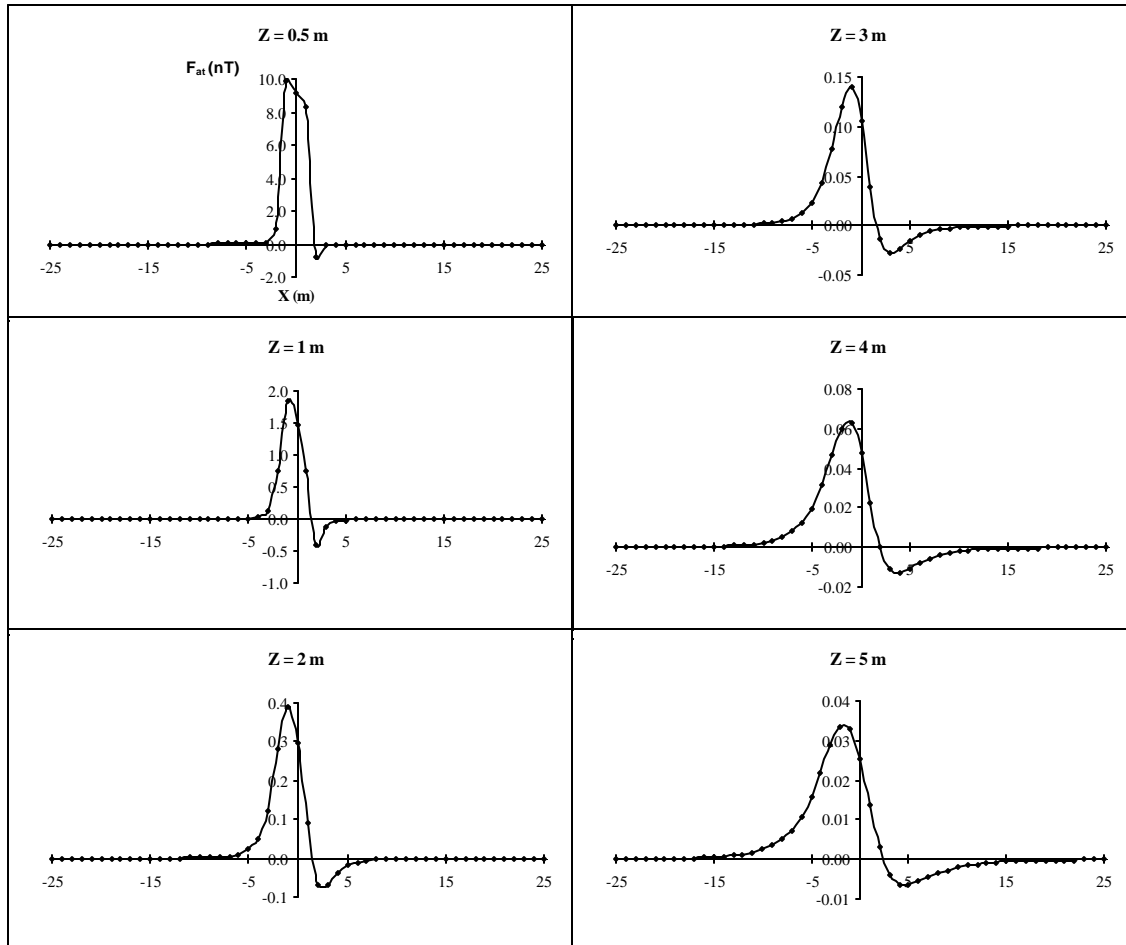
Figure 3.17 Synthetic, triple-source magnetic anomalies computed for three equal radii and equal depth uniformly magnetized spheres spaced 1 m apart for various depths replotted to a common scale.
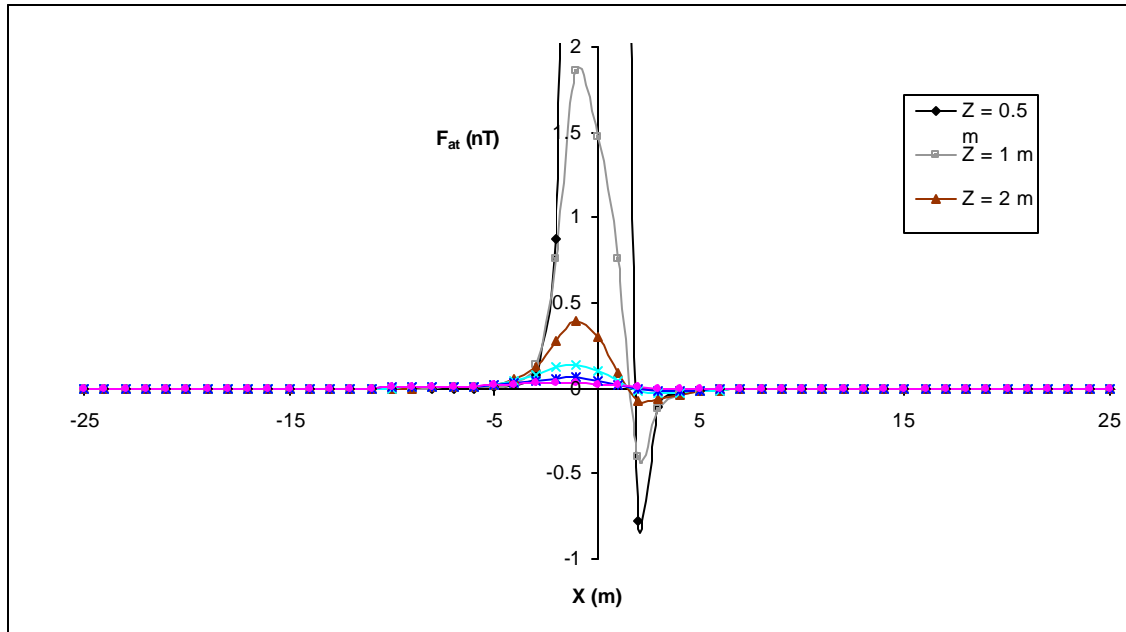
because the superposition of three adjacent high amplitude narrow anomalies produced one higher amplitude broader anomaly. The deeper pilot signal correlated better with the shallow anomaly triple profiles then they did with the shallow single anomaly profiles because the adjacent anomalies produced a broader peak which was more similar to deeper anomalies.

Conclusions

The profile created by adjacent of continuous anomalies is the superposition of the multiple individual signals. This composite anomaly will tend to be broader and will therefore appear to be deeper than it would individually which is one drawback for using cross-correlation as a depth estimator for adjacent anomaly sources. The determination of the horizontal position of the multiple sources was most accurate in the correlograms with the 0.5 m deep source pilot signals. This pilot signal also yields spurious peaks with smaller amplitudes.

Parameter 7: The Effect of Varying the Spacing Between Anomaly Sources

Purpose

To determine what effect varying the separation distance between anomaly sources had on the efficacy of cross-correlation to resolve separate anomaly sources and to identify their positions and depths.

Method

Two groups of equally spaced anomaly source profiles were generated. One had three anomaly sources at the same depth (0.5, 1, or 2 m) and the other had three anomaly sources at different depths (0.5, 1, and 2 m). The first group contained four profiles (A1 - A4) each with three anomaly sources at the following depths (0.5, 1, and 2 m) with consistent separation between the sources of 3, 5, 9, or 14 m (Figure 3.19). The second group contained three sets of four profiles (B1 - B4, C1 - C4, and D1 - D4) each with three equal depth anomaly sources,

Figure 3.18 A comparison of correlograms for the cross-correlation between synthetic triple-source magnetic anomalies computed for three 0.5 m deep anomaly sources and single anomaly source pilot signals with 11 samples computed for single anomaly sources buried at various depths.
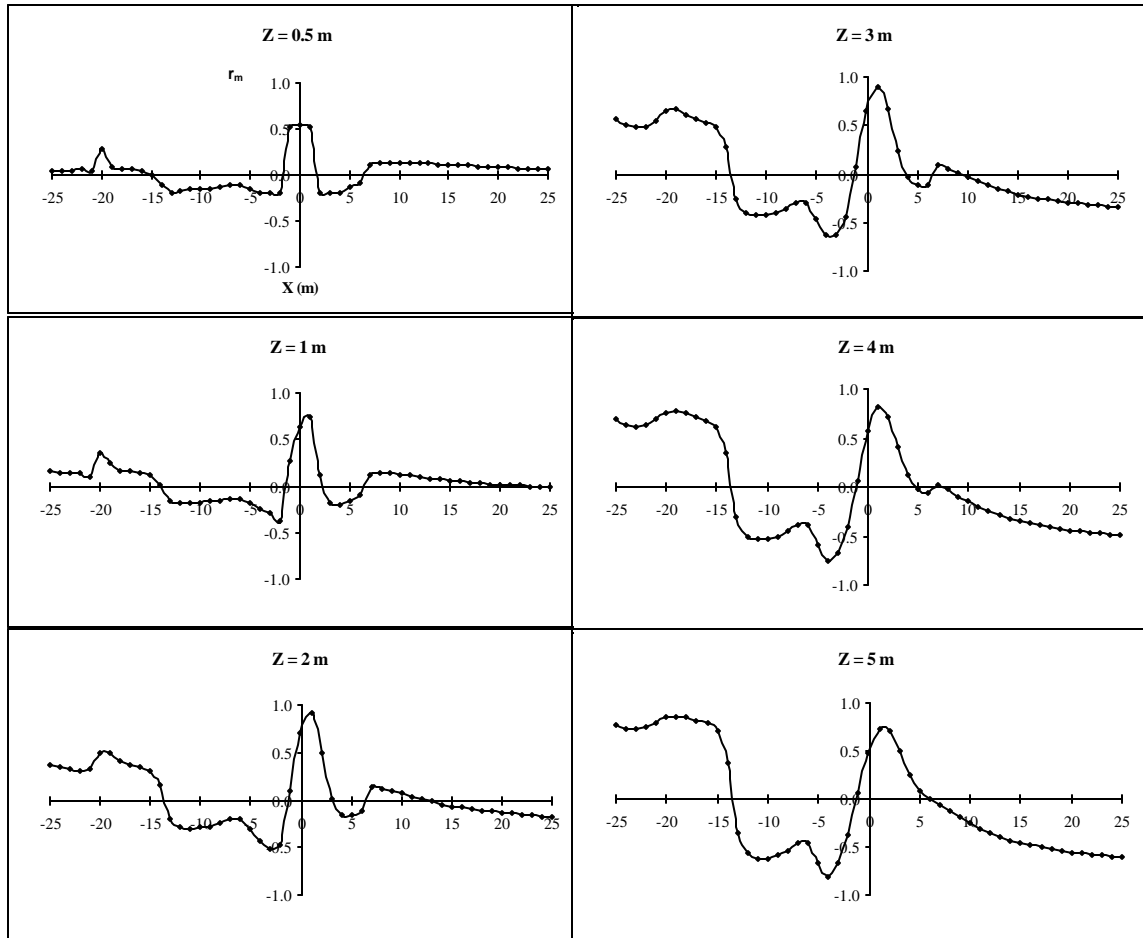
Figure 3.19 A comparison of synthetic magnetic anomalies for three anomaly sources with different depths (0.5, 1 & 2 m). A1) The anomaly source centers are spaced 3 m apart. A2) The anomaly source centers are spaced 5 m apart. A3) The anomaly source centers are spaced 9 m apart. A4) The anomaly source centers are spaced 14 m apart.
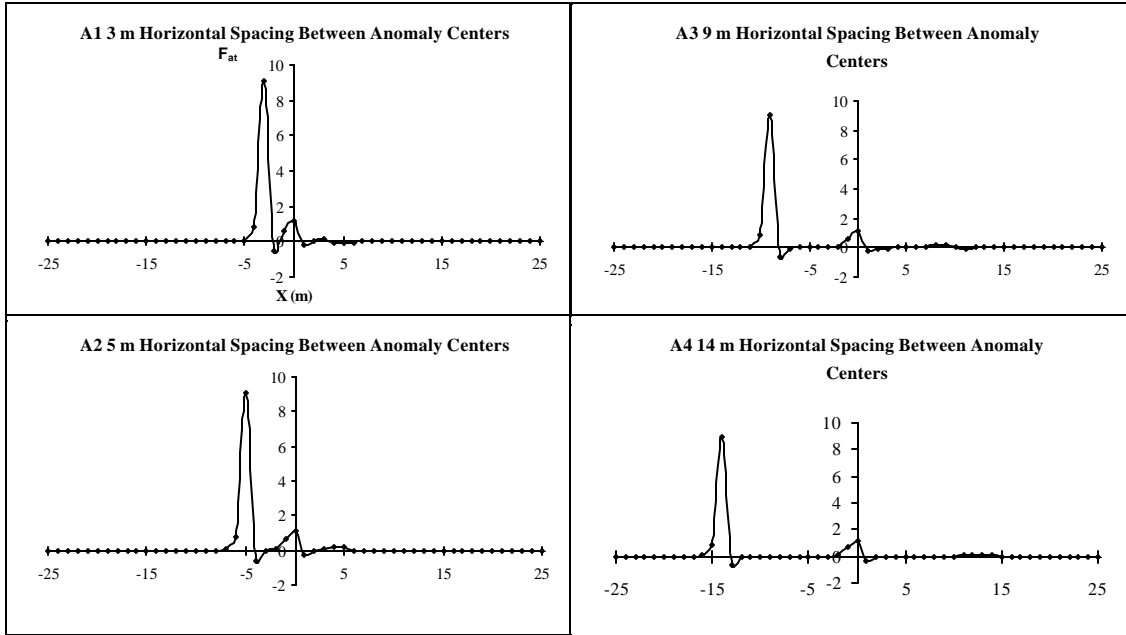
depth (0.5, 1, or 2 m), with consistent separation between the anomaly sources of 3, 5, 9, or 14 m (Figures 3.20 and 3.21). Tests were conducted to investigate the ability of cross-correlation to resolve and locate anomaly sources from multiple anomaly source profiles with variations in the separation distance between anomaly sources, the number of samples in pilot signals, added random noise, and the depth of anomaly sources used to compute pilot signals.

Observations

The cross-correlations with profiles A1 – A4 mimicked those of the single anomaly source profiles and used all the same parameters, noise levels and pilot signals. The added noise was scaled based on the greatest r_m values of the profile, therefore the noise factor ratio was actually larger for the lower amplitude (i.e. shallower) anomaly sources. Profiles sets B through D were cross-correlated with pilot signals with 19 samples computed for anomaly sources with six different depths (0.5, 1, 2, 3, 4, and 5 m).

Pilot signals with few to intermediate numbers of samples (5, 11, and 15), produced greater anomaly peak amplitudes when cross-correlated with profiles A1 – A4 than did the pilot signals with larger numbers of samples (19 and 31) for the same anomaly source depth (Figure 3.22). In the presence of a S/N ratio of 20/1 (Figure 3.23) the pilot signals with 11 and 15 samples maintained higher r_m values for the cross-correlation with all three anomaly sources than did the pilot signals with either 19 or 31 samples. It was not possible to resolve the locations of the anomaly sources in the correlogram for the pilot signal with 5 samples, because of the presence of abundant spurious peaks caused by cross-correlation with noise. In addition the cross-correlation did not preserve the relative amplitudes of the anomalies.

The S/N ratio of the cross-correlation correlograms is greater than the original profiles for no noise and added noise with a S/N ratio of 20/1 with the pilot signals having 11, 15 and 19

Figure 3.20 A comparison of synthetic magnetic anomalies for three anomaly sources at the same depths, either (0.5, 1 or 2 m). B1, C1, & D1) The anomaly source centers are spaced 3 m apart on each profile. B2, C2, & D2) The anomaly source centers are spaced 5 m apart on each profile.
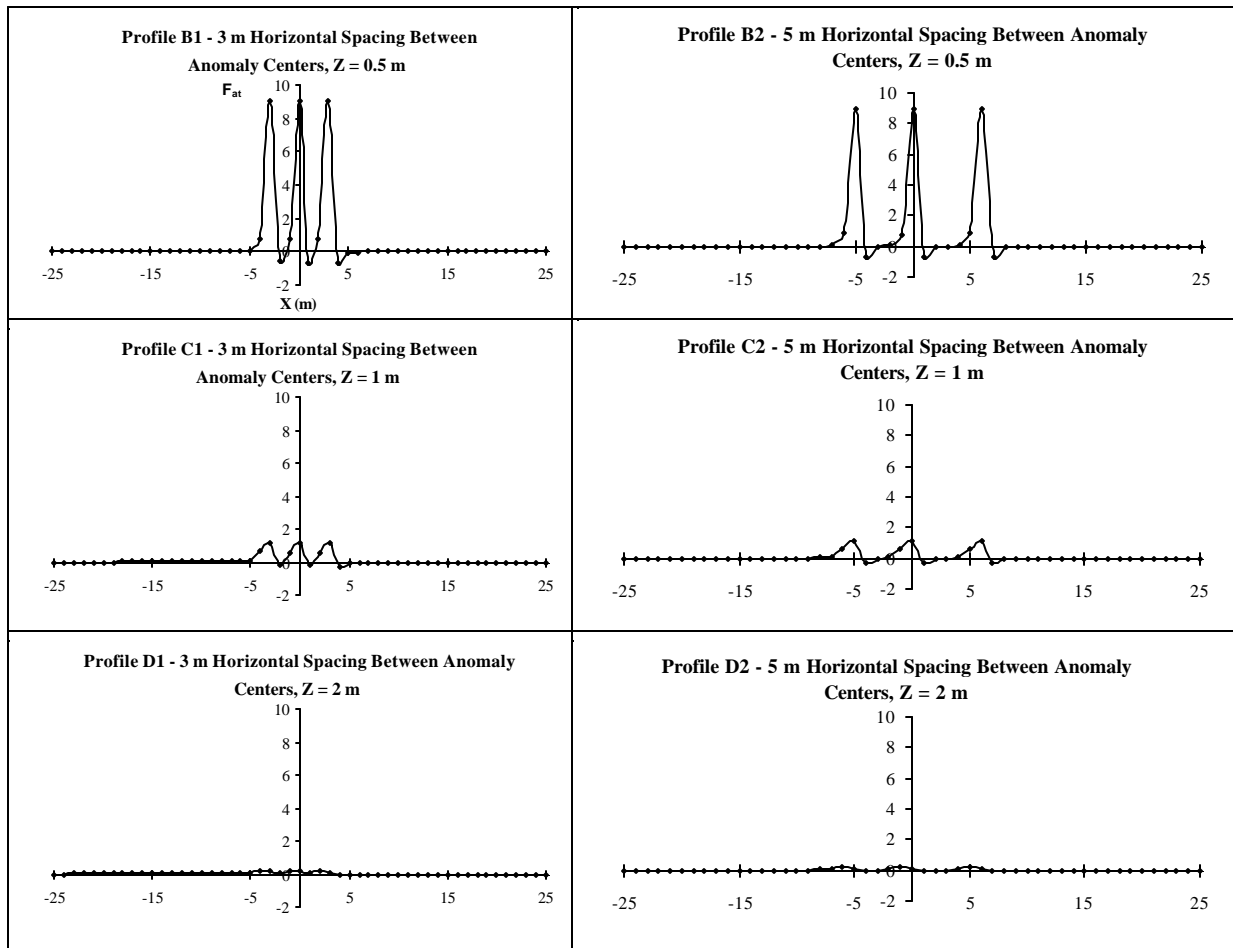
Figure 3.21 A comparison of synthetic magnetic anomalies for three anomaly sources at the same depths, either (0.5, 1 or 2 m). B3, C3, & D3) The anomaly source centers are spaced 9 m apart on each profile. B4, C4, & D4) The anomaly source centers are spaced 14 m apart on each profile.
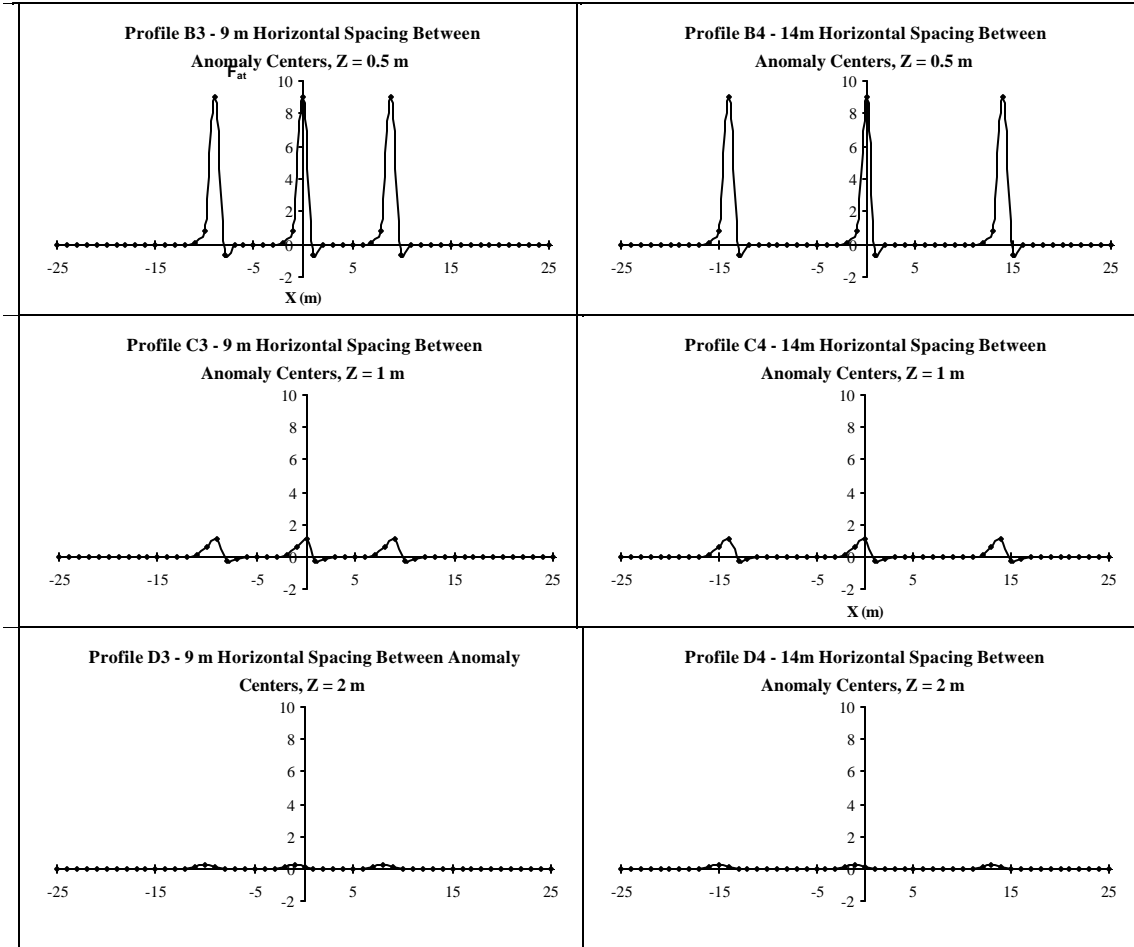
Figure 3.22 A comparison of correlograms for the cross-correlation between profile A3, from Figure 3.19, with no noise added and pilot signals computed for a 2 m deep source with five different numbers of samples.
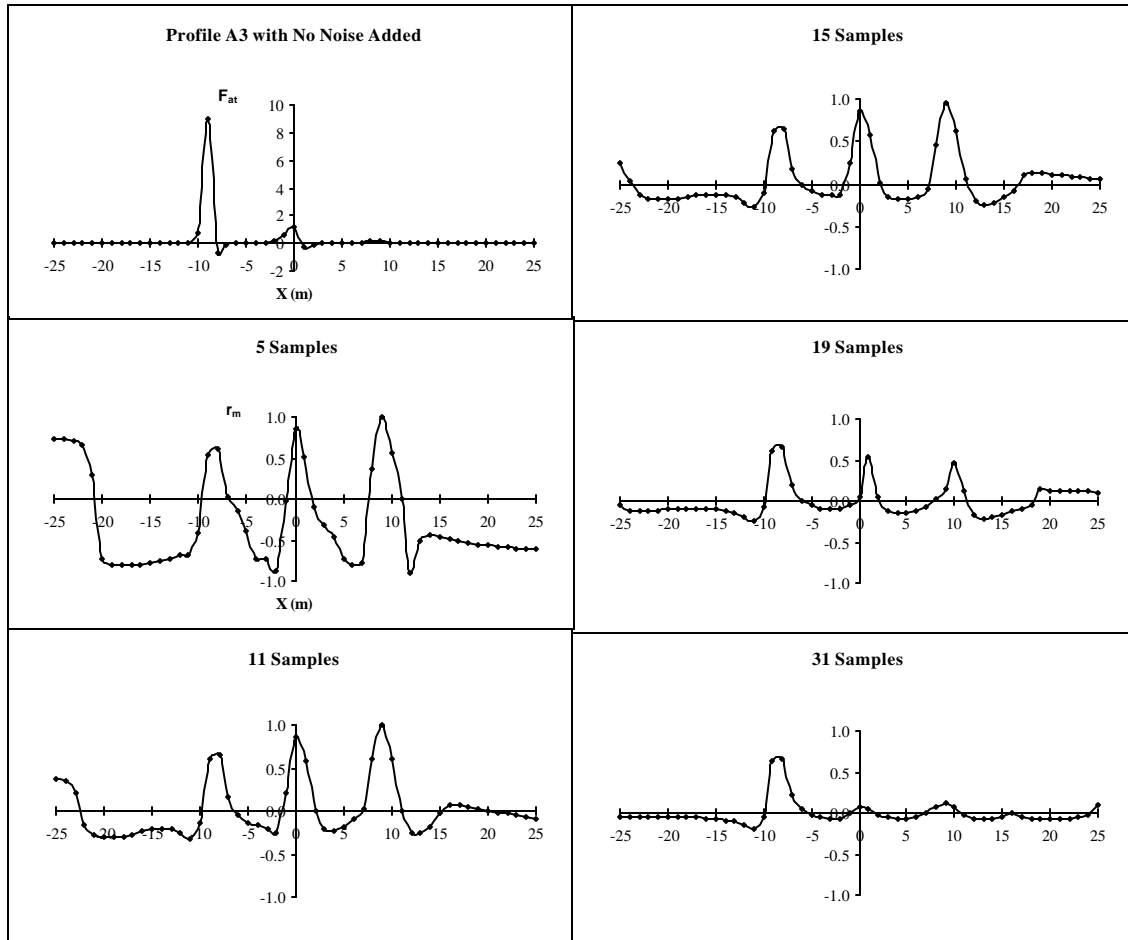
Figure 3.23 A comparison of correlograms for the cross-correlation between profile A3, from Figure 3.19, with added random noise of a (1/20) noise factor and pilot signals computed for a 2 m deep source with five different numbers of samples.
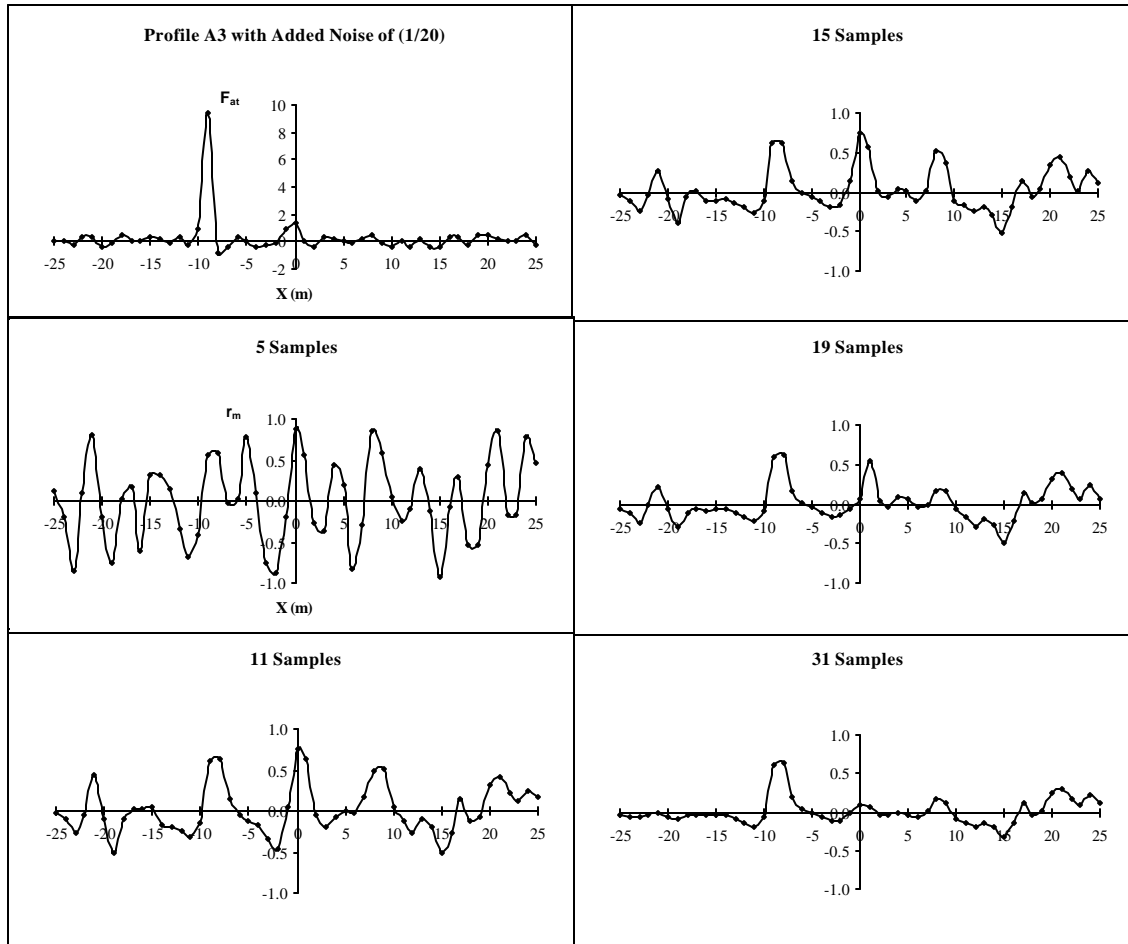
sample s, for a S/N ratio of 4/1 added noise with pilot signals with 11 and 15 samples and for a S/N ratio of 1/1 noise for pilot signals with 11 samples (Figure 3.24).

The greater the number of samples in the pilot signals the more the noise was reduced, though cross-correlations with the 31 sample pilot signals tended to decrease the amplitude of the deeper anomaly peaks, while at the same time making them more difficult to resolve (Figures 3.23 – 3.25). The cross-correlations with 5 sample pilot signals did a poor job of resolving anomaly sources at any noise level.

The ability of cross-correlation to resolve shallow anomaly sources, 0.5 m deep, which are horizontally near to deeper anomaly sources, 1 or 2 m deep, was unaffected by the separation distance between the anomaly sources (Figure 3.26). However it was more difficult for cross-correlation to resolve these deeper anomaly sources, 1 or 2 m deep, as the separation distance between the sources decreased (Figure 3.26). These 1 and 2 m deep anomaly sources were not resolvable at an anomaly source separation of 3 m, but were resolvable at a separation of 5 m.

Since shallow anomaly sources generated narrower anomalies than deeper anomaly sources, they were easier to resolve as separate anomaly peaks as the horizontal spacing between anomaly sources decreased (Figure 3.26).

Three anomaly source profiles with varying source separation distances were cross-correlated with pilot signals computed for source depths of (0.5, 1, and 2 m). For profiles with different anomaly source depths and an anomaly source separation of 3 m or less, only the shallow source is resolvable in the correlograms and it decreases in amplitude with increasing pilot signal source depth (Figure 3.26).

For profiles with differing anomaly source depths and an anomaly source separation of at least 5 m, an increase in pilot signal source depth will produce a small decrease in r_m amplitude

Figure 3.24 A comparison of correlograms for the cross-correlation between profile A3, from Figure 3.19, with added random noise of a (1/4) noise factor and pilot signals computed for a 2 m deep source with five different numbers of samples.
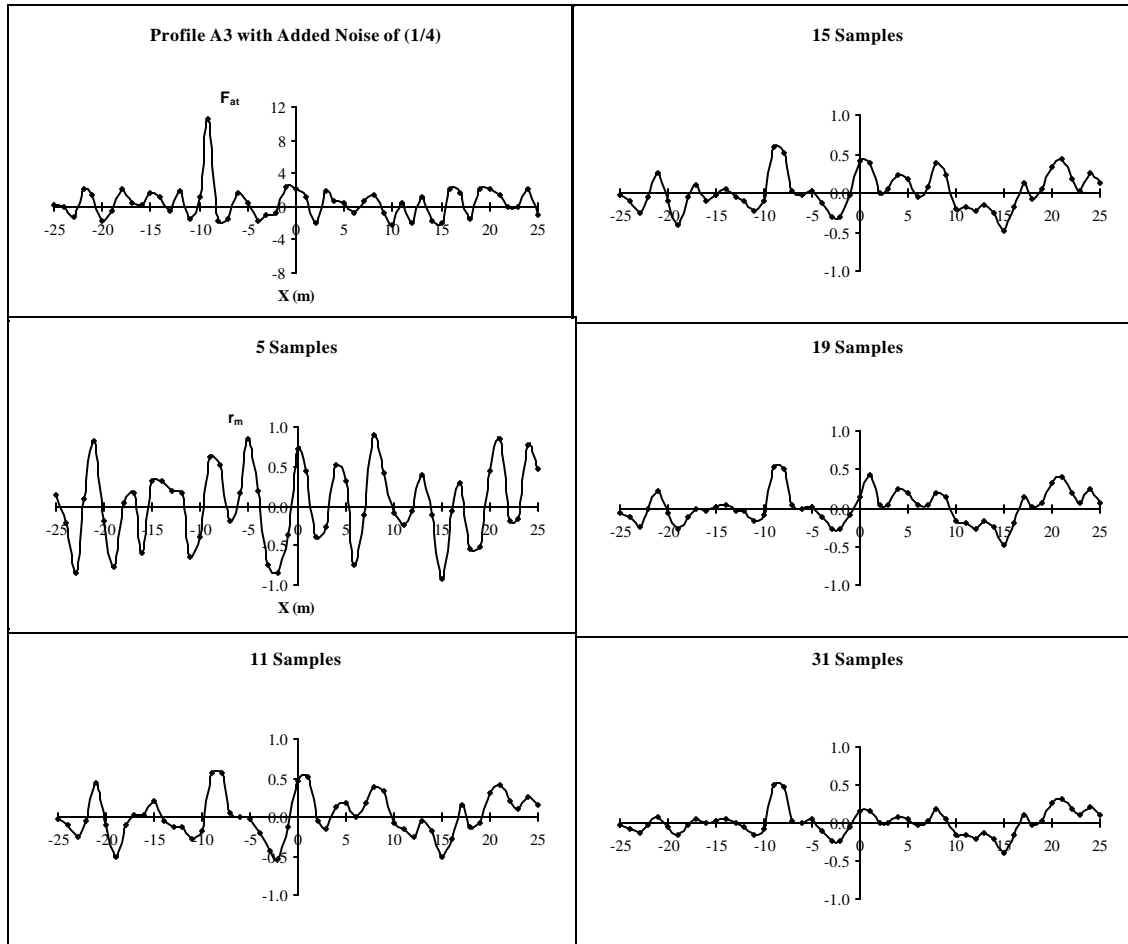
Figure 3.25 A comparison of correlograms for the cross-correlation between profile A3, from Figure 3.19, with added random noise of a (1/1) noise factor and pilot signals computed for a 2 m deep source with five different numbers of samples.
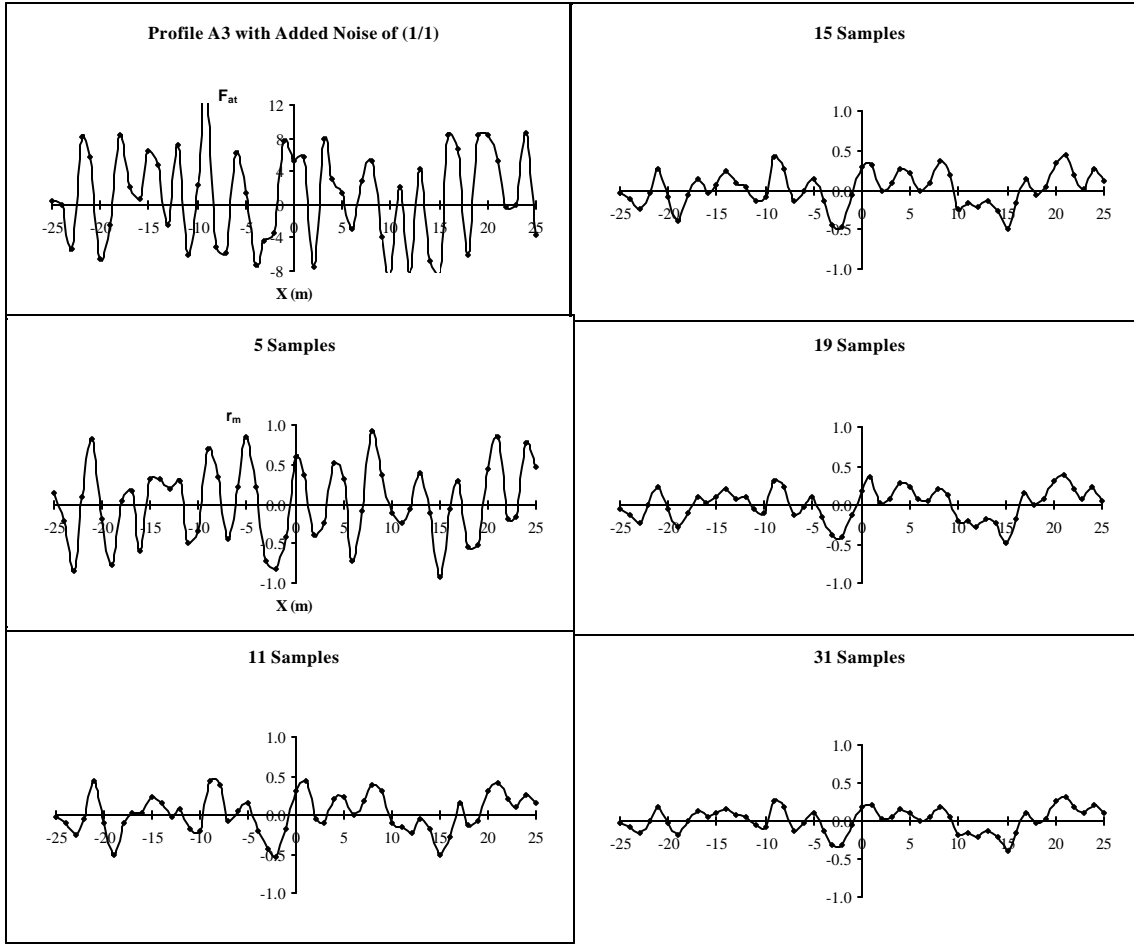
Figure 3.26 A comparison of resolution in correlograms for the cross-correlation of synthetic profiles A1 - A4 (Figure 3.19) with pilot signals with 11 samples computed for source depths of (0.5, 1 and 2 m). The affect of variation in the spacing distance between anomaly sources is presented down the columns. The affect of variation in the depth of pilot signal anomaly sources is presented across the rows. (*) denote the locations of anomaly sources cross-correlated with a pilot signal of the same depth.
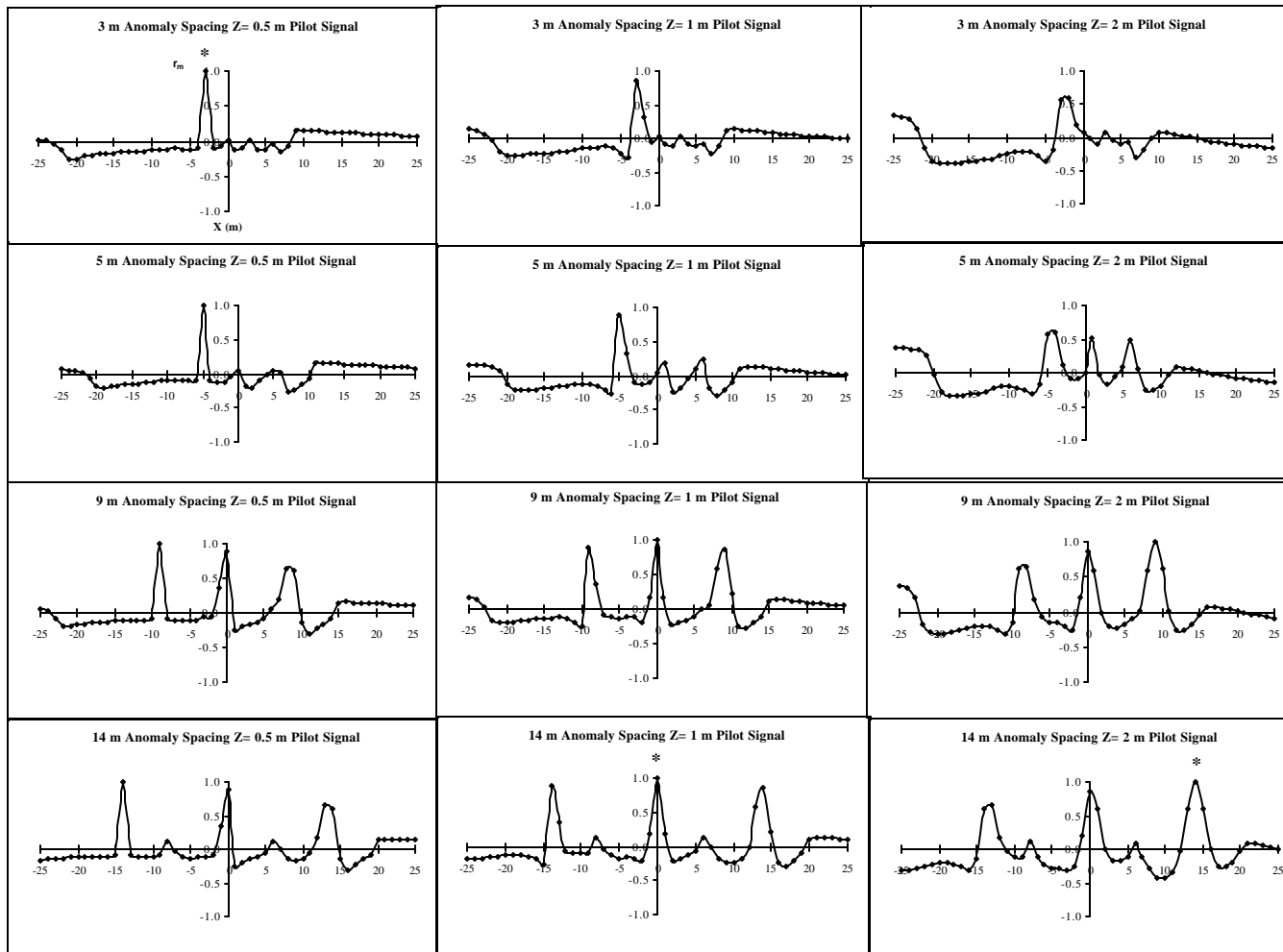
for the shallower anomaly sources and an increase in the r_m amplitudes of the deeper anomaly sources in the cross-correlation correlograms (Figure 3.26). This change allows the depth of the anomaly sources to be estimated based on a comparison of correlograms for pilot signals computed for a range of source depths.

The r_m amplitudes for profiles with anomaly sources at the same depth follow the same trends as single anomaly source profiles, when cross-correlated with pilot signals computed for a range of source depths.

When profiles with equal depth anomaly sources separated by 3m or less are cross-correlated with increasing source depth pilot signals, a single broad anomaly source is observed instead of three individual anomaly sources (Figure 3.27).

Conclusions

The pilot signals with intermediate number of samples, 11 and 15, provided the best resolution of both shallow and deep anomalies for multiple anomaly source profiles. The closer anomaly sources are together the more difficult it is to resolve them as individual sources and they instead are cross-correlated as a single broader anomaly. An estimation of anomaly depths is possible by comparing correlograms for pilot signals computed for different source depths if individual sources are resolvable. Anomaly sources were generally resolvable up to added noise with a S/N ratio 4/1 depending on the number of samples in the pilot signal.

Vertical Gradient Cross-Correlations

Purpose

To determine the efficacy of cross-correlation for identifying the positions and depths of anomaly sources in vertical magnetic gradient anomaly source profiles and how they compare with the total field cross-correlations.

Figure 3.27 The effect of cross-correlation between pilot signals for different source depths and profiles with three closely spaced anomaly sources. Correlograms of the cross-correlation between profile D1 (Figure 3.20) and pilot signals computed for different source depths each with 19 samples.
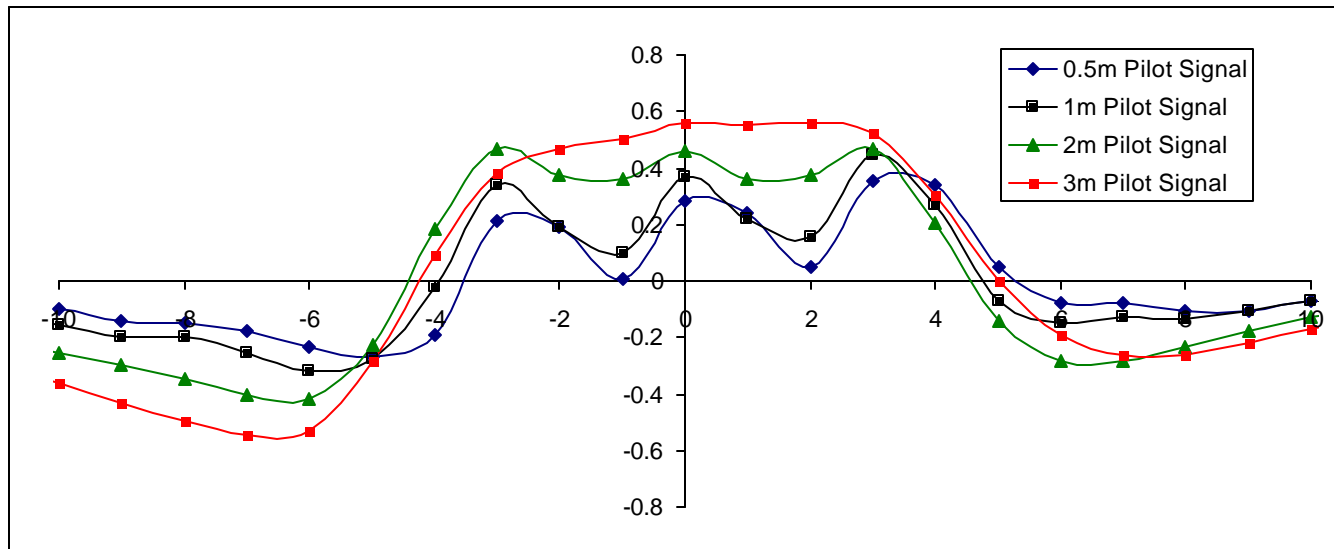
Method

      Vertical gradient cross-correlations investigated pilot signals with differing numbers of samples points, profile and pilot signal anomaly source depth, addition of random noise, and the separation distance between multiple anomaly sources. These tests were conducted in the same manner as those for the total field anomalies except with vertical gradient profiles and pilot signals. When total field anomaly and vertical gradient correlograms were compared, the total field anomaly pilot signals source depths were equal to the distance between the vertical gradient pilot signal source and the lower gradiometer probe.

Conclusions

      The vertical gradient cross-correlation tests produced nearly identical correlograms as the total field anomaly source tests for the same parameter values, and thus the same conclusions were drawn (Figure 3.28). This is because the cross-correlations of total field and vertical gradients are based on computation from the same anomaly sources just with different units, nT and nT/m. Cross-correlation is determining if an anomaly source is present and where it is located, irrespective of the units as long as both signal and profile have the same units or scalars of the same units, i.e., centimeters and meters.

      These cross-correlation were conducted on profiles without regional trends or diurnal fluctuations in the local magnetic field. It would be beneficial to use cross-correlations on vertical gradient data because these variations do not affect vertical gradients. Since both total field and vertical gradient magnetic data should produce the same cross-correlations, a comparison of results from both would be useful for confirming the presence and or depth of potential anomaly sources.

Figure 3.28 A comparison between cross-correlations of Fat and vertical gradient profiles. The synthetic Fat and vertical gradient profiles were each computed for a 1 m deep anomaly source and cross-correlated with pilot signals computed for a 1 m deep source with 11 samples. A) No noise was added to the profiles. B) Random noise was added with a noise factor of (1/20). C) Random noise was added with a noise factor of (1/1).
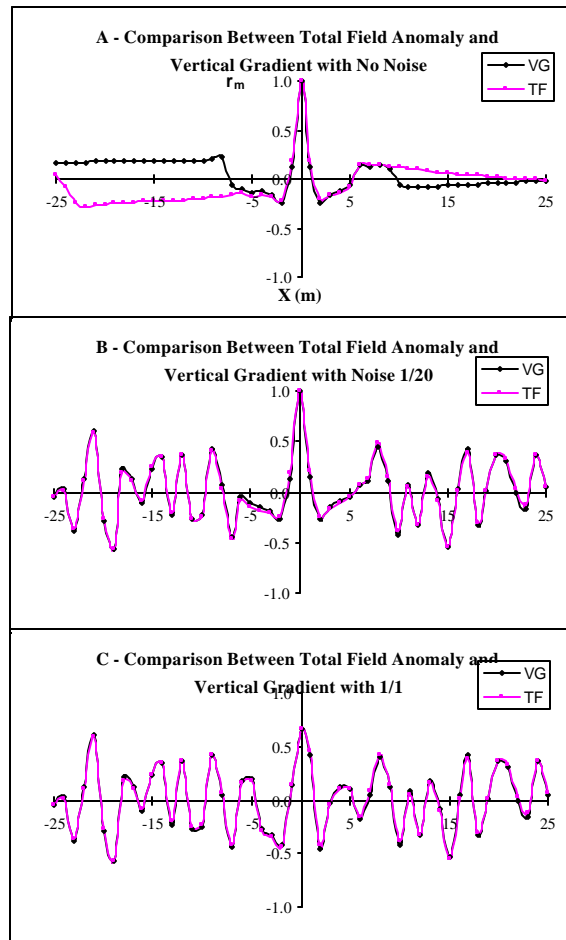
Lake Herrick Control Profiles Cross-Correlation Tests

The cross-correlation technique was applied to a set of real data with a known anomaly source in order to test the synthetic cross-correlation conclusions.

Purpose

The purpose of this experiment was to determine if cross-correlation could resolve an anomaly source of known location and depth from a real data set.

Methods of Control Profile Experiment

Data were collected from six transects along the same line with a GEM Systems GSM-19 Overhauser magnetometer/gradiometer. Both total field and vertical magnetic gradient were recorded. Data were collected along three pairs of transects, each 50 m in length with samples collected at 0.5 m intervals. The separation between the two gradiometer probes was held constant, though the height of the probes above the ground changed for each transect pair, so as to produce the effect of an anomaly buried at different depths (transects 2a and 2b at 0.56 m, transects 3a and 3b at 0.94 m, and transects 4a and 4b at 1.82 m).

The transects were located on Baseball Field #5 at Lake Herrick, Athens, Georgia. The transects trended 4 degrees west of magnetic north and were oriented in order to stay as far as possible from the stadium lights located around the field and to maintain as near a north-south transect as possible. The magnetic anomaly source was a rectangular steel plate with the dimensions of 20.2 cm by 20.3 cm by 2.5 cm. The plate was placed on the ground surface of the transect at the (x) position of 32 m in order to separate it from several existing anomalies identified on the transect. The transects with the suffix (a) were collected without the presence of the steel plate, while those transects with the suffix (b), were collected with the steel plate located on the transect. Thereby data was collected at each probe height setting both with and

without the anomaly source present. These six total field control profiles are presented in Figure 3.29, and six vertical gradient control profiles are presented in Figure 3.30.

Profile Descriptions

The total field profiles were similar to each other, and showed a large amplitude long wavelength dipolar anomaly from (x) = 0 to 14 m (Anomaly A). A high amplitude monopole was present from (x)= 24 to 28 m (Anomaly B). A very low amplitude anomaly (Anomaly C) was present in some of the profiles from (x)= 44.5 to 47.5 m. It was difficult to determine if this anomaly was a monopole or dipole because of its low magnitude and because it was located on a regional trend, which increased toward the north. The steel plate anomaly (Anomaly SP) was visible in the transects at (x) = 32 m, except for profile 4b, in which it was incorporated into the northern flank of Anomaly B.

The vertical gradient profiles (Figure 3.30) had the same anomaly locations as the total field profiles except that the relative amplitude of Anomaly A as compared to the other anomalies was decreased in the vertical gradient profiles while the relative amplitude of Anomaly SP was increased. In addition, the regional trend present in the total field profiles was absent, and Anomaly C was clearly a dipole. The negative half of the Anomaly SP dipole was visible in profile 4b, while the positive half was superimposed with the northern flank of Anomaly B. The amplitudes of anomalies A, B and C for both the total field and vertical gradient decreased as the gradiometer probes were moved farther above the steel plate.

Pilot Signals

Two sets of pilot signals were used in the cross-correlation with the control profiles. The first set of pilot signals, the subtracted pilot signals, were computed by taking the differences of each transect pair, i.e., 2b - 2a = signal 2, 3b - 3a = signal 3, and 4b - 4a = signal 4, for both the

Figure 3.29 Three pairs of total field control profiles collected at Lake Herrick for three different height settings of the gradiometer probes. The height above the ground surface of the lower gradiometer probe is noted for each profile. The locations of the four anomalies are labeled.
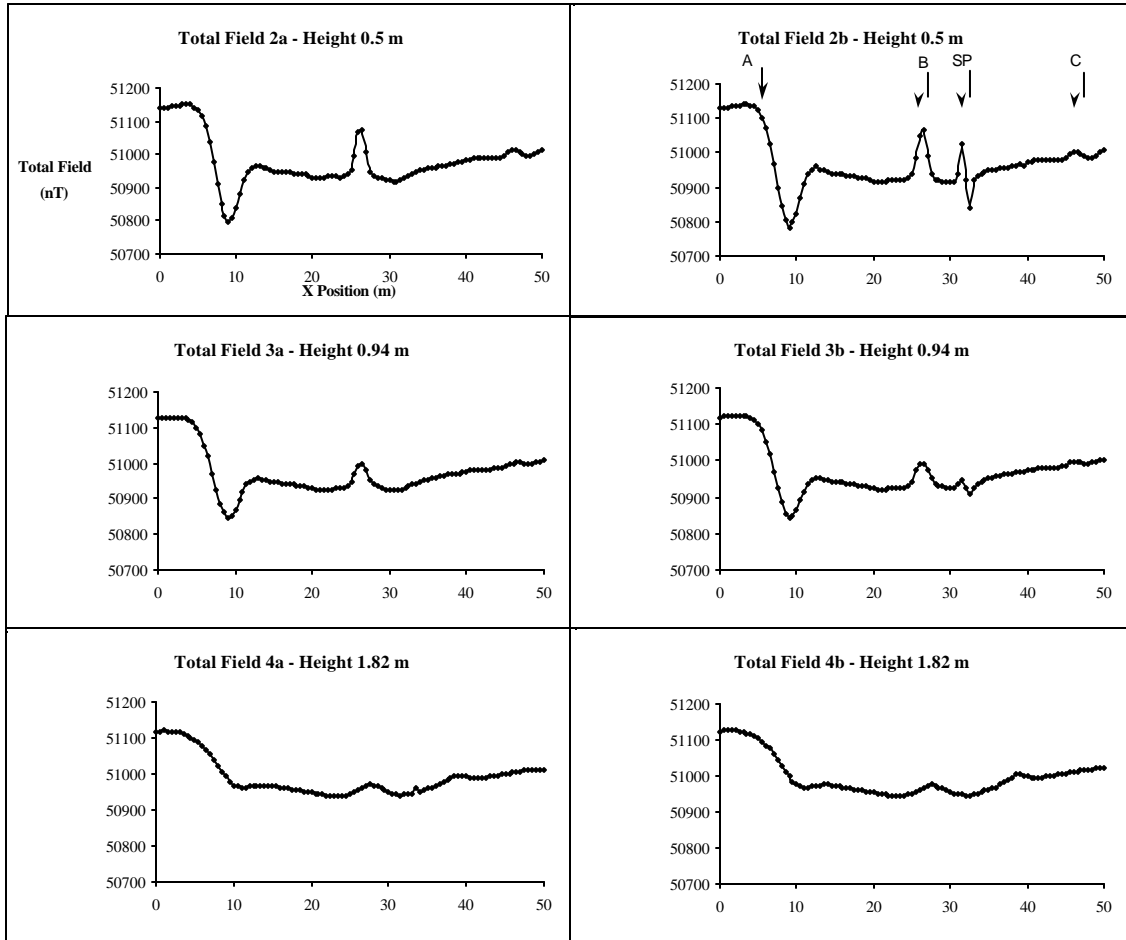
Figure 3.30 Three pairs of vertical gradient control profiles collected at Lake Herrick for three different height settings of the gradiometer probes. The height above the ground surface of the lower gradiometer probe is noted for each profile. The locations of the four anomalies are labeled.
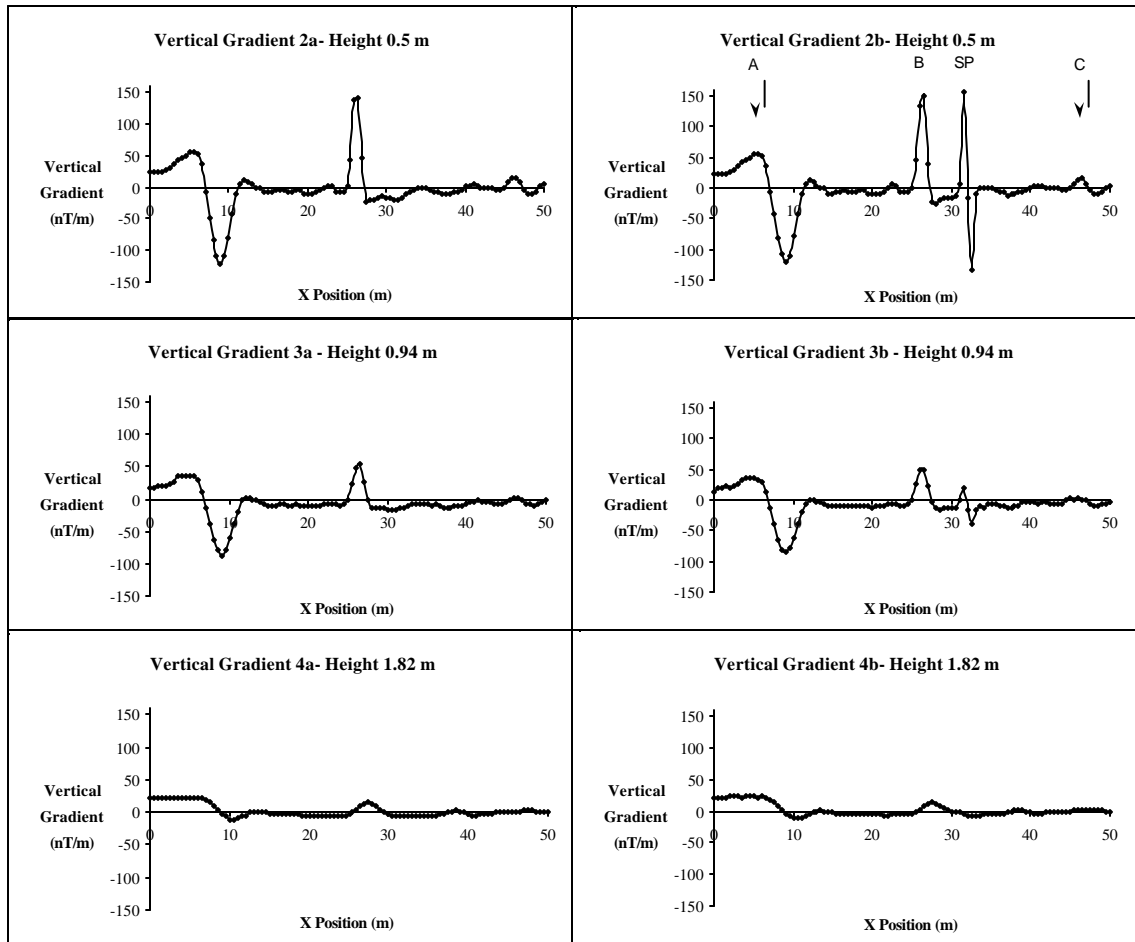
total field and vertical gradient profiles, (Figure 3.31). Cross-correlation was conducted with these perfect signals in order to compare the effectiveness of using computed spherical signals for cross-correlation. The profiles were cross-correlated with each of the three subtracted signals with 19 sample points to investigate the effect of the variation in signal depth. The profiles were also cross-correlated with their respective signal with 11, 15 and 19 sample points to investigate the effect of differing numbers of sample points.

The second set of pilot signals were computed for homogenous spheres buried at depths of 0.5, 1, 2, 3, 4, and 5 m for both total field and vertical gradient (Figures 3.32 and 3.33). The total field and vertical gradient profiles were cross-correlated with six source depth pilot signals with 11, 15, and 19 sample points. The purpose of this was to determine the efficacy of using a sphere as a simplified anomaly source for a non-spherical anomaly source and the effect of differing numbers of pilot signal sample points. The spherical anomaly source pilot signals were created using the parameters in Table 3.1.

Table 3.1 Parameters used for the Lake Herrick spherical pilot signal computation

(z) Depth to Sphere (meters)	0.5, 1, 2, 3, 4, & 5
(r) Radius Sphere (meters)	0.5
(k) Magnetic Susceptibility Contrast (cgs emu)	0.00004
(Fe) Earth Magnetic Field (nT)	51135
(i) Inclination of Earth's Magnetic field (degrees)	63
(α) Alpha (degrees)	4

The parameters r and k were set to the same values as for the synthetic tests, though as demonstrated in previous sections these values are only scalars and therefore the actual values used are unimportant. The values for Fe, i, and α were computed using the 2000 IGRF in the same was as for the synthetic tests, by using the Geomag v 4.0 software by NOAA. The earth's magnetic field was computed for Lake Herrick, Athens, Georgia (latitude: north 33 degrees, 56

74

Figure 3.31 Subtracted pilot signals for both the total field and vertical gradient, each with 19 samples.
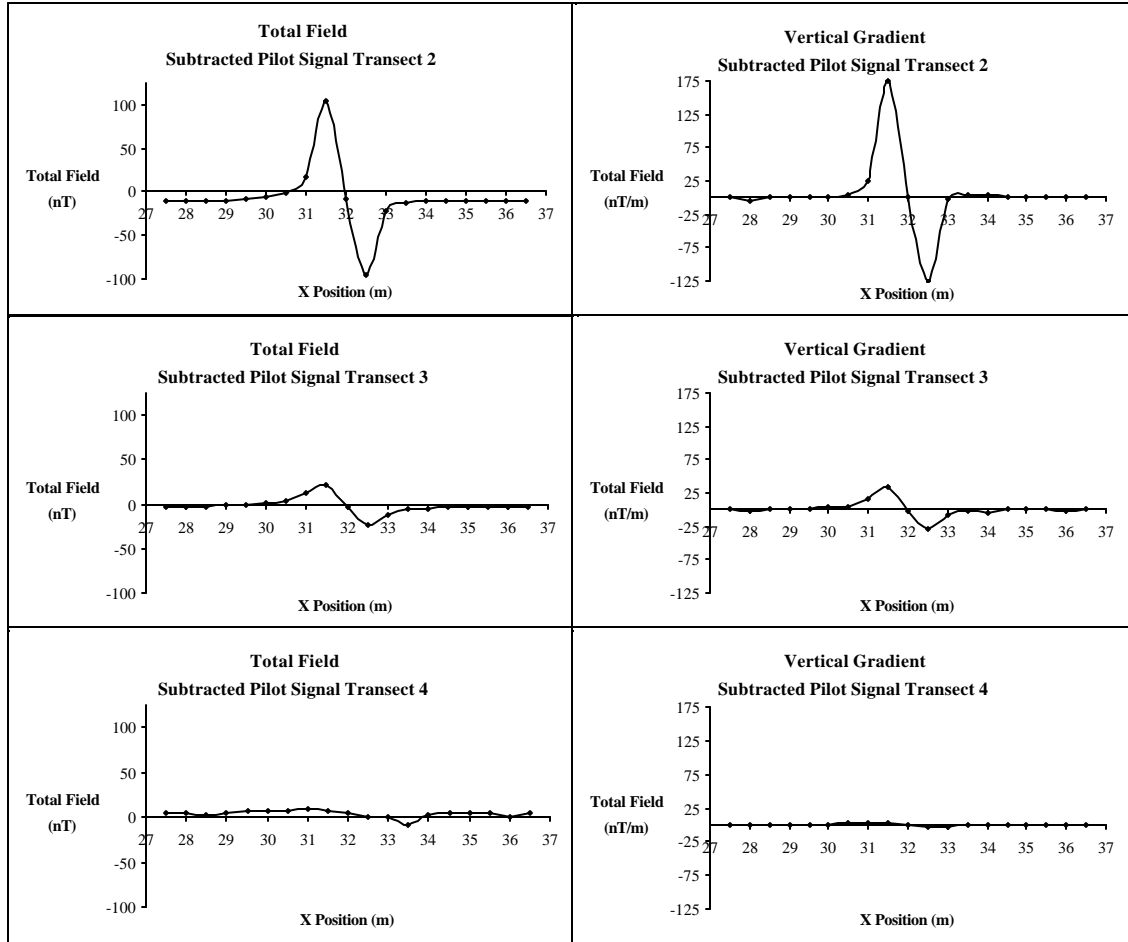
Figure 3.32 Synthetic spherical Fat pilot signals computed for six different anomaly source depths each with 19 samples.
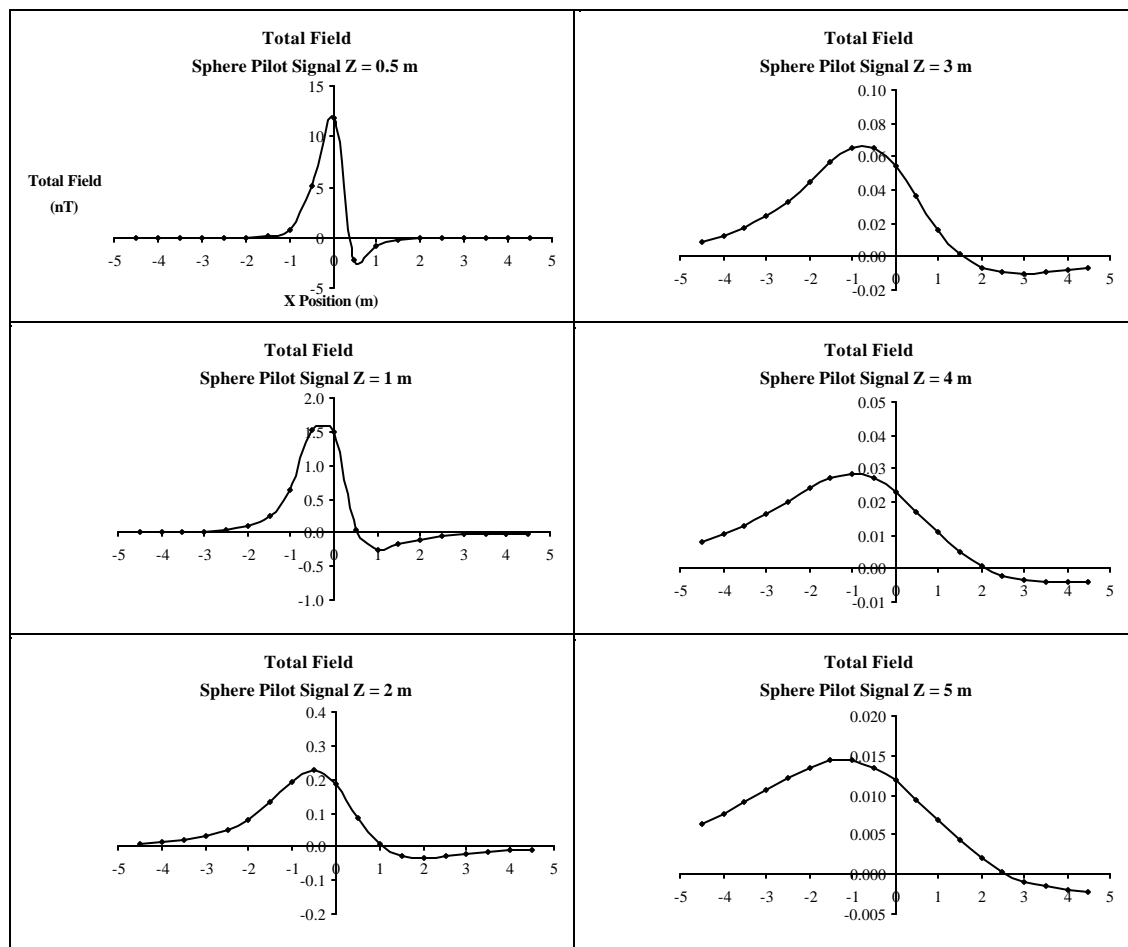
Figure 3.33 Synthetic spherical vertical gradient pilot signals computed for six different anomaly source depths each with 19 samples.
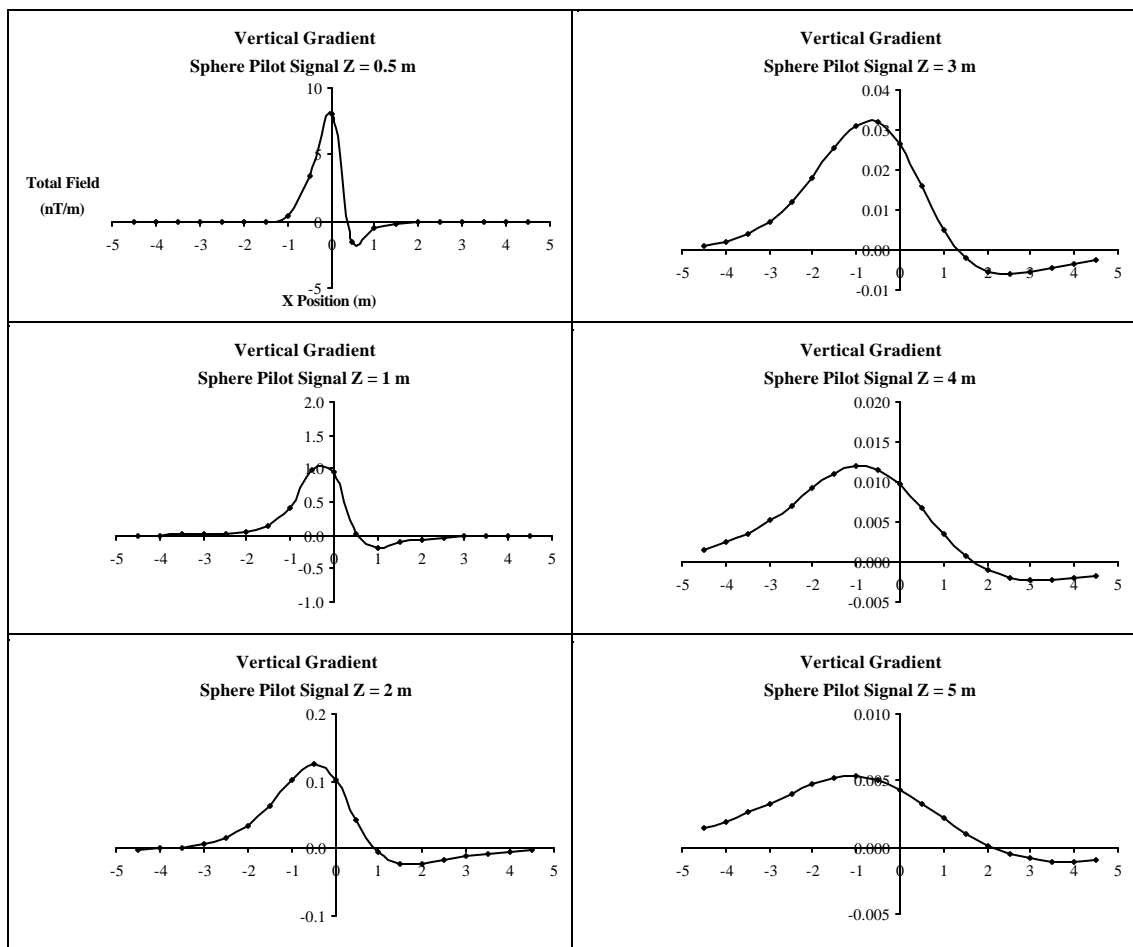
minute, 3 seconds; longitude: west 83 degrees, 22 minutes, 2.3 seconds; elevation: 630 feet) for March 12, 2003.

Observations

a. Subtracted Pilot Signals

The total field subtraction pilot signals (2 and 3) produced resolvable correlation peaks for the Anomaly SP when cross-correlated with total field Profiles 2b, 3b, and 4b (Figures 3.34 – 3.36). The cross-correlation of the profiles with subtraction pilot signal (2) produced greater amplitude correlation peaks than signals 3 or 4. The correlation peak amplitudes were greater in the profile 2b correlograms, than in either the 3b or 4b profile correlograms. For this reason depth determination was not possible for the total field profiles with the subtraction pilot signals. The use of the subtraction pilot signals (2 and 3) increased the S/N ratio by increasing the relative amplitude ratio of Anomaly SP to Anomaly B on the correlograms.

Increasing the number of pilot signal sample points decreased the amplitudes of all correlograms (Figure 3.37), though it had the greatest effect on the correlograms for profiles 3a, 3b, 4a, and 4b. The ratio of the amplitudes of Anomaly SP to Anomaly B decreased greatly between the profile 3b correlograms for pilot signals with 11 and 19 sample points. The width of anomaly peaks on correlograms was also useful for locating buried sources. In addition the cross-correlations removed the northward increasing regional trend from the profiles.

The vertical gradient subtraction pilot signals (2, 3, and 4) produced correlation peaks for Anomaly SP when cross-correlated with vertical gradient Profiles 2b, 3b, and 4b, though the peak amplitudes created with the signal (4) were very low and could have been mistaken for noise (Figures 3.34 – 3.36). Depth resolution was possible for both profiles 2b and 3b, as the correlogram for profile 2b exhibited the greatest peak amplitude for Anomaly SP when cross-

Figure 3.34 A comparison of correlograms for the cross-correlations between total field and vertical gradient profiles 2b (Figures 3.29 & 3.30) and the three total field and vertical gradient subtraction pilot signals (2, 3, & 4) (Figure 3.31), each with 19 samples.

Figure 3.35 A comparison of correlograms for the cross-correlations between total field and vertical gradient profiles 3b (Figures 3.29 & 3.30) and the three total field and vertical gradient subtraction pilot signals (2, 3, & 4) (Figure 3.31), each with 19 samples.

Figure 3.36 A comparison of correlograms for the cross-correlations between total field and vertical gradient profiles 4b (Figures 3.29 & 3.30) and the three total field and vertical gradient subtraction pilot signals (2, 3, & 4) (Figure 3.31), each with 19 samples.
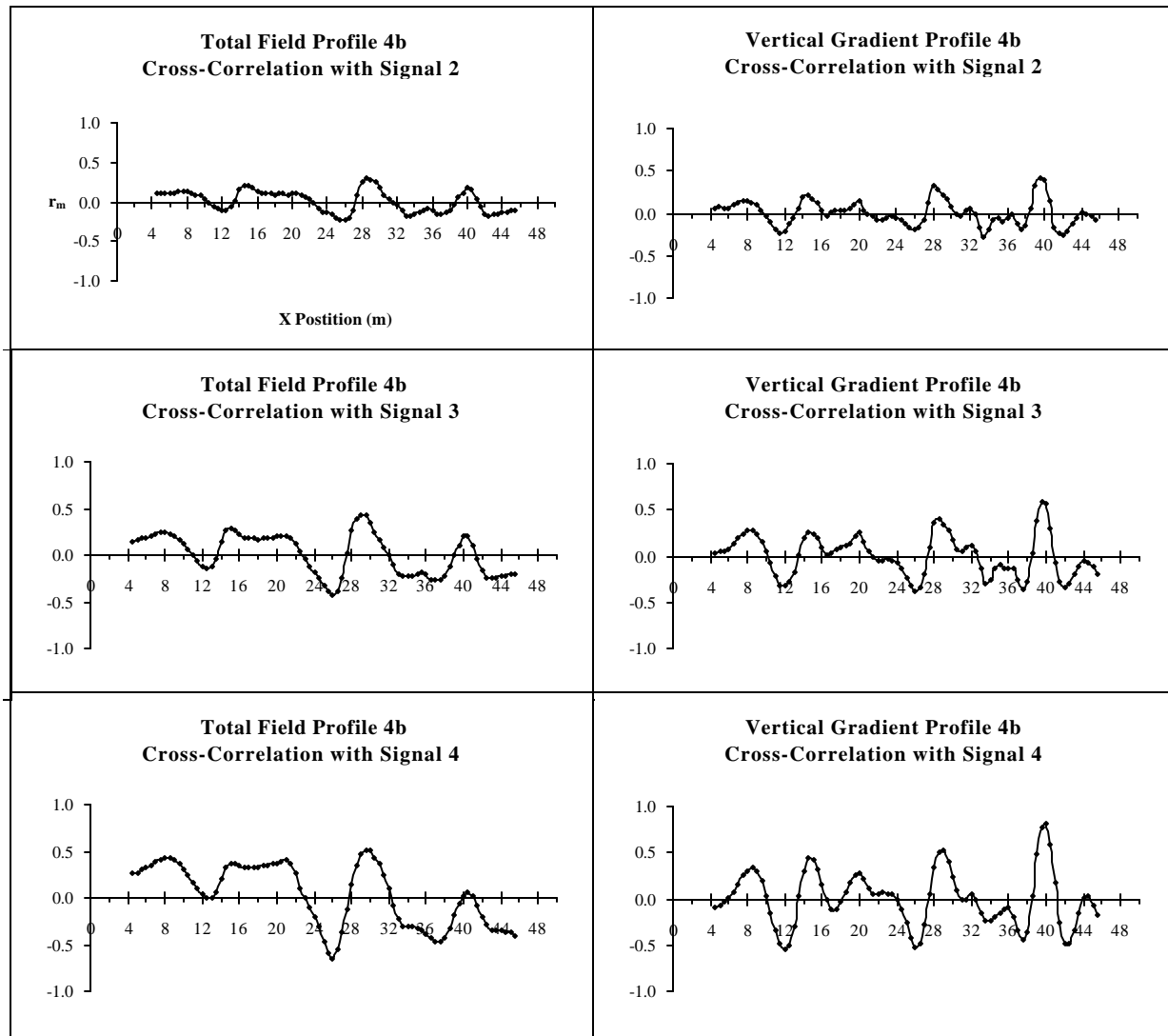
Figure 3.37 A comparison of correlograms for the cross-correlations between total field and vertical gradient profiles 3b (Figures 3.29 & 3.30) and the total field and vertical gradient subtraction pilot signal (3) (Figures 3.32 & 3.33) with three different number of samples (11, 15, & 19).
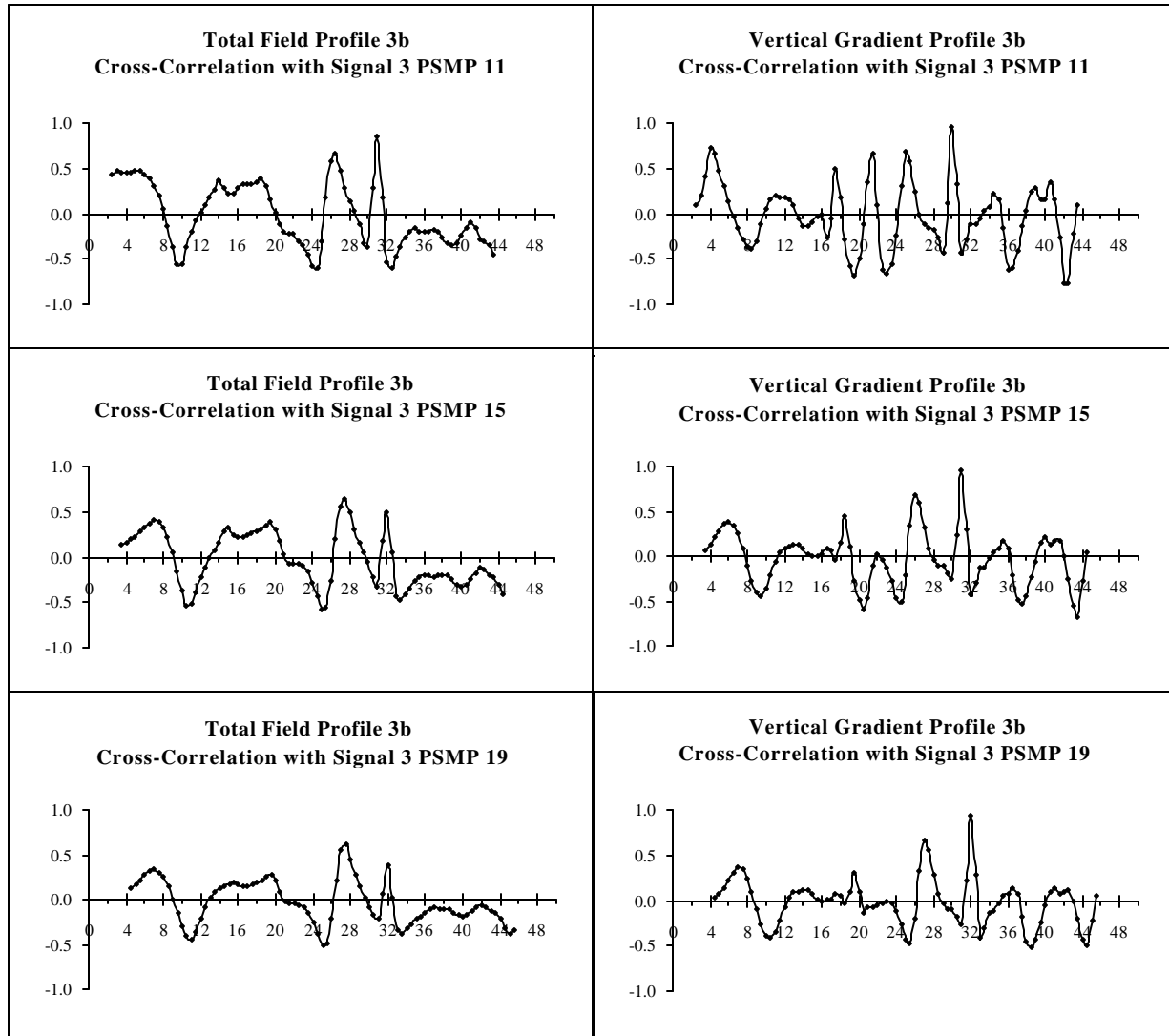
correlated with signal (2), while the correlogram for profile 3b exhibited the greatest peak amplitude for Anomaly SP when cross-correlated with signal (3). The peak amplitude for Anomaly SP was greatest in the correlogram of profile 4b when it was cross-correlated with signal (3), which demonstrated lesser depth resolution.

Decreasing the number of pilot signal samples increased the amplitudes of all correlograms, though the amplitudes of the noise increased by a greater amount than did the Anomaly SP peaks (Figure 3.37). In addition the number of spurious peaks increased as the number of pilot signal samples decreased.

b. Spherical Source Pilot Signals

The amplitudes of the Anomaly SP peaks in the total field spherical anomaly pilot signal correlograms decreased with both increasing profile anomaly source depth and increasing pilot signal source depth, and were difficult to resolve or were irresolvable at pilot signal source depths greater than 2 m (Figure 3.38). It was not possible to determine the anomaly source depths of Anomaly SP as its maximum amplitude was always associated with the correlogram of the $Z = 0.5$ m source pilot signal.

The amplitudes of the correlograms increased as the number of pilot signal samples decreased, though the increase was greatest for Anomaly SP, while the amplitude of Anomaly B increased only slightly (Figure 3.39). The cross-correlations removed the northward increasing regional trend from the profiles.

Vertical gradient correlograms demonstrated a moderate ability to determine the depths of profile anomaly sources (Figure 3.40). The 2b profiles had the greatest Anomaly SP amplitudes in the $(z) = 0.5$ m pilot signal correlograms. The 3b profiles had very similar amplitudes with r_m values of 0.854 and 0.822, in the correlograms for the pilot signals of $(z) =$

Figure 3.38 A comparison of correlograms for the cross-correlations between total field profile 3b (Figure 3.29) and the synthetic Fat pilot signals computed for spherical sources at six depths (Figure 3.33), each with 15 samples.
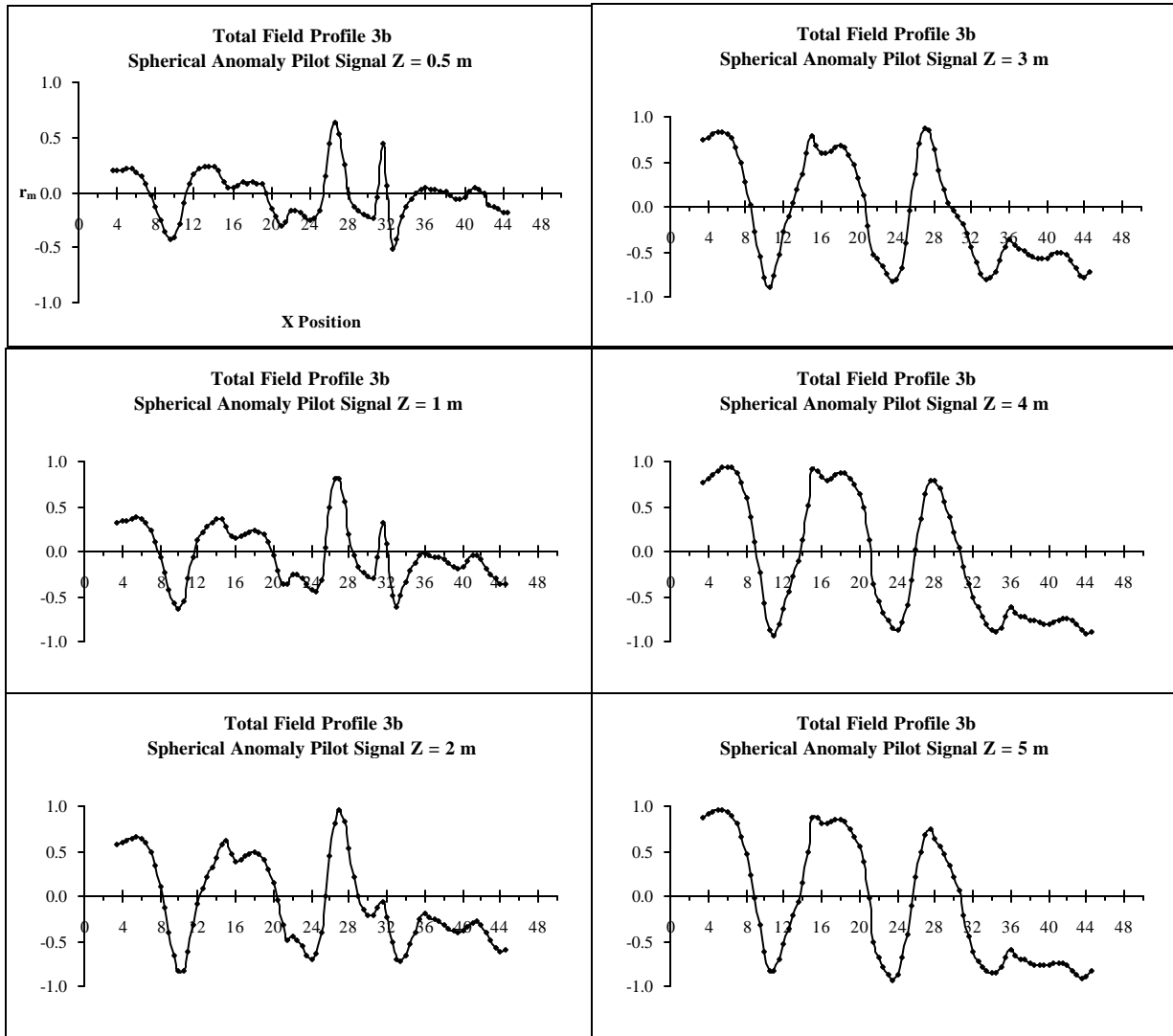
Figure 3.39 A comparison of correlograms for the cross-correlations between total field and vertical gradient profiles 3b (Figures 3.29 & 3.30) and the synthetic Fat and vertical gradient pilot signals (Figures 3.32 & 3.33) computed for a 1 m deep source with three different numbers of samples (11, 15, & 19).
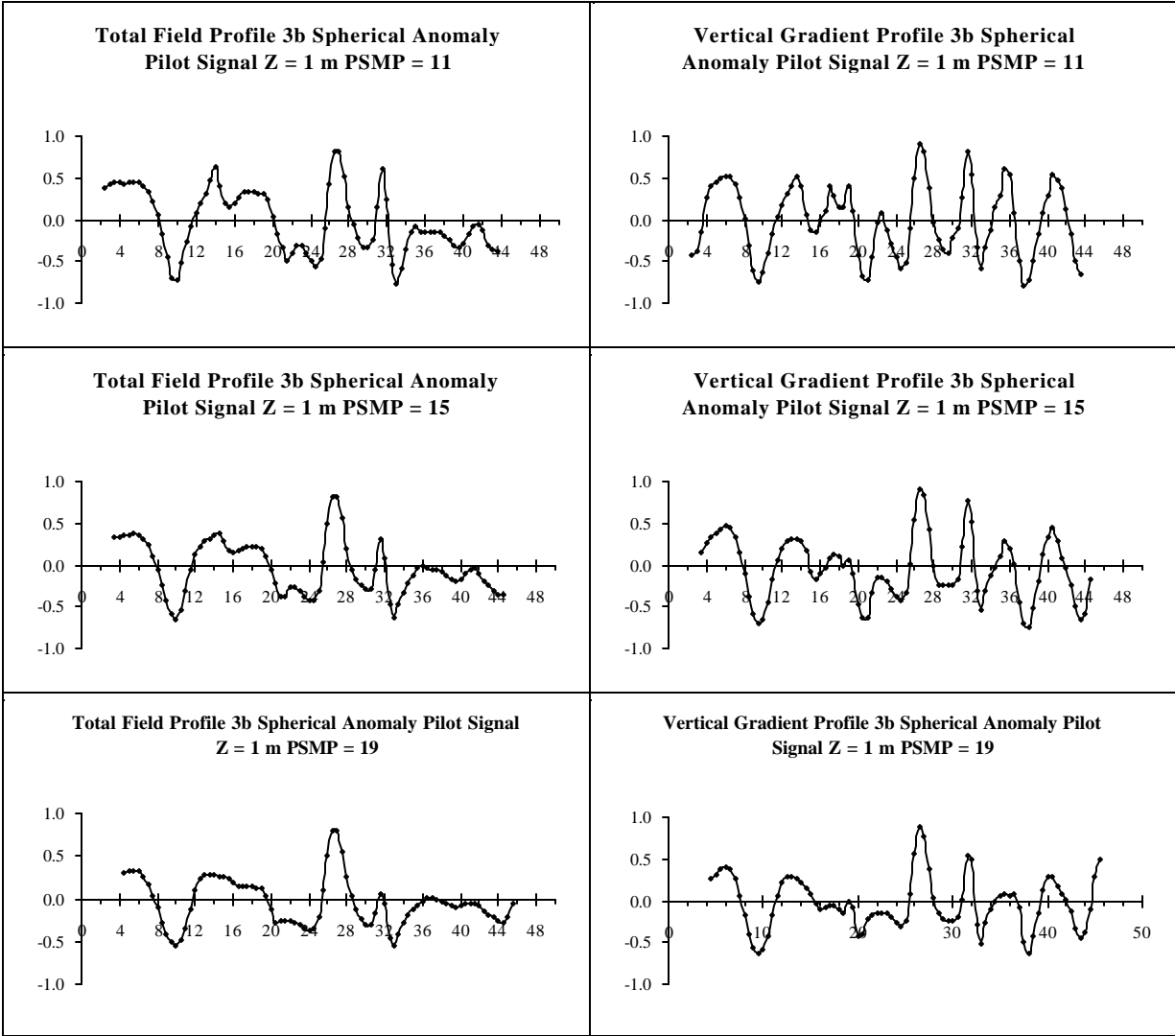
Figure 3.40 A determination of the depth of the Anomaly B source. A comparison of correlograms for cross-correlations between vertical gradient profiles 2b, 3b, and 4b (Figure 41) with a synthetic vertical gradient pilot signal computed for a A) 1 m deep spherical anomaly source with 15 samples. B) 2 m deep spherical anomaly source with 15 samples. C) 3 m deep spherical anomaly source with 15 samples.
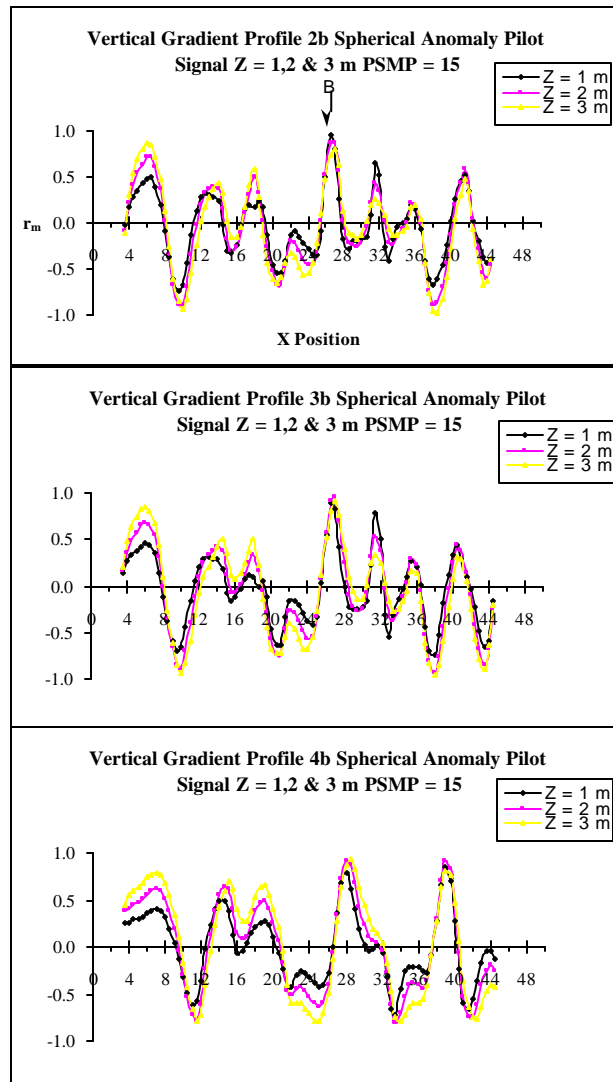
0.5 and 1 m respectively for pilot signal with 11 samples. These r_m values were within less than 5% of each other well within possible error, from which can be concluded that the anomaly source for Anomaly SP from profile 3b was in the range of 0.5 to 1 m deep, its actual effective depth was 0.94 m. The determination of the source depth for Anomaly SP in the 4b correlograms was more difficult because the anomaly peak began to combine with the peak of Anomaly B as the pilot signal source depth increased. The r_m amplitude values for profile 4b were 0.241 and 0.352 for pilot signal source depths of 1 and 2 m respectively for 11 samples points. The Anomaly SP peak just began to combine with the Anomaly B in the correlogram for pilot signal (z) = 2 m, and therefore it may not be an accurate estimator of depth.

It was important to consider correlograms from pilot signals with different numbers of sample points, as the Anomaly SP peak for profile 4b was not resolvable in the correlograms for pilot signals with 15 or 19 samples.

It appeared however that the depth of the source of Anomaly B could be estimated as its peaks exhibited maximum amplitude for pilot signals with anomaly depths of 1, 2 and 3 m for profiles 2b, 3b and 4b respectively. As would be expected the apparent depth of the anomaly increased as the height of the gradiometer probes were increased. Therefore it was estimated that the source of Anomaly B was between 1 and 1.5 m bgs (Figure 3.40).

A decrease in the number of samples in pilot signals produced an increase in both the correlogram amplitudes and the number of spurious peaks caused by cross-correlation with noise (Figure 3.41).

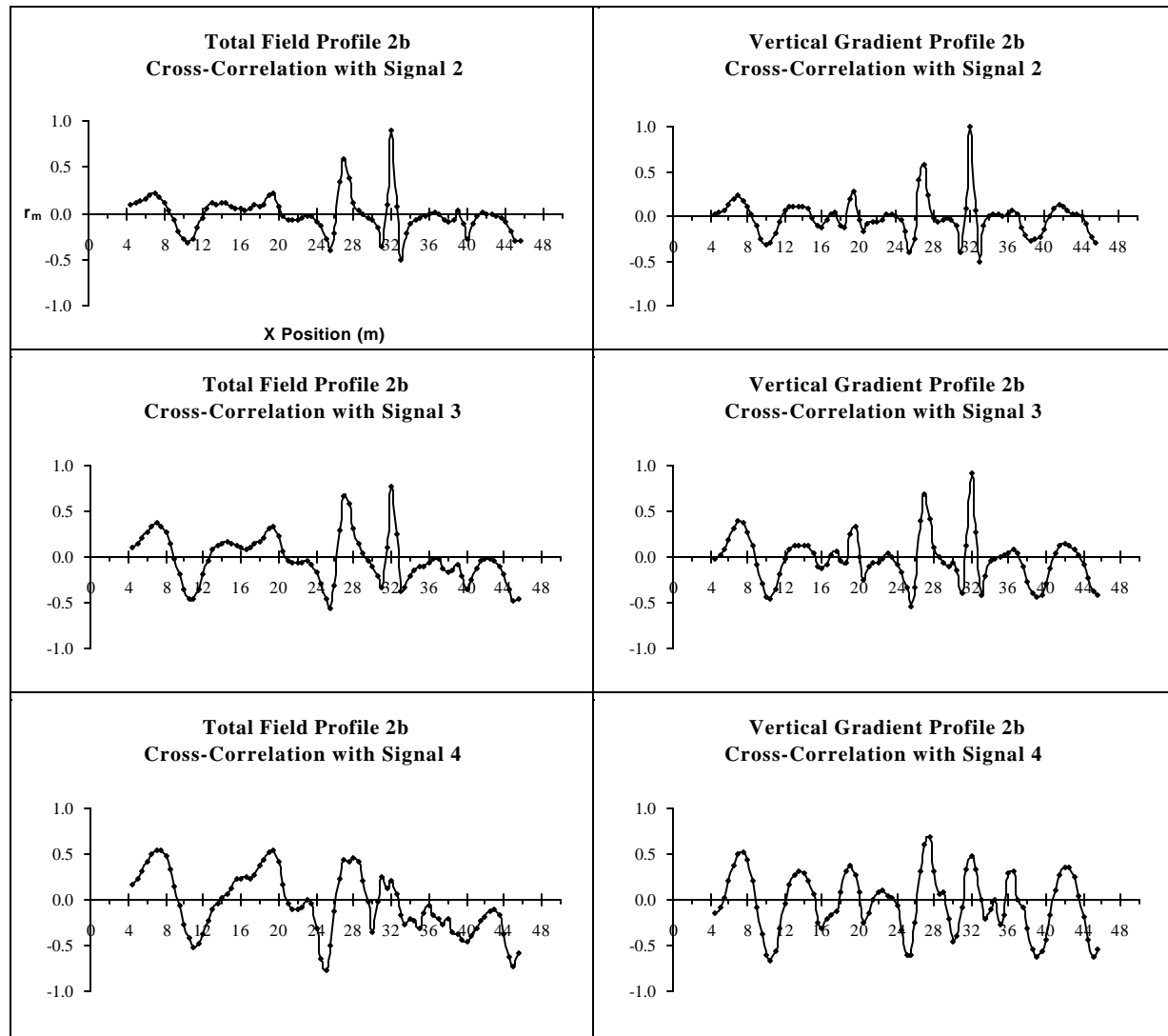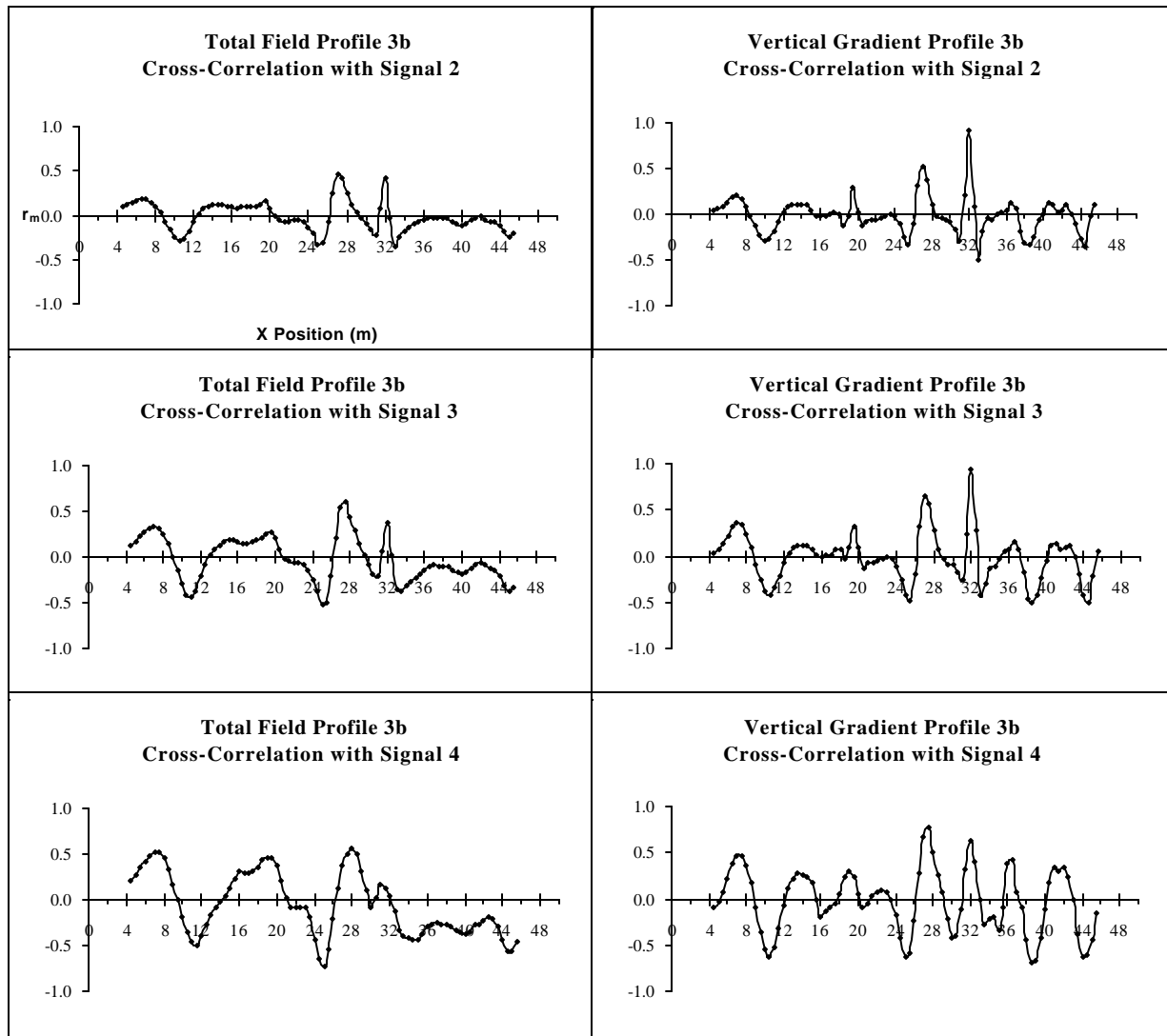**Figure 3.41 A comparison of correlograms for the cross-correlations between vertical gradient profile 3b (Figure 3.30) and the synthetic vertical gradient pilot signals (Figure 3.33) computed for spherical sources at six depths, each with 15 samples.**
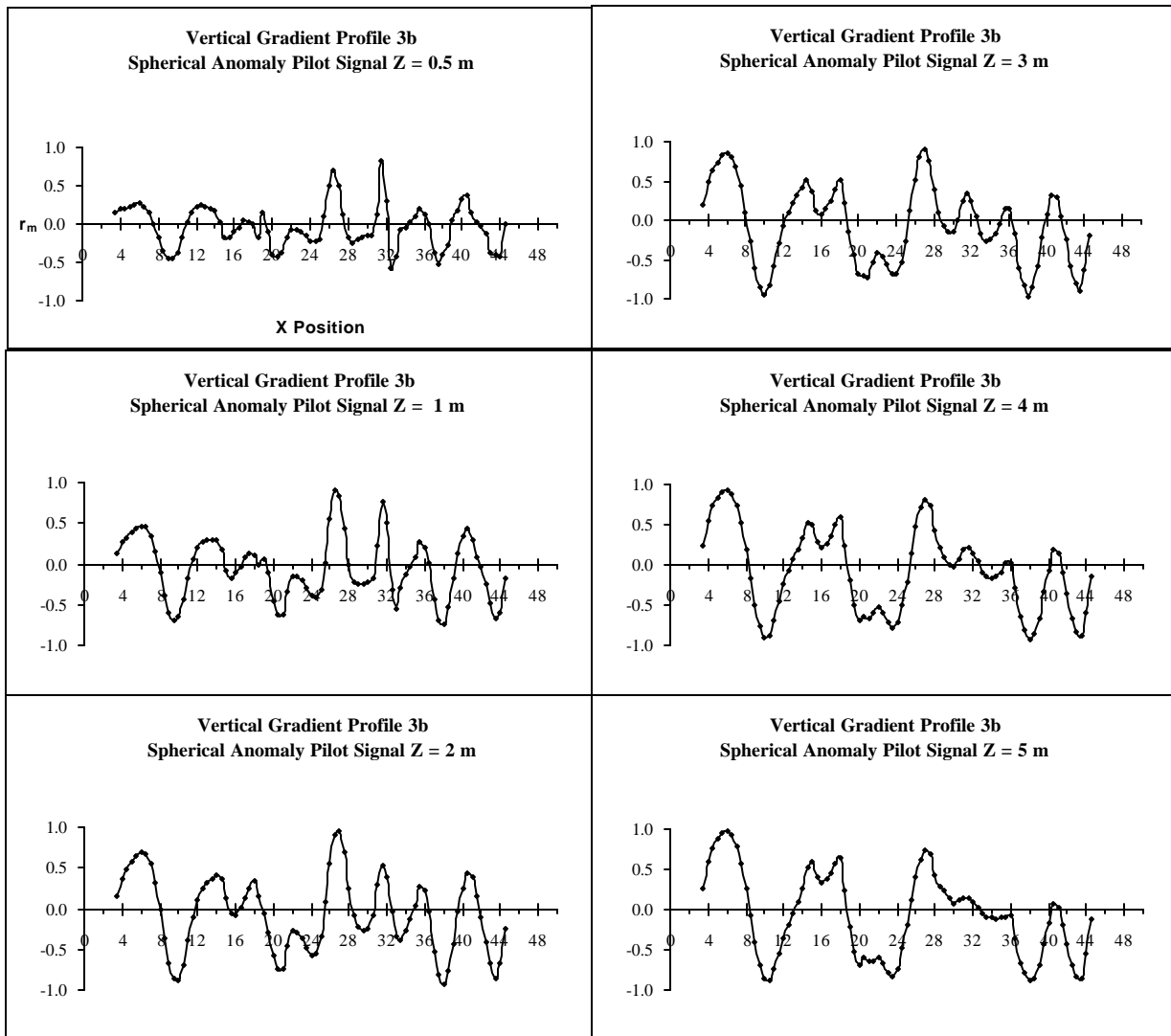
Conclusions

a. Subtracted Pilot Signals

Cross-correlation increased the S/N ratio for total field profiles 2b and 3b. It wasn't possible to positively locate Anomaly SP in total field profile 4b because it was superimposed on the northern flank of Anomaly B. The cross-correlations removed the regional trend that was present in the profiles. Cross-correlation also reduced the relative amplitude of Anomaly A while it increased the amplitudes of Anomalies B and SP.

The cross-correlation correlograms of the vertical gradients were similar to those for the total field except that the amplitudes of the narrow peaks were increased. The relative amplitudes of Anomaly SP to Anomaly B were greater for the vertical gradient cross-correlations than for the total field. The vertical gradient cross-correlations were able to discriminate Anomaly SP in the transect 4b anomaly using all three signals. The vertical gradient cross-correlations produced better S/N ratios for pilot signals with larger numbers of samples.

Cross-correlation of the vertical gradient profiles produced a better resolution of narrower anomaly signals, although it also increased the amplitudes of any narrow spurious noise peaks.

b. Spherical Source Pilot Signals

The use of spherical anomaly source pilot signals in cross-correlation for non-spherical anomaly source was successful for shallow anomaly sources, though less so for deeper sources. The Anomaly SP peak was resolvable during cross-correlation in total field profiles 2b and 3b and in vertical gradient profiles 2b, 3b and 4b at lesser numbers of pilot signal samples. Cross-correlation with pilot signals with greater numbers of samples reduced the overall correlogram amplitudes but also reduced the number of spurious peaks. Cross-correlation with the vertical gradient profiles produced greater resolution of anomaly source depth than did the total field. In

determining the depths of anomaly sources it was important to compute correlograms for differing numbers of pilot signal samples, as certain anomalies were only resolvable for pilot signals with certain numbers of samples.

c. Comparison of Subtracted and Spherical Source Pilot Signals

Cross-correlation with the subtracted pilot signals produced greater S/N ratios than their equivalent cross-correlations with the spherical anomaly source pilot signals. This was as expected because the subtracted signals were nearly perfect matches while the spherical anomaly source pilot signals were computed for a geometry different than the actual anomaly source. Even with this difference the spherical anomaly pilot signals adequately located Anomaly SP (Figure 3.42).

Discussion of the Cross-Correlation Analysis of Magnetic Data Using Synthetic and Control Profiles

a. Determining the Presence of an Anomaly Source Based on the Signal to Noise Ratio

The ability to detect the presence of anomaly sources from profiles and correlograms was a function of the signal-to-noise ratio. There were certain parameters that affected the S/N of the cross-correlation correlograms as compared to the S/N of the profiles. These parameters included the number of samples in pilot signals, the number of sources, and the separation distance between anomaly sources.

The number of samples in the pilot signal affected the number of complete and partial cross-correlation comparisons between a pilot signal and a profile, i.e., a pilot signal with 31 samples would allow a lesser number of complete and greater number of partial cross-correlations than a pilot signal with 11 samples for a given profile. The pilot signals with fewer

Figure 3.42 A comparison between cross-correlation correlograms for subtraction pilot signals and synthetic spherical anomaly pilot signals. A) Correlogram of the cross-correlation between total field profile 3b (Figure 3.29) and both the total field subtraction signal (3) and the synthetic Fat pilot signal computed for a 1 m deep spherical source (Figures 3.31 & 3.32), each signal having 19 samples. B) Correlogram of the cross-correlation between vertical gradient profile 3b (Figure 3.30) and both the vertical gradient subtraction signal (3) and the synthetic vertical gradient pilot signal computed for a 1 m deep spherical source (Figures 3.31 & 3.33), each signal having 19 samples.
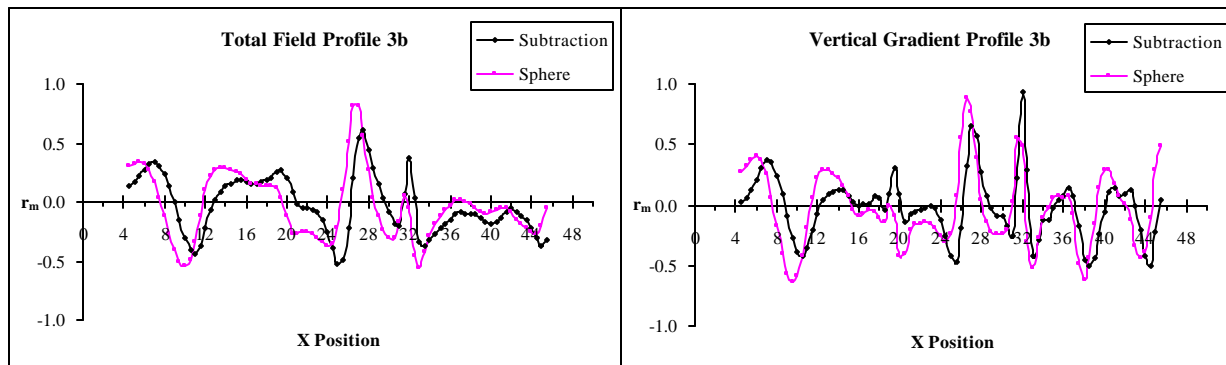
(11 and 15) samples tended to produce correlograms with overall higher r_m values and more numerous spurious peaks, while pilot signals with a greater number of samples produced correlograms with lower r_m values and fewer spurious peaks. This was because pilot signals with fewer samples correlated better with the portions of profiles with narrow peaks for both anomaly source signals and random noise. The pilot signals with 5 samples had too few samples as they correlated well with very narrow peaks and noise producing unusable wildly oscillating correlograms (Figures 3.13 and 3.14). Poor correlations were produced for low amplitude and narrow anomaly signal by the cross-correlations of profiles with pilot signals with numerous samples. It is suggested that pilot signals with multiple numbers of samples possibly in the 11 – 31 range be used when conducting cross-correlations in order to compare the correlograms since pilot signals with differing numbers of samples would cross-correlate better with different parts of the profile.

Neither the radii nor magnetic susceptibility contrast of the anomaly sphere in either the profile or pilot signal had any effect on the cross-correlation correlogram when all other parameters were constant.

The cross-correlation correlogram is based on the ratios of the amplitudes of each point to each other point on a profile of the magnetic field values (y-axis values) as opposed to the shape of the curve in terms of its 2-D (x and z) dimensions. Because of this, two curves with different 2-D shapes but with the same amplitude ratios would cross-correlate well with each other. For this reason any factor which increased or decreased the amplitudes of a profile by a constant, either additive or multiplicative, would not effect the cross-correlation correlogram, because the curve still had the same amplitude ratios. These types of scalars included the diameter of a

homogenous spherical anomaly source, a linear (constant) regional trend and the magnetic susceptibility of an anomaly.

Figure 3.43 presents three profiles, a raw profile, the raw profile with every point multiplied by a factor of 10 and the raw profile with 10 added to every point. These three same shape profiles with different absolute amplitudes were cross-correlated with the same 0.5 m depth anomaly source pilot signal, producing three identical correlograms (Figure 3.43).

The factors which did effect the cross-correlation correlograms were those that non-uniformly altered the amplitude ratios of the points on the profile yielding differences in shape, for example the superposition of multiple anomalies, a non-constant regional trend, or random noise. These factors either added or subtracted from the anomaly source amplitudes, either over part or all of an anomaly source signal. Because of this, when cross-correlating it was not important what anomaly source sphere diameter or magnetic susceptibility contrast was used for the pilot signals, as long as they were constant for all pilot signals. The actual diameter or magnetic susceptibility of the pilot signal being cross-correlated wouldn't matter for determining depth, because those factor are only scalars and don't affect the cross-correlation.

It was found that pilot signals with fewer numbers of samples were better at resolving closely spaced anomaly sources. It was more difficult to locate anomaly sources in profiles with closely spaced multiple anomalies because the individual anomaly signals could be combined by superposition into a single anomaly peak, which could alter the relative signal amplitudes, and the perceived position of the anomaly source. Anomaly sources could more easily be located if the cross-correlations were conducted with pilot signals with multiple numbers of samples and pilot signals computed for multiple anomaly source.

Figure 3.43 A comparison of cross-correlations for profiles with different absolute amplitudes. A) A comparison of the shapes of three profiles computed for a 0.5 m deep source. Profiles E2 and E3 are modified versions of E1. B) Correlogram of the cross-correlation between each of the profiles in (A) and a pilot signal computed for a 0.5 m deep source with 11 samples.
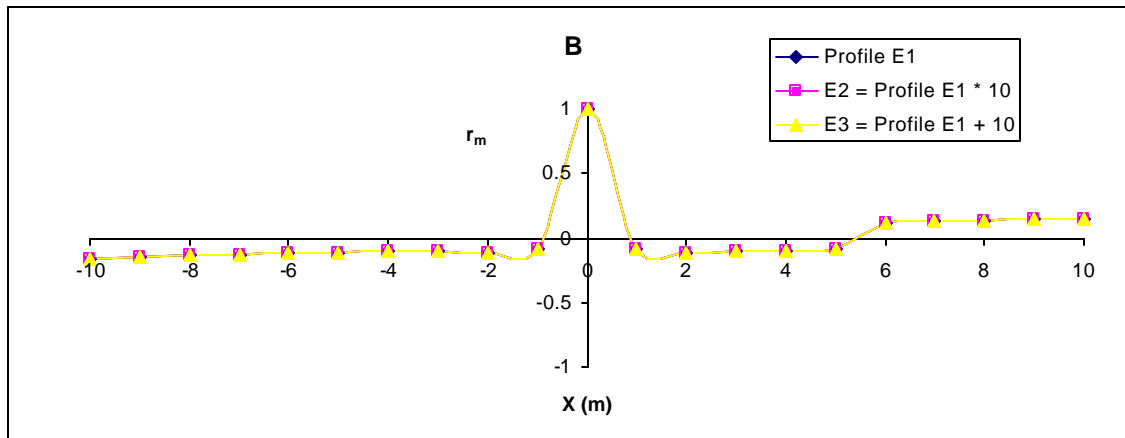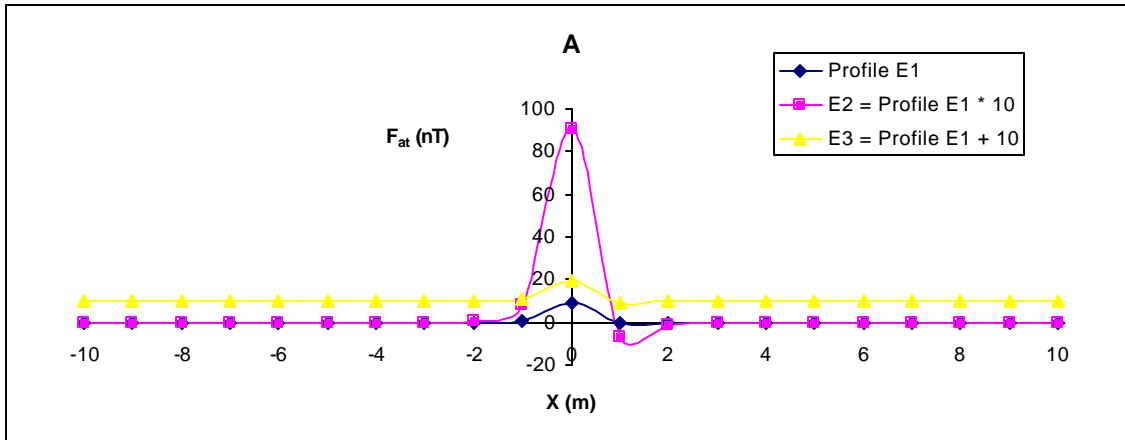
The signal to noise ratio could be greatly increased in profiles with multiple anomaly sources at different depths provided the sources were sufficiently separated to prevent a detrimental superposition of signals. Cross-correlation could increase the amplitude ratios of low-amplitude anomalies in profiles that were overshadowed by higher amplitude shallower sources (Figure 3.26).

Since the vertical gradient and total field correlograms should be nearly identical, their comparison would increase the S/N ratio by helping to confirm or reject the presence of anomaly sources. In addition by the nature of collecting the vertical gradient data, any large or nonlinear regional trends or large diurnal fluctuations present in the total field data would have been removed.

b. Determining the Horizontal Position of an Anomaly Source

Cross-correlation can help to constrain the horizontal position of anomaly sources. The apex of an anomaly source peak on a correlogram was at the horizontal position of the anomaly source because the greatest correlation occurred when the profile and pilot signal were most similar, i.e. when their sources were at the same position. Cross-correlation produced similar results to the reduction to the pole method, i.e. the magnetic anomaly asymmetry caused by magnetic latitude was removed and the apex of the anomaly source peaks was moved directly over the anomaly source (Baranov, 1957; Baranov and Naudy, 1964; von Frese, 1984; Silva, 1986; Scollar et al., 1990; Blakely, 1995). Horizontal position was difficult to determine for anomaly sources located horizontally close together as such anomaly groups tended to cross-correlate as a single anomaly source with a broad width peak. The horizontal resolution of source locations was within one to two data points because the maximum amplitude of the anomaly source profiles are displaced from the source of the position for deeper sources.

c. Estimating the Depth of an Anomaly Source

The anomaly source depth of a pilot signal was an important factor for locating anomaly sources, because changes in the depth of an anomaly source drastically altered the shape of its magnetic field signal. Since the details of signal shape were sensitive to source depth, the determination of source depth of a known anomaly peak could be accomplished with cross-correlation. An anomaly peak identified from a profile as a possible anomaly source could be cross-correlated with pilot signals for a wide range of anomaly source depths. The source depth of the pilot signal for the correlogram with the highest r_m value amplitude peak at the (x) position of the identified anomaly source would likely be closest to the center of the source object. If multiple anomaly source peaks were present in a profile, then cross-correlation with pilot signals for a range of source depths would provide the depths of the anomaly sources relative to each other. Depending on the diameter of the anomaly source the estimate would be slightly deeper than the outer edge of the object because the pilot signal are calculated for the center of a sphere.

d. Cross-Correlation of Lake Herrick Control Profiles

The use of a spherical anomaly source for the computation of pilot signals that were cross-correlated with non-spherical anomaly sources was successful for shallow anomaly sources, though less so for deeper sources, as demonstrated by the Lake Herrick data. The known anomaly source was resolvable during cross-correlation in two of the three total field profiles and in all three of the vertical gradient profiles. Cross-correlation with the vertical gradient produced a greater resolution of narrower anomaly signals than did the total field, though it also increased the amplitudes of any narrow spurious peaks.

It was not possible to determine the depths of a known anomaly sources with the total field data as the maximum cross-correlation amplitude was always associated with the

96

correlogram of the shallowest source pilot signal of (z) = 0.5 m. The vertical gradient

correlograms demonstrated a moderate ability to determine the depths of the known anomaly

source. The shallow source was accurately located, while the depths of the middle and deep

sources were each estimated to be located between two depths.

Applying Cross-Correlation Analysis to the Monte Pallano Data: The Archaeological

Problem

An archaeogeophysical investigation was conducted in the Sangro River Valley, on

Monte Pallano, Italy, in the area of Trench 8000 between May 7 – 14, 2002. A research team

from the University of Georgia, the United States Department of Agriculture – Forest Service,

and Oberlin College, conducted the investigation.

The areas investigated included:

1) Monte Pallano Grid 1 – North of Trench 8000

2) Monte Pallano Grids 2 & 5 – West of Trench 8000

3) Monte Pallano Grid 3 & 4 - East of Trench 8000

GPR data was collected at all five grids, while magnetic total field and vertical gradient

data were collected at Grids 1a, 2, 4, and 5. The GPR data collected for Grids 3, 4, and 5 was

along single lines with multiple transects per line. The locations of the five grids in relation to

the prior archaeological investigations are presented on Figure 3.44.

The purpose of collecting data from Grid 1 was to determine if any buried walls or

architectural features were present north of Trench 8000. Grid 1 was located in a grassy field

northeast and upslope of Trench 8000 with the Y-axis parallel to the trench's north edge (Figure

3.45). Grid 1 was a rectangular grid, the X-axis was 11 m in length and trended 39 degrees east

of true north, and the Y-axis was 24 m in length and extended west northwest. Grid 1 consisted
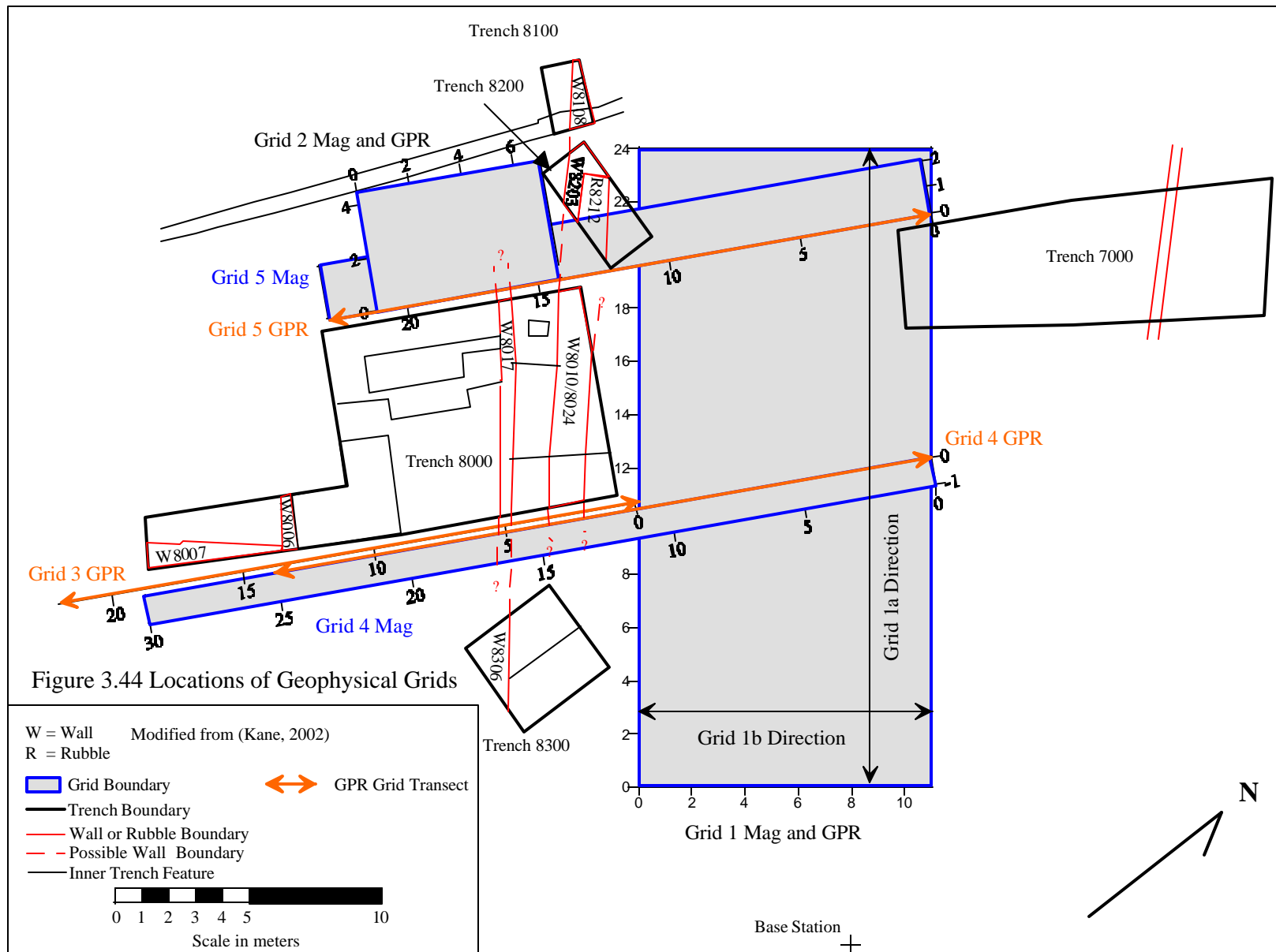
Figure 3.44 Locations of Geophysical Grids
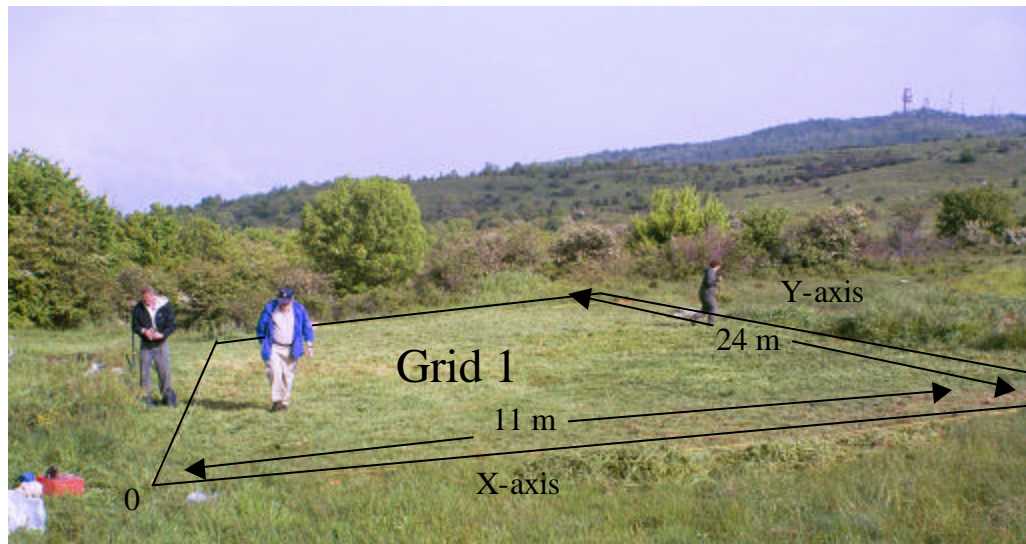
Figure 3.45 An outline of Grid 1 showing its dimensions. The origin is in the lower left corner. This photograph looks toward the west.
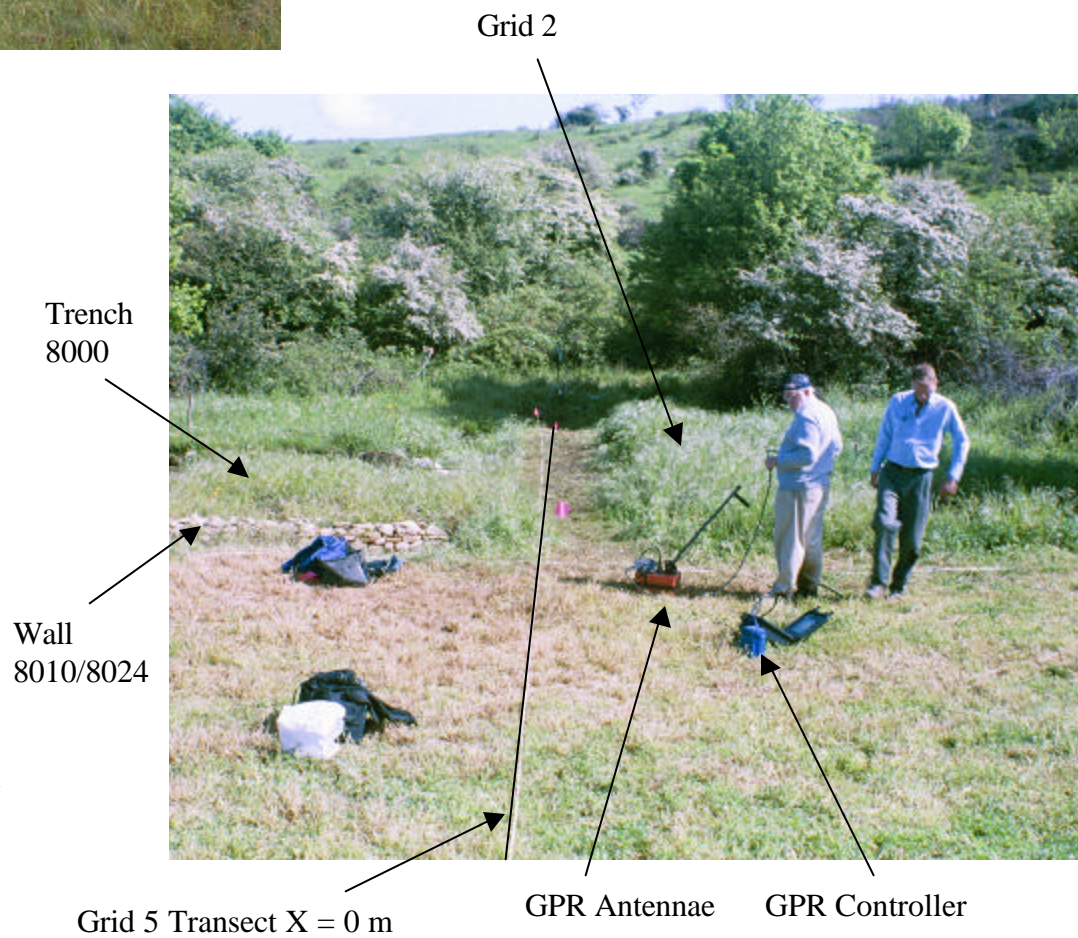
Figure 3.46 The locations of Grids 2 and 5. The GPR antennae and controller. This photograph looks toward the south.

of two perpendicular grids, 1a and 1b. The transects for Grid 1a were 24 m in length and collected parallel to the Y-axis, while the transects for Grid 1b were 11 m in length and collected parallel to the X-axis. GPR data was collected for both Grids 1a and 1b while magnetic data was only collected for Grid 1a.

The purpose of collecting data from Grid 2 was to determine if Wall 8017 continued west and if any other walls were present just west of Trench 8000. Grid 2 was a rectangular grid located west of Trench 8000. The 7 m long X-axis was parallel to the western edge of the Trench 8000 and extended north 36 degrees east of true north (Figure 3.46). The 4.5 m long Y-axis was perpendicular to the western edge of Trench 8000 and extended west.

The purpose of collecting data along Grids 3, 4, and 5 was to record data perpendicularly across limestone walls to determine whether they were detectable with the GPR and magnetometer. In addition, pipe tests were conducted for Grid 3 - 5 to compute the velocity of radar waves in the soil by determining the two way travel time of the GPR signal reflected off a buried metal pipe.

Grid 3 was a 23 m long transect with its northern point on the southern edge of Grid 1 at (0, 10.5) and extended south along the eastern edge of Trench 8000. Grid 4 partially overlapped Grid 3 with its northern point on the northern boundary of Grid 1 at (11, 12.3), passing through (0, 10.5) on Grid 1 and extended for another 19 m south along the eastern edge of Trench 8000 for a total length of 30 m. The magnetic survey utilized the entire 30 m though Grid 4 was truncated to a length of 25 m for the GPR data collection because the last 5 m was too rocky. The purpose of Grid 4 was to tie the Grid 3 data to the previously surveyed Grid 1 data. Buried stone walls 8017, 8006 and 8007 were crossed by Grids 3 and 4, though it was uncertain if Wall 8010 also existed beneath these grids.

The Grid 5 transects were conducted to verify the presence of the two buried stone walls 8010/8024 and 8017 which were present in Trench 8000. Grid 5 was located west of Trench 8000 and nearly parallel to its western edge (Figure 3.46). Grid 5 extended from it northern point at (11, 21.5) on Grid 1 to (0, 19.5) on Grid 1 and south for another 12 m for a total length 23m. The eastern edge of Grid 5 coincided with the eastern edge of Grid 2.

Instrumentation

A GEM Systems GSM-19 Overhauser magnetometer/gradiometer was used to survey Grids 1, 2, 4, and 5 at Monte Pallano (Figure 3.44). The magnetic gradiometer consisted of a pair of proton precession magnetometers mounted a fixed distance apart on a vertical pole. The gradiometer measured both the earth's magnetic field and the vertical magnetic gradient. The vertical magnetic gradient is the difference in the intensities measured by the two magnetometers, divided by the distance between them (Breiner, 1973). The nanoTeslas (nT) is the SI unit for the earth's magnetic field strength and is equal 10^{-5} oersteds, the cgs unit. The magnetometer is useful for locating shallow subsurface magnetic anomalies. Archaeological features that are detectable by the magnetometer include hearths, walls and structures, pottery, bricks, buried pathways, tombs, inhabited sites, and iron objects i.e., swords, helmets, daggers (Breiner, 1973).

Magnetic data for Grids 1, 2, 4, and 5 were collected along transects at 1 m intervals with a spacing of 1 meter between transects (Linington, 1970; Aitken, 1974;). Vertical gradient readings were collected at each location until there were 3 consecutive readings within 1 nT/m of each other. This was to ensure that the readings were consistent and representative of the site conditions and not influenced by diurnal flucuations. In addition one total field reading was collected at each location.

Total field and gradiometer readings were collected at a base station before and after the grid transects were completed to monitor the diurnal changes. The base station was located 7 m east of Grid 1. Two people collected the magnetic data, one held the staff at arms length and oriented the probes toward a consistent eastern direction while the other operated the control box and recorded data manually in a field book. Prior to data collection, both operators verified they were magnetically clean, with the exception of eyeglasses, which were necessary to operate the instrument.

A sensitivity test was conducted at Grid 1 prior to data collection to determine what gradiometer probe sensor spacing was best suited for this site. Magnetic data were collected along the same transect from the southeast corner of the grid to the northwest corner at 1 m intervals for two different probe separation distances of 1 and 1.44 m. It was determined that a sensor spacing of 1.44 m was best for this site because of the greater sensitivity (Figure A.1).

Magnetometer data were collected at Grid 1 along 12 transects parallel to the X – axis, each 24 m in length. Grid 2 magnetic data were collected along five transects each 7 m in length. These transects were located at the half meter grid increments, i.e., (y) = 0.5 m, 1.5 m etc. Grid 4 magnetic data were collected along two transects, each 30 m in length. Grid 5 magnetic data were collected along three transects, each 23 m in length.

Magnetic Data Processing

Magnetic profiles and contour maps were created both to visualize the raw data and as the basis for the cross-correlation analyzes. Profiles and contour maps were created for Grids 1, 2, 4, and 5 for both the total field and vertical gradient data. All profiles were spaced 1 m apart with data points every 1 m (Figures A.2 – A.13). The total field and vertical gradient magnetic data were each contoured using kriging with Surfer 7.0 in order to visualize trends in the X – Y

plane. A contour interval of 5 nT was used for the total field data and 1 nT/m was used for the vertical gradient data. Profiles were created for Grid 1 parallel to both the Y and X axes, i.e., Grids 1a and 1b respectively.

Diurnal corrections were made for the Grid 1 total field data for transects (x) = 7 to 11 m (Burger, 1992). The base station data for transects (x) = 0 to 6 m was incomplete and therefore diurnal corrections was not possible for those transects. Diurnal corrections were made for the Grid 2 total field data. No diurnal corrections were made for Grid 4 or 5 because these grids had few data points and were therefore collected quickly.

Missing data points from Grid 1 were averaged from the nearest four grid points and compared with neighboring profiles to insure averaging produced reasonable values. The data gap at points (0, 21) and (0, 22) where Trench 8200 was located were averaged from points (0, 20) and (0, 23). These points were necessary for cross-correlation but values in this data gap were ignored for purposes of interpretation.

The Cross-Correlation of Monte Pallano Data

Cross-correlations were conducted on Monte Pallano magnetic data for Grids 1, 4, and 5 to identify the presence of anomaly sources and determine the position and depth of the sources. Profiles for Grids 4 and 5 were cross-correlated to determine if buried limestone walls at the site were resolvable in the correlograms. Profiles sets 1a and 1b for Grid 1 were cross-correlated to increase the chance of locating buried stonewalls trending in any direction. Profiles for Grid 2 were not cross-correlated because they had too few data points which prevented the use of adequatly sized pilot signals.

Synthetic pilot signals were computed for both total anomaly field and vertical gradient for homogenous spherical anomaly sources with centers at depths of 0.5, 1, 2, 3, 4, and 5 m with

a lower probe height of 0.5 m above ground surface and a probe separation of 1.44 m. All pilot signals were computed with the same parameter values as for the synthetic cross-correlation tests with the exception that the values for (α) were 51 degrees for Grid 1a, 39 degrees for Grid 1b, 38 degrees for Grid 4 and 38 degrees for Grid 5.

Cross-correlations were conducted with pilot signals with 11 and 15 samples for the 12 Grid 1a profiles, which were 24 m in length and a pilot signal with 11 samples for the 25 Grid 1b profiles, each 11 m in length. Pilot signals with greater numbers of samples 19 and 31 were not used because few to none complete cross-correlations would be possible since the data profiles were only 24 and 11 m in length. The two 30 m long Grid 4 profiles and the three 23 m long Grid 5 profiles were each cross-correlated with pilot signals with 11 samples.

The correlograms for the cross-correlations with pilot signals with 11 and 15 samples were very similar. The only differences were that those for pilot signals with 11 samples had slightly higher amplitudes than those for pilot signals with 15 samples (Figure A.14). All subsequent discussion of cross-correlation analyses pertain to the cross-correlations with the pilot signals with 11 samples.

Comparison of Cross-Correlation Peaks and Troughs

The horizontal position and estimated source depths of probable anomalies were determined by locating the maximum and minimum values of peaks and troughs on correlograms as discussed in the synthetic cross-correlation section. The pilot signal depth that was cross-correlated to produce the greatest r_m value should be closest to the anomaly source depth. It was assumed that the pilot signal depth of the correlogram with the greatest positive value for a peak or greatest negative value for a trough of a profile would be the depth of the anomaly source that created that peak or trough. For example if a negative cross-correlation trough was located at the

(x) position of 5 m on four correlograms for a single profile then the pilot signal depth of the correlogram with the greatest negative value at that trough location was assumed to be the depth of the anomaly source (Figure 3.47). The horizontal position, r_m value, and pilot signal depth were compiled for each maximum positive peak and maximum negative trough for each set of correlograms for Grids 1a, 1b, 4, and 5. The positions of these peaks and troughs were plotted on a plan view grids in order to determine if any linear trends, i.e. buried walls were present. The cross-correlation peaks and troughs for both sets of Grid 1 profiles (1a and 1b) were combined for total field and for the vertical gradient data.

The maximum peak and trough data were then filtered in order to determine which points grouped together and could form possible anomaly features. The peaks and troughs were filtered by their r_m values (> 0.5 or < -0.5) and (>0.8 or < -0.8) to exclude those points not strongly correlated in order to determine which features had the greatest correlation coefficients and therefore the greatest possibility of being an anomaly source.

The maximum peak and trough data was also filtered by their estimated depths, with the following intervals, (0.5, 1, 2, 3, 4, 5, 0.5 – 3, and 4 – 5 m) in order to determine if nearby data points clustered at certain depth intervals and therefore were possibly related to the same anomaly feature. The Grid 4 and 5 data were only filtered by depth for (0.5 – 3, and 4 – 5 m) because each had so few profiles. These filtering plots are presented in Figures A.15 – A.31.

Summary of the Cross-Correlation of the Monte Pallano Magnetic Data

For this project I was primarily searching for buried walls. Therefore, data points were grouped in possible anomaly features based on their linearity, nearness, relative correlation coefficients and estimated depths of data points. In addition, trough and peak features did not cross except when both were strongly linear. It was assumed that adjacent data points of the

Figure 3.47 Comparison of correlograms of different pilot signal source depths, Grid 1b Y = 6 m with 10 samples. The squares and numbers denote the pilot signal depth which had the greatest rm value.
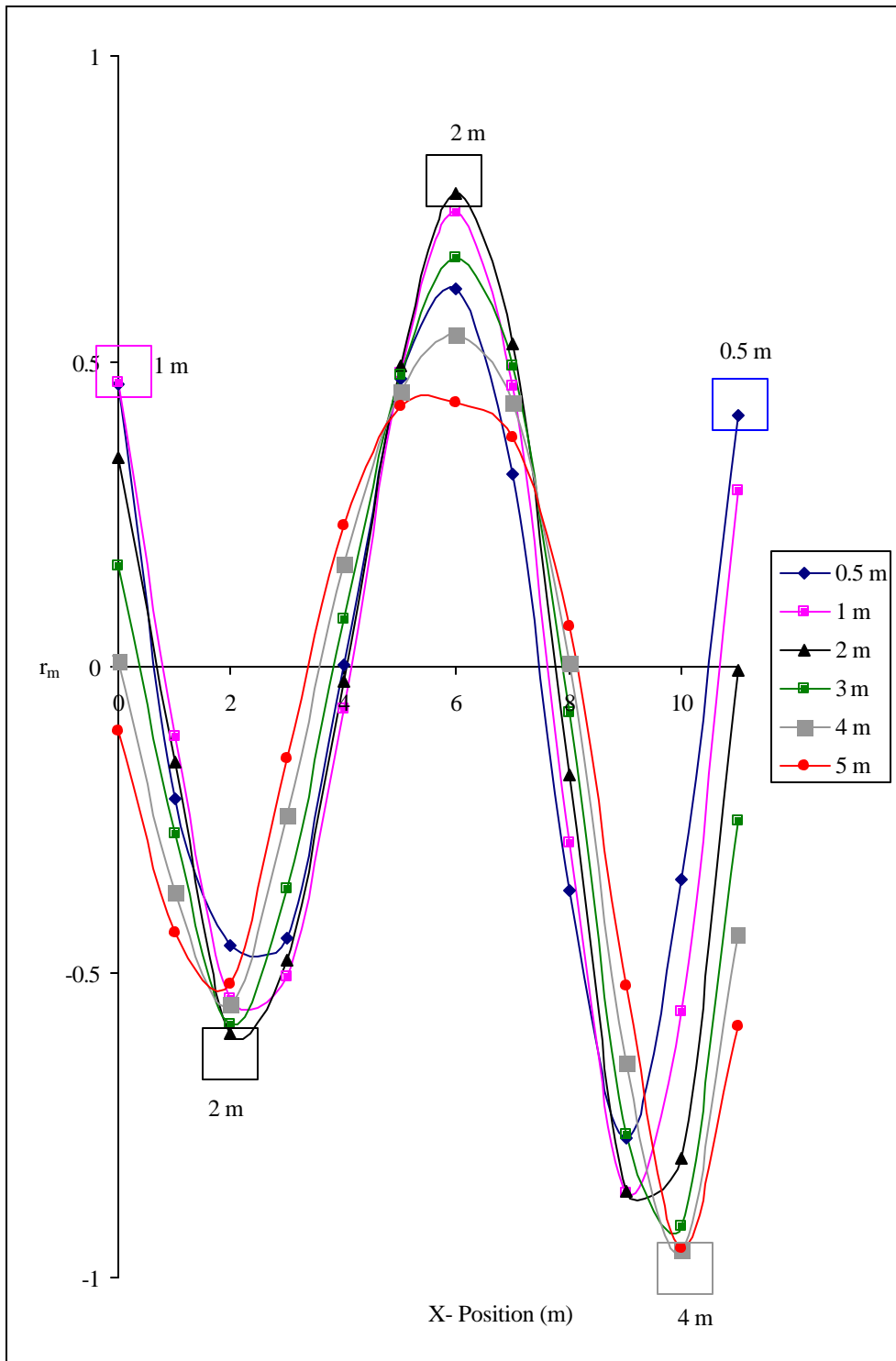
same type (i.e., peak or trough) would be part of the same possible anomaly source feature. Irregular shaped possible anomaly features could be rock piles, debris, partial or destroyed walls, concentrations of magnetite, or noise. For Grids 1, 4, and 5 the anomaly areas were determined separately for the total field and the vertical gradient data, and then a comprehensive interpretation was made for each grid for those anomaly areas that were identified by both the total field and vertical gradient cross-correlations.

The stonewalls which have been excavated at Monte Pallano were made of limestone and were assumed to possess a negative magnetic susceptibility contrast (k) in relation to the surrounding clay sediment. For this reason limestone walls should have appeared as negative cross-correlations, i.e. troughs on correlograms when a profile is cross-correlated with a pilot signal computed for an anomaly source with a positive (k) value. The troughs could also have represented rock piles, limestone bedrock, or troughs filled with low magnetic susceptibility material (Tite, 1972; Aitken, 1974; Weymouth, 1986). The peaks were indicative of features with higher magnetic susceptibility such as magnetite rich sediments, baked clay or iron objects. In addition to separate features, the cross-correlation troughs and peaks could have been the locations of the other halves of dipolar anomalies.

Ground Penetrating Radar Studies at Monte Pallano

The purpose for collecting the GPR data at Monte Pallano was to corroborate the locations of anomaly sources with the magnetic data and to identify possible anomaly sources not detectable by the magnetometer. The effectiveness of GPR for locating buried stonewalls at Monte Pallano had been demonstrated previously by Garrison and Schneider (2001). In addition, GPR data could be collected quickly as compared with most other geophysical methods.

Instrumentation

The GPR instrument used for this survey was a Geophysical Survey Systems Inc. (GSSI) Model SIR 2000 unit, which was composed of a digital console, cable, 400 megahertz (MHz) antenna, and a 12-volt battery (Figure 3.46). The GPR emits high frequency radar pulses from a mobile antenna of a set frequency as it is pulled across the ground surface. The antenna alternates very quickly, several thousands of times a second, between emitting radar pulses and receiving the radar signals which are reflected back by subsurface objects, (archaeological features or bedding planes). The radar waves are reflected as they come in contact with substances of differing electrical and magnetic properties. The depth of an object can be determined by recording the two-way travel time of the reflected wave if the velocity of radar waves is known or estimated for the subsurface (Conyers and Goodman, 1997).

GPR data were collected for Grids 1 – 5 continuously along transects with marks placed every 1 m (Figure 3.44). It rained most of the days of the survey, which caused the soil on Monte Pallano to become saturated. This attenuated the GPR signal and decreased reflection amplitude and depth penetration. The GPR transect lines for Grids 1a, 1b and 2 were spaced 0.5 m apart in order to have adequate lateral resolution to locate buried walls (Neubauer et. al., 2002) The GPR transects were snaked in order to save time during data collection.

The GPR data were collected with 8 bits, 512 samples per scan and 32 scans per second. Every four traces recorded were stacked into a single trace during data collection to reduce noise and anomalous reflections caused by ground irregularities and thereby increase the S/N ratio (Fisher et al., 1992). The stacking used a running average so that adjacent scans were combined into one (GSSI, 1995). A low-pass filter of 800 MHz was applied during data collection to remove high frequency noise such as radio transmissions and electrical disturbances. A high-

pass filter of 30 MHz was applied during data collection to remove instrument noise (Bucker et al., 1996; Milsom, 1996). Five gain points were used with decibel values of (–4, 42, 63, 66 and 73) from shallowest to deepest. This gain was used to prevent clipping of the shallower portion of the signal and to enhance the deeper portion of the signal, which had greater energy attenuation (Sternberg and McGill, 1995; Milsom, 1996).

GPR data were collected at both Grid 1a and 1b in order to locate features trending in either direction and to provide redundancy in the data. Grid 1a consisted of 23 transects, each 24 m in length, spaced at 0.5 m intervals along the X - axis, from (x) = 0 to 11 m. The first two lines of Grid 1a, (x) = 0 and 0.5 m, were only 20.2 m in length because the corner of Trench 8200 intersected Grid 1 at (y) = 20.2 to 24 m. No data was collected for the last 3.8 m of these two transects. Grid 1b consisted of 49 transects, each 11 m in length, spaced at 0.5 m intervals along the Y-axis, from (y) = 0 to 24 m. Because of the presence of Trench 8200 no data was collected for the first meter along lines from (y) = 20 to 22.5 m. A time window of 60 nanoseconds (ns) was used for Grids 1a and 1b.

GPR data were collected at Grid 2 along transects parallel to the X - axis, beginning in the southeastern corner of the grid. Data were collected along ten transects spaced at 0.5 m intervals along the Y–axis with a time window of 70 ns.

GPR data were collected along two transects of Grid 3 and one transect of Grid 4 with time windows of 60 ns. A 2" diameter metal auger with a 1" diameter metal rod inside was inserted into the eastern wall of Trench 8000, at a depth of 30 cm bgs (Figure 3.48). This point was located 10 m south of the northern end of the Grid 3.

GPR data were collected at Grid 5 along two transects 23 m in length along the same line with 60 ns time windows. A 2" diameter metal auger with a 1" diameter metal rod inside was

Grid 4 GPR transect

Ground surface Z = 0

15cm bgs

Pipe

Eastern wall of Trench 8000
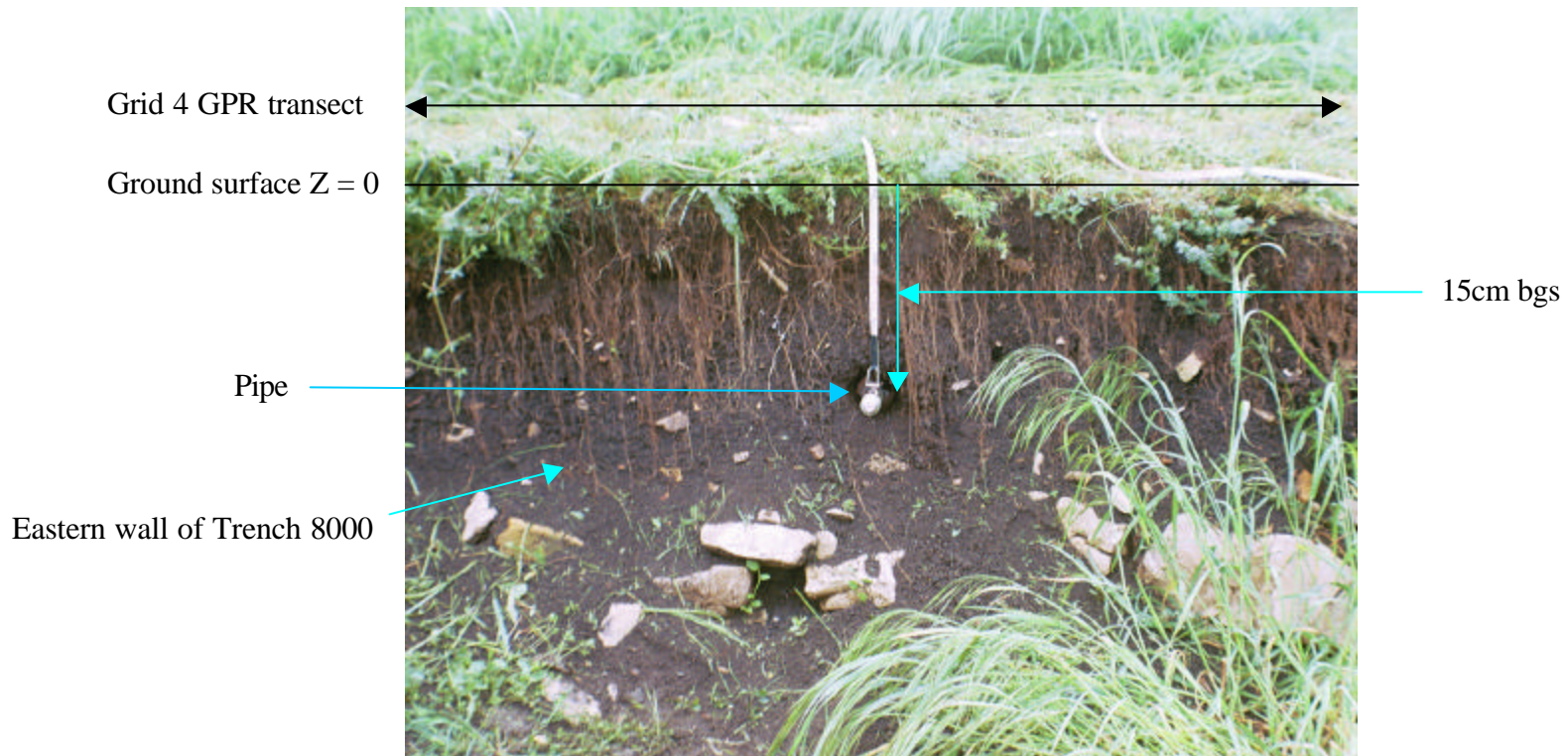
Figure 3.48 A pipe test for determining the velocity of the soil. A metal auger is inserted 15 cm bgs. The GPR antennae transect passes perpendicular to the pipe. This photograph looks toward the east wall of Trench 8000.

inserted into the western wall of Trench 8000 at a depth of 15 cm, and located 21 m from

northern point on Grid 1 (11, 21.5).

Soil Velocity Analysis

In order to process the GPR data and determine the locations and depths of anomaly

sources it was necessary to compute the relative dielectric permittivity (RDP) of the soil in the

area of Trench 8000 on Monte Pallano.   The RDP is a dimensionless value based on the

electromagnetic properties of a material through which the radar waves are passing. RDP is a

measure of materials ability to allow radar energy to pass through it. Some examples of the

different RPD values of materials are presented in Table 3.2 for comparison (GSSI (1995), Davis

and Annan (1989), Conyers and Goodman, 1997).

Table 3.2 Typical relative dielectric permittivity (RDP) of common materials, using a 100 MHz

antenna

Material	RDP	Material	RDP
Air	1	Coal	4-5
Freshwater	80	Dry Silt	3-30
Ice	3-4	Saturated Silt	10-40
Seawater	81-88	Clay	5-40
Dry Sand	3-5	Permafrost	4-5
Saturated Sand	20-30	Average Surface Soil	12
Volcanic ash/pumice	4-7	Dry Sandy Coastal Land	10
Limestone	4-8	Rich Agricultural Land	12
Shale	5-15	Concrete	15
Granite	5-15	Asphalt	3-5

Source Modified from Davis and Annan (1989), Geophysical Survey Systems, Inc. (1995), Conyers and Goodman (1997)

Materials with higher RDP values attenuate radar energy propagation to a greater degree than do smaller RDP values. Metallic objects cannot be penetrated by radar waves and will therefore reflect back all of the radar energy (Conyers and Goodman, 1997). Differences in the dielectric permittivity of materials are caused by variations in their composition, bulk density, water content, porosity, and temperature (Olhoeft, 1981). The magnetite content is also important because high concentrations in a soil will increase its magnetic permeability and thereby increases the attenuation of radar energy (Conyers and Goodman, 1997).

Pipe tests were conducted at Grids 3, 4 and 5 with a 2-inch diameter metal pipe placed at depths of 15 and 30 cm bgs (Figure 3.48) (Sternberg and McGill, 1995). The RDP was computed for the soils at Monte Pallano using the following equation (Conyers and Goodman, 1997):

$$\sqrt{K} = \frac{C}{V} \qquad (7)$$

and the velocity of radar waves passing through soil was computed using the following equation:

$$V = \frac{2Z}{TT} \qquad (8)$$

In equation 7 **K** is the RDP of the soil (dimensionless), **C** is the speed of light in a vacuum (0.2998 meters per nanosecond), and **V** is the velocity of the radar waves passing through the subsurface material (in meters per nanosecond). The value of **V** was computed with equation 8 in which **TT** is the two-way vertical travel time of the radar waves reflected off the metal pipe (nanoseconds) and **Z** is the depth to the pipe below the surface (meters).

A range of values were computed for the RPD of the subsurface at Monte Pallano, (42.194) to (60.603) with an average RDP of (48.24) which equates to a radar wave velocity of 0.0432 m/ns (Table 3.3). These variations could be caused by heterogeneous water content of

the soil across the site, differing locations and depths of the steel pipe and that velocity data was collected on two different days. The clayey soil on Monte Pallano was fairly wet because of daily rain showers during the course of the fieldwork. This RDP value was indicative of a material with high signal attenuation and thus limited depth penetration.

Table 3.3 Summary of computed RDP values from the velocity tests

Grid	File	Transect length (m)	Position of pipe (m)	Depth to pipe (m)	Two-way reflection time from pipe (ns)	RPD
3	83	22	10.5	0.3	13	42.19
4	92	24	22	0.15	6.5	42.19
5	93	23	20	0.15	6.93	47.96
5	94	23	20	0.15	7.79	60.60
					Average RDP	48.24

Note: Time windows = 60 ns

The time windows were converted to depth using this RPD value such that a 60 ns time window had an approximate depth penetration of 1.31 m while a 70 ns window had an approximate depth penetration of 1.51 m. Cultural material had only been excavated to a depth of 1 to 2 m in the area of Trench 8000.

GPR Resolution

The resolution of 3-D features with GPR is a function of the wavelength and frequency of the radar waves emitted by the antenna and the RDP of the soil through which the radar waves passes (Davis and Annan 1989). The distance between the top and bottom surfaces of a 3-D feature must be at least one wavelength thick so that reflections can occur at both surfaces. Planar surfaces such as soil layers or a clay floor would only be identifiable by a single reflection unless they exceeded the thickness of minimum resolution. Equations 9 and 10 were used to

compute the wavelength of the radar waves in soil and thus the resolution of the GPR (Conyers and Goodman, 1997).

$$\lambda_{air} = \frac{C}{f} \qquad (9)$$

$$\lambda_{subsurface} = \frac{\lambda_{air}}{\sqrt{K}} \qquad (10)$$

In equations 9 and 10 $\mathbf{l}_{air}$ was the wavelength of the radar waves in air (m), $\mathbf{C}$ was the speed of light in a vacuum (0.2998 meters per nanosecond), $\mathbf{f}$ was the center frequency of the radar waves generated by the antenna (cycles/sec), $\mathbf{l}_{subsurface}$ is the wavelength of radar waves in the subsurface (m), and $\mathbf{K}$ was the RDP of the soil (dimensionless). Therefore the 400 MHz antenna used in this study produced radar waves with a wavelength of 0.75 m in air. The resolution of the 400 MHz antenna was equal to the wavelength of radar waves passing through the subsurface, which was computed to be 0.1079 m, for a RDP of (48.24).

GPR Disturbances During Data Collection

The positions of disturbances encountered by the GPR antenna during data collection were recorded to prevent confusion with potential anomaly sources (Figure B.1). These disturbances represent rocks, surface irregularities, and grass clumps crossed by the GPR antenna while it was pulled along transects. These bumps will often manifest on the radargrams as narrow high amplitude features which originate at the very top of the radargram at depth = 0 cm i.e. time = 0 ns.

GPR Data Processing

The GPR data was processed with software GPR SLICE, GPR processing software created by Dean Goodman. This software is useful for creating amplitude time slices and

radargrams. The GPR transect data files were checked and corrected for missing or extra user

marks added during data collection. Alternate transect files were reversed to remove the effects

of snaking.

Radargrams

Radargrams were created for Grids 1a, 1b, 2, 3, 4, and 5 with depths computed for an

RDP value of 48.24 and are presented in Figures (B2 – B.11 and 4.5) and summarized in Table

3.4.

Table 3.4 Summary of GPR grids

Grid	Files	Number of radargrams	Length of radargrams (m)	Time window (ns)	Equivalent depth (cm)
1a	10-32	23	24	60	131
1b	34-82	49	11	60	131
2	119-128	10	7	70	151
3	83-84	2	22	60	131
4	92	1	25	60	131
5	93-94	2	23	60	131

Radargrams were created with a logarithmic transform to subdue these mid depth values

and to amplify the signal of the deeper values. Trench 8200 intersected the first two radargrams

of Grid 1a (x = 0 and 0.5 m) from (y = 20 – 24 m) and therefore those portions of the radargrams

were ignored for purposes of interpretation.

Amplitude Time Slices

Amplitude time slices were created for Grids 1a, 1b, and 2 but not for Grids 3, 4, and 5

because they had too few transects. Amplitude time slices are horizontal plots of the GPR

amplitude data for specific time windows, effectively looking at thin horizontal layers within the

ground. Time slices are helpful for visualizing horizontally extensive features such as walls.

These time slices were created by first interpolating the area between the GPR transects, by the method of kriging, to create continuous horizontal data (Conyers and Goodman, 1997). The reflected radar wave energy at each position within the grid was averaged over a time window and then each value was squared to enhance the anomaly features (Goodman, 2002). The time slices were computed for squared amplitude values with a horizontal averaging search radii of 0.75 and 1.1 m. The GPR SLICE manual (Goodman, 2002) suggests using a search radius with a minimum diameter of one and a half times the distance between transects, which produced a minimum radius of 0.75 m. The larger the search radii the greater the area averaged over and the lower the resolution. The 1.1 m radii search distance was too large and produced a blurred images with low resolution, while the 0.75 m radii produced slices with greater resolution. In addition the thickness and amount of overlap of the time slices was varied to determine the optimal settings. The horizontal time slices for Grids 1a, 1b, and 2 were created with a search radius of 0.75 m, a 6 ns thickness with 3 ns overlap (Figures B.12 – B.14).

Locations of Anomaly Features

The locations of anomaly sources were determined for each grid based on the time slices, radargrams and the locations of the GPR disturbances. Four different types of anomalies were classified and denoted with the following letters, linear features (L) i.e. walls or ditches; areas (A) i.e. debris scatters or rock piles; points (P) i.e. small sources, rocks, or bumps; and contacts (C) i.e. geologic or stratigraphic contacts. Anomalies were given suffixes of (1a, 1b, or 2) to designate which grid and set of transects they were identified from. For example (1b - L2) is the second linear feature identified in Grid 1b.

The anomaly features identified by the GPR and magnetic analyses were compared in order to determine which areas coincided. The GPR and magnetic cross-correlation depth

estimates were also compared at these locations. This final interpretation was presented in map

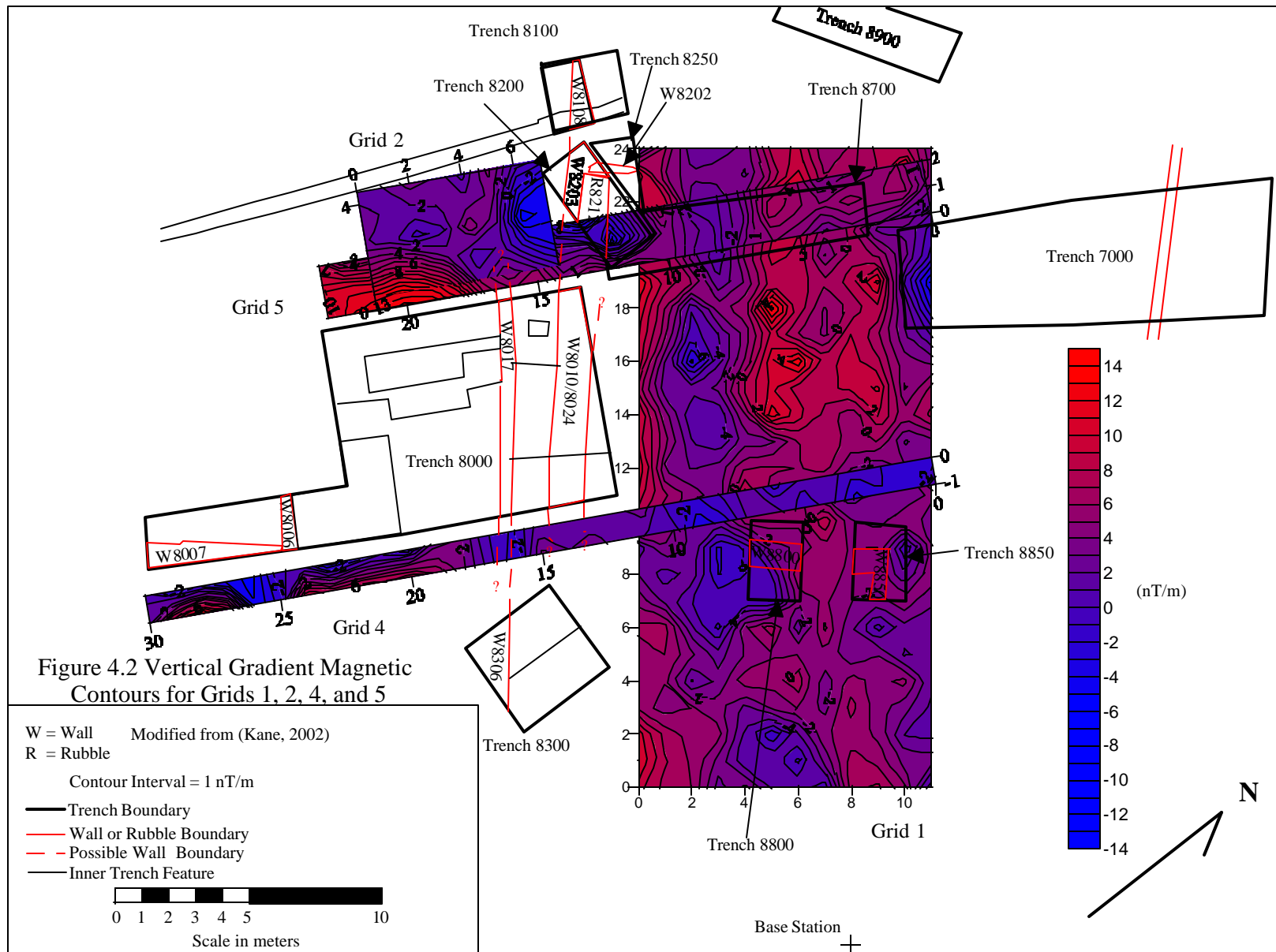form along with a discussion of anomaly sources and their estimated depths.

CHAPTER IV

MONTE PALLANO MAGNETIC AND GROUND PENETRATING RADAR

ANALYSES

Monte Pallano Magnetic Data Analysis

Total field and vertical gradient magnetic data was collected at Monte Pallano to determine the locations of buried walls. In addition to the standard visualizations of profiles and contour plots, this thesis further developed the analysis of magnetic data with the statistical technique of cross-correlation.

The total field and vertical gradient magnetic contour plots for Grids 1, 2, 4, and 5 are presented in Figures 4.1 and 4.2. The color scale and contour interval is the same for each grid. The total field and vertical gradient magnetic profiles for Grids 1, 2, 4, and 5 and the plots depicting the filtering outcomes of the cross-correlation peak and trough values for Grids 1, 4, and 5 are presented in Figures A.2 – A.31 in Appendix A.

Following is a discussion of the interpretation of the Monte Pallano magnetic cross-correlation interpretation for the combined total field and vertical gradient data for Grids 1, 4, and 5 and an interpretation of the Grid 2 profiles and contour plots. Anomaly areas identified separately for the total field and vertical gradient cross-correlation data for Grids 1, 4, and 5 are presented in Figures A.32 and A.33 in Appendix A.

Figure 4.1 Total Field Magnetic Contours
for Grids 1, 2, 4, and 5

W = Wall   Modified from (Kane, 2002)
R = Rubble

Contour Interval = 5 nT

Trench Boundary
Wall or Rubble Boundary
Possible Wall Boundary
Inner Trench Feature

0 1 2 3 4 5   10
Scale in meters

Figure 4.2 Vertical Gradient Magnetic
Contours for Grids 1, 2, 4, and 5

W = Wall   Modified from (Kane, 2002)
R = Rubble

Contour Interval = 1 nT/m

Trench Boundary
Wall or Rubble Boundary
Possible Wall Boundary
Inner Trench Feature

0 1 2 3 4 5   10
Scale in meters

Grid 4 Combined Magnetic Interpretation

The locations of the combined total field and vertical gradient anomaly features identified for Grid 4 from the peak and trough cross-correlation analysis are presented in Figure 4.3 and summarized in Table 4.1.

Table 4.1 Summary of Grid 4 magnetic anomaly features

Anomaly feature	Depths estimates to the center of the anomaly source (m)	Anomaly source
4 - P1	0.5 - 1	Possibly (+k) deposit
4 - P2	0.5 - 1	Possibly Wall 8010
4 - T1	0.5, 2, 3, & 5	Feature 1 - T6 in Grid 1
4 - T2	0.5, 1, 2 & 5	Feature 1 - T3 in Grid 1
4 - T3	1 & 5	Wall 8017
4 - T4	0.5 - 1	Walls 8006 and 8007

The anomaly feature 4 - T3 was most likely caused by Wall 8017, which extended beneath Grid 4 east into Trench 8300 as Wall 8306. The anomaly feature 4 - T4 was produced by Walls 8006 and 8007 with a depth estimate of 0.5 to 1 m. The anomaly feature 4 – P1 may have been a shallow high magnetic susceptibility deposit or the positive half of a dipole that included 4 – T2. Wall 8010 might have produced the peak anomaly feature 4 – P2, though it was located further north than Wall 8010 would be if it continued east. Other peaks and troughs were related to features identified in Grid 1, presented in a later section.

Grid 5 Combined Magnetic Interpretation

The locations of the combined total field and vertical gradient anomaly features identified Grid 5 from the peak and trough cross-correlation analysis are presented in Figure 4.3 and summarized in Table 4.2.

Figure 4.3 Magnetic Cross-Correlation Anomaly Areas

Trench 8100
Trench 8250
Trench 8200
W8202
Trench 8700
Trench 8900
Grid 2
Grid 5
Grid 4
W8108
R8212
W8203
1 - P1
1 - T1
5 - T1
5 - T2
5 - T3
5 - T4
1 - T7
5 - P1
Trench 7000
1 - T2
1 - P2
4 - T1
W8017
W8010/8024
1 - P3
Trench 8000
1 - T3
4 - T2
4 - P1
1 - T6
W8106
4 - T3
4 - P2
W8800
W8850
Trench 8850
W8007
4 - T4
1 - T4
W8306
1 - P4
1 - T5
1 - P5
Trench 8300
Trench 8800
Grid 1
Base Station

W = Wall   Modified from (Kane, 2002)
R = Rubble

Trench Boundary
Wall or Rubble Boundary
Possible Wall Boundary
Inner Trench Feature

(-) K Anomaly Area
(+) K Anomaly Area

0 1 2 3 4 5   10
Scale in meters

N

The anomaly feature 5 - T3 was located above the position where Wall 8010 would have extended west beneath Grid 5, and anomaly features 5 - T4 was located above the position where Wall 8017 would have extended west beneath Grid 5. Other peaks and troughs related to features identified in Grid 1, presented in a later section.

Table 4.2 Summary of Grid 5 magnetic anomaly features

Anomaly feature	Depths estimates to the center of the anomaly source (m)	Anomaly source
5 - P1	1, 2, 3, & 5	Feature 1 - P1 in Grid 1
5 - T1	0.5 & 2	Feature 1 - T7 in Grid 1
5 - T2	0.5, 2, & 3	Feature 1 - T1 in Grid 1
5 - T3	5	Possibly Wall 8010
5 - T4	0.5 & 5	Possibly Wall 8017

Discussion of Grids 4 and 5

The analysis of the Grid 4 and 5 data has demonstrated that the cross-correlation technique can be used to identify and locate buried stonewalls. The total field and vertical gradient data produced very similar results from the cross-correlation analyses for location, r_m value and depth estimates. The depths estimated for Walls 8010 and 8017 were deeper than would be expected based on the excavations. One factor that could have affected the estimate was that the depth estimated the distance to the center of the anomaly source and not its outer edge. Alternatively the wall may have been partially collapsed thereby increasing the amount of rock at the base of the wall and increasing the amount of negative magnetic susceptibility material at depth.

Grid 1 Combined Magnetic Interpretation

Five anomalous areas of positive correlation, peaks, and seven anomalous areas of negative correlation, troughs, were identified for Grid 1 (Figure 4.3). The depth ranges for these areas are presented in Table 4.3. Anomalous areas 1 - T1 through 1 - T5 formed a discontinuous linear feature, possibly a limestone terrace wall similar to walls 8010 and 8017. Anomalous areas 1 - T6 and 1 - T7 could have been east-west trending wall sections or foundations. Alternatively these troughs could have been an expression of the underlying bedrock, possibly a limestone ridge or a linear ditch filled with low magnetic susceptibility material. The peak features could have been collections of high magnetic susceptibility material, possibly small iron objects or pottery sherds, burned clay, or an eroded section of bedrock replaced with soil with a higher magnetic susceptibility.

Table 4.3 Summary of Grid 1 magnetic anomaly features

Anomaly feature	Depths estimates to the center of the anomaly source (m)	Anomaly source
1 - P1	0.5 - 1	
1 - P2	0.5 - 1	
1 - P3	0.5 - 1	
1 - P4	0.5, 1, & 5	
1 - P5	5	
1 - T1	2 - 3	Possibly part of a wall or trench
1 - T2	0.5, 2, & 3	Possibly part of a wall or trench
1 - T3	0.5 - 3	Possibly part of a wall or trench
1 - T4	0.5 - 2	Possibly part of a wall or trench
1 - T5	0.5, 2, & 5	Possibly part of a wall or trench
1 - T6	0.5 & 5	Possibly part of a wall or foundation
1 - T7	4 - 5	Possibly part of a wall or foundation

Grid 2 Contour Plot and Profile Interpretation

The Grid 2 magnetic data was not cross-correlated because of its small grid size as explained above. A brief discussion of the features identified from the profiles and contour plots follows.

Portions of a large dipole were present within Grid 2, with the centers of the poles located at (1, 0) and (6.25, 2.5) (Figure 4.1). The anomaly source of this dipole feature was possibly the buried stonewall 8017 that trended east west and was present in Trench 8000. This wall intersected Grid 2 between (x) = 4.25 and 4.85 m, and is believed to continue west beneath Grid 2. Wall 8010 was present beneath the negative portion of the dipole just north of Grid 2 as it extends west to Trench 8200 as Wall 8203 and then into Trench 8100 as Wall 8108.

The Grid 2 vertical gradient contours exhibited the same trend as the total field with a large dipole anomaly present with a positive gradient of 13 nT/m at (1, 0) and a negative gradient of –5 nT/m at (6.25, 2.5) (Figure 4.2).

Magnetic Data Cross-Correlation as a Tool for Anomaly Characterization at Monte Pallano

The cross-correlation analysis technique of identifying and grouping data points with either positive r_m values, peaks, or and negative r_m values, troughs, has demonstrated the ability to locate the buried stone walls 8010, 8017, 8006, and 8007 beneath Grids 3, 4, and 5. The great similarity between the total field and vertical gradient cross-correlations increased the accuracy of the interpretations.

The cross-correlations were able to identify the same north-west trending peaks and troughs as the original profiles and contour maps but were also able to divide those peaks and troughs into separate areas based on their source depths and r_m values. In addition the cross-

125

correlation analysis located several east-west trending features not discernable on the profiles and contour maps.

The depth estimates for the anomalous features were surprisingly consistent between neighboring data points, though in some instances the depths (4 to 5 m) seemed too great based on the depth of the anthropogenic material excavated at Monte Pallano. These estimates could be indicative of the limestone bedrock, collapsed walls, or rock piles.

Monte Pallano Ground Penetrating Radar Data Analysis

The GPR data were collected at Monte Pallano to determine the locations of buried walls and to corroborate the magnetic cross-correlation analyses. The radargrams for Grids 1a, 1b, 2, 4, and 5 and the time slices for Grids 1a, 1b, and 2 are presented in Figures B.2 – B.14 in Appendix B. The radargrams for Grid 3 are presented later in this chapter. A summary of the GPR anomaly areas identified for Grids 1 - 5 is presented in Figure 4.4; interpretations of the radargrams for Grid 3 are presented in Figure 4.5; and separate Grid 1a and Grid 1b anomaly area interpretations are presented in Figures 4.6 and 4.7.

Control Grids 3, 4, and 5 GPR Interpretation

Two transects were collected for Grid 3 each 22 m in length, one transect was collected for Grid 4, 25 m long, and two transects were collected for Grid 5, 23 m long. Table 4.4 summarizes the features crossed by these transects.

The locations of the anomaly features were identified on the radargrams for Grid 3 (Figure 4.5). A wall crossed oblique to its trend direction by a GPR antenna should exhibit hyperbolic shaped reflections on the radargram (Sternberg and McGill, 1995). Several of these hyperbola peaks are present on the Grid 3 radargrams. The locations of Walls 8017, 8006 and 8007 were discernable from the radargram. It was unknown how far Wall 8010 extended east
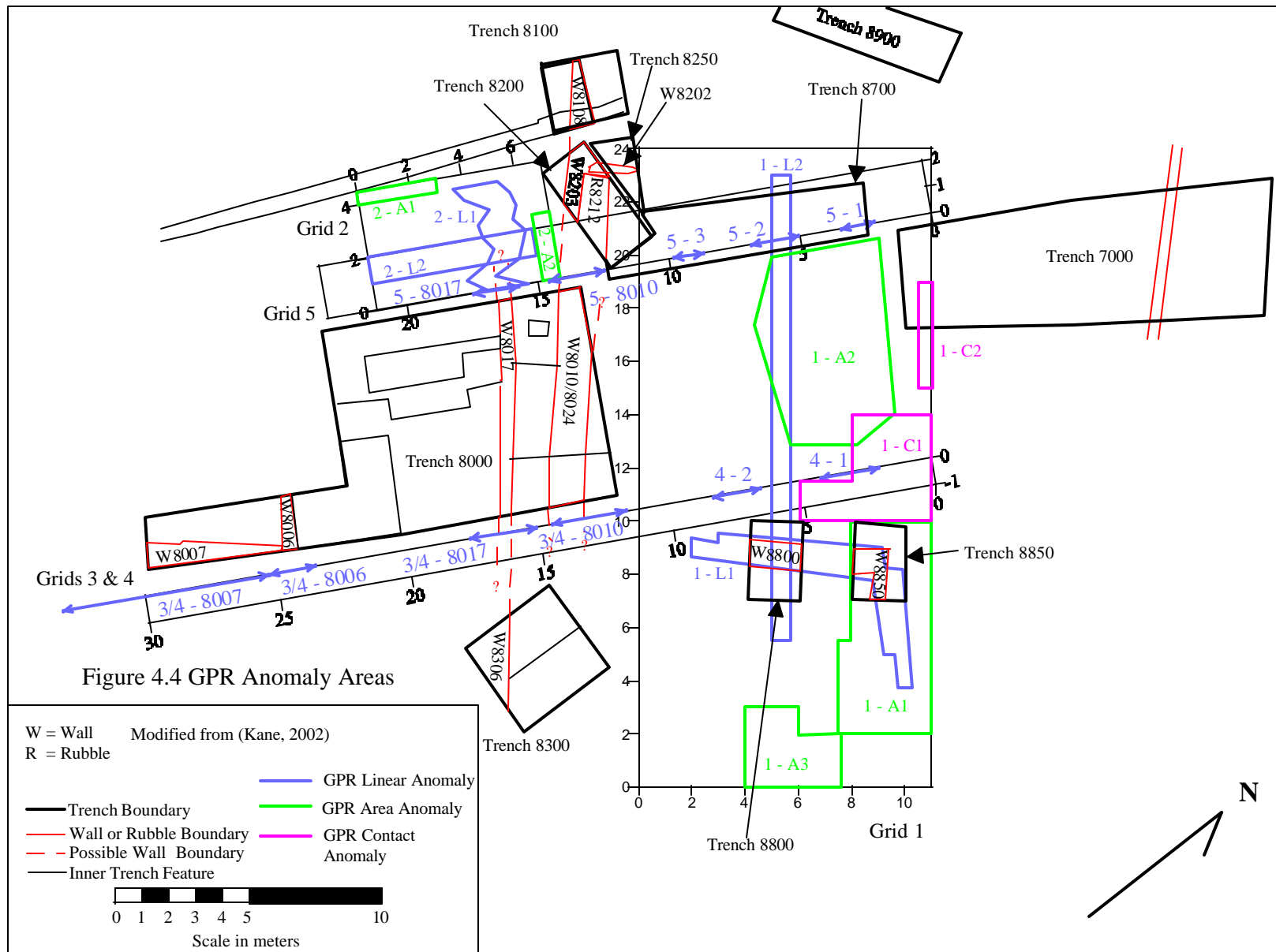
Figure 4.4 GPR Anomaly Areas

W = Wall   Modified from (Kane, 2002)
R = Rubble

Trench Boundary
Wall or Rubble Boundary
Possible Wall Boundary
Inner Trench Feature

GPR Linear Anomaly
GPR Area Anomaly
GPR Contact Anomaly

0 1 2 3 4 5   10
Scale in meters

Trench 8100
Trench 8900
Trench 8250
Trench 8200
W8202
Trench 8700
Trench 7000

Grid 2
Grid 5
Grids 3 & 4

Trench 8000
Trench 8300
Trench 8800
Trench 8850

Grid 1

N
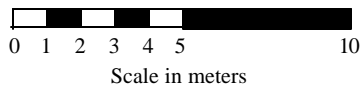
Figure 4.5 Grid 3 Radargrams

Monte Pallano lines 83 _84
400 MHz GPR Survey Logarithim Transform

File83: y= 0m

Wall 8017

Pipe

Wall 8006

Wall 8007

Wall 8010 ?

File84: y= 22m

Wall 8010 ?

Wall 8017

Wall 8006

Wall 8007

Figure 4.6 Grid 1a GPR Anomaly Areas

Trench 8100
Trench 8250
Trench 8200
W8202
1a-L2 1a-L3
Trench 8700

W8108
W8203
R8212
Trench 7000

W8017
W8010/8024
1a-A3
1a-C2

Trench 8000
1a-C3 1a-C1

W8009
1a-L1
W8800
W8851
Trench 8850

W8007
1a-A1

W8306
1a-A2

Trench 8300
Trench 8800
Grid 1a

W = Wall   Modified from (Kane, 2002)
R = Rubble

——— Trench Boundary   ——— GPR Linear Anomaly
——— Wall or Rubble Boundary   ——— GPR Area Anomaly
– – – Possible Wall Boundary   ——— GPR Contact
——— Inner Trench Feature   Anomaly

0 1 2 3 4 5   10
Scale in meters

N

Figure 4.7 Grid 1b GPR Anomaly Areas

Trench 8100
Trench 8250
Trench 8200
W8202
Trench 8700
Trench 8900

Trench 7000

W8108
W8203
R8212
W8017
W8010/8024
Trench 8000
W8006
W8007

1b-L2
1b-L3
1b-P1
1b-P2
1b-P3
1b-A3
1b-L8
1b-P4
1b-P5
1b-P6
1b-L9
1b-L7
1b-C1
1b-L5
W8800
1b-L1
W8850
Trench 8850
1b-A4
1b-A1
1b-L6
1b-A2
1b-L4

Trench 8300
W8306
Trench 8800
Grid 1b

W = Wall   Modified from (Kane, 2002)
R = Rubble

GPR Point Anomaly   GPR Linear Anomaly
Trench Boundary   GPR Area Anomaly
Wall or Rubble Boundary   GPR Contact
Possible Wall Boundary   Anomaly
Inner Trench Feature

0 1 2 3 4 5   10
Scale in meters

N

and whether it was present beneath Grids 3 and 4 since it was not present in Trench 8300. The

radargram seems to indicate that it extended beneath Grids 3 and 4 though only excavation can

verify this. These radargrams demonstrated that buried limestone walls could be detected at this

site with GPR. The horizontal positions of the walls were slightly offset in the two radargrams,

which may have been caused by the fact that the two transects were collected in opposite

directions. The radargrams for Grids 4 and 5 were similar to those for Grid 3, except that Walls

8006 and 8007 are not present on the Grid 5 transects, and are included in Figures B.10 and B.11

in Appendix B.

Table 4.4 Summary of GPR features identified in Grids 3, 4, and 5

Anomaly feature	Estimated source depth range (cm)	Anomaly source
4 - 1	(20 to 131)	Feature 1 – C1 in Grid 1
4 - 2	(42 to 131)	Trough
3/4 - 8010	(10 to 120)	Wall 8010
3/4 - 8017	(10 to 131)	Wall 8017
3/4 - 8006	(10 to 131)	Wall 8006
3/4 - 8007	(10 to 131)	Wall 8007
5 - 1	(12 to 98)	Possible wall
5 - 2	(12 to 131)	Feature 1 – L2 in Grid 1
5 - 3	(30 to 131)	Possible wall
5 - 8010	(10 to 100)	Wall 8010
5 - 8017	(10 to 90)	Wall 8017

Grid 1 GPR Interpretation

Grid 1a

Nine anomaly features were identified from the Grid 1a GPR data, which included three areas, three linear features, and three geologic/stratigraphic contacts and are presented on Figure 4.6 and summarized in Table 4.5. Feature 1a – A1 is a roughly circular area that is present over a depth interval of 78 cm. It was possibly a remnant of the rock pile which was previously located in this area, though as it appears to extend to 117 cm it is more likely to be debris or an architectural feature. It is adjacent to the eastern edge of Grid 1 and probably continues beyond the grid's edge. 1a – A2 is an L-shaped feature present over a depth interval of 32 cm and is possibly the remnants of a wall or rockpile. 1a – A3 is an anomaly area with no distinct feature but a consistent areal extent over a depth interval of 26 cm which could represent rocks debris or a variation in moisture content.

The L-shaped feature 1a - L1 is very similar to the wall sections 8800 and 8850, which form a L-shaped corner. 1a - L1 extends both west of Wall 8800 and south of Wall 8850, suggesting these wall sections continue. The feature 1a - L1 was estimated to be shallow 19 cm, which is consistent with the excavation of the walls discovered just below the surface. Features 1a - L2 and 1a – L3 were overlapping linear features possibly resembling walls or different courses of stones from the same wall.

1a – C1 and 1a – C3 are northwest dipping structures present across several radargrams over depth intervals of 40 and 10 cm respectively. 1a – C2 is a shallow trough feature present on transect (x) = 10 m and a northwesterly dipping surface from 25 to 40 cm on transects (x) = 10.5 and 11 m. These features are possibly dipping or eroded bedrock surfaces, distinct stratigraphic

Table 4.5 Grid 1a GPR anomaly summary

Feature Type	Anomaly	Anomaly depth range (cm)	Maximum amplitude depth range (cm)	Boundary Coordinates			Comments
				Southern extent	Northern extent	Western extent	
Areas	1a - A1	(39 to 117)	(91 to 97)	(8, 5)	(11, 10)		Circular feature
	1a - A2	(46 to 78)	(65 to 71)	(4, 0)	(7.75, 3)		(L) shaped feature
	1a - A3	(39 to 65)	(46 to 52)	(5, 11)	(11, 21)		(L) shaped feature which approximates the walls excavated in Trenches 8800 and 8850
Linear features	1a - L1	(19 to 39)	(26 to 32)	(9.5, 5)	(9, 8.75)	(3, 9.25)	Long northwest trending wide linear feature.
	1a - L2	(52 to 129)	(91 to 97)	(4.5, 5)	(6, 24)		Same location as L2 but occurs shallower with different dimensions
	1a - L3	(26 to 39)	(26 to 33)	(5, 5.5)	(5.75, 23)		A northwestern dipping surface, location coincides with 1b - C1
Geologic/Stratigraphic Contacts	1a - C1	(90 to 130)		(8, 10)	(11, 14)		Shallow trough and dipping structure
	1a - C2	(25 to 40)		(10.5, 15)	(11, 19)		Northwest dipping structure
	1a - C3	(98 to 108)		(6.5, 9)	(6.5, 11)		

layers, or possibly sediment/soil layers with a moisture content different from the adjacent layers.

Grid 1b

Twenty anomaly features were identified from the Grid 1b GPR data, which included four areas, one geologic/stratigraphic contact, nine linear features, and six points and are presented on Figure 4.7 and summarized in Table 4.6. Area 1b – A3 contains a possible short northwest trending linear section, a wall foundation perhaps, and an areal scatter of small anomaly points over a shallow depth interval of 26 cm. Area features 1b – A1 and 1b – A2 are adjacent roughly circular areas of high reflection amplitudes over medium depth intervals of 38 and 52 cm respectively. 1b- A4 overlaps the areal extents of 1b - A1 and 1b - A2 at a deeper depth interval of 45 cm. These areas are possibly wall extensions/foundations of L1, or are part of the rock pile previously located in this area (S. Kane Personal Communication, 2002). These three areas appear to extend off the northern edge of the grid.

Feature 1b – L1 is an L-shaped feature produced by the shallow Walls 8800 and 8850. This feature indicates that these walls extend beyond their excavated limits. 1b – L2 is a linear feature with the same orientation as Wall 8202 in Trench 8200 and may be a northern extension of this wall. Features 1b – L3 through 1b – L9 are linear features which could be indicative of buried walls, eroded bedrock, or varying moisture levels.

1b – C1 is a south-western dipping surface with over a depth interval of 15 cm and could represent a dipping or eroded bedrock surface, distinct stratigraphic layer, or possibly a sediment/soil layer with a moisture content different from the adjacent layers.

Table 4.6 Grid 1b GPR anomaly summary

Feature Type	Anomaly	Anomaly depth range (cm)	Maximum amplitude depth range (cm)	Boundary Coordinates Southern extent	Northern extent	Western extent	Comments
Areas	1b - A1	(46 to 84)	(71 to 78)	(8, 5)	(11, 10)		Roughly circular areas of high amplitude reflection
	1b - A2	(26 to 78)	(71 to 78)	(7.5, 2)	(11, 5.5)		Circular area
	1b - A3	(39 to 65)	(52 to 58)	(5.5, 17)	(9, 21)		Could be a wall or pile of rocks, strong amplitude reflections.
	1b - A4	(78 to 123)	(91 to 97)	(8, 3)	(11, 10.5)		Combination of areas A1 and A2 when they merge at depth.
Geologic/Stratigraphic Contact	1b - C1	(95 to 110)	(95 to 110)	(6, 10)	(11, 11.5)		Small trough dips toward the west - coincides with 1a - C1
Linear features	1b - L1	(0 to 70)	(26 to 33)	(10, 3.75)	(9.75, 9)	(2, 8)	(L) shaped feature possibly bumps associated with course of wall stones excavated
	1b - L2	(58 to 129)	(117 to 123)	(0, 22.5)	(10, 23.25)		At the same orientation as wall 8202 in Trench 8200
	1b - L3	(65 to 129)	(78 to 91)	(0, 19.5)	(10, 20.25)		
	1b - L4	(39 to 84)	(65 to 78)	(0, 1.25)	(5.5, 2.75)		
	1b - L5	(39 to 129)	(65 to 71)	(0.5, 2)	(1.5, 7.5)		
	1b - L6	(39 to 91) and (117 to 129)	(65 to 78)	(0, 3.75)	(11, 5.5)		
	1b - L7	(78 to 84)	(78 to 84)	(5, 11)	(5.5, 20)		
	1b - L8	(39 to 129)	(52 to 58)	(7.5, 13.5)	(8, 20)		
	1b - L9	(84 to 110)	(78 to 84)	(0.5, 13)	(9.5, 14)		
Points	1b - P1	(65 to 84)	(71 to 78)	(5.5, 19.5)			
	1b - P2	(65 to 84)	(71 to 78)	(8, 19.5)			
	1b - P3	(65 to 84)	(71 to 78)	(4.75, 17.5)			
	1b - P4	(65 to 84)	(71 to 78)	(7.5, 17)			
	1b - P5	(65 to 84)	(71 to 78)	(5.5, 14.25)			
	1b - P6	(65 to 84)	(71 to 78)	(8, 14)			

Composite GPR Interpretation of Grids 1a and 1b

Grid 1 GPR anomaly features are presented in Figure 4.4 and summarized in Table 4.7. 1 – L1 is composed of features 1a – L1 and 1b – L1, which were very similar L-shaped anomalies and were most likely expressions of Walls 8800 and 8500. The GPR data suggests that these walls extend beyond what is found in the excavations. 1 - L2 is composed of features 1a – L2 and 1b – L7 which both indicated the presence of a linear feature with elements at depths from 52 to 129 cm. 1 – L2 was possibly another terrace wall as it was parallel to the two know terrace walls 8010 and 8017, located just south in Trench 8000. Alternatively it may be a ridge in the limestone bedrock or a stratigraphic layer with a lower water content than the surrounding soil. 1 – A1 is composed of several overlapping anomaly areas 1a-A1, 1b – A1, 1b – A2, and 1b – A4. This area contained no definite structures and may be an expression of debris, rocks, or varying moisture levels. This area abuts the eastern edge of Grid 1 and therefore most likely extend east beyond the grid boundary. 1 – A2 is a composite of features 1a – A3, 1b – A3, 1b – L3, 1b – L8, 1b – L9, and points 1b – P1 through 1b – P6. This area contained numerous features at a range of depths between 39 and 129 cm. 1 – A2 possibly contained building foundations/ walls, debris, or variation in moisture content. Feature 1 – C1 was a northwesterly dipping layer made up of 1a – C1, 1a – C3, and 1b – C1. This feature is either the dipping or eroded bedrock surface or a dipping stratigraphic layer. 1a – C2 is shallow trough feature present on transect (x) = 10m and a northwesterly dipping surface from 25 to 40 cm on transects (x) = 10.5 and 11 m. This feature is possibly a dipping or eroded bedrock surface, stratigraphic layer, or a layer with a greater amount of moisture.

136

Table 4.7 Composite summary of GPR features identified in Grid 1

Feature type	Anomaly feature	Anomaly depth range (cm)	Anomaly Source
Linear	1 - L1	(0 to 70)	Walls 8800 and 8850
	1 - L2	(52 to 129)	Possible terrace wall
Area	1 - A1	(26 to 123)	Possible debris or rocks
	1 - A2	(39 to 129)	Possible building foundation or walls
	1 – A3	(46 to 78)	(L) shaped feature
Contact	1 - C1	(90 to 130)	Geologic or stratigraphic dipping surface
	1 - C2	(25 to 40)	Shallow trough and dipping structure

Grid 2 GPR Interpretation

Two linear and two area GPR features were identified in Grid 2 and are summarized in Table 4.8 and Figure 4.4. 2 – L1 was an expression of Wall 8017, which extended west from Trench 8000 and was present at a depth interval of 13 to 151 cm. The radargrams and time slices suggested that this wall may have ended between (y) = 4 to 4.5 m. 2 – L2 was possibly a north – south trending feature, present from a depth interval of 47 to 154 cm. This feature may have been a buried stonewall or debris scatter. 2 – A1, present in the northeast corner of Grid 2, was most likely caused by reflections from Wall 8010, which was located just north of Grid 2. 2 – A2 was located in the southwest corner of Grid 2 and may have been a series of bumps caused by a line of rocks nearly parallel to the western edge of Grid 2. This line of rocks might have been the surface expression of a buried wall.

Table 4.8 Summary of GPR features identified in Grid 2

Feature type	Anomaly	Anomaly depth range (cm)	Maximum amplitude depth range (cm)	Anomaly source
Linear	2 - L1	(12 to 151)	(27 to 40)	Wall 8017
	2 - L2	(47 to 151)	(94 to 107)	Possible wall
Area	2 - A1	(12 to 151)	(27 to 40)	Possible expression of Wall 8010
	2 - A2	(0 to 151)	(0 to 13)	Possible expression of a line of surface stones

Synthesis of Monte Pallano Magnetic and Ground Penetrating Radar Results

The sixteen areas identified from the comparison of GPR and magnetic data are presented in Figure 4.8 and summarized in Table 4.9. These anomaly areas were corroborated with both the magnetic and GPR data were denoted with the prefix MG. Wall 8017 was identified beneath Grids 2, 3, 4, and 5 with both GPR and magnetic data, MG2 and MG4. Wall 8010 was identified beneath Grid 5, MG5, while the presence of 8010 beneath Grids 3 and 4 was uncertain. A corroboration between magnetic and GPR data, MG3, was present 1 m north of the wall's actual position. This may indicate that the wall changed direction toward the north or this may have been an expression of a different feature. A small portion of Wall 8007 was identified in both the magnetic and GPR data, MG1, while Wall 8006 was not.

The remaining eleven features were located in Grid 1, MG6 – MG16. The anomaly areas MG6, MG7 and MG8 may have been elements of a linear structure, possibly a wall, as might have been MG7, MG9, and MG10. MG12 was most likely a southwest extension of Wall 8800. MG16 was possibly an expression of the subsurface bedrock or stratigraphy based on the GPR radargrams. The remaining areas may have been sections of walls, ditches, rock piles, debris scatters or magnetite variations in the soil. Excavation would be necessary to verify if these anomaly areas were anthropogenic in nature.

138

Trench 8100

Trench 8250

Trench 8200

W8202

Trench 8700

Grid 2 Mag and GPR

W8108

W8203

R8212

MG4

MG5

MG6

MG7

MG8

Grid 5 Mag

Trench 7000

Grid 5 GPR

MG9

W8017

W8010/8024

MG10

Grid 4 GPR

Trench 8000

MG11

MG16

W8106

MG15

W8007

MG3

Grid 3 GPR

MG2

W8800

Trench 8850

MG1

Grid 4 Mag

W8850
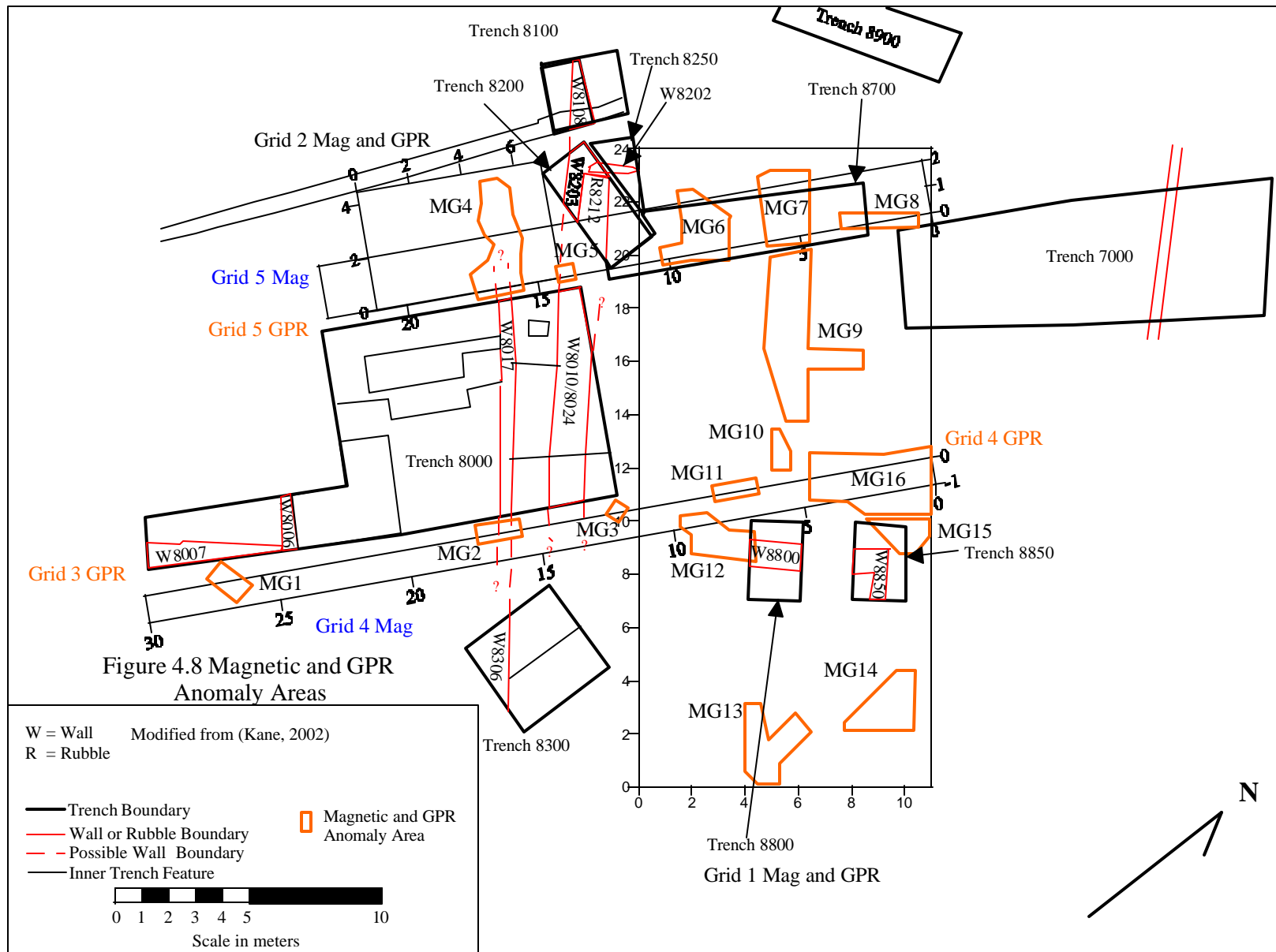
Figure 4.8 Magnetic and GPR
Anomaly Areas

W8306

MG12

MG13

MG14

Trench 8300

Trench 8800

Grid 1 Mag and GPR

W = Wall   Modified from (Kane, 2002)
R = Rubble

N

Trench Boundary
Wall or Rubble Boundary
Possible Wall Boundary
Inner Trench Feature

Magnetic and GPR
Anomaly Area

0 1 2 3 4 5   10
Scale in meters
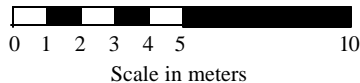
The anomaly source depth ranges determined from the GPR data and the depth to the source's center estimated from the magnetic cross-correlation analyses are presented for each anomaly feature in Table 4.7. The depth estimates matched closely for several of the features, MG1, MG3, MG9, and MG11, but many of the magnetic depth estimates varied from 50 to 500 cm. These features could contain elements that contribute to the signal at multiple depths for example different courses of a stonewall, multiple levels of debris, or rock deposits. The superposition of the signals from multiple anomalies can create a broader peaked signal that would cross-correlate as a deeper source anomaly. Excavation is necessary to verify the depth intervals of these anomaly features.

Table 4.9 Summary of combined magnetic and GPR anomaly features

Anomaly feature	GPR depth range (cm)	Estimated magnetic depth to object's center (cm)	Anomaly source
MG1	(10 to 130)	(50 to 100)	Wall 8007
MG2	(10 to 131)	(100 and 500)	Wall 8017
MG3	(10 to 120)	(50 to 100)	Possibly Wall 8010
MG4	(10 to 151)	(50 and 500)	Wall 8017
MG5	(10 to 100)	(500)	Wall 8010
MG6	(30 to 130)	(50, 200 and 300)	Possibly a wall section
MG7	(12 to 131)	(50 to 500)	Possibly a wall section
MG8	(12 to 98)	(50 to 200 and 400 to 500)	Possibly a wall section
MG9	(39 to 129)	(50 to 100)	Possibly a wall section
MG10	(52 to 129)	(50 and 500)	Possibly a wall section
MG11	(42 to 130)	(50 to 100)	
MG12	(0 to 70)	(50 to 300 and 500)	Possibly extension of Wall 8800
MG13	(46 to 78)	(50, 200, and 500)	Possibly a foundation corner
MG14	(53 to 129)	(500)	
MG15	(53 to 129)	(50 and 500)	
MG16	(20 to 131)	(50, 200, 300, and 500)	Possibly a geologic contact

CHAPTER V

CONCLUSION

The purpose of this thesis was to identify the locations of buried stonewalls and other anthropogenic features using GPR and magnetic data. In particularly this study focused on the development of the cross-correlation analysis technique for magnetic data, using synthetic tests, and applied to the Monte Pallano magnetic data. The combined techniques of GPR and magnetics with cross-correlation analysis jointly identified the locations of sixteen anomaly areas within Grids 1 – 5. Four of these anomaly areas, MG1, MG2, MG4, and MG5, mark the positions of known buried stonewalls, 8010, 8017, and 8007, within Grids 2 – 5 while one area, MG3, suggested the presence of an anomaly 1 m north of Wall 8010 within Grids 3 and 4 though it was uncertain if it was related to Walls 8010. Eleven other anomaly areas were located within Grid 1 based on the combined GPR and magnetic data. Areas MG7, MG9 and MG10 suggested the presence of a discontinuous linear feature, possibly a terrace wall, a ditch, or an expression of the underlying bedrock. The areas MG6, MG7 and MG8 might have also been sections of a linear feature. Area MG12 was the probable south-west extension of Wall 8800. There was evidence of dipping stratigraphy or bedrock based on the anomaly area MG16. The locations of these anomaly areas can be used to help guide future excavation investigations in the Trench 8000 area of Monte Pallano.

The identification of the sixteen corroborated anomaly features, MG1 – MG16, demonstrates the viability of using the combination of GPR with total field and vertical gradient magnetics for geophysical surveying at Monte Pallano. The presence of these anomalies did not discount the

potentially anthropogenic nature of the anomaly areas identified separately by the GPR and magnetic methods, though it has demonstrated that no one instrument is sufficient for locating all features. Multiple techniques are often necessary to delineate a site adequately because of the varying physical properties of the materials contained within. This does not suggest that GPR and magnetics are the most successfully combined techniques, but that the choice of the geophysical techniques to employ should be based on the site conditions, the investigation goals, and the economic and temporal resources of the project. The physical properties of the features of interest, the soil conditions, the size of the study area, and the desired horizontal resolution will all effect the choice of geophysical methods for a specific project.

The synthetic cross-correlation tests were important for understanding which parameters affected the ability of cross-correlation to resolve the horizontal and vertical positions of buried anomaly sources. The use of a homogeneous sphere as an anomaly source proved adequate for modeling buried walls with cross-correlation. The main advantages of using a sphere were that the chosen radii and magnetic susceptibility contrast of the pilot signal's anomaly source were unimportant to cross-correlation as they were only scalar quantities.

The number of samples in the pilot signal and the range of depths used to compute the pilot signal were the most important controllable parameters during cross-correlation. It was essential to have a pilot signal computed for an adequate number of samples to prevent the correlation of noise obscuring the anomalies of interest. Utilizing pilot signals for a range of sample numbers also assisted in identifying the presence and locating the positions of anomaly sources, though the limited grid extents at Monte Pallano prevented the cross-correlation with pilot signals with more than fifteen samples. It is recommended to use pilot signals with a minimum of eleven samples when employing cross-correlation to locate shallow architectural

features such as buried walls. It is necessary to collect magnetic data beyond the area of interest in order to allow the use of pilot signals with adequate numbers of samples for cross-correlation. The range and number of anomaly source depths used to compute the pilot signals should be determined by the features being investigated and the desired depth resolution. It is also important to consider the probe height when determining these values.

Cross-correlation increased the signal to noise ratio of both low amplitude anomaly signals and noise. Cross-correlation had difficulty separating closely spaced anomalies because the signals combined through superposition and formed a single broad peak which was interpreted as a single deep anomaly source instead of multiple shallower sources. While the superposition of signals skewed the depth estimate to a deeper value, it had little effect on the ability of cross-correlation to locate the horizontal position of the anomalies.

Cross-correlation proved to be a successful processing technique for both total field and vertical gradient magnetic data. The ability of cross-correlation to accurately locate the horizontal positions of anomaly sources was demonstrated by identifying Walls 8010, 8017, and 8006 and the corroboration of other anomaly locations with the GPR data. Cross-correlation was less successful at pinpointing the depths of some anomaly sources. Some of the depth estimates of anomaly areas from the cross-correlation analysis of the magnetic data differed from the GPR depths, with some of the magnetic depths estimates spanning a large range -+(50 to 500 cm). This suggested the presence of multiple anomaly sources or a source with elements at multiple depths. Additional work is necessary to compare the estimated cross-correlation depths with the actual depths.

Future investigation into the uses of cross-correlation for magnetic data processing should include a testing of the effects of different pilot signal source geometries. Additional

experimentation is needed to determine the effectiveness of cross-correlation at different site and soil conditions and with a variety of anomaly source types. A greater understanding is needed concerning the relation between the estimated depth and the actual source depth, and what effect source geometry and source size has on these depth estimates. The cross-correlation of magnetic data could also be applied to environmental or engineer applications, as anomaly sources such as drums, tanks or pipes could be easily modeled with simple geometries.

This archaeogeophysical investigation can serve as a starting point for any future geophysical prospection on Monte Pallano. Additional geophysical data should be collected beyond the limits of Grid 1 in order to better delineate the extent of the anomalies at the edges of the grid. The anomaly areas identified should be helpful for planning future excavation activities within Grid 1. It may be useful to employ other geophysical techniques such as resistivity to corroborate the GPR and magnetic data about possible wall locations.

This thesis has demonstrated the usefulness of cross-correlation for locating anomaly sources, but cross-correlation is by no means the answer at all sites. Cross-correlation is a technique in the toolbox of the geophysicist for identifying and locating anomaly sources. As with all geophysical processing techniques it is only applicable to certain sites, conditions and anomaly sources. A healthy skepticism and an understanding of the strengths of limitations of the techniques employed are necessary for any geophysical prospection undertaking.

REFERENCES

Aitken, M. J., 1958, Magnetic Prospecting I – The Water Newton Survey, Archaeometry, V. 1, p. 24 – 28

Aitken, M. J., M. S. Tite, 1962, Proton magnetometer surveying on some British hill‑forts, Archaeometry, V. 5, p. 126 - 134

Aitken, M. J., 1974, Physics and Archaeology, Oxford University Press, Oxford, England

Aitken, M. J. and J. C. Alldred, 1964, A simulator-trainer for magnetic prospection, Archaeometry, V. 7, p. 28 - 35

Aitken, M. J., G. Webster, and A. Rees, 1958, Magnetic prospecting, Antiquity, V. 32, p. 270-271

Alldred, J. C. and M. J. Aitken, 1966, A fluxgate gradiometer for archaeological surveying, Prospezioni Archeologiche, V. 1, p. 53 - 60

Agarwal R. G., and E. R. Kanasewich, 1971, Automatic Trend Analysis and Interpretation of Potential Field Data, Geophysics, V. 36 NO. 2, p. 339-348

Alder, M. J., 1988, Locating archaeological features in magnetic data by cross‑correlation, Archaeometry, V. 30, NO. 1, p. 145 - 154

Arzate, J. A., L. Flores, R. E. Chavez, L. Barba, and L. Manzanilla, 1990, Magnetic prospecting for tunnels and caves in Teotihuacan, Mexico: Geotechnical and environmental geophysics, edited by Stanley Ward, Society of Exploration Geophysicists, p. 155 - 162

Arlsan, Ermanno, Giancarlo Biella, Graziano Boniolo, Donatella Caporusso, Roberto De Franco, Alfredo Lozej, Luigi Veronese, 1999, Geophysical investigations of the Olonium Roman site (Northern Como Lake), Journal of Applied Geophysics V. 41, p. 169-188

Aspinall, A. and J. Lynam, 1968, Induced polarization as a technique for archaeological surveying, Prospezioni Archeologiche, V. 3, p. 91 - 93

Barker, Graeme, 1977, The Archaeology of Samnite Settlement in Molise, Antiquity, V. 51, NO. 201, p. 20 – 24

Baranov, V., 1957, A new method for interpretation of aeromagnetic maps: pseudo-gravimetric anomalies, Geophysics, V. 22, p. 359 - 383

Baranov, V. and H. Naudy, 1964, Numerical calculation of the formula of reduction to the magnetic pole, Geophysics, V. 29, p. 67 - 79

Bennett, Matthew, 1998, Dictionary of Ancient and Medieval Warfare, Stackpole Books, Mechanicsburg, Pennsylvania

Bhattacharyya, B. K., 1965, Two-dimensional harmonic analysis as a tool for magnetic interpretation, Geophysics, V. 30, p. 829 – 857

Bhattacharyya, B. K., 1978, Computer modeling in gravity and magnetic interpretation, Geophysics, V. 43, p. 912 – 929

Bhattacharyya, B. K. and M. E. Navolio, 1976, A fast Fourier transform method for rapid computation of gravity and magnetic anomalies due to arbitrary bodies, Geophysical Prospecting, V. 24, 633 - 649

Bispham, E.H, G. J. Bradley, J. W. J. Hawthorne and S. Kane, 2000, Towards a phenomenology of Samnite fortified centers, Antiquity V. 74, p. 23 – 24

Black, G. A., and R. B. Johnston, 1962, A test of magnetometry as an aid to archaeology, American Antiquity, V. 28, P. 199 - 205

Blakely, Richard J., 1995, Potential theory in gravity and magnetic applications, Cambridge University Press,

Breiner, S., and M. D. Coe, 1972, Magnetic exploration of the Olmec civilization, American Scientist, V. 60, NO. 5, p. 566 - 575

Breiner, S. 1973, Applications Manual for Portable Magnetometers, Geometrics, Sunnyvale, California, p. 58

Bucker, F., M. Gunter, H. Hortsmeyer, A. G. Green, and P. Huggenberger, 1996, Three-Dimensional Mapping of Glaciofluvial and Deltaic Sediments in Central Switzerland Using Ground Penetrating Radar. Proceedings of the Sixth International Conference on Ground Penetrating Radar, p. 45 - 50

Burger, Robert H., 1992, Exploration Geophysics of Shallow Subsurface, Prentice Hall Inc., Englewood Cliffs, NJ, p. 489

Burns, P. K, 1981, Magnetic reconnaissance in the Dolores Archaeological Program: Unpublished master's thesis, Anthropology Department, University of Nebraska, Lincoln

Burns, P. K., R. Huggins, and J. W. Weymouth, 1983, Study of correlation between magnetic reconnaissance and excavation in Dolores Program: Dolores Archaeological Program Technical Reports, Report No.: DAP-078, prepared for U.S. Bureau Reclamation, Salt Lake City, Utah

Chavez, R. E., M. E. Camara, A. Tejero, L. Barba, and L. Manzanilla, 2001, Site Characterization by Geophysical Methods in The Archaeological Zone of Teotihuacan, Mexico, Journal of Archaeological Science, V. 28 p. 1265-1276

Cicchitti A., L. Cuomo, C. Iacovone, and N. Tieri, 1996, - Monte Pallano: Scenari naturali e
    persistenze storico-archeologiche, p. 5-33 Lanciano

Colonna, G., 1955, Pallanum, una citta dei Frentani, Archeologia Classica V. 7 p. 164-178

Conyers, Lawrence B. and Dean Goodman, 1997, Ground Penetrating Radar, An Introduction
    for Archaeologists, Alta Mira Press, Walnut Creek California,

Dabrowski, K. and R. E. Linington, 1967, Test use of a proton magnetometer near Kalisz,
    Poland, Prospezioni Archeologiche, V. 2, p. 29 - 42

Davis, John C., 1986, Statistics and data analysis in geology, John Wiley & Sons, Inc.

Davis, J. L. and A. P. Annan, 1989, Ground-penetrating radar for high-resolution mapping of soil
    and rock stratigraphy, Geophys. Prosp., 37, 531 – 551

Dench, Emma, 1995, From Barbarians to New Men – Greek, Roman, and Modern Perceptions of
    the Peoples of the Central Appennines, Clarendon Press, Oxford, p. 255

Eppelbaum, Lev V., Boris E. Khesin, and Sonya E. Itkis, 2001, Prompt Magnetic Investigations
    of Archaeological Remains in Areas of Infrastructure Development: Israeli Experience,
    Archaeological Prospection, V. 8, p. 163-185

Faustoferri, Amalia and John Lloyd, 1998. Monte Pallano: a Samnite fortified centre and its
    hinterland. Journal of Roman Archaeology V. 11, p. 5-22

Fisher, E., G. A. McMechan, and A. P. Annan, 1992, Acquisition and Processing of Wide-
    Aperture Ground-Penetrating Radar Data. Geophysics V. 57 p. 495-504

Garrison, Ervan and Kent Schneider, 2001, Sangro Valley Project, Italy, Limited Geophysical
    Testing of Selected Areas,

Geomag v 4.0 software by NOAA, 2000 IGRF (http://ngdc.noaa.gov/cgi-
    bin/seg/gmag/fldsnth2.pl) Last visited (7/14/2003)

Geophysical Survey Systems, Inc, 1995, SIR System – 10A+ Training Notes, GSSI, North
    Salem, New Hampshire

Goodman, Dean, 1994, Ground-Penetrating Radar Simulation in Engineering and Archaeology,
    Geophysics, V. 59, p. 224 - 232

Goodman, Dean, 2002, GPR SLICE Ground Penetrating Radar Imaging Software Users Manual,
    Geophysical Archaeometry Laboratory, p. 85

Green, J. N., E. T. Hall, and M. L Katzev, 1967, Survey of a Greek ship-wreck off Kyrenia,
    Cyprus, Archaeometry, V. 10, p. 47 – 56

Green, J. N., and C. Martin, 1970, Metal detector survey of the wreck of the Armada ship 'Santa
    Maria de la Tosa, Prospezioni Archeologiche, V. 5, p. 95 – 100

Green, J. N., and C. Martin, 1970a, Metal detector survey at Dun an Oir, Prospezioni
    Archeologiche, V. 5, p. 101 – 106

Hall, E. T., 1966, The use of the proton magnetometer in underwater archaeology,
    Archaeometry, V. 9, p. 32 - 44

Hartman, Ronald R, Dennis J. Teskey, and Jeffrey L. Friedberg, 1971, A system of rapid digital
    aeromagnetic interpretation, Geophysics, V. 36 NO. 5, p. 891 – 918

Heese, Albert, 1999, Multi-parametric survey for archaeology: how and why, or how and why
    not?, Journal of Applied Geophysics, V. 41, p. 157 – 168

Hildebrand, J. A., A. M. Wiggins, P. C. Henkart, and L. B. Conyers, 2002, Comparison of
    Seismic Reflection and Ground-penetrating Radar Imaging at the Controlled
    Archaeological Test Site, Champaign, Illinois, Archaeological Prospection, V. 9, p. 9 - 21

Johnston, R. B., 1961, Archaeological application of the proton magnetometer in Indiana
    (U.S.A), Archaeometry, V. 4, p. 71 –72

Johnston, R. B., 1964, Proton magnetometry and its applications to archaeology. An evaluation

at Angel Site. Indiana Historical Society, Prehistorical Research Series V. 4, NO. 11, p.

45 - 140

Jones, Hal J., and John A. Morrison, 1954, Cross-Correlation Filtering, Geophysics, V. 19, NO.

4, p. 660-683

Kane, Susan, 2002, (Figure 2.6)

La Regina, A., 1989, I Sanniti, In AA. VV., Italia. Omnium Terrarum parens, Milan, p. 301 - 394

Le Borgne, E., 1955, Susceptibilite magnetique anormale du sol superficial, Ann. Geophys.V.

11, p. 399 – 419

Le Borgne, E., 1960, Influence du feu sur les proprietes magnetiques du sol, Ann. Geophys. V.

16, p. 159 – 195

Leucci, Giovanni, 2002, Ground-penetrating Radar Survey to Map the Location of Buried

Structures under Two Churches, Archaeological prospection, V. 9, p. 217 - 228

Linington, R. E., 1961, Quaderni di Geofisica Applicata, No. 22, Fondazione Lerici, Milan

Linington, R. E., 1964, The use of simplified anomalies in magnetic surveying, Archaeometry,

V. 7, p. 1 - 13

Linington, R. E., 1966, An extension to the use of simplified anomalies in magnetic surveying,

Archaeometry, V. 9, p. 51 – 60

Linington, R. E., 1967, Magnetic survey at la Civita, Tarquinia, Prospezioni Archeologiche, V.

2, P. 87 - 89

Linington, R. E., 1970, Techniques used in archaeological field surveys, Phil. Trans. Roy. Soc.

London A. V. 269, p. 89 – 108

Linington, R. E., 1972, A summary of simple theory applicable to magnetic prospecting in archaeology, Prospezioni Archeologiche, V. &, p. 9 - 60

Lloyd, J., N. Christie and G. Lock. 1997, From the mountain to the plain: landscape evolution in the Abruzzo. An interim report on the Sangro Valley Project (1994-5). Papers of the British School at Rome, LXV

May, J, 1970, Dragonby: an interim report on excavations on an Iron Age and Romano-British site near Scunthorpe, Lincolnshire, 1964 – 9, Antiquar. J. 50, p. 222 - 245

Milsom, J., 1996, Field Geophysics (second edition), The Geological Field Guide Series, John Wiley and Sons Ltd., New York

Morrison, F., C. W. Clewlow, and R. F. Heizer, 1970, Magnetometer survey of the La Venta Pyramid, Contributions of the University of California Archaeological Research Facility, V. 8, p. 1 - 20

Mudie, J. D., 1962, A digital differential proton magnetometer, Archaeometry, V. 5, p. 135 -139

Naudy, Henri, 1971, Automatic Determination of Depth on Aeromagnetic Profiles, Geophysics, V. 36, NO. 4, p 717 – 722

Neubauer, W., A. Eder-Hinterleitner, S. Seren, and P. Melichar, 2002, Georadar in the Roman Civil Town Carnuntum, Austria: An Approach for Archaeological Interpretation of GPR Data, Archaeological Prospection, V. 9, p. 135 - 156

Oakely, S. P., 1995, The Hill- Forts Of The Samnites, Archaeological Monograph of the British School at Rome, NO. 10, British School at Rome London

Olhoeft, G. R., 1981, Electrical Properties of Rocks. In Physical Properties of Rocks and Minerals, edited by Y.S Touloukian, W.R. Judd and R.F. Roy, McGraw-Hill, New York, p. 257 – 330

Olhoeft, G. R., 2000, Maximizing the information return from ground penetrating radar, Journal of Applied Geophysics, V. 43, p. 175 – 187

Pallottino, M., 1955, The Etruscans, Harmondsworth

Parrington, Michael, 1979, Geophysical and Aerial Prospecting Techniques at Valley Forge National Historical Park, Pennsylvania, Journal of Field Archaeology, V. 6, p. 193 - 201

Pattantyus, A. M., 1986, Geophysical results in archaeology in Hungary, Geophysics, V. 51, p. 561 - 567

Pentz, Harold H., 1940, Formulas and curves for the interpretation of certain two-dimensional magnetic and gravitational anomalies, Geophysics, V. 5 p. 295 - 306

Peters. Leo J., 1949, A direct approach to magnetic interpretation and its practical application, Geophysics, V. 14, p. 290 – 320

Pipan, M., L. Baradello, E. Forte, and I. Finetti, 2001, Ground Penetrating Radar Study of Iron Age Tombs in Southeastern Kazakhstan, Archaeological Prospection, V. 8, p. 141 – 155

Rainey, Froelich, and Carlo M. Lerici, 1967, The Search for Sybaris (1960 – 1965), Lerici, Rome, p. 313

Reppert, Philip M., F. Dale Morgan, and M. Nafi Toksoz, 2000, Dielectric constant determination using ground-penetrating radar reflection coefficients, Journal of Applied Geophysics, V. 43, p. 189 - 197

Robinson, Edwin S. and Cahit Coruh, 1988, Basic Exploration Geophysics, John Wiley and Sons Inc., p. 562

Salmon E. T., 1967, Samnium and the Samnites. Cambridge University Press

Salmon E. T., 1982, The Making of Roman Italy, Cornell University Press, p. 212

Sangro Valley Project, 1996 The 1996 Survey and Excavation Season, p. 13, Last visited

(1/21/02) http://units.ox.ac.uk/departments/archaeology/projects/sangro/report.htm

The Sangro Valley Project: Field School Guide Intro, 1999, Background, p. 7, Last visited

(2/07/02) http://www.sangro.org/background/background.html

The Sangro Valley Project: Reports, 2000, The Oxford University-Oberlin College 1999 Field

Season: Monte Pallano (Abruzzo, Italy), Last visited (2/07/02)

http://www.sangro.org/reports/2000.html

The Sangro Valley Project: Reports, 2001, The Oxford University-Oberlin College 1999 Field

Season: Monte Pallano and Acquachiara (Abruzzo, Italy), Last visited (1/18/02)

http://www.sangro.org/reports/2001.html

Sarris, A., E. Anthanassopoulou, A. Doulgeri-Intzessiloglou, Eu. Skafida, and J. Weymouth,

2002, Geophysical Prospection Survey of an Ancient Amphorae Workshop at Tsoukalia,

Alonnisos (Greece), Archaeological Prospection, V. 9, p. 183 - 195

Schneider, William A. and Milo M. Backus, 1968, Dynamic Correlation Analysis, Geophysics,

V. 33, NO. 1, p. 105 - 126

Scollar, Irwin, 1965, A contribution to magnetic prospecting in Archaeology, Archaeo-Physica

Band 15 der Beihefte der Bonner, Jahrbucher, p 21 – 92

Scollar, Irwin, and F. Krueckeberg, 1966, Computer treatment of magnetic measurements from

archaeological sites, Archaeometry, V. 9, p. 61 - 71

Scollar, Irwin, 1970, Fourier transform methods for the evaluation of magnetic maps,

Prospezioni Archeologiche, V. 5, p. 9 - 41

Scollar, Irwin, A. Tabbagh, A. Heese, I, Herzog, 1990, Archaeological Prospecting and Remote Sensing, Topics in Remote Sensing V. 2, Cambridge University Press, Cambridge, England, p.674

Scollar, Irwin, B. Weidner, and K. Segeth, 1986, Display of archaeological magnetic data, Geophysics, V. 51, p. 623 - 633

Silva, J. B C., 1986, Reduction to the pole as an inverse problem and its application to low-latitude anomalies, Geophysics, V. 51, p. 369 - 382

Squyres, Coy, H., 1975, Geology of Italy, The Earth Sciences Society of Libyan Arab Republic – 15 Annual Field Conference Tripoli, L.A.R, Volume II

Sternberg, Ben K., and James W. McGill, 1995, Archaeology studies in southern Arizona using ground penetrating radar, Journal of Applied Geophysics V. 33, p. 209 – 225

Sun, Jingsheng and Roger A. Young, 1995, Recognizing surface scatter in ground-penetrating radar data, Geophysics, V. 60, p. 1378 - 1385

Talwani, M., 1965, Computation with the help of a digital computer of magnetic anomalies caused by bodies of arbitrary shape, Geophysics, V. 30, p. 797 - 817

Tieman, Hans J., 1993, Description of scanless method of stacking velocity analysis, Geophysics, V. 58, NO. 11, p. 1596 – 1606

Tite, M. S., 1961, Alternative instruments for magnetic surveying, Archaeometry, V. 4, p. 85 – 90

Tite, M. S., 1966, Magnetic prospecting near the geomagnetic equator, Archaeometry, V. 9 p. 24 - 31

Tite, M. S., 1967, The magnetic survey. Appendix to M Avery, J. E. G. Sutton and J. W. Banks: Rainsborough, Nothants, England – Excavations 1961 – 5, Proc. Prehist. Soc., V. 33, p. 296 - 300

Tite, M. S. and C. Mullins, 1970, Electromagnetic prospecting on archaeological sites using a soil conductivity meter, Archaeometry, V. 12, NO. 1, p. 97 – 104

Tite, M. S., 1972, Methods of Physical Examination in Archaeology, New York Academic Press

Tillard, Sylvie and Jean-Claude Dubois, 1995, Analysis of GPR data: wave propagation velocity determination, Journal of Applied Geophysics, V. 33, p. 77 – 91

Topp, G. C., J. L. Davis, and A. P. Annan, 1980, Electromagnetic determination of soil water content; measurements in coaxial transmission lines, Water Resources Research, V. 16 p. 574 - 582

Vacquier, Victor, Nelson C. Steenland, Roland G. Henderson, and Isadore Zietz, 1951, Geological Society of America, Memoir 47,

Vaughan C. J., 1986, Ground-penetrating radar surveys used in archaeological investigations, Geophysics, V. 51, NO. 3, p. 595 - 604

Vickers, R. S, L. T. Dolphin, and D. Johnson, 1976, Archaeological Investigations at Chaco Canyon Using Subsurface Radar. In Remote Sensing Experiments in Cultural Resource Studies, edited by T.R. Lyons, p. 81-101. Chaco Center, USDI-NPS and University of New Mexico, Albuquerque

Von Frese, R. R. B., 1984, Archaeomagnetic anomalies at midcontinental North American archaeological sites, Historical Archaeology, V. 18, NO. 2, p. 4 – 19

Von Frese, R. R. B., and V. E. Noble, 1984, Magnetometry for archaeological exploration of historical sites, Historical Archaeology, V. 18, NO. 2, p. 38 – 53

Weymouth John W. and R. Huggins, 1981, Magnetic survey of the Edwards I (34GR8) sites in
     western Oklahoma: Report submitted to the Oklahoma Archaeological Survey,
     University of Oklahoma

Weymouth John W. and B. Bevan, 1983, Combined magnetic and ground penetrating radar
     survey of an archaeological site in Oklahoma, Digest, Vol. I, Section WP.3, International
     Geoscience and Remote Sensing Symposium (San Francisco), New York, IEEE

Weymouth John W., 1986, Geophysical methods of site surveying: Advance in Archaeological
     Methods and Theory, V. 9, Academic Press, Inc., p. 311 - 395

Yilmaz, Ozdogan, 1987, Seismic Data Processing, Society of Exploration Geophysicists p. 526

Young, Charles T., and David R. Droege, 1986, Archaeological applications of resistivity and
     magnetic methods at Fort Wilkins State Park, Michigan, Geophysics, V. 51, NO. 3, p.
     568 – 575

Zhou, Hui and Motoyuki Sato, 2001, Archaeological Investigation in Sendai Castle using
     Ground Penetrating Radar, Archaeological Prospection, V. 8, p. 1 - 11

APPENDIX A

MONTE PALLANO MAGNETIC DATA ANALYSIS

Profile and Contour Plot Descriptions

The total field and vertical gradient magnetic profiles and contour plots for Grids 1, 2, 4, and 5 are presented in (Figures A.2 – A.13) and (Figures 4.1 and 4.2) respectively.

Grid 1

Total Field

The total field values ranged from 46160 to 46225 nT. The total field data exhibited continuous linear trends of peaks and adjacent troughs in the Grid 1a total field profiles and contour plot. These trends included troughs from (2.5, 0) – (2, 24), and (8.25, 0) – (8, 24) and a peak from (5.5, 0) to (5, 24).

The strong parallel banding of negative and positive values is indicative of a site wide feature(s) or linear concentrations of magnetite in the soil. The small range of total field values suggests a magnetically clean site with little to no modern anthropogenic magnetic contamination.

Vertical Gradient

The vertical gradient data showed similar trends to the total field data and had values ranging from –11 to 6 nT/m. The western half of Grid 1 had the largest range of gradients and the only occurrences of high positive gradients. There were three large dipole anomalies with their centers located at (4, 10), (4, 16), and (9, 19). There was a linear east-west trending array of positive gradients with amplitudes of 3 to 4 nT/m along the southern boundary of the grid

between (y) = 10 to 19 m. Parallel to this and just north was a linear trend of negative gradients with amplitudes of -7 to –8 nT/m from (x) = 2 to 4 m and (y) = 4 to 24 m. Parallel to and north of these negative values were two east-west trending lines of high positive gradients with amplitudes of 4 to 6 nT/m from (x) = 4.5 to 6.5 m, (y) = 14 to 24 m, and (x) = 7.75 to 10 m, (y) = 14 to 24 m. In between these two lines of positive values were points with slightly negative gradients of amplitudes of -1 nT/m.

The largest negative gradient of -9 nT/m was located along the northern edge of Grid 1 at (y) = 19 m. In the eastern half of the grid most of the gradients were negative with amplitudes of –5 and –6 nT/m.

Grid 2

Total Field

The total field values ranged from 46216.03 – 46255.67 nT. Portions of a large dipole were present with the centers of the poles located at (1, 0) and (6.25, 2.5). The anomaly source of this dipole feature was possibly the buried stonewall 8017 that trended east west and was present in Trench 8000. This wall intersected Grid 2 between (x) = 4.25 and 4.85 m, and is believed to continue west beneath Grid 2. Wall 8010 was present beneath the negative portion of the dipole just north of Grid 2 as it extends west to Trench 8200 as Wall 8203 and then into Trench 8100 as Wall 8108.

Vertical Gradient

The vertical gradient contours exhibited the same trend as the total field with a large dipole anomaly present with a positive gradient of 13 nT/m at (1, 0) and a negative gradient of – 5 nT/m at (6.25, 2.5).

Grid 4

Total Field

The total field values ranged from 46207 – 46236.37 nT. Linear troughs were present in both profiles at 3 m, 9 m, 16 m – the position of Wall 8017 and at 26 m - the position of Wall 8007. In addition linear troughs are present at (-1, 5) and (0, 6). Positive values were exhibited between (23.9 – 30 m), the location of Walls 8006 and 8007, for (y = -1 m) and negative values for (x = 0 m). The pattern of adjacent high and low values as for Walls 8006 and 8007 was present for (x = 18 – 24) (y = -1 – 0), suggesting the presence of a wall or rocks. There were no strong negative gradient values between (x = 12 – 14 m) i.e. the position where Wall 8010 should be if it extended east beneath Grid 4.

Vertical Gradient

The vertical gradient values ranged from –6 to 10 nT/m. The locations of linear troughs and peaks were present at the same positions as for the total field data.

Grid 5

Total Field

The total field values ranged from 46199.11 - 46251.31 nT. Linear troughs were present from (16, 0) to (16, 1) the location of Wall 8017, (14, 0) to (14, 1) possibly the edge of Wall 8017, (8, 0) to (8, 2), and (4, 0) to (4 2). Low total field values of (46206.44 to 46199.11 nT) were present at (12, 1) and (13, 2) which was the location of Wall 8010. Similar values were also present in Grid 2 adjacent to Wall 8203 and the rubble R8212 in Trench 8200. Large amplitude peaks (46239.95 to 46251.31 nT/m) were present at (20, 0) to (20, 2).

Vertical Gradient

The vertical gradient profiles and contours followed the same trends as those for the total field. The vertical gradient values ranged from –14 to 14 nT/m. Linear troughs were present at the same locations as for the total field data.

Large negative gradient values (-10.41 to -12.05 nT/m) were present at (12, 1) and (13, 2) with a smaller value of 1.97 nT/m at (12, 0) which was the location of Wall 8010. Similarly large negative values were also present in Grid 2 adjacent to Wall 8203 and the rubble R8212 in Trench 8200. Large amplitude peaks with values of (4.74 – 14.4 nT/m) were present at (20, 0) to (20, 2).

Monte Pallano Cross-Correlation Results

Cross-Correlation Interpretations

The plots depicting the filtering of the Monte Pallano magnetic cross-correlation peak and trough data for Grids 1, 4, and 5 is presented in Figures A.15 – A31. Figures A.32 and A.33 present the peak and trough locations and anomaly areas for the total field and vertical gradient cross-correlation data.

Grid 4

The locations, depths, and strengths of total field and vertical gradient cross-correlations are summarized for each identified anomaly area in Table A.1. The anomalies 4TF-T3 and 4VG-T3 are most likely caused by Wall 8017, which extended beneath Grid 4 east into Trench 8300 as Wall 8306. The anomalies 4TF-T4 and 4VG-T4 were produced by Walls 8006 and 8007 with a depth estimate of 0.5 to 1 m. The peak anomalies 4TF-P2 and 4VG-P2 might have been produced by Wall 8010. Other peaks and troughs relate to features identified in Grid 1, presented in a later section.

Table A.1 Grid 4 Cross-correlation summary

Both Points Present

	Total Field or Vertical Gradient	Point 1	Point 2	>0.5 or < -0.5 (rm values)	>0.8 or <-0.8 (rm values)	Depths present (m)	Anomaly Source
Peaks	4TF-P1	(7, -1)	(7, 0)			0.5 - 1	
	4TF-P2	(13, -1)	(12, 0)			0.5	Possible Wall 8010
	4TF-P3	(22, -1)	(22, 0)	Yes		3 & 5	
	4VG-P1	(7, -1)	(8, 0)				
	4VG-P2	(13, -1)	(12, 0)			0.5 - 1	Possible Wall 8010
Troughs	4TF-T1	(3, -1)	(2,0)			0.5 & 5	Feature 1 - T6 in Grid 1
	4TF-T2	(10, -1)	(10, 0)	Yes	Yes	2 & 5	Feature 1 - T3 in Grid 1
	4TF-T3	(17, -1)	(16, 0)	Yes	Yes	5	Wall 8017
	4TF-T4	(26, -1)	(27, 0)	Yes		0.5 - 1	Walls 8006 and 8007
	4VG-T1	(3, -1)	(1,0)	Yes		2 & 3	Feature 1 - T6 in Grid 1
	4VG-T2	(9, -1)	(10, 0)	Yes		0.5 - 1	Feature 1 - T3 in Grid 1
	4VG-T3	(17, -1)	(17, 0)			1 & 5	Wall 8017
	4VG-T4	(26, -1)	(27, 0)	Yes	Yes	1	Walls 8006 and 8007

Grid 5

The locations, depths, and strengths of total field and vertical gradient cross-correlations are summarized for each identified anomaly area in Table A.2. The total field and vertical gradient anomaly features 5TF-T3 and 5VG-T3 identified from the cross-correlation data were located above where Wall 8010 would extend west beneath Grid 5, and anomaly features 5TF-T4 and 5VG-T4 were located above where Wall 8017 would extend west beneath Grid 5. Other peaks and troughs relate to features identified in Grid 1, presented in a later section.

Table A.2 Grid 5 Cross-correlation summary

Both Points Present

	Anomaly Feature	Point 1	Point 2	Point 3	>0.5 or < -0.5 (rm values)	>0.8 or <-0.8 (rm values)	Depths present (m)	Anomaly Source
Peaks	5TF-P1	(6, 0)	(6, 1)	(6, 2)	Yes		2, 3, & 5	Grid 1 Feature P1
	5TF-P2	(22, 0)	(23, 1)	(22,3)	Yes	Yes	4 & 5	
	5VG-P1	(3, 0)	(3, 1)	(2, 2)			0.5 & 1	
	5VG-P2	(6, 0)	(5, 1)	(6, 2)	Yes		1 & 5	Grid 1 Feature P1
	5VG-P3	(10, 1)	(11, 2)				1 & 2	
	5VG-P4	(22, 0)	(23, 1)		Yes	Yes	5	
Troughs	5TF-T1	(1, 0)	(0, 1)	(0, 2)	Yes	Yes	0.5 & 2	Grid 1 Feature T7
	5TF-T2	(10, 0)	(9, 1)	(9, 2)			0.5 & 3	Grid 1 Feature T1
	5TF-T3	(14, 1)	(15, 2)		Yes	Yes	5	Possibly Wall 8010
	5TF-T4	(16, 0)	(17, 1)				0.5 & 5	Possibly Wall 8017
	5VG-T1	(1, 0)	(0, 1)		Yes	Yes	0.5 & 2	Grid 1 Feature T7
	5VG-T2	(9, 0)	(8, 1)	(9, 2)			0.5 & 2	Grid 1 Feature T1
	5VG-T3	(14, 0)	(14, 1)	(15, 2)	Yes	Yes	5	Possibly Wall 8010
	5VG-T4	(16, 0)	(18, 1)				5	Possibly Wall 8017

Grid 1

Nine peak anomaly areas and thirteen trough anomaly areas were identified for both the total field and vertical gradient. The locations, depths, and strengths of total field and vertical gradient cross-correlations are summarized for each identified anomaly area in Table A.3.

Table A.3 Summary of anomalous features identified for the Grid 1 total field and vertical gradient cross-correlations

Anomaly Feature	50% or greater of an anomaly feature present		Depths present (m)	Anomaly Feature	50% or greater of an anomaly feature present		Depths present (m)
	>0.5 or < -0.5 (r_m values)	>0.8 or <-0.8 (r_m values)			>0.5 or < -0.5 (r_m values)	>0.8 or <-0.8 (r_m values)	
TF-P1a			1	VG-P1	Yes	Yes	5
TF-P1b	Yes		0.5	VG-P2	Yes	Yes	5
TF-P1c	Yes		1	VG-P3	Yes		0.5 & 1
TF-P2a	Yes		1	VG-P4	Yes		5
TF-P2b	Yes	Yes	2	VG-P5			0.5
TF-P2c	Yes		1	VG-P6	Yes	Yes	0.5 & 4
TF-P2d	Yes		2	VG-P7	Yes		0.5 & 1
TF-P3			0.5	VG-P8	Yes		1
TF-P4	Yes		5	VG-P9			0.5 & 1
TF-T1a	Yes		3	VG-T1	Yes		2
TF-T1b	Yes		2	VG-T2			0.5
TF-T1c	Yes		0.5	VG-T3	Yes	Yes	5
TF-T1d	Yes		2	VG-T4	Yes	Yes	2 & 3
TF-T1e	Yes		0.5 & 1	VG-T5	Yes	Yes	5
TF-T2a	Yes	Yes	5	VG-T6			0.5
TF-T2b	Yes	Yes	4	VG-T7			0.5
TF-T2c	Yes	Yes	5	VG-T8	Yes	Yes	3
TF-T2d	Yes	Yes	1	VG-T9	Yes	Yes	2
TF-T2e	Yes	Yes	4	VG-T10			0.5
TF-T3			5	VG-T11	Yes	Yes	3
TF-T4	Yes	Yes	2 & 5	VG-T12	Yes		0.5
TF-T5	Yes	Yes	5	VG-T13	Yes		1

Total Field

There were several large linear features that extended the majority of the length of Grid 1, two troughs (TF-T1 and TF-T2) and two peaks (TF-P1 and TF-P2). These linear features were

subdivided into multiple separate features based on depth estimates and correlation coefficients.

Several other east-west trending linear features were identified for both the peaks and troughs.

Vertical Gradient

Filtering of the vertical gradient data produced less continuous linear features than for the total field but instead numerous smaller anomalies, many of them linear in nature (VG-P1, VG-P2, VG-P3, VG-P4, VG-P7, VG-P8, VG-P9, VG-T5, VG-T6, VG-T9, VG-T10, and VG-T11).

Figure A.1 A comparison of the sensitivity of the gradiometer with two different probe separation distances.
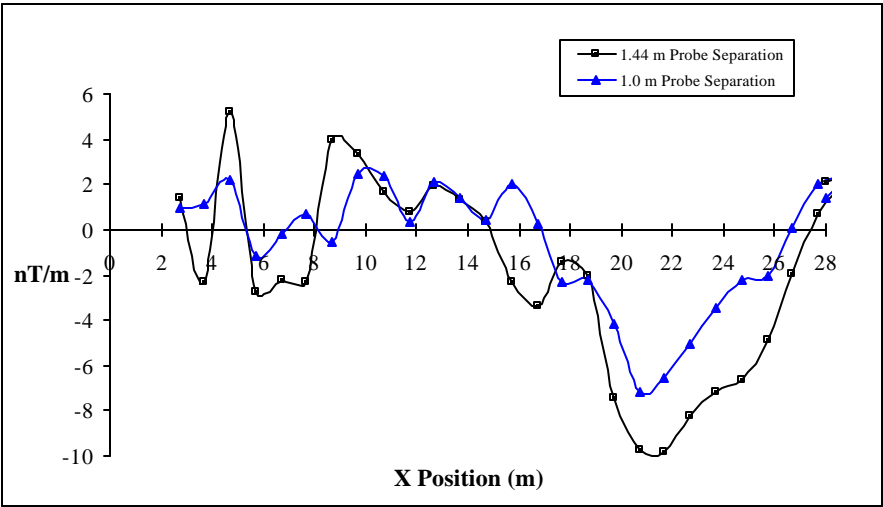
Figure A.2 Grid 1a total field magnetic profiles X = 0 - 5 m
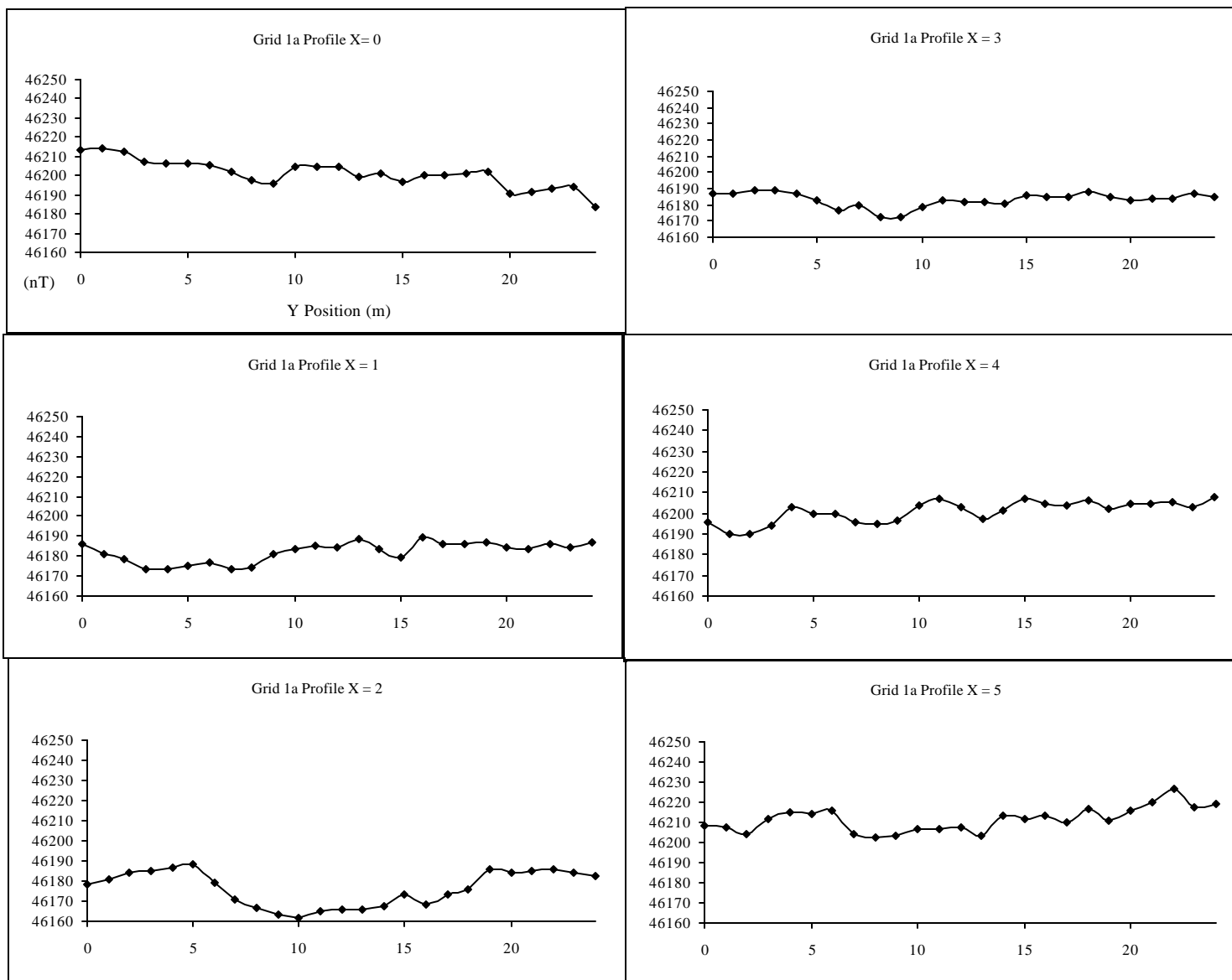
Figure A.3 Grid 1a total field magnetic profiles X = 6 - 11 m

Grid 1a Profile X = 6

Grid 1a Profile X = 9

Grid 1a Profile X = 7

Grid 1a Profile X = 10

Grid 1a Profile X = 8

Grid 1a Profile X = 11

Y Position (m)

(nT)
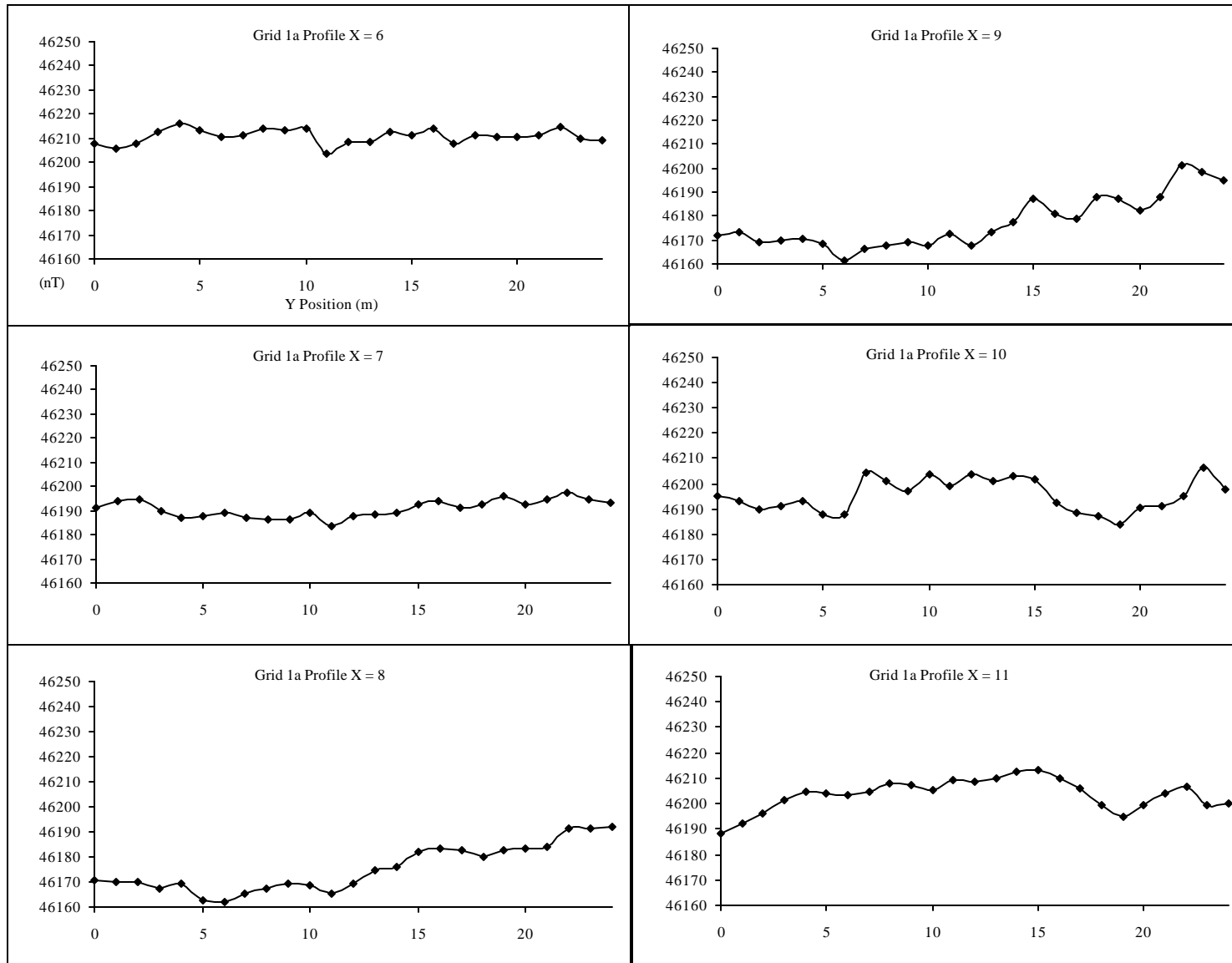
Figure A.4 Grid 1b total field magnetic profiles Y = 0 - 8 m
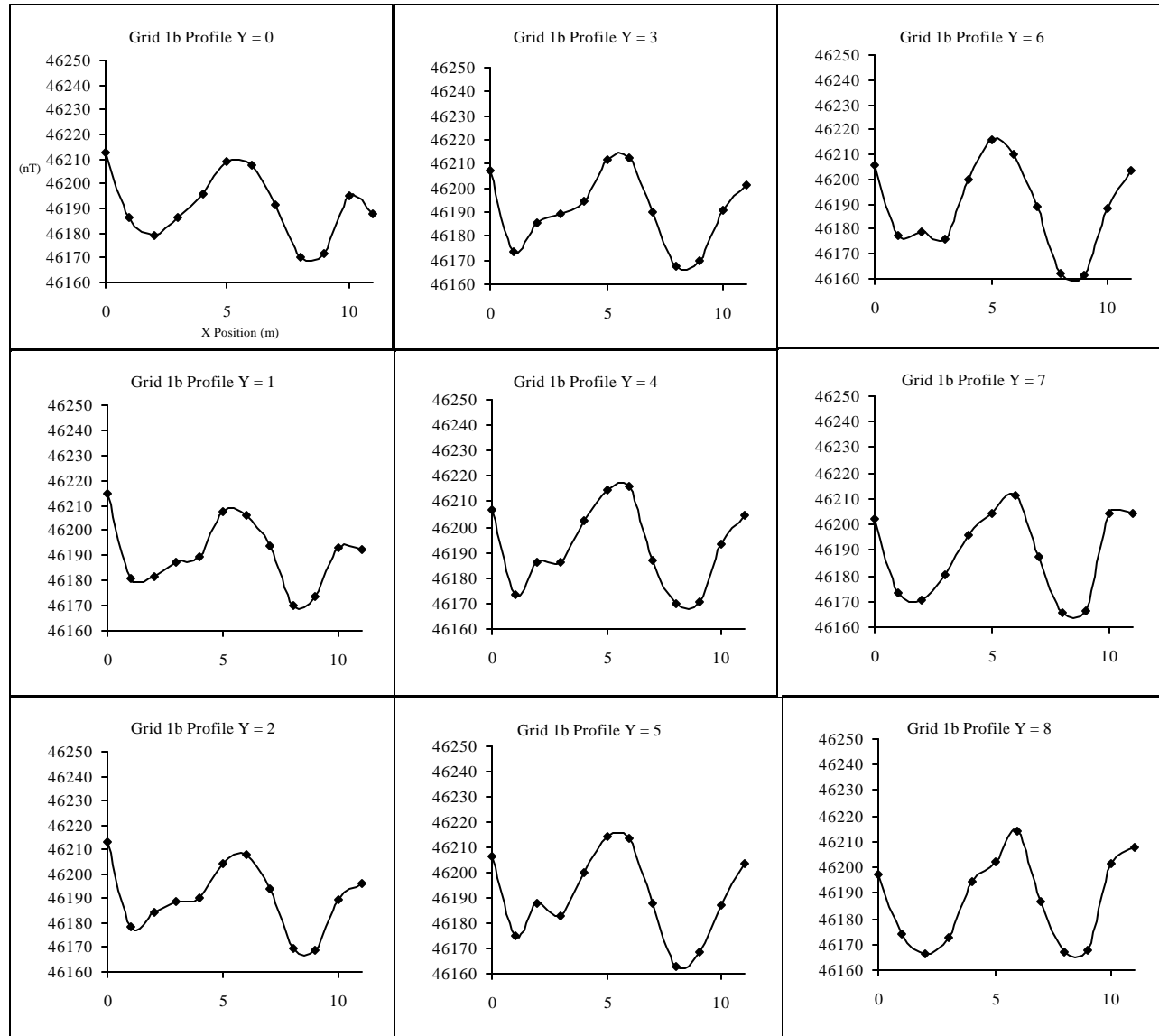
Figure A.5 Grid 1b total field magnetic profiles Y = 9 - 17 m
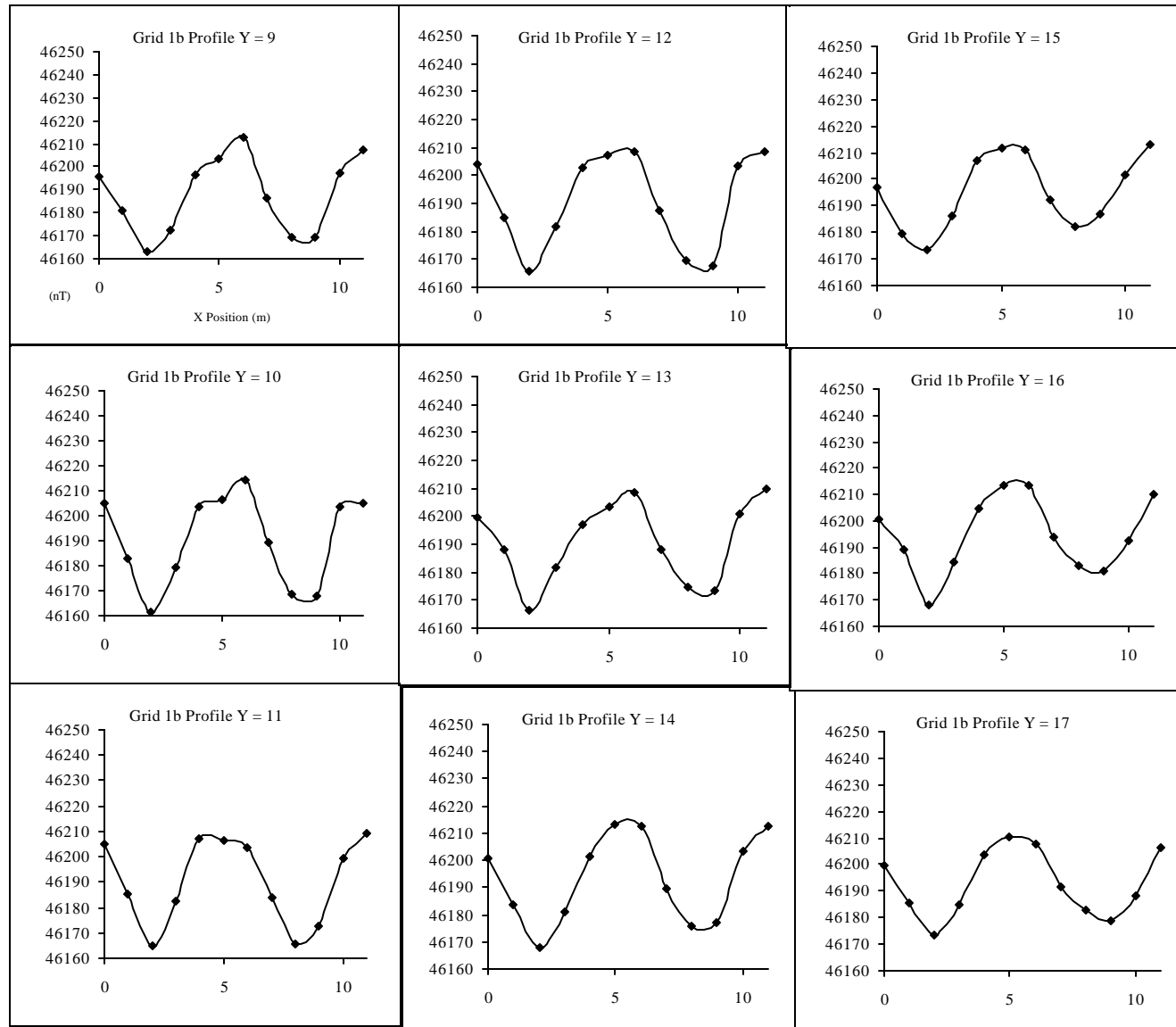
Figure A.6 Grid 1b total field magnetic profiles Y = 18 - 24 m
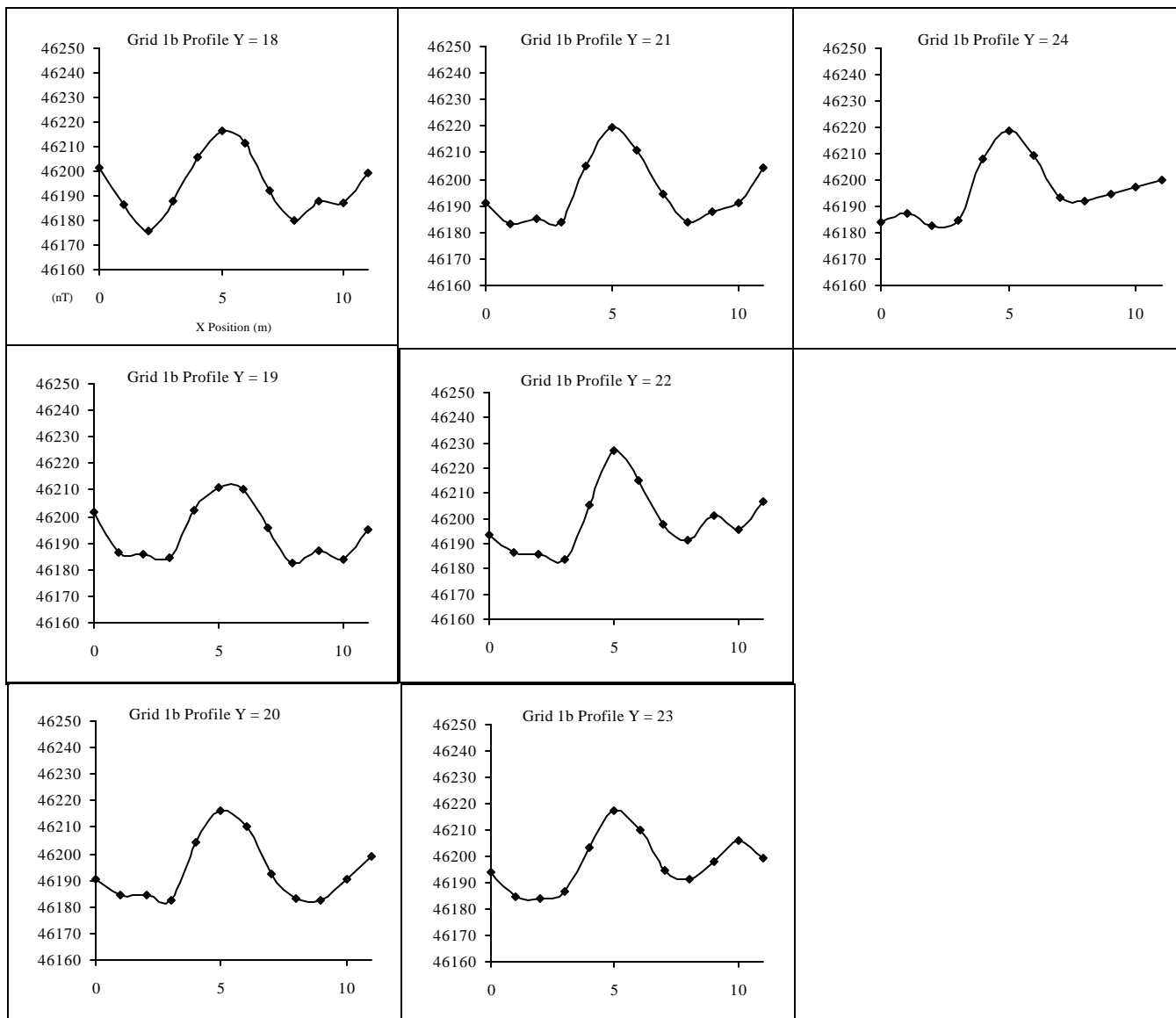
Figure A.7 Grid 1a vertical gradient magnetic profiles X = 0 - 5 m
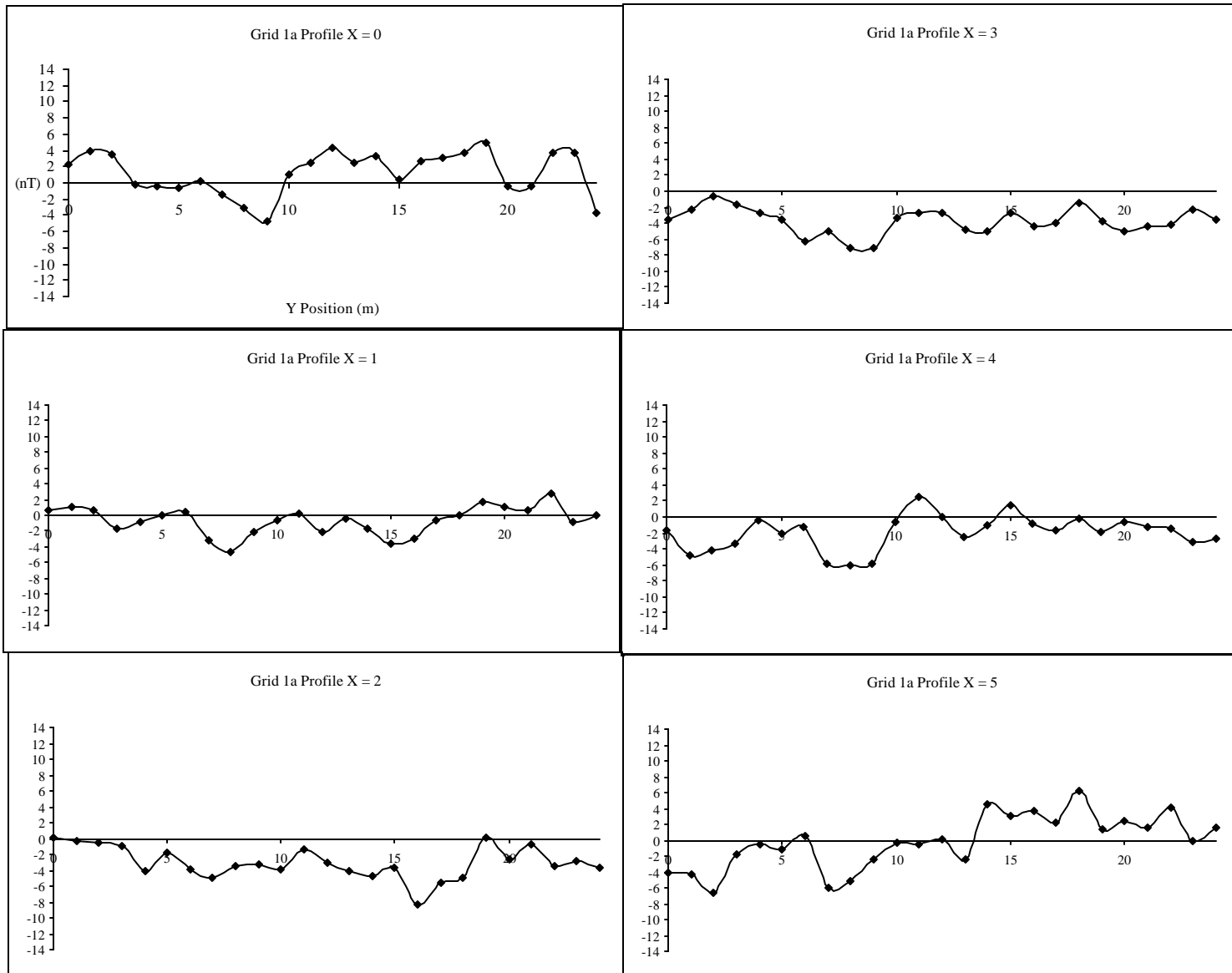
Figure A.8 Grid 1a vertical gradient magnetic profiles X = 6 - 11 m
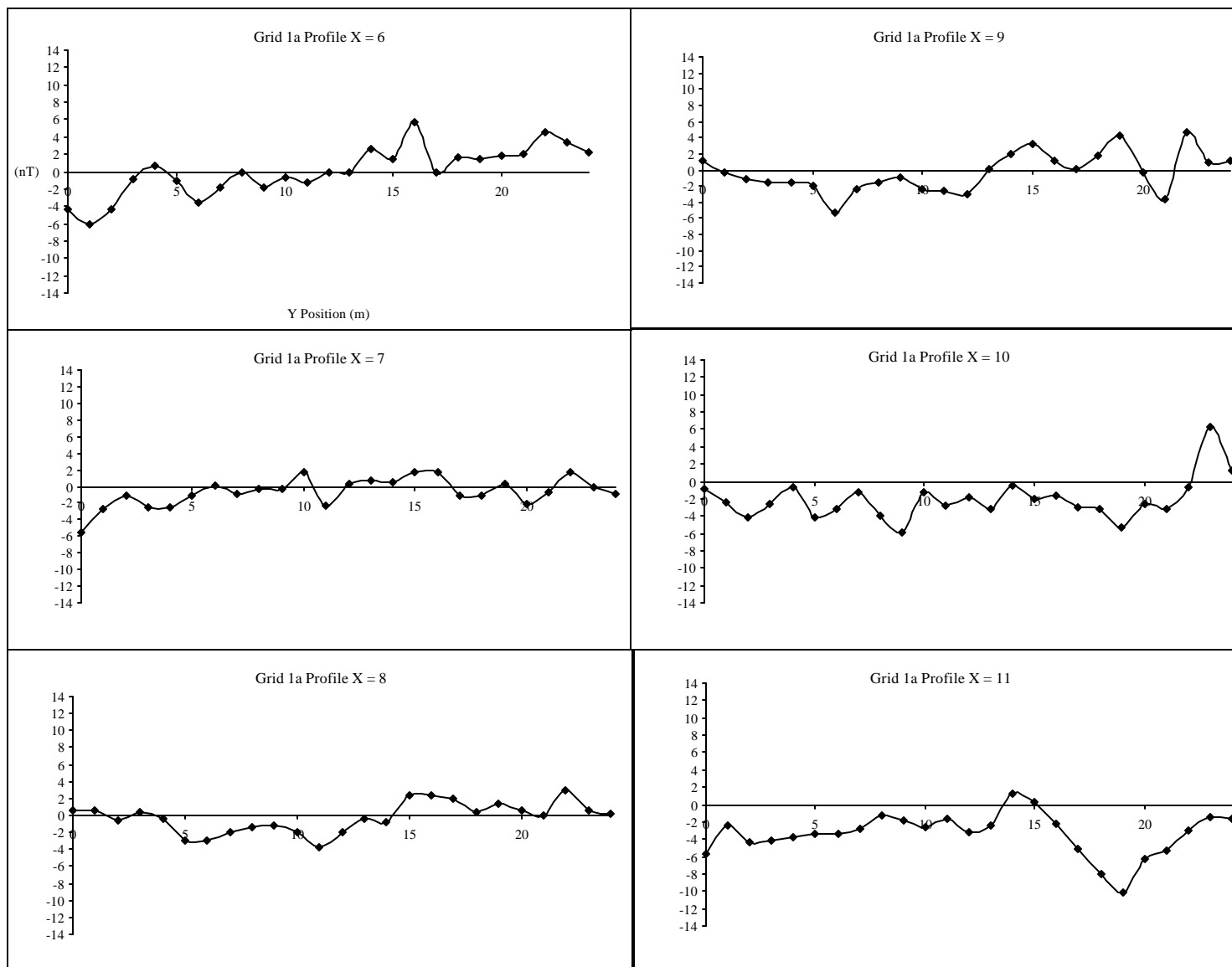
Figure A.9 Grid 1b vertical gradient magnetic profiles Y = 0 - 8 m
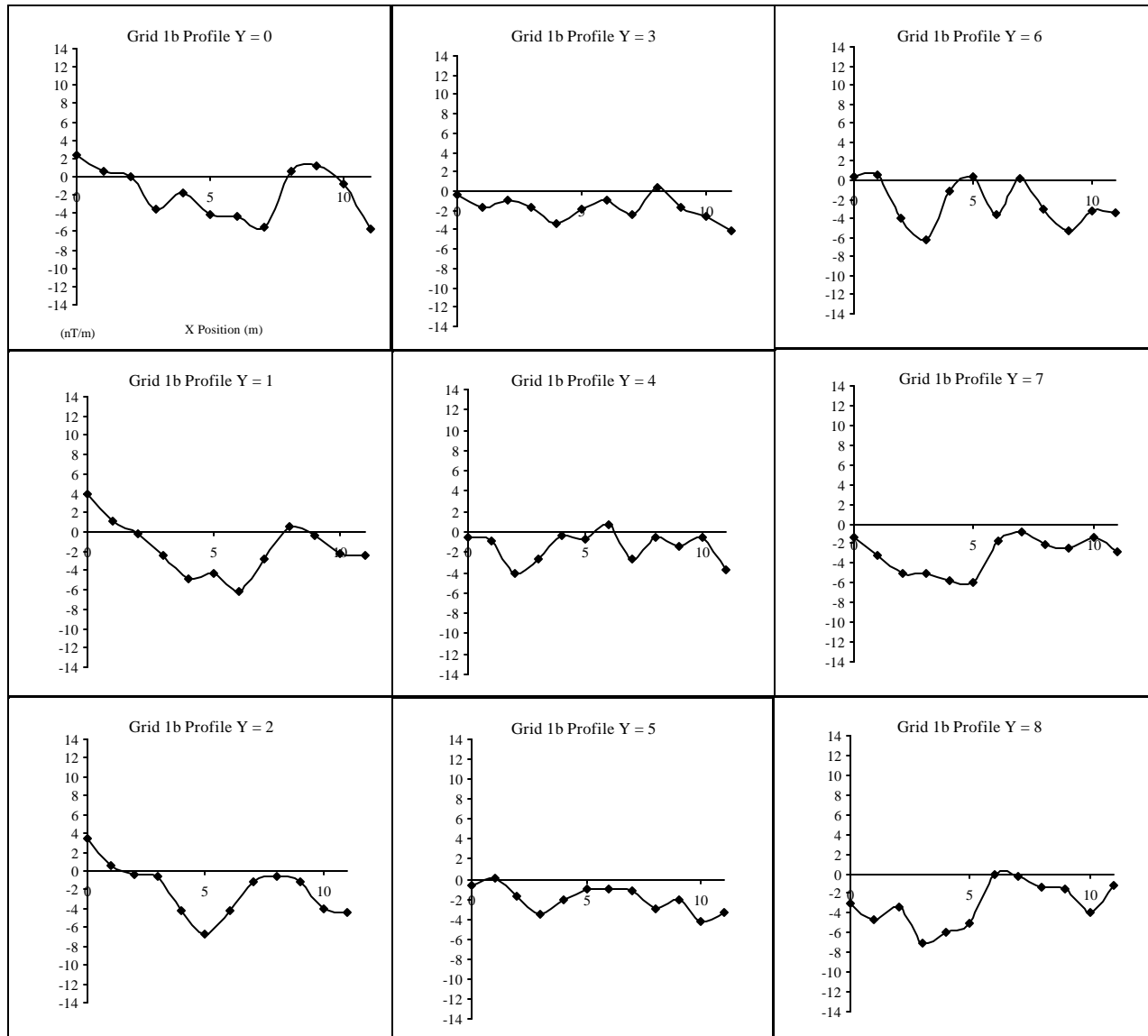
Figure A.10 Grid 1b vertical gradient magnetic profiles Y = 9 - 17 m
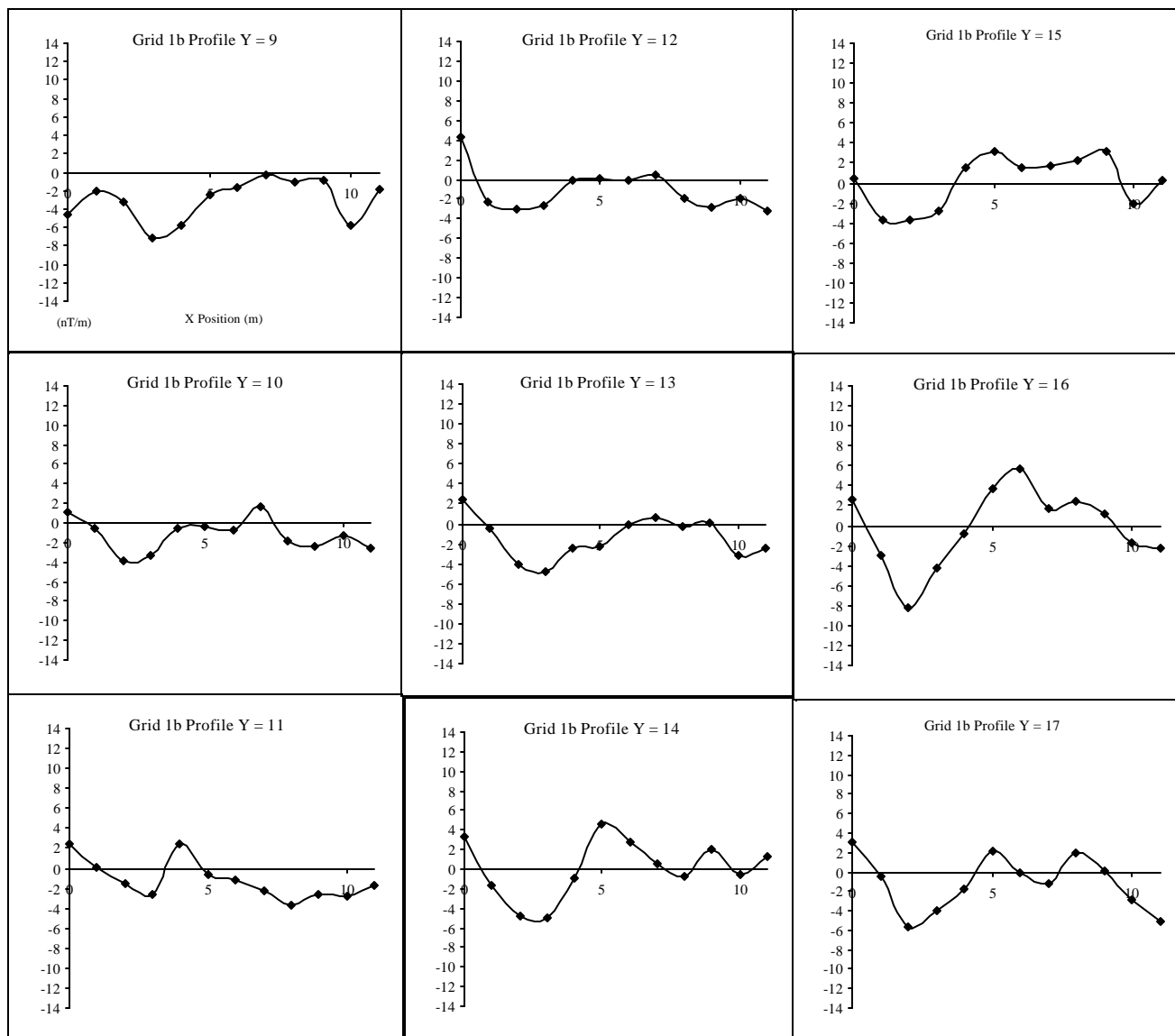
Figure A.11 Grid 1b vertical gradient magnetic profiles Y = 18 - 24 m
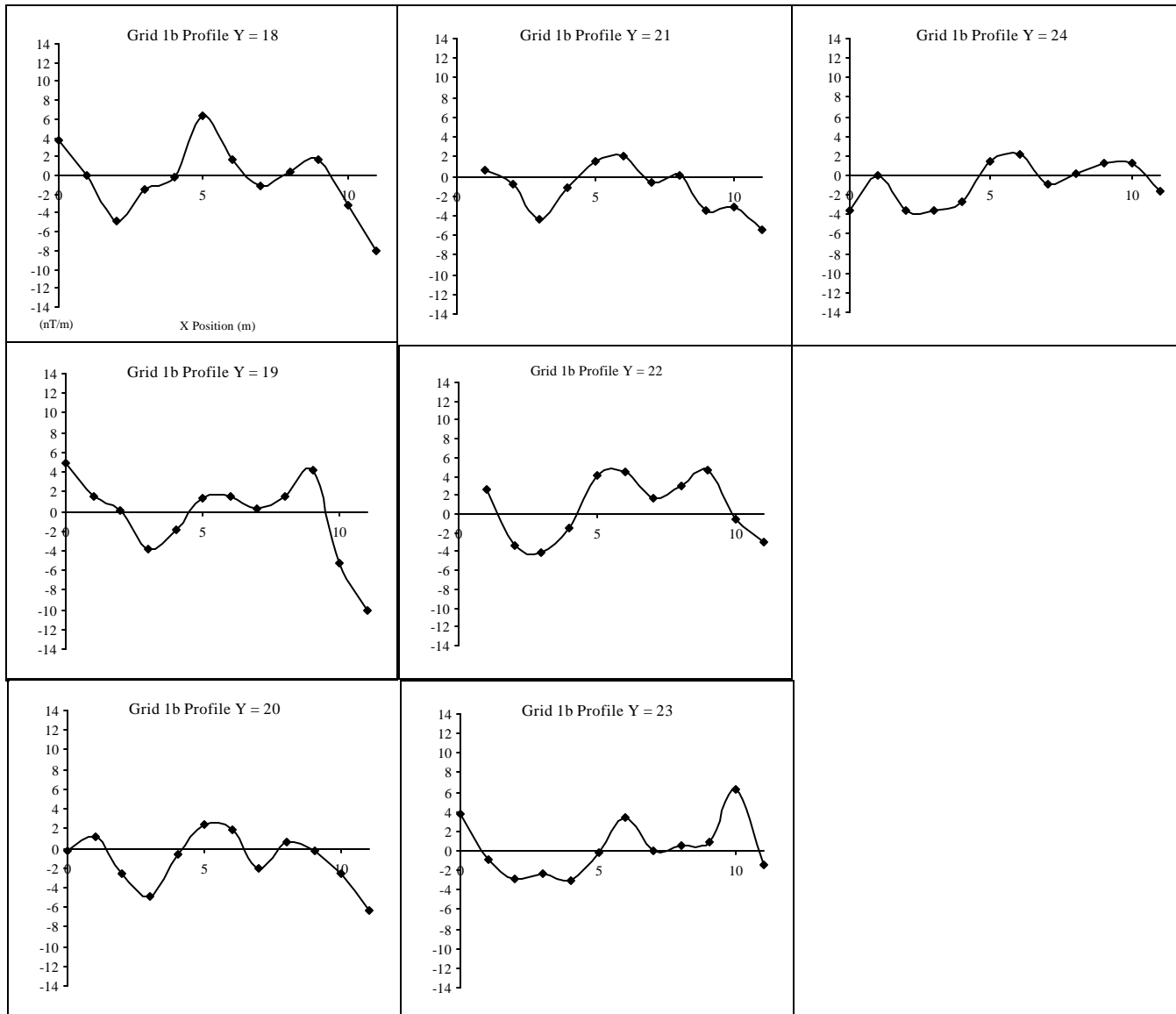
Figure A.12 Grid 2 total field magnetic profiles X = 0.5 - 4.5 m   Figure A.13 Grid 2 vertical gradient magnetic profiles X = 0.5 - 4.5 m
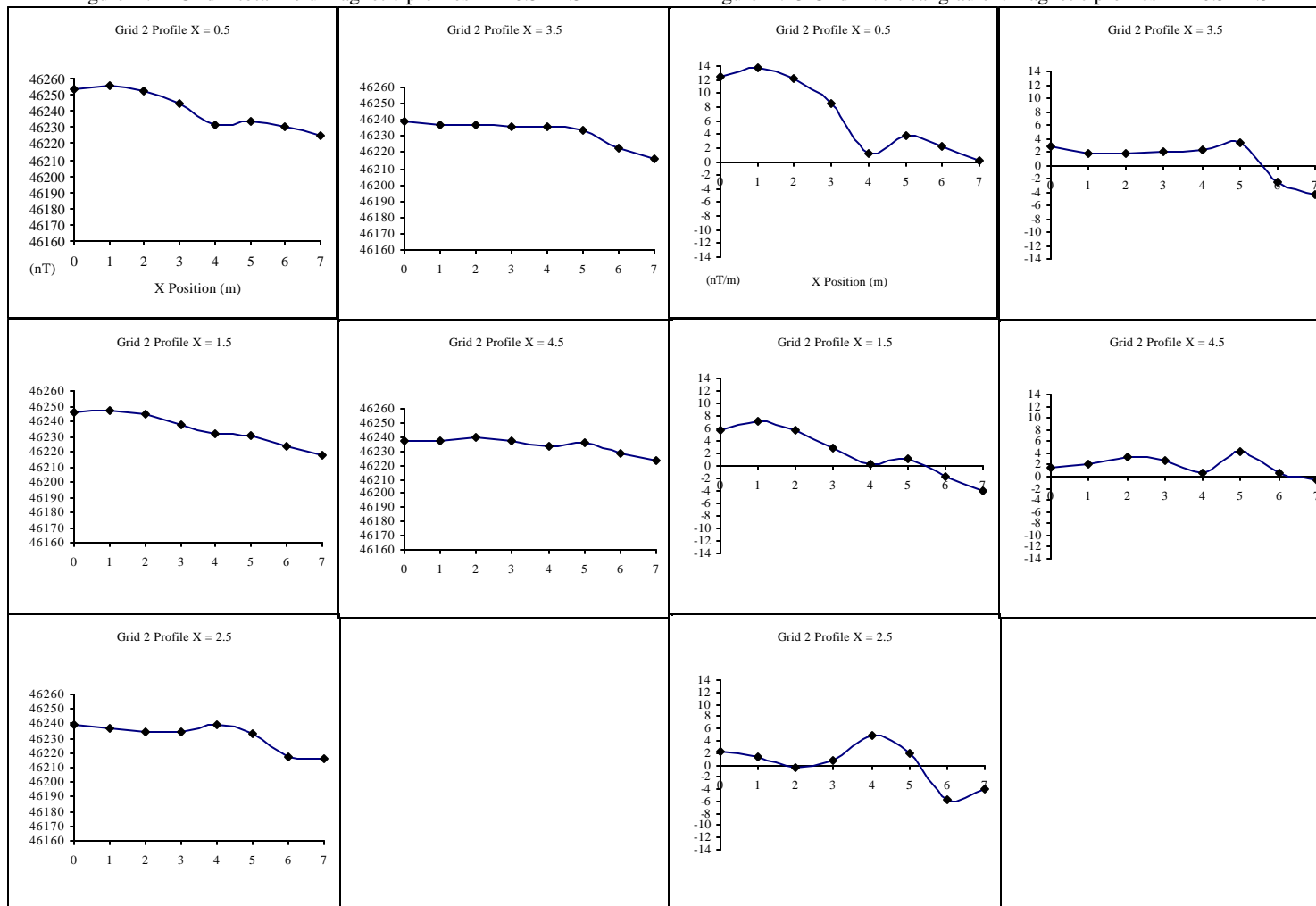
Figure A.14 Comparison of Correlograms for Pilot Signals Computed with 11 and 15 Samples
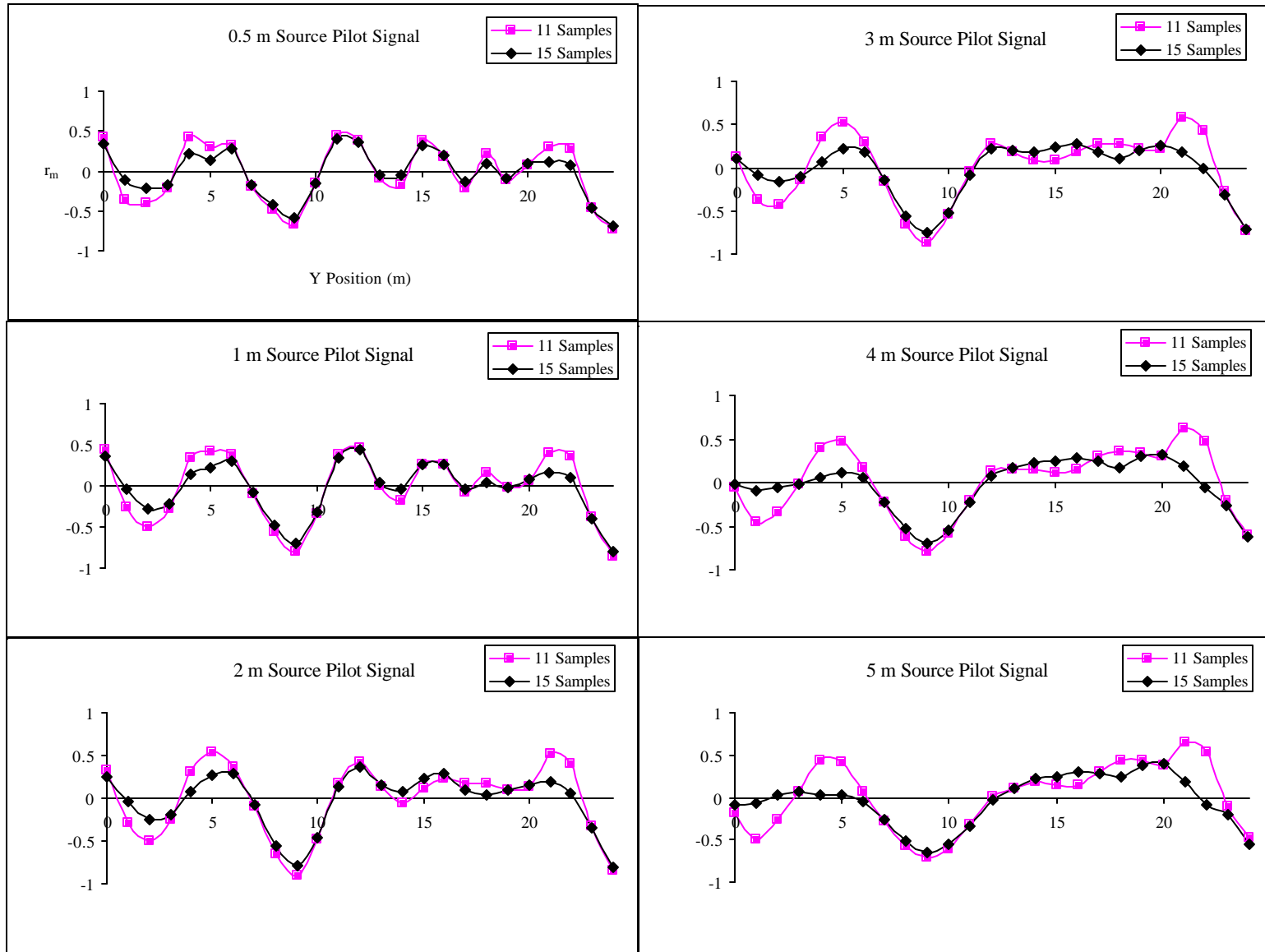
Figure A.15 Grid 4 peaks and troughs identified from the total field and vertical gradient cross-correlation analyses
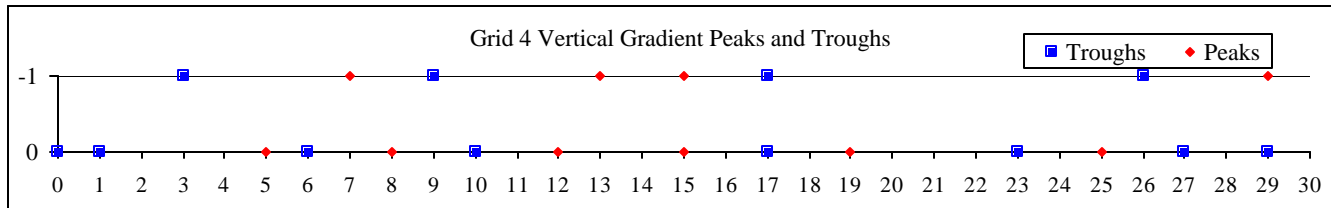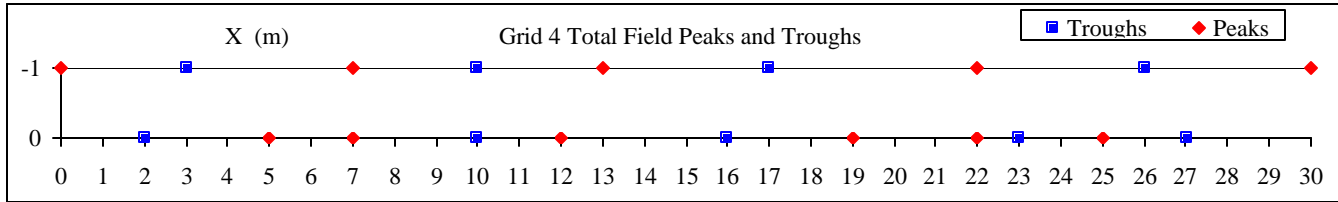
Figure A.16 Grid 4 peaks and troughs filtered by rm value (>0.5 or <-0.5) and (>0.8 or <-0.8)
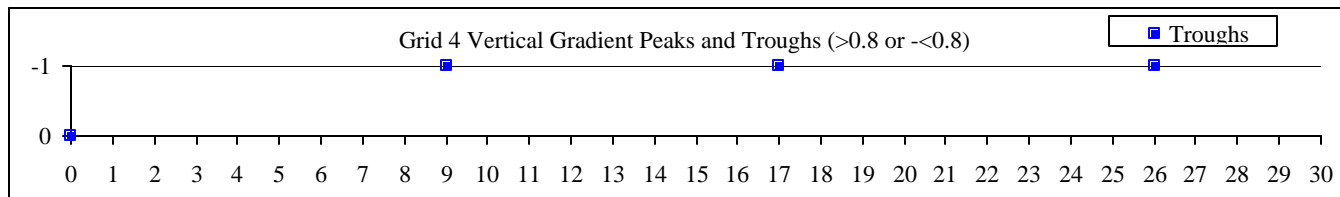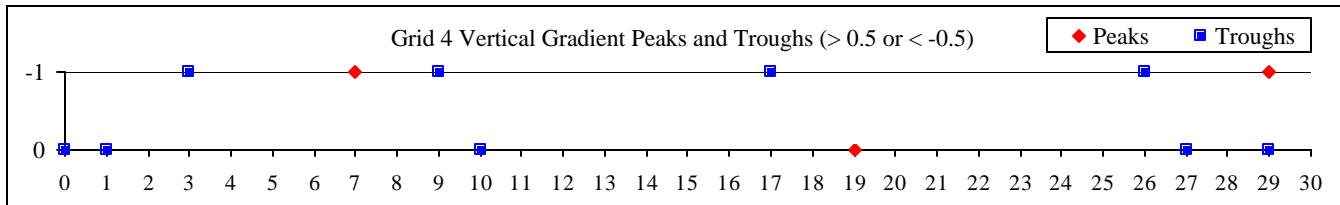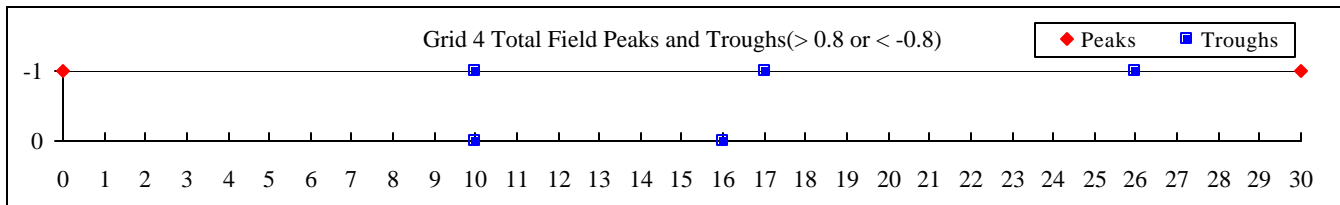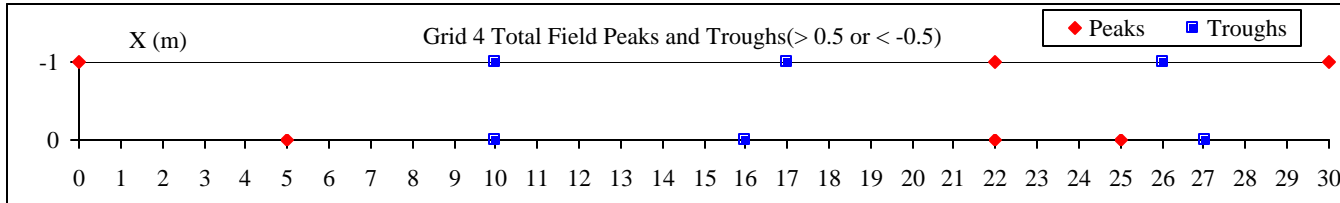
Figure A.17 Grid 4 peaks and troughs filtered by estimated depth (0.5 - 3 m) and (4 - 5 m)
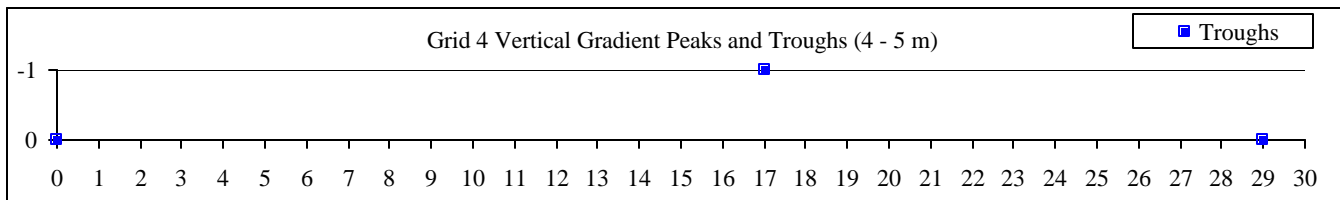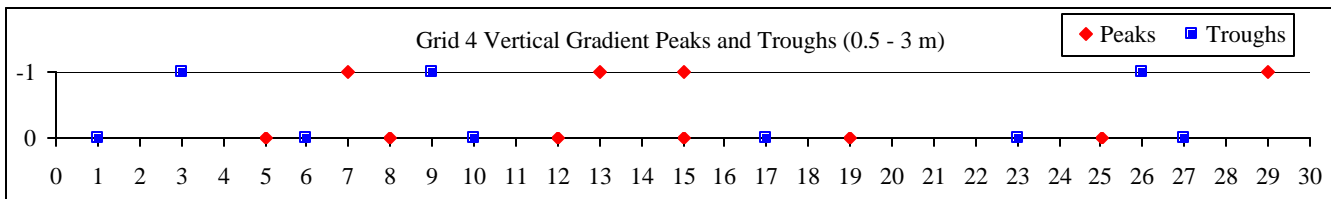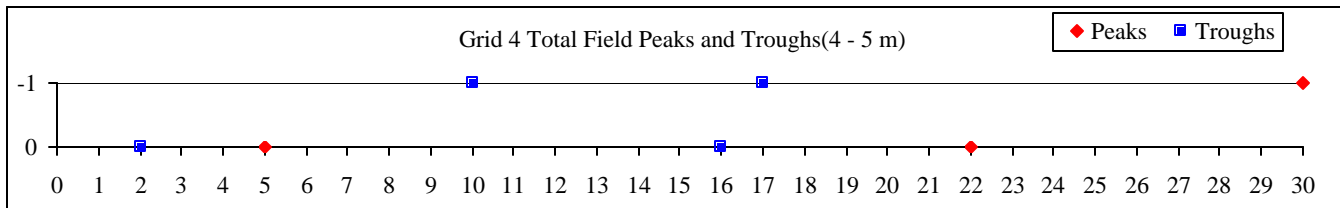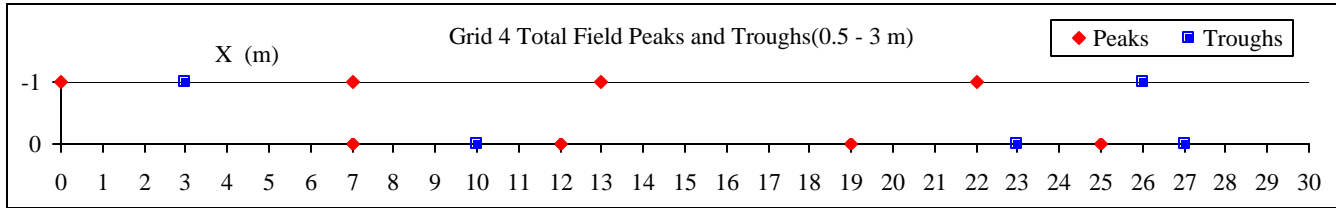
Figure A.18 Grid 5 peaks and troughs identified from the total field and vertical gradient cross-correlation analyses
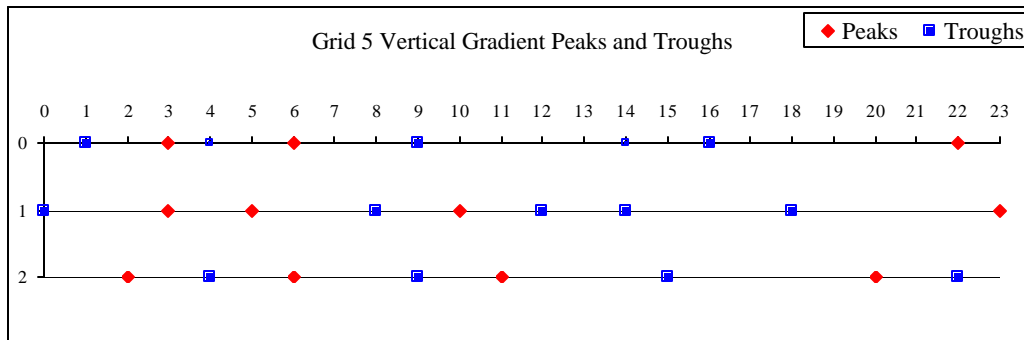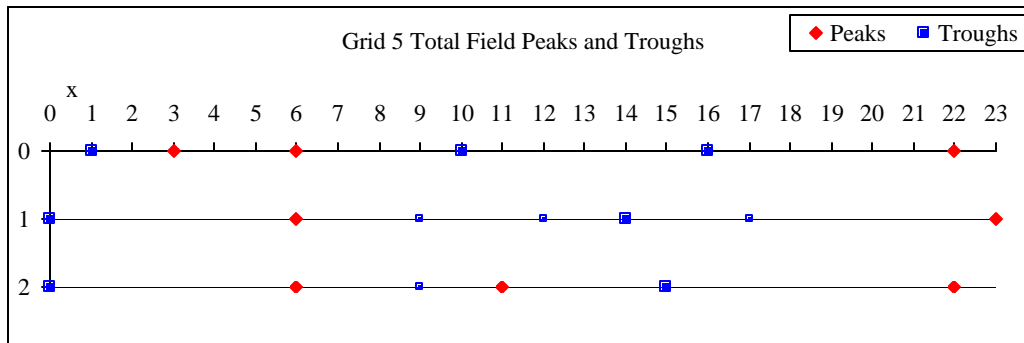
Figure A.19 Grid 5 peaks and troughs filtered by rm value (>0.5 or <-0.5) and (>0.8 or <-0.8)
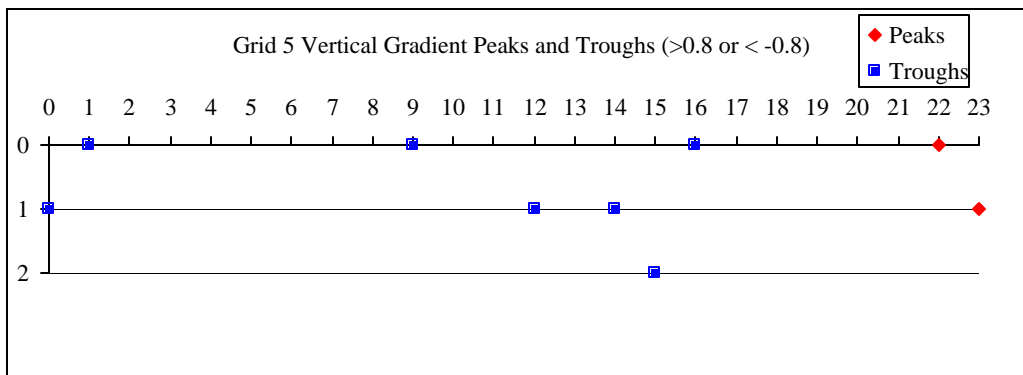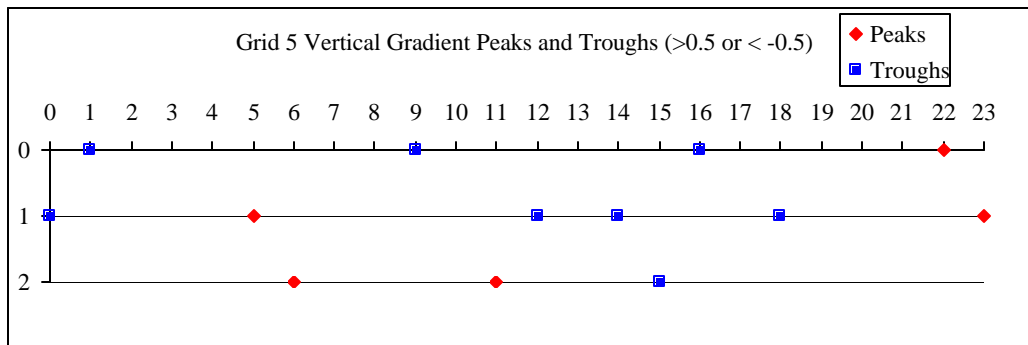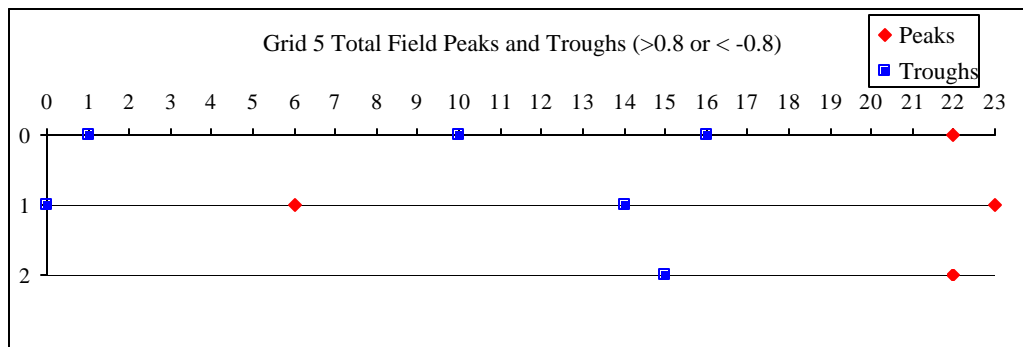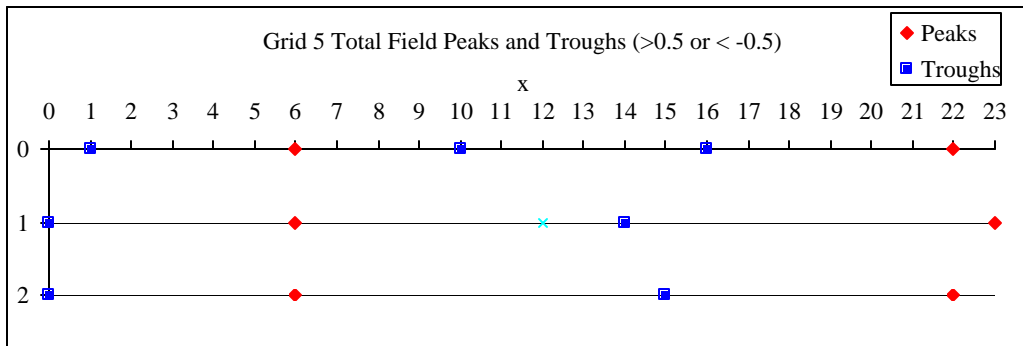
Figure A.20 Grid 5 peaks and troughs filtered by estimated depth (0.5 - 3 m) and (4 - 5 m)
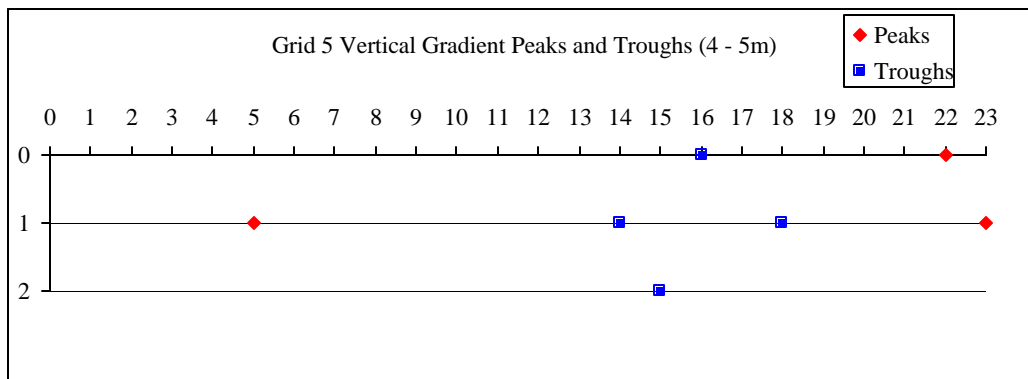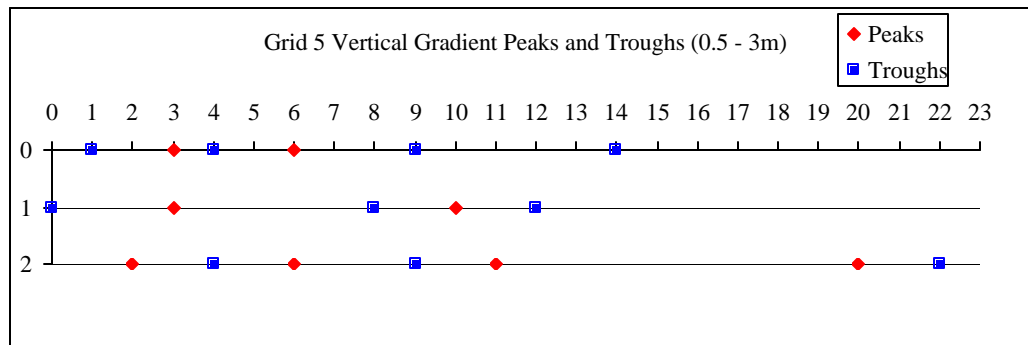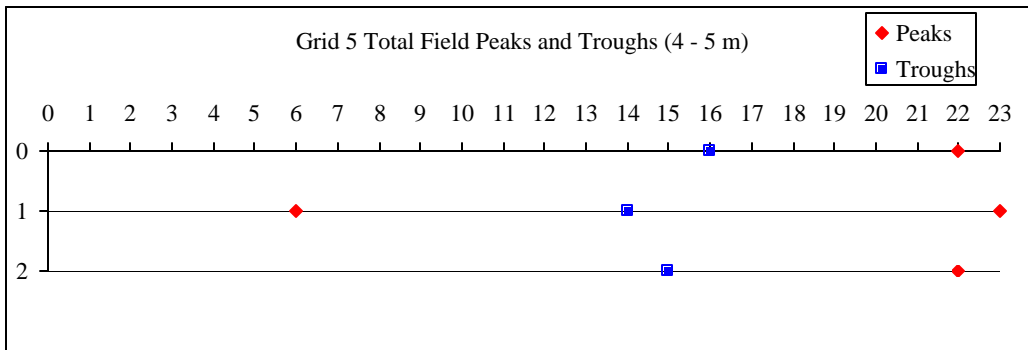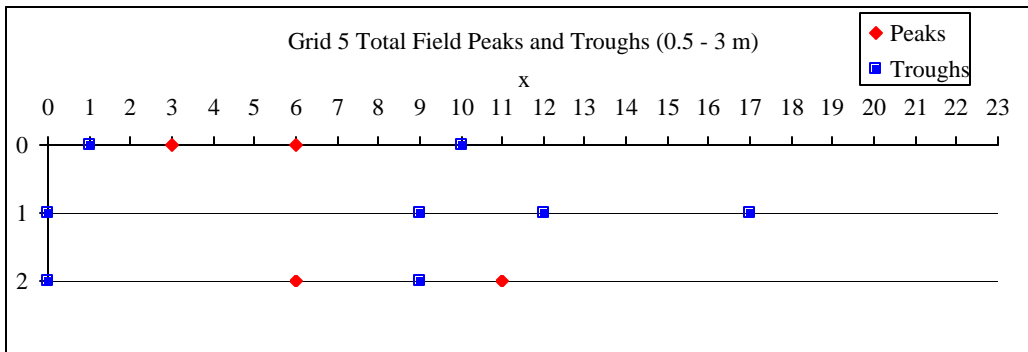
Figure A.21 Grid 1 peaks and troughs identified from the total field and vertical gradient cross-correlation analyses
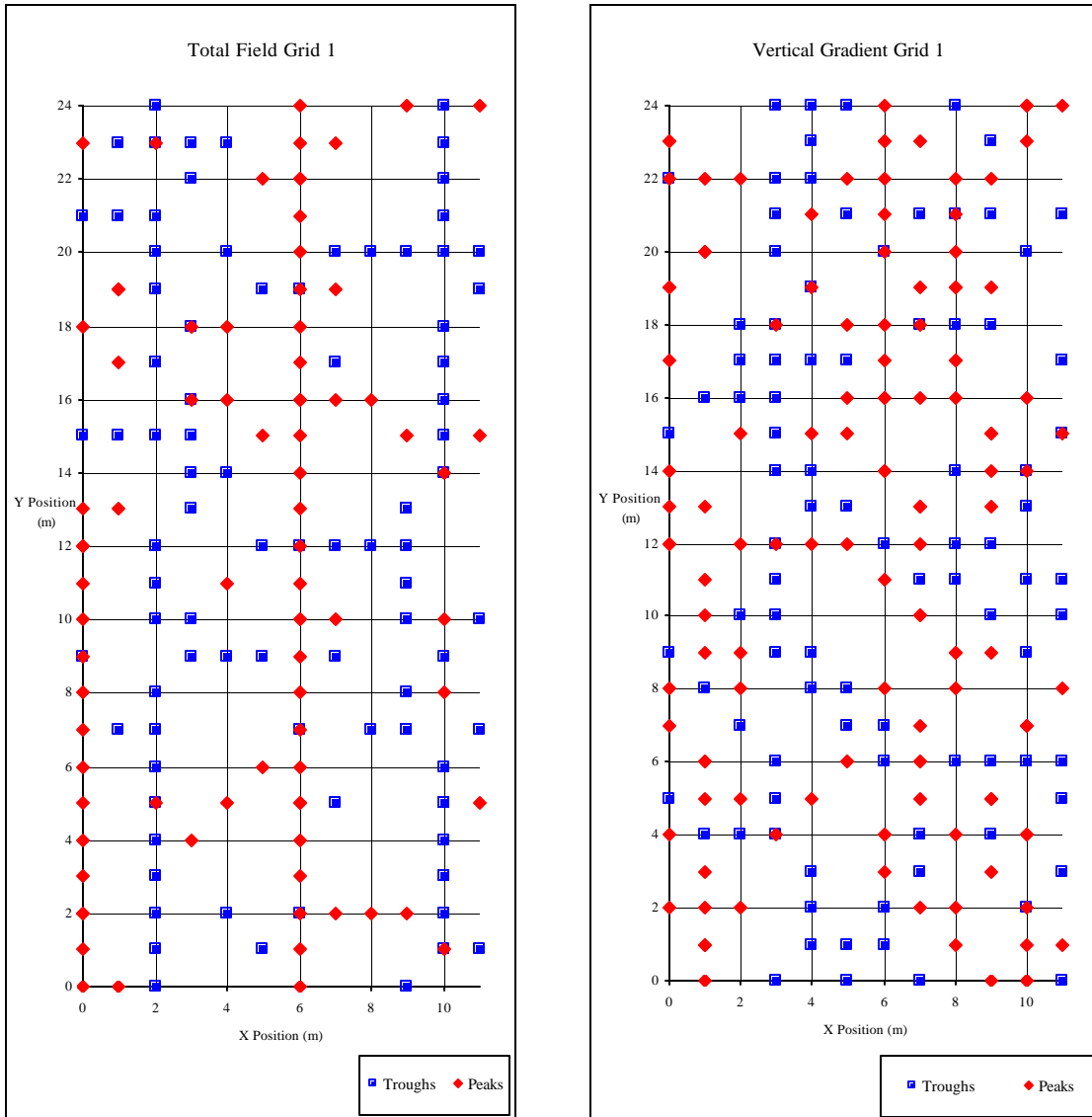
Figure A.22 Grid 1 peaks and troughs filtered by rm value (>0.5 or <-0.5)
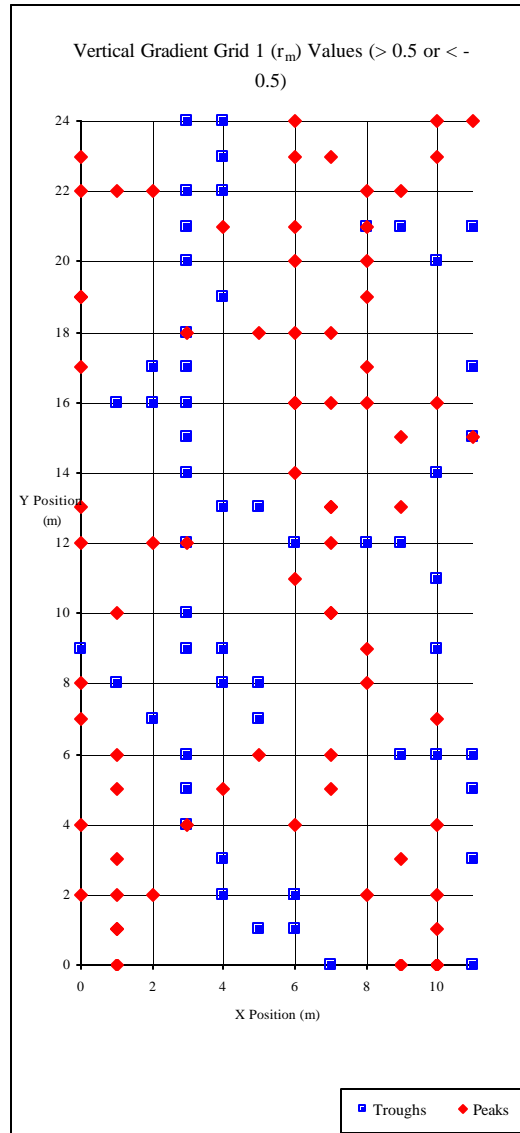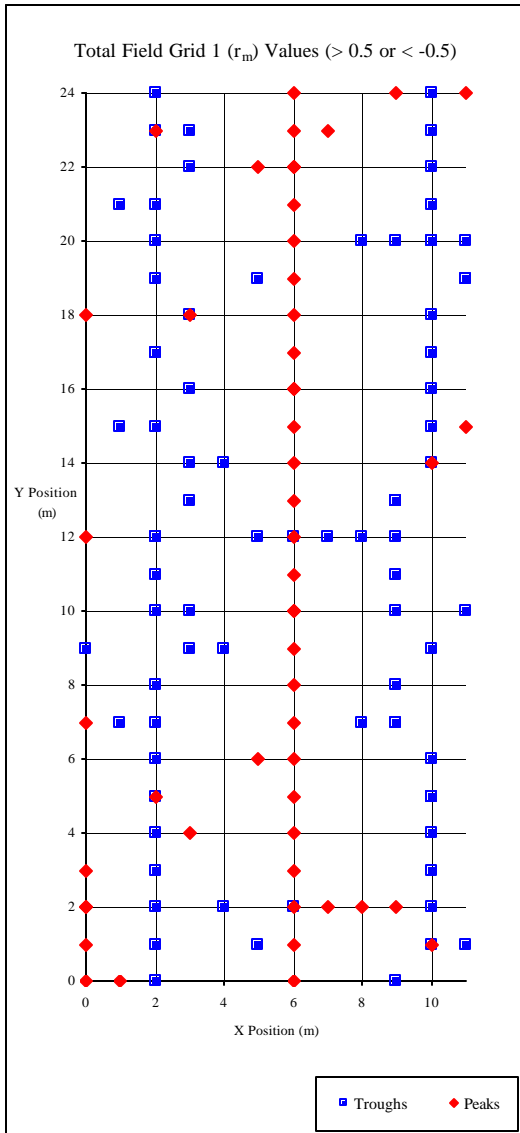
Figure A.23 Grid 1 peaks and troughs filtered by rm value (>0.8 or <-0.8)
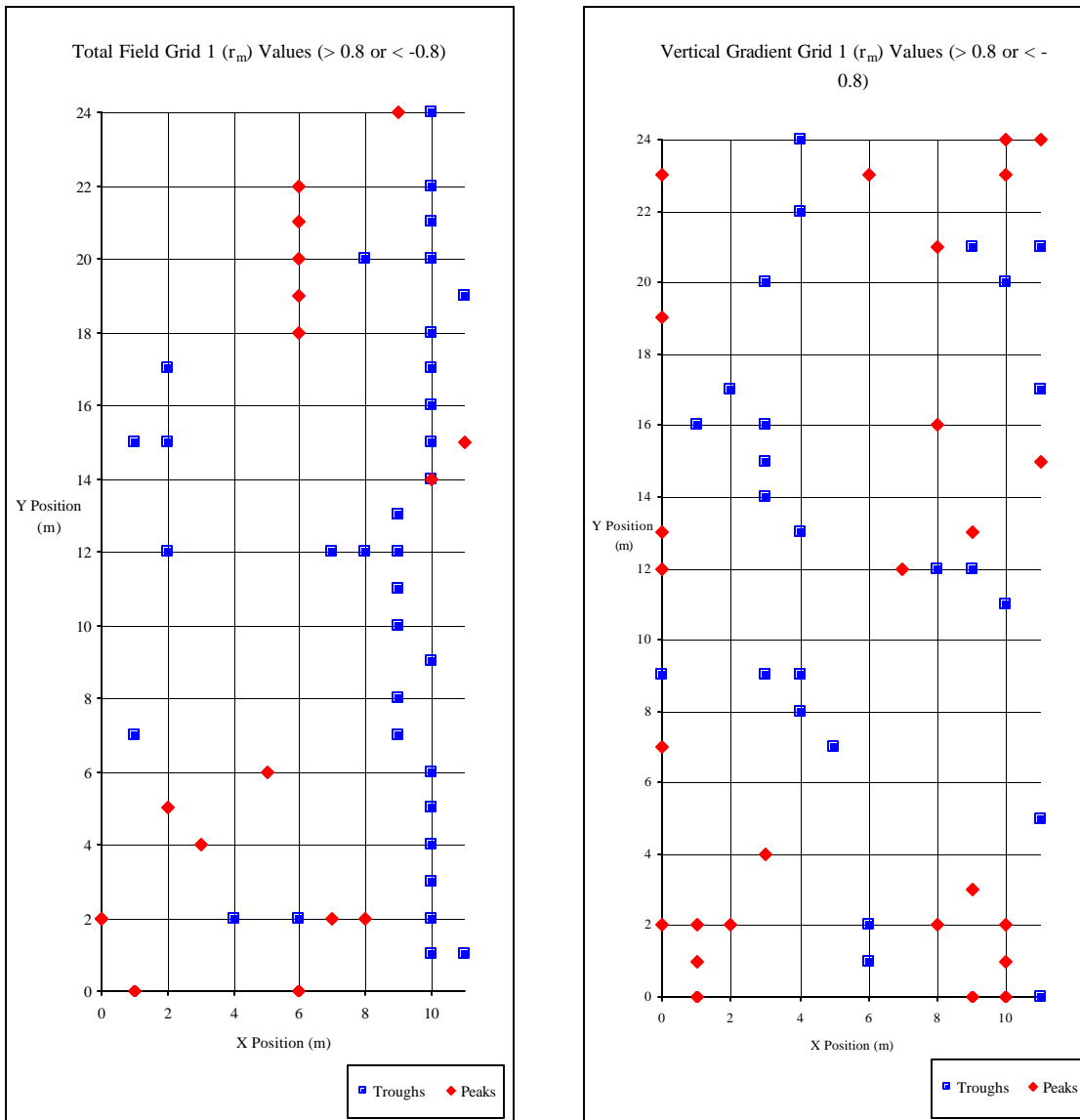
Figure A.24 Grid 1 peaks and troughs filtered by estimated depth (0.5 m)
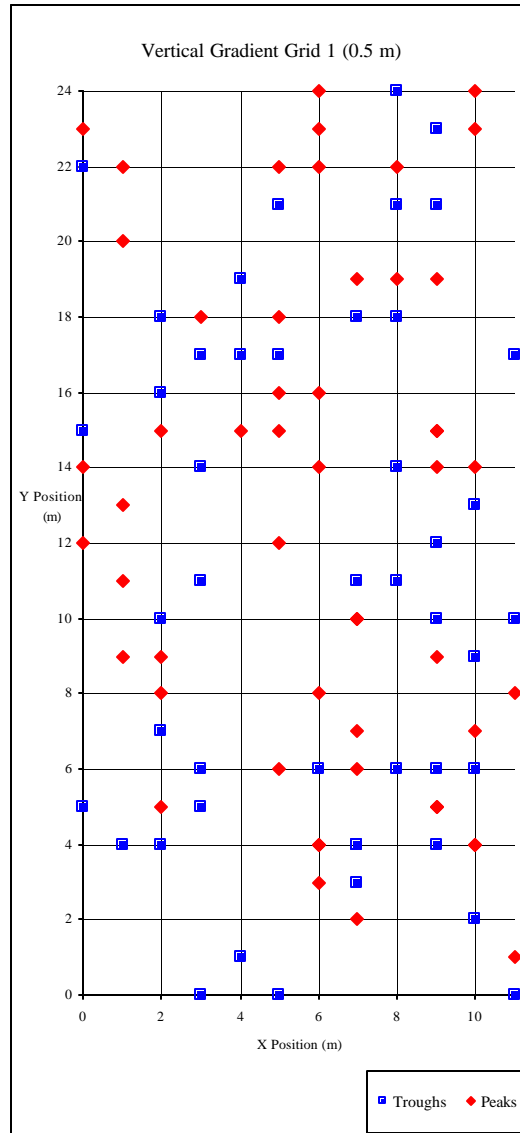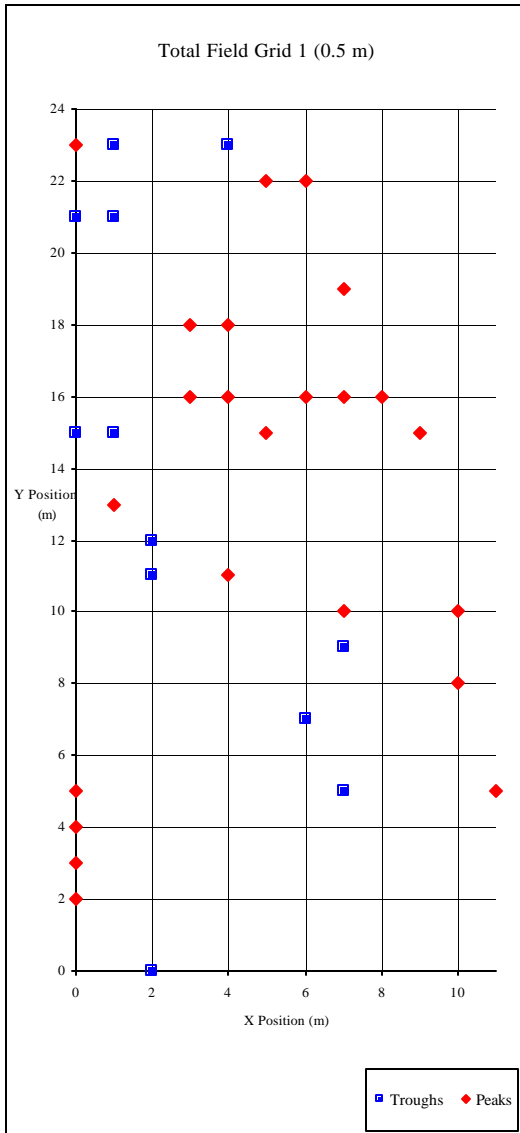
Figure A.25 Grid 1 peaks and troughs filtered by estimated depth (1 m)
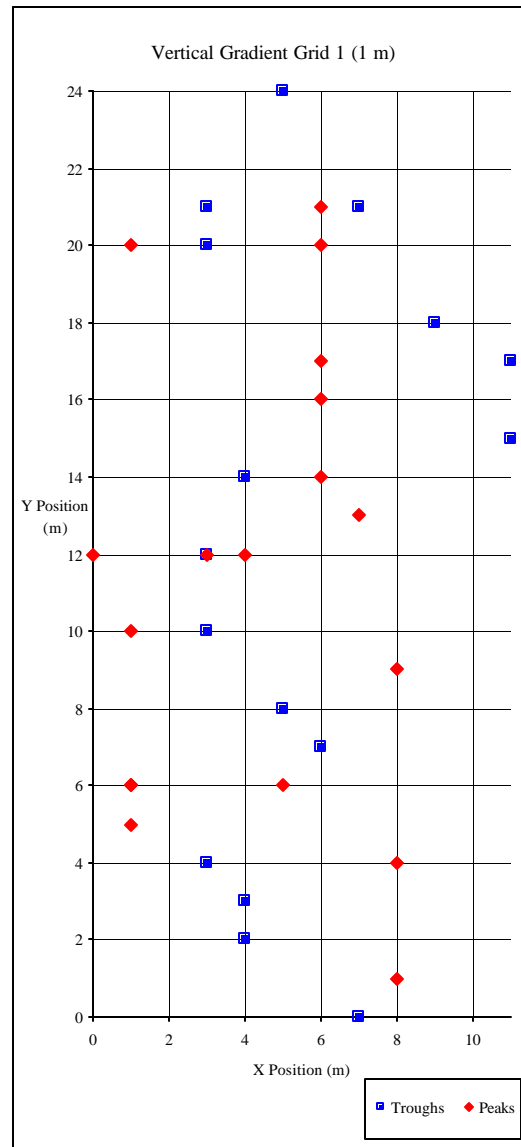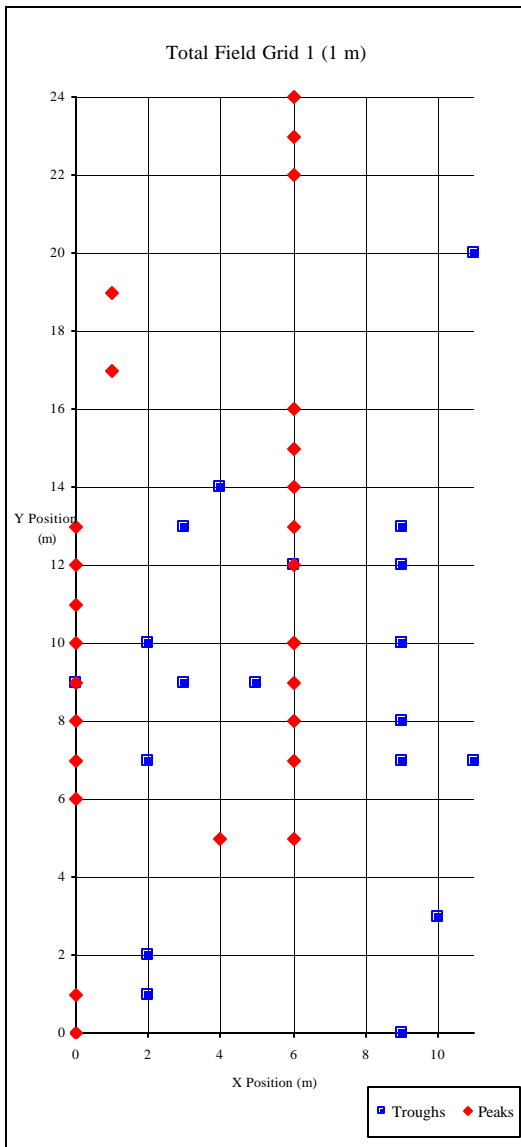
Figure A.26 Grid 1 peaks and troughs filtered by estimated depth (2 m)
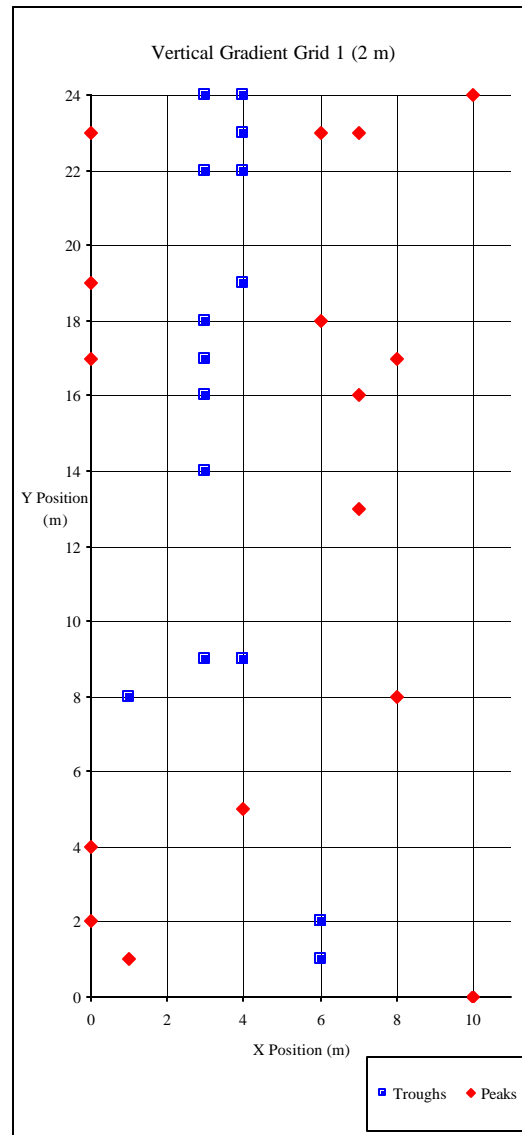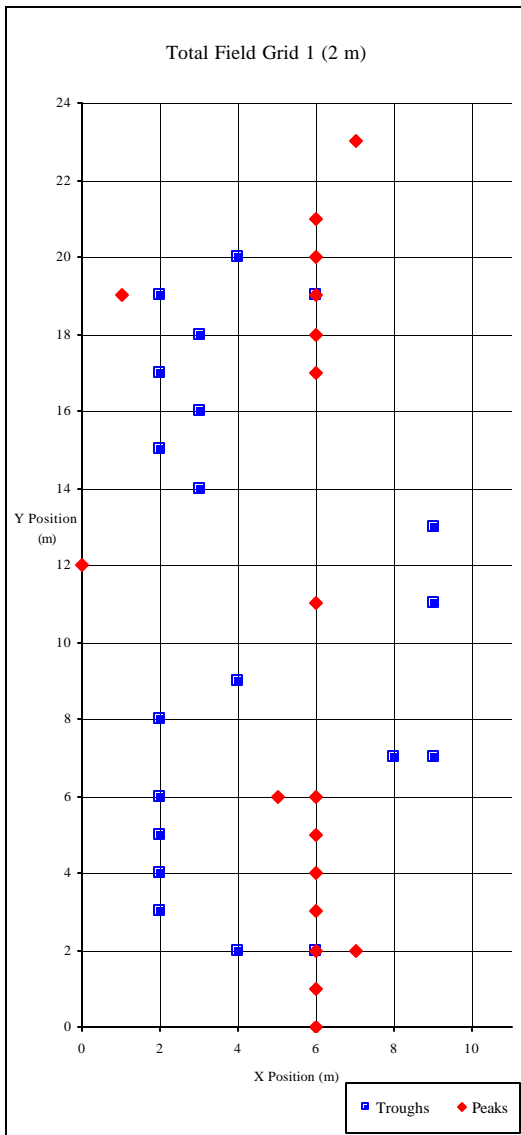
Figure A.27 Grid 1 peaks and troughs filtered by estimated depth (3 m)
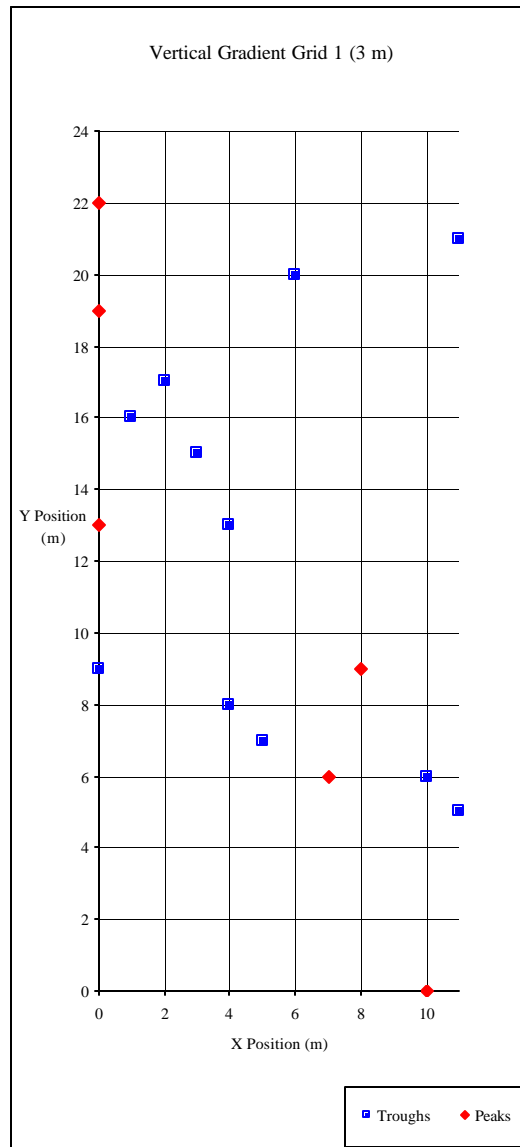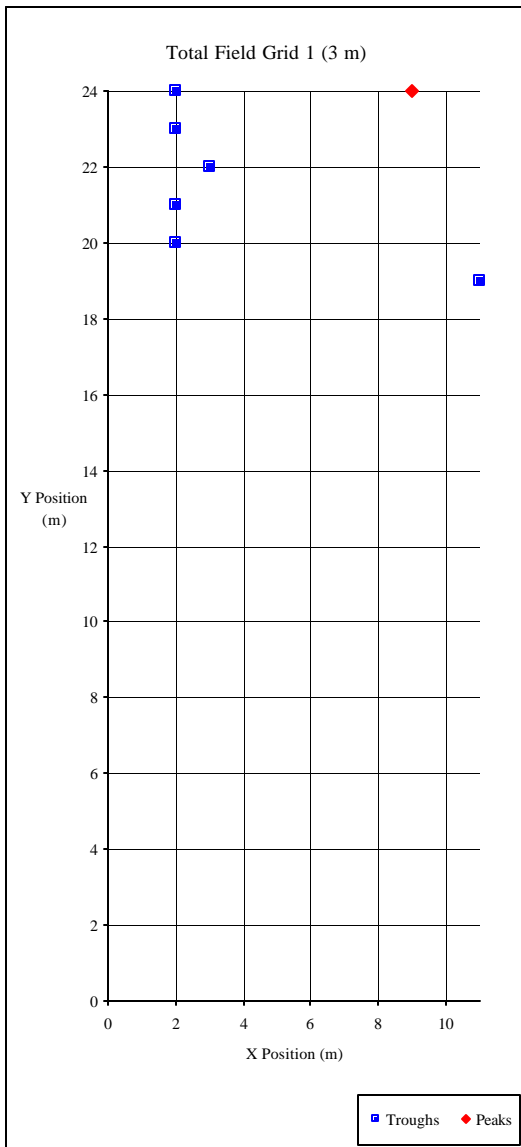
Figure A.28 Grid 1 peaks and troughs filtered by estimated depth (4 m)
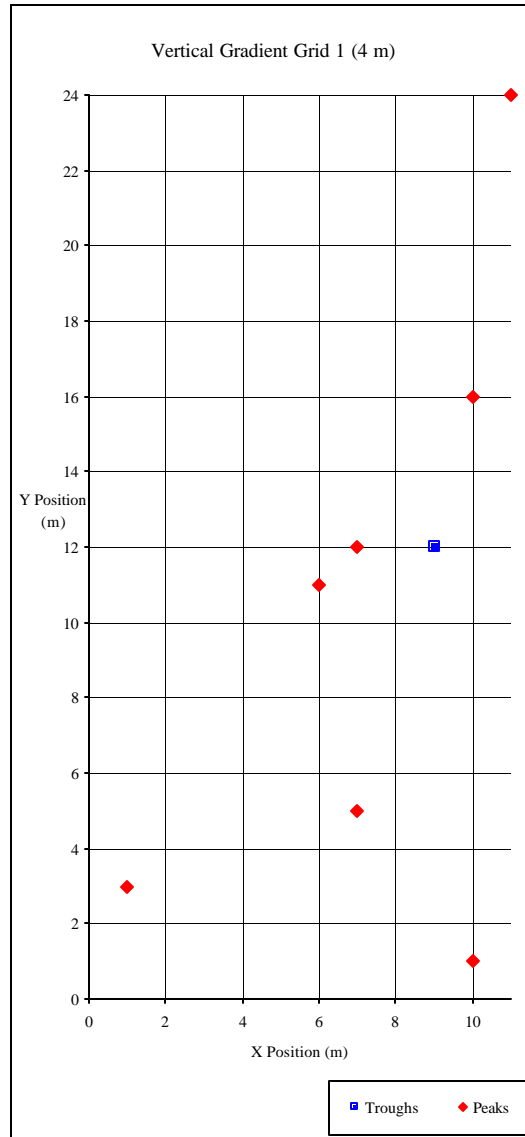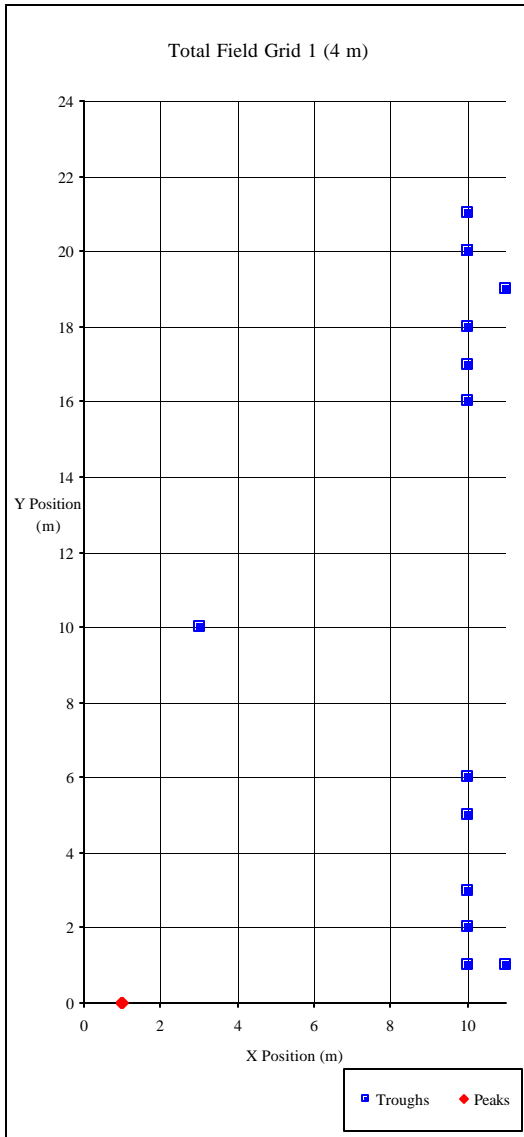
Figure A.29 Grid 1 peaks and troughs filtered by estimated depth (5 m)
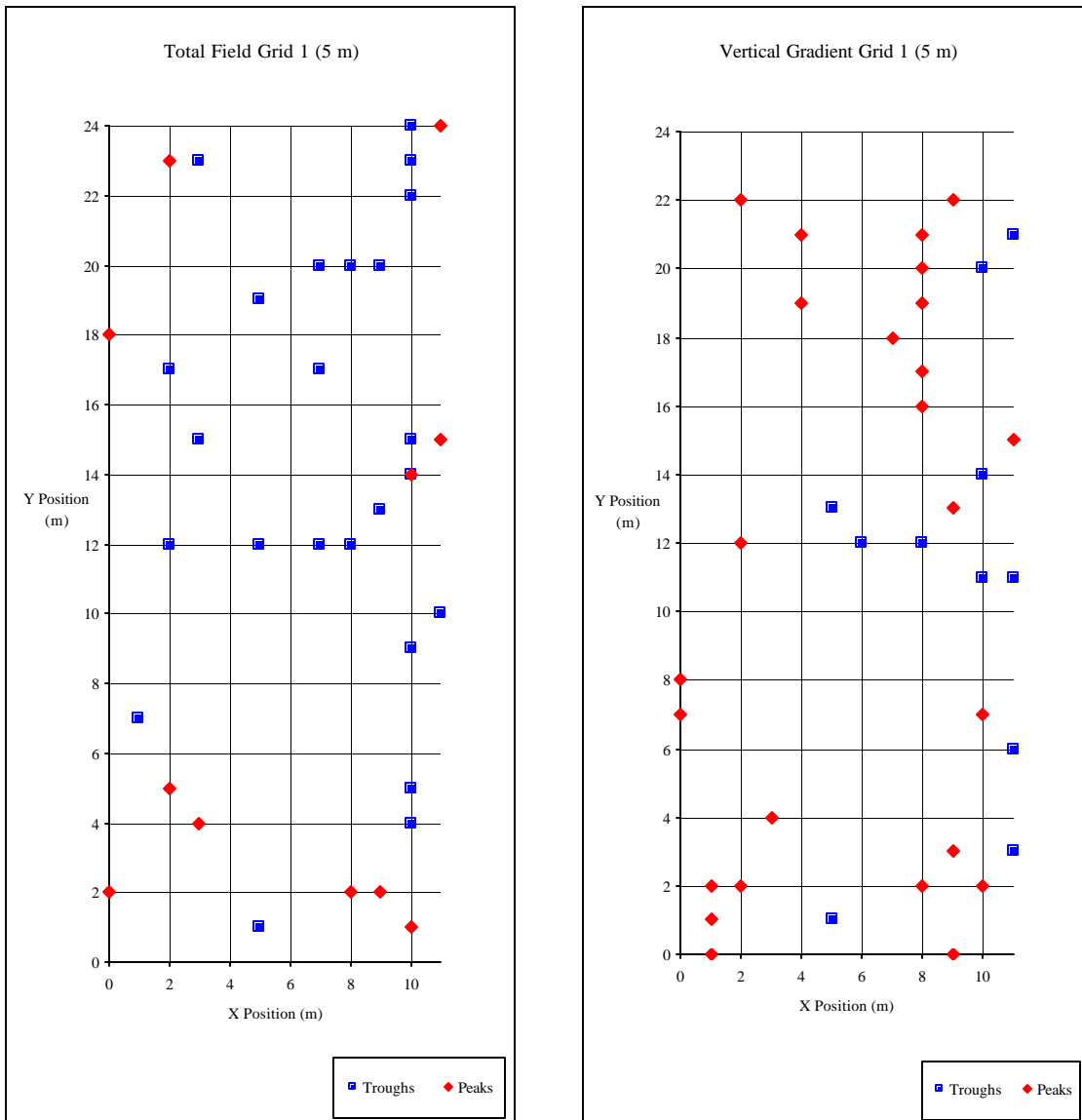
Figure A.30 Grid 1 peaks and troughs filtered by estimated depth (0.5 - 3 m)
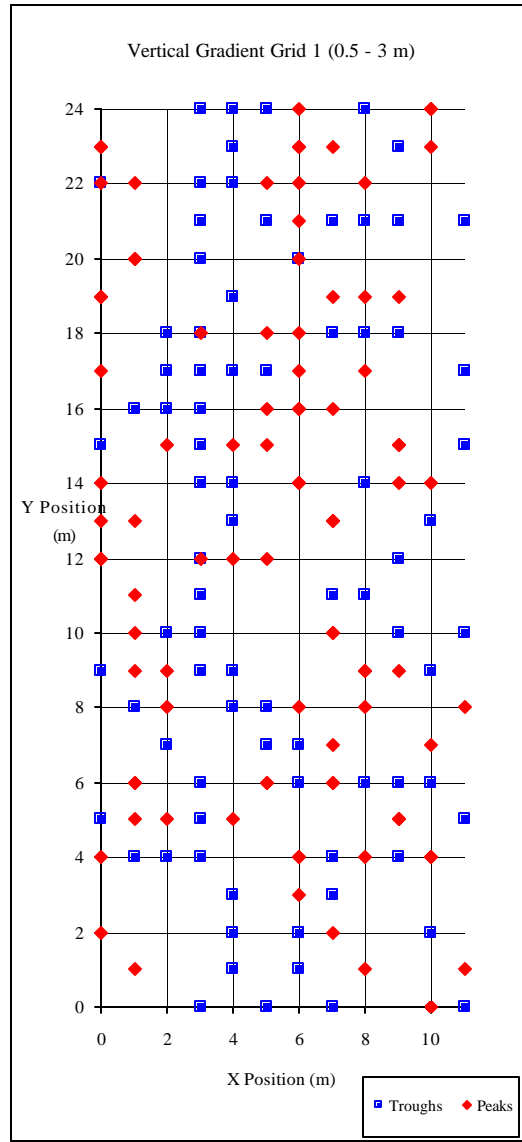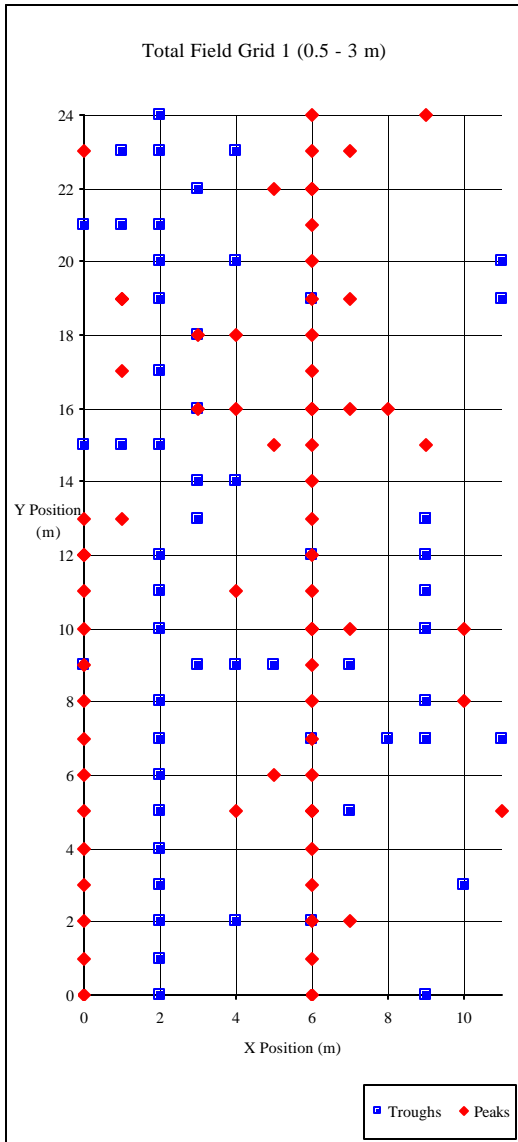
Figure A.31 Grid 1 peaks and troughs filtered by estimated depth (4 - 5 m)

Figure A.32 Grids 1, 4 and 5 Total Field Cross-Correlation Peaks and Troughs

Figure A.33 Grid 1, 4 and 5 Vertical Gradient Cross-Correlation Peaks and Troughs
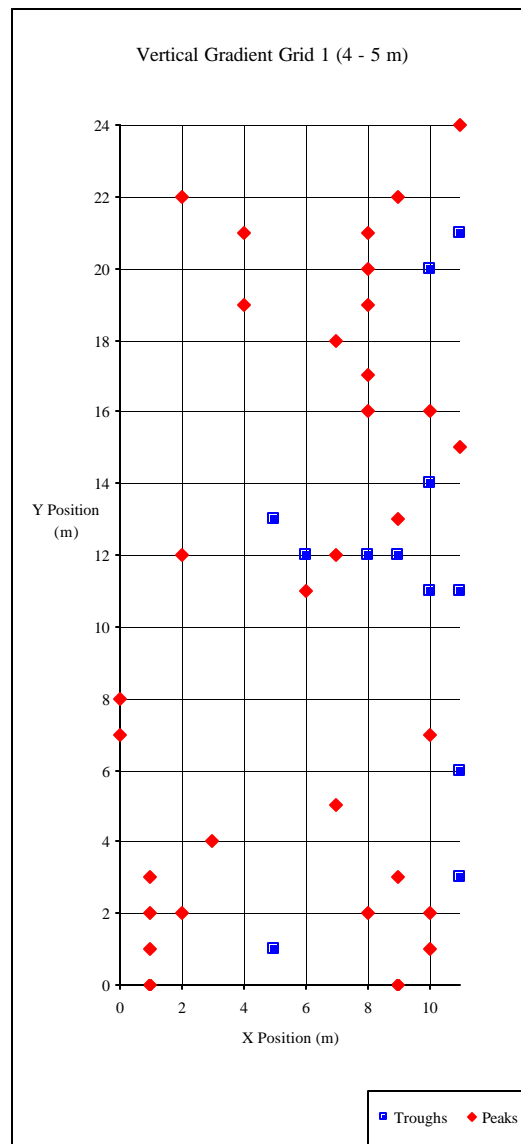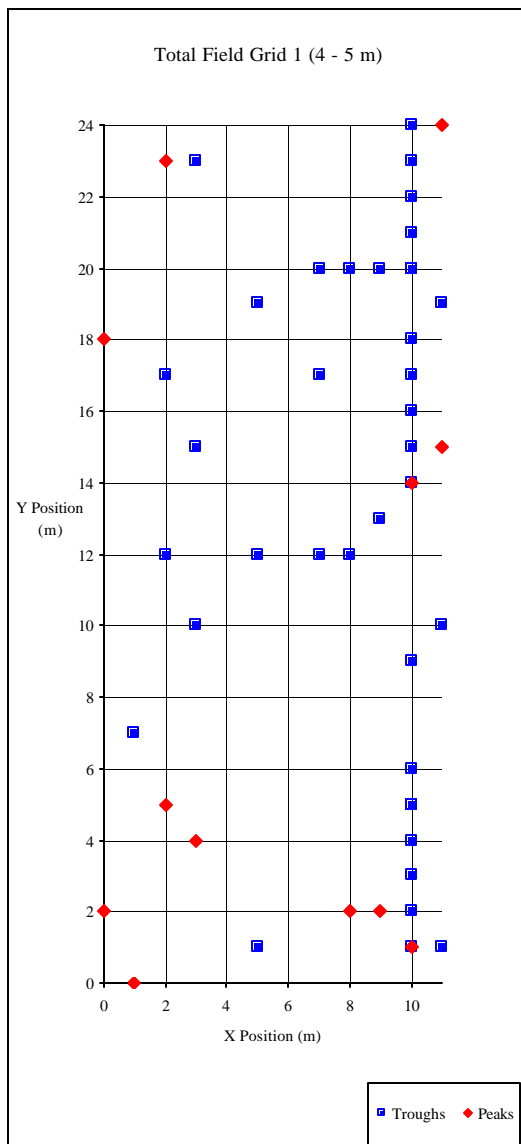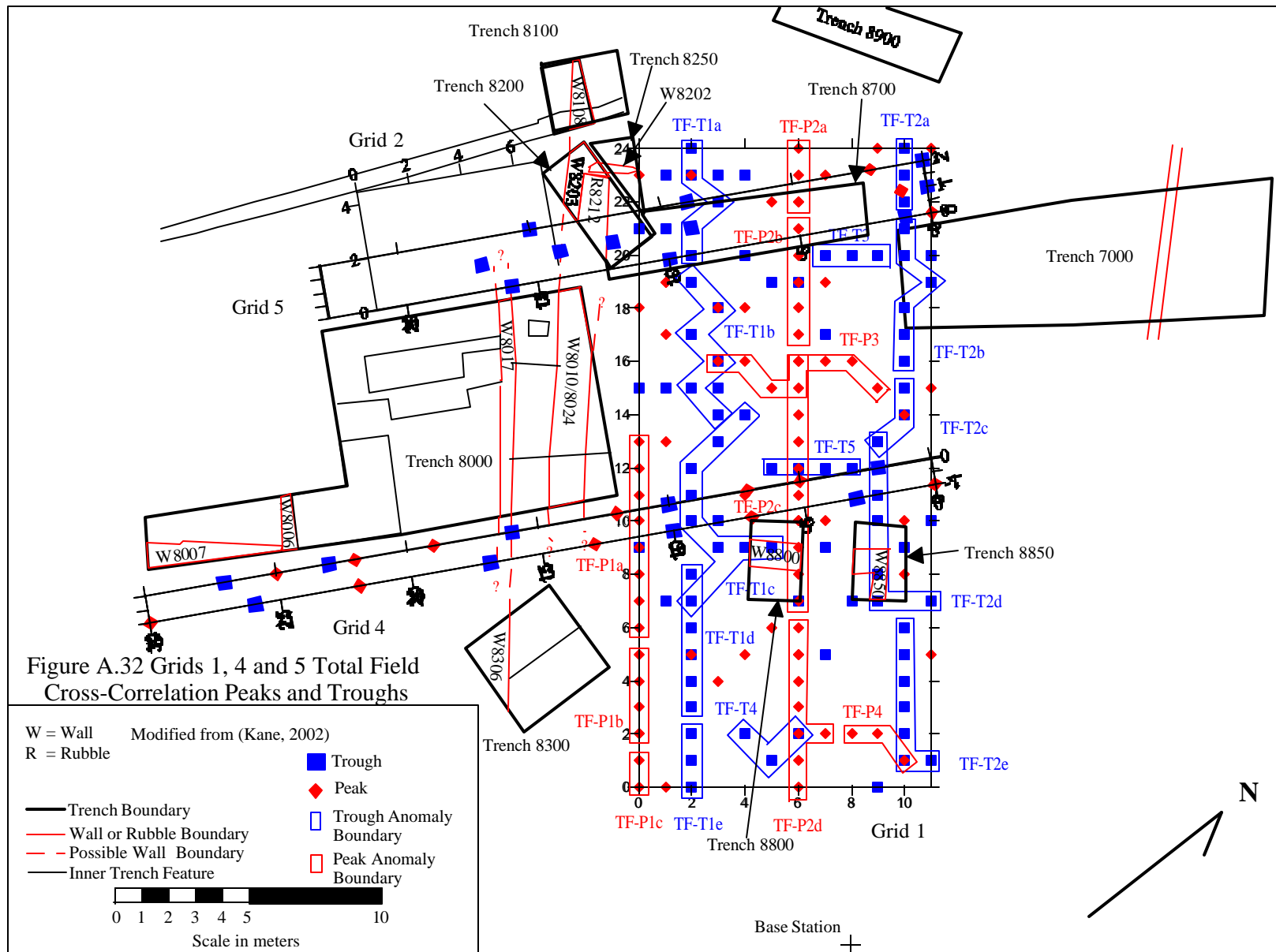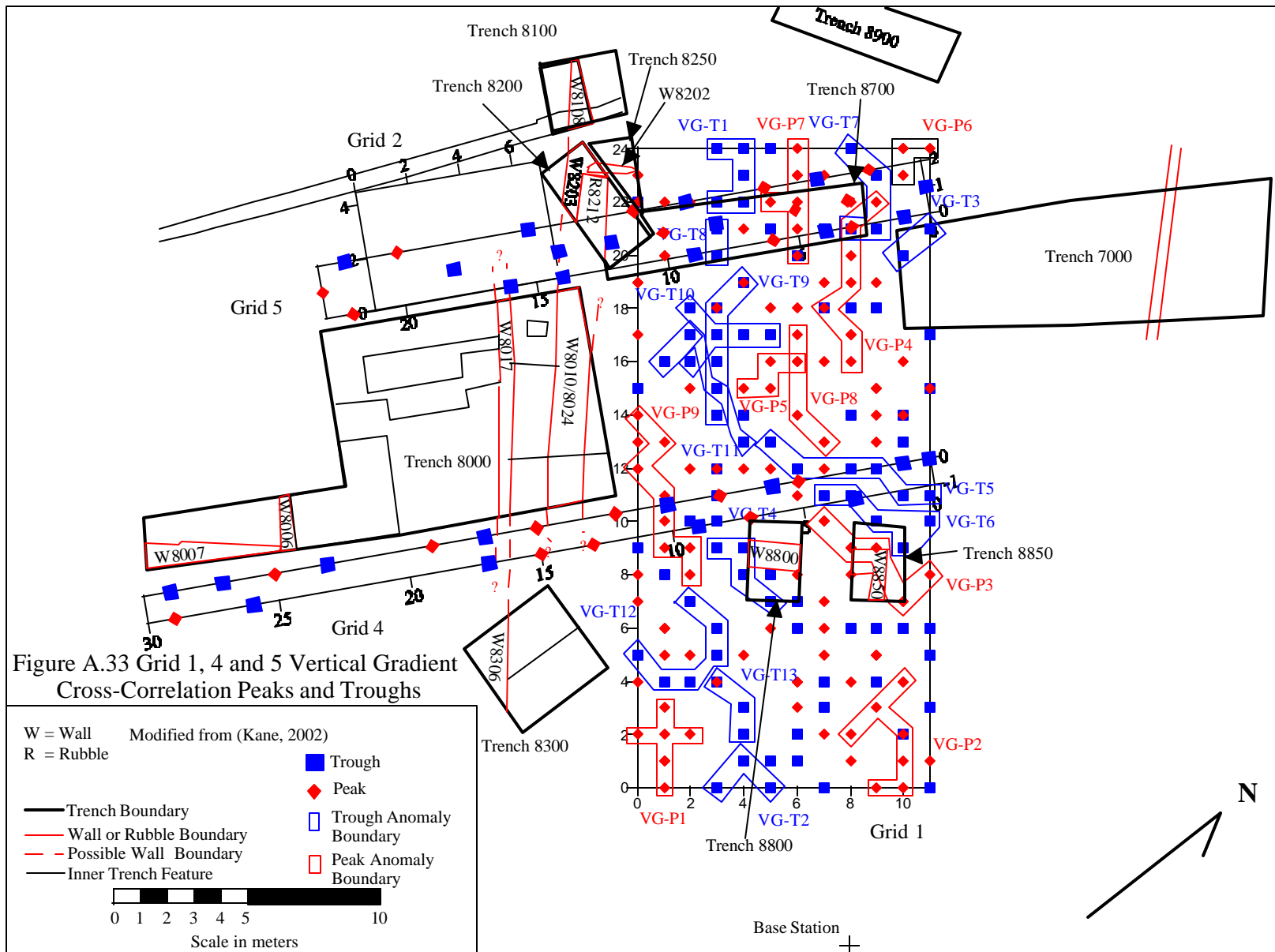
Figure A.34 Grid 4 total field magnetic profiles Y = -1 - 0 m   Figure A.35 Grid 4 vertical gradient magnetic profiles Y = -1 - 0 m
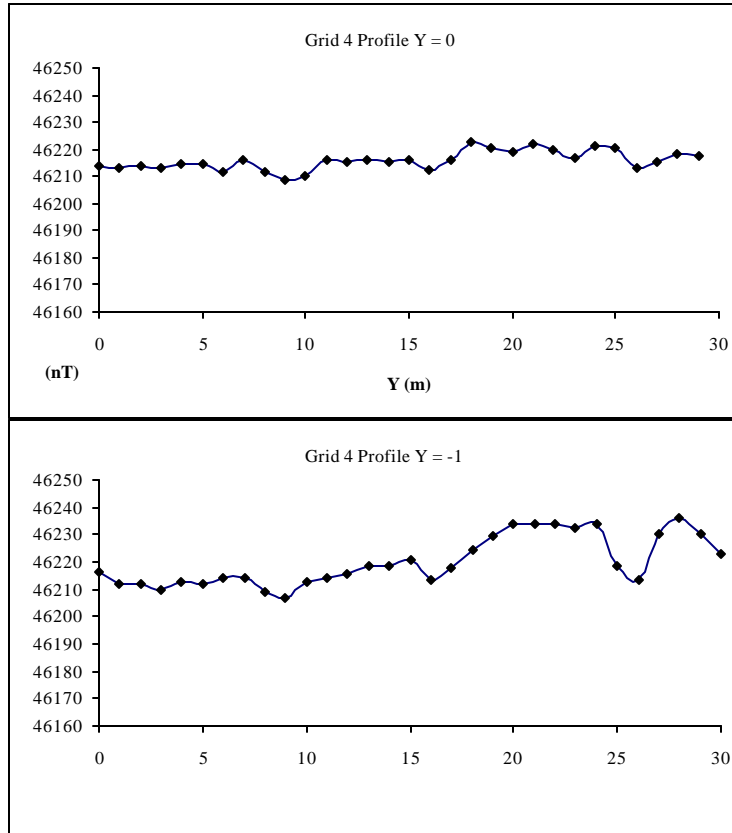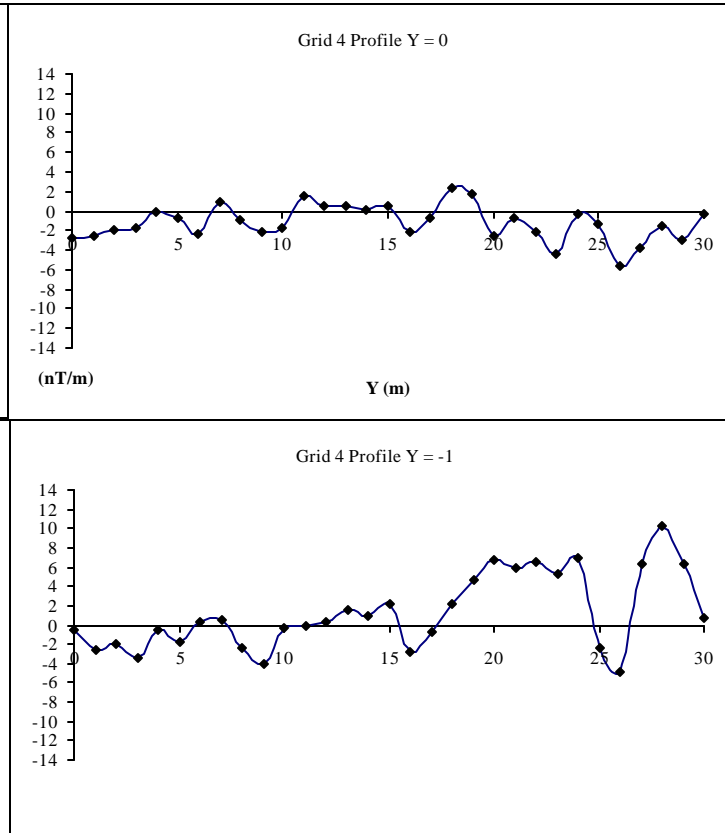
Figure A.36 Grid 5 total field magnetic profiles Y =0 - 2 m   Figure A.37 Grid 5 vertical gradient magnetic profiles Y = 0 - 2 m

Grid 5 Profile Y = 0

Grid 5 Profile Y = 0

Grid 5 Profile Y = 1

Grid 5 Profile Y = 1

Grid 5 Profile Y = 2

Grid 5 Profile Y = 2
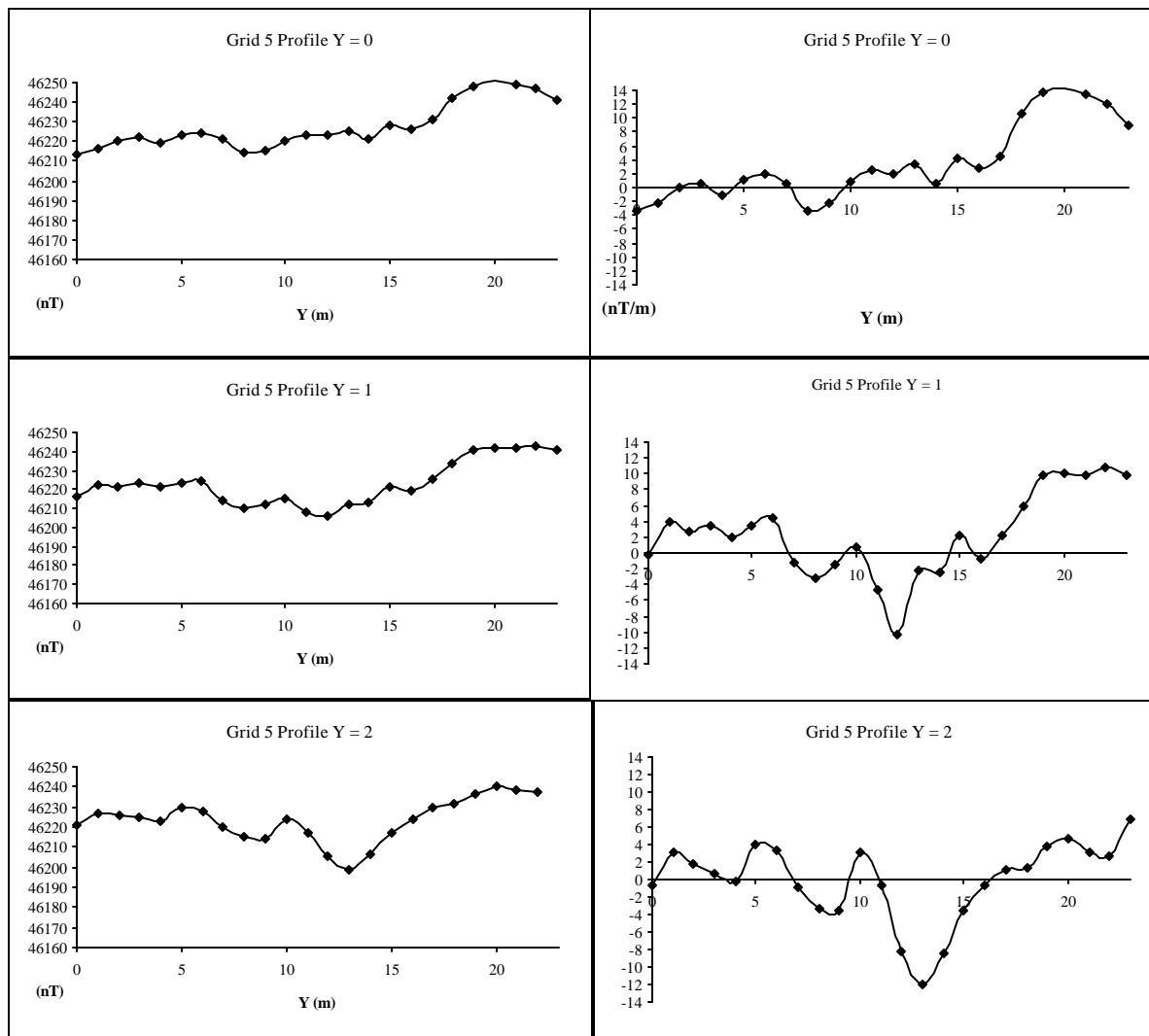
APPENDIX B

MONTE PALLANO GPR RADARGRAMS AND TIMESLICES

Trench 8100

Trench 8200

W8108

W8203

R8212

E8203

Trench 7000

W8017

W8010/8024

Trench 8000

W8006

W8007

Figure B.1 Grid 1 GPR
Disturbance Locations

W8306

Trench 8300

W = Wall   Modified from (Kane, 2002)
R = Rubble

● Grid 1a GPR
  Disturbances

◆ Grid 1b GPR
  Disturbances

——— Trench Boundary
——— Wall or Rubble Boundary
– – – Possible Wall Boundary
——— Inner Trench Feature

0 1 2 3 4 5   10
          Scale in meters

N

Figure B.2 Grid 1a Radargrams for X = 0 to 3.5 m
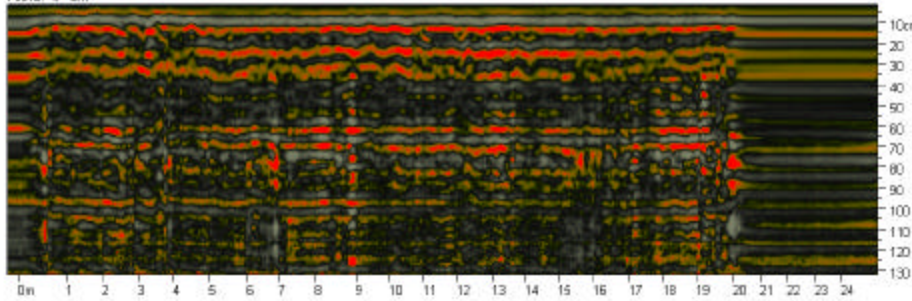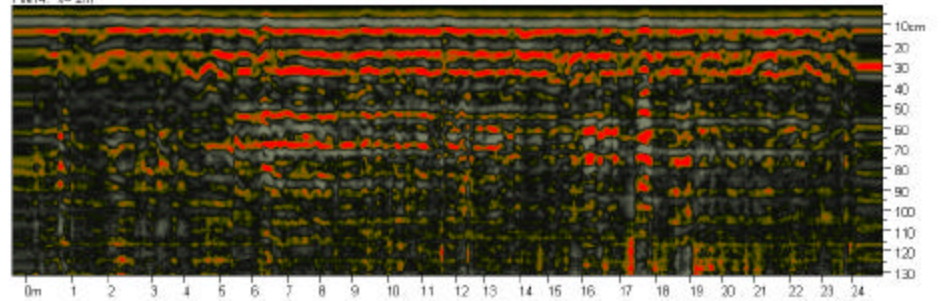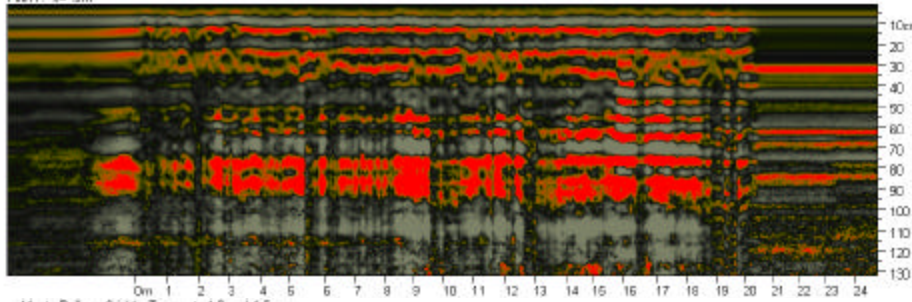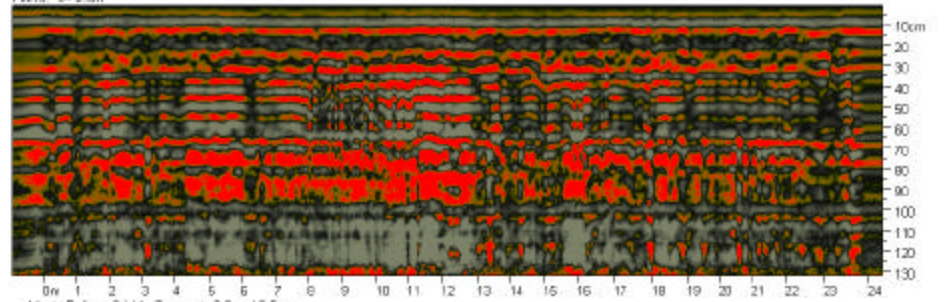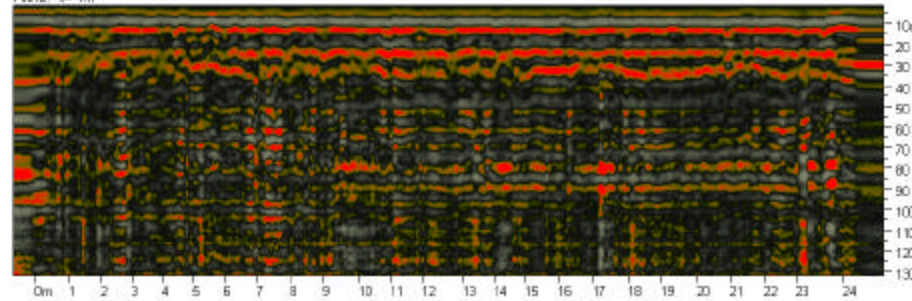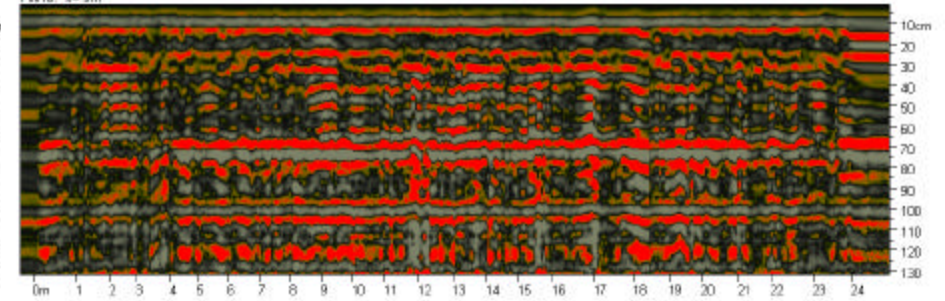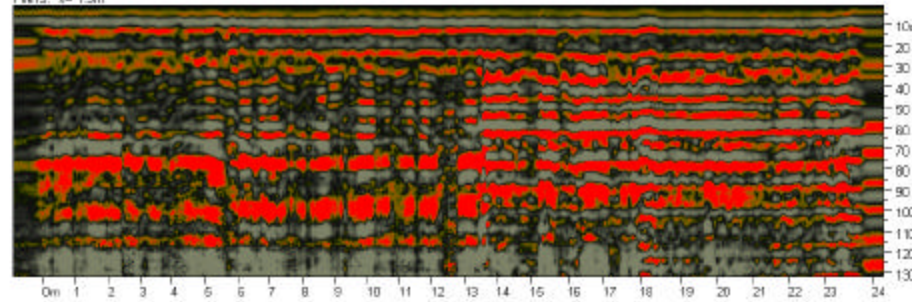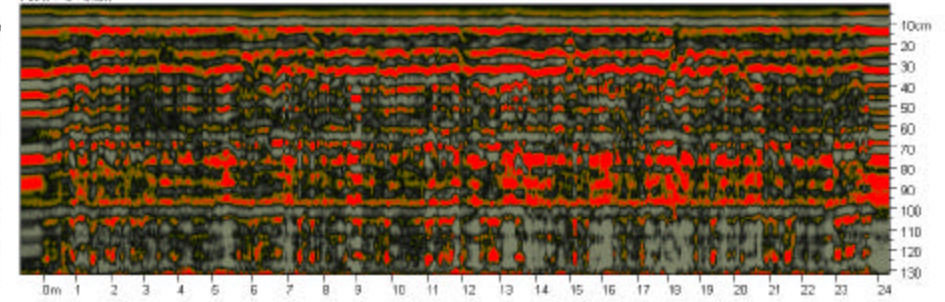
Figure B.3 Grid 1a Radargrams for X = 4 to 7.5 m
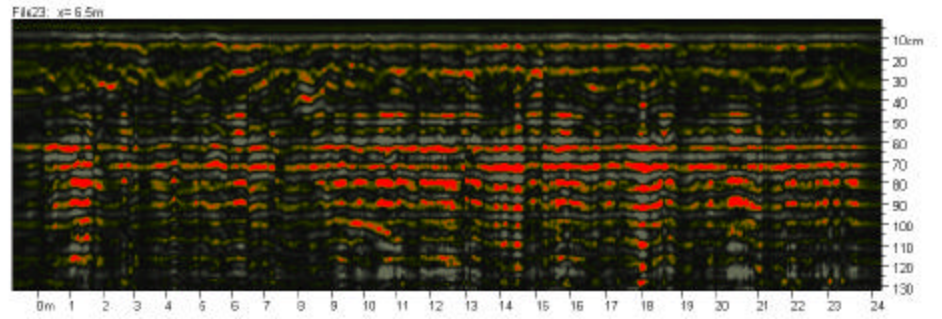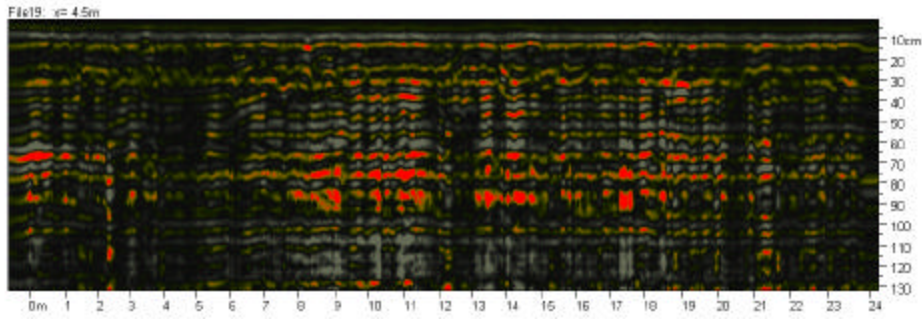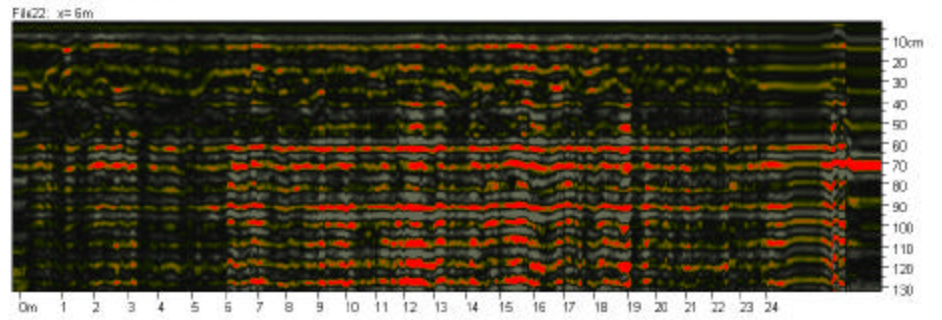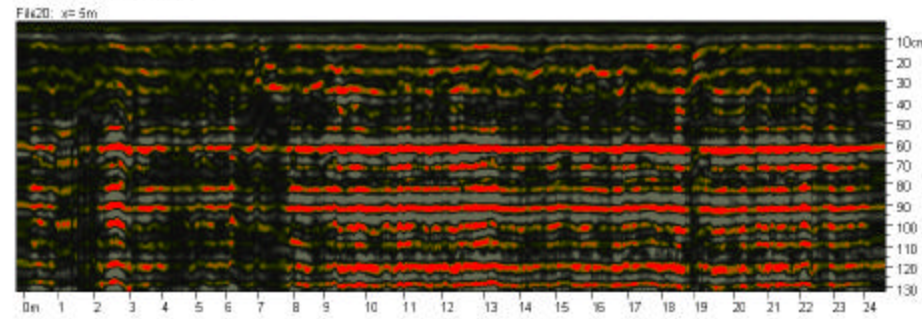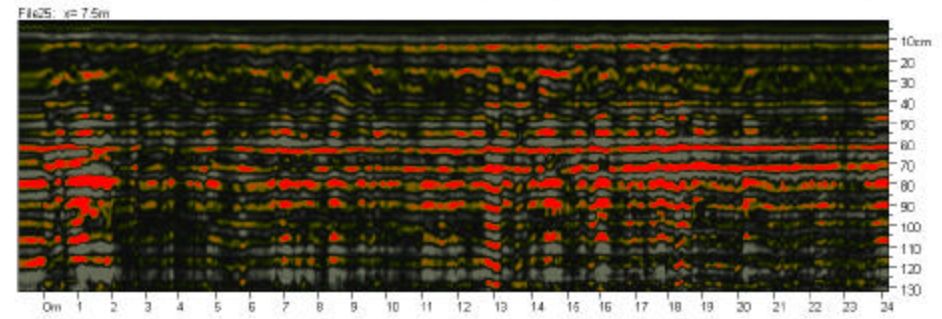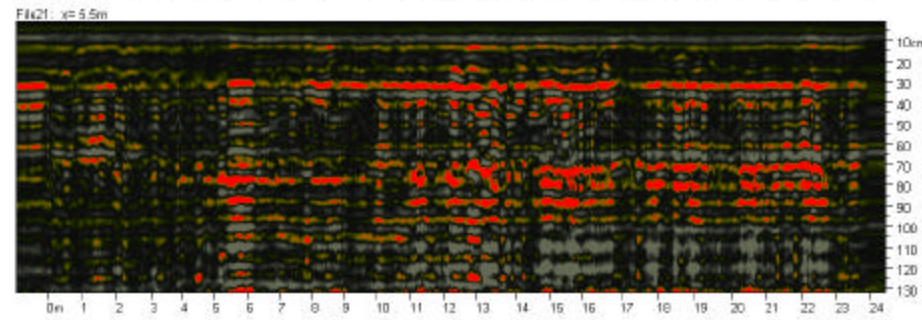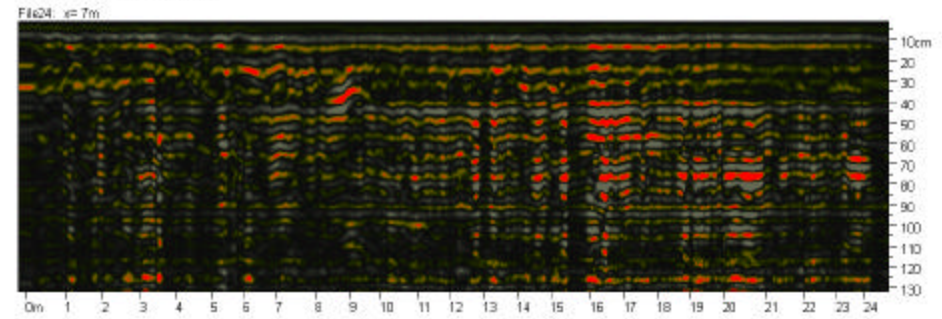
Figure B.4 Grid 1a Radargrams for X = 8 to 11 m
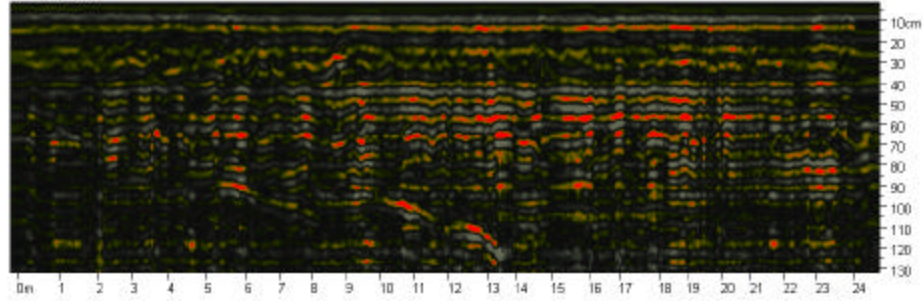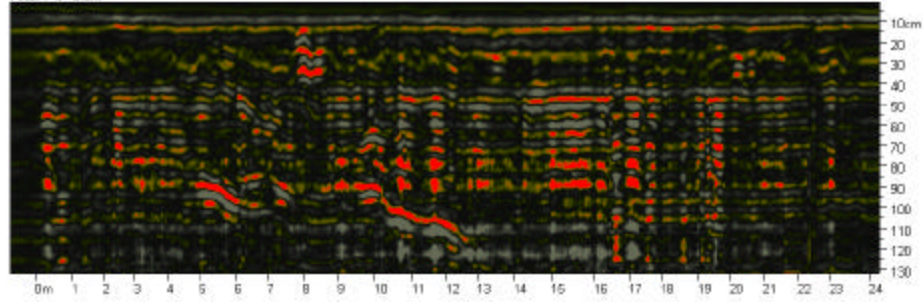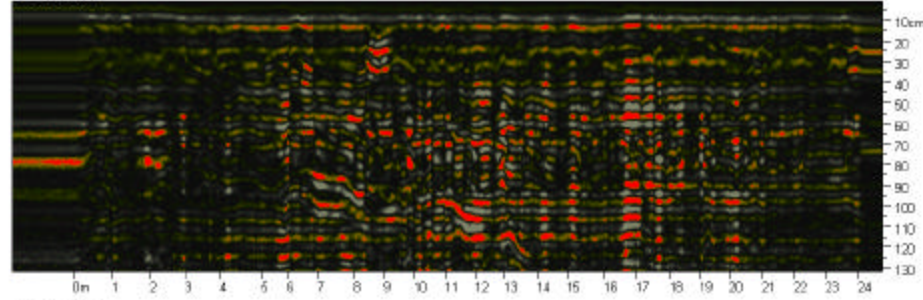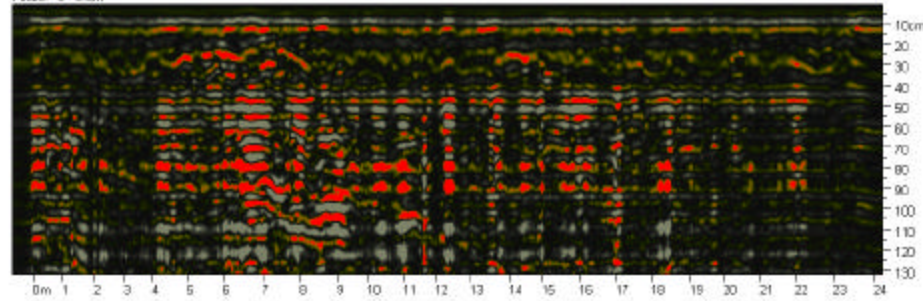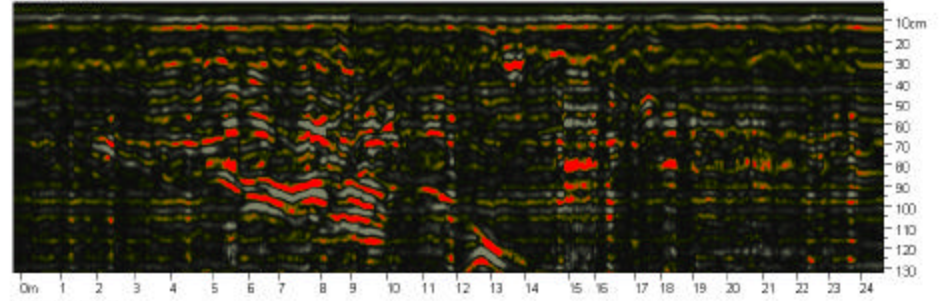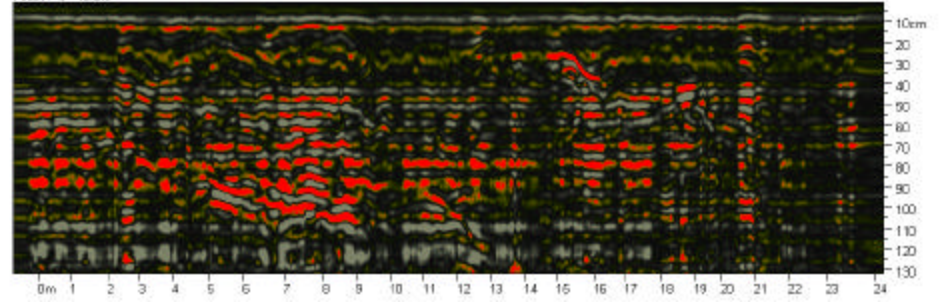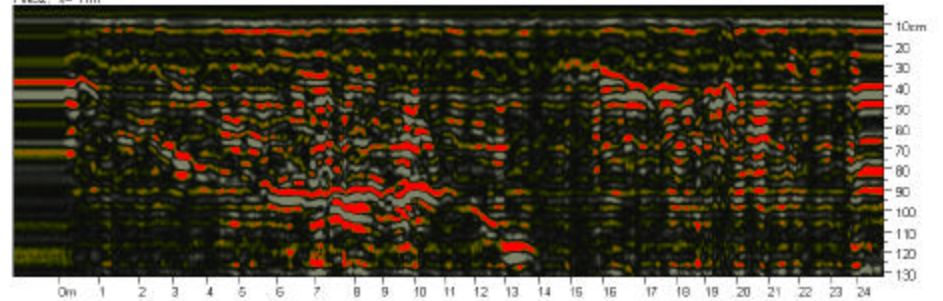
Figure B.5 Grid 1b Radargrams for Y = 0 to 7.5 m
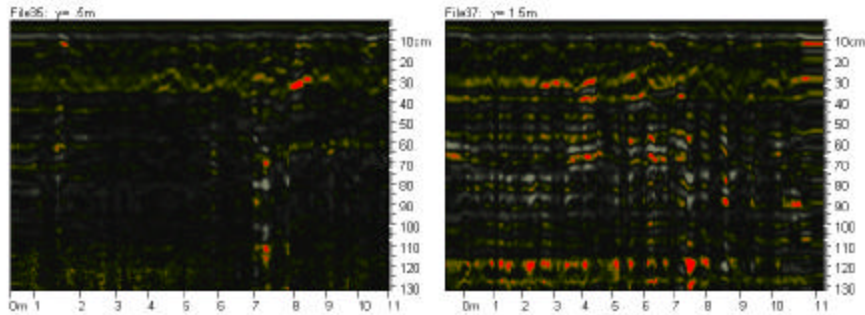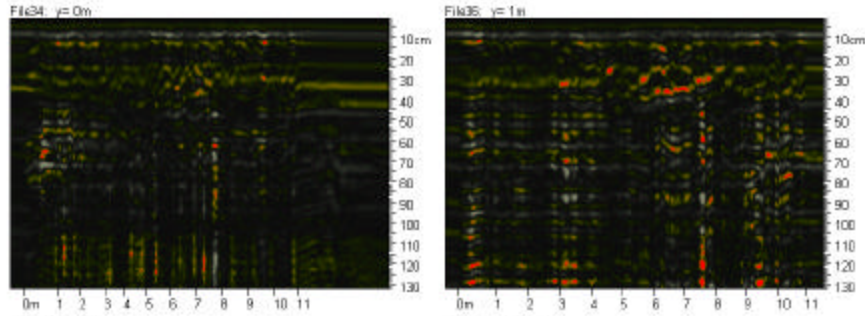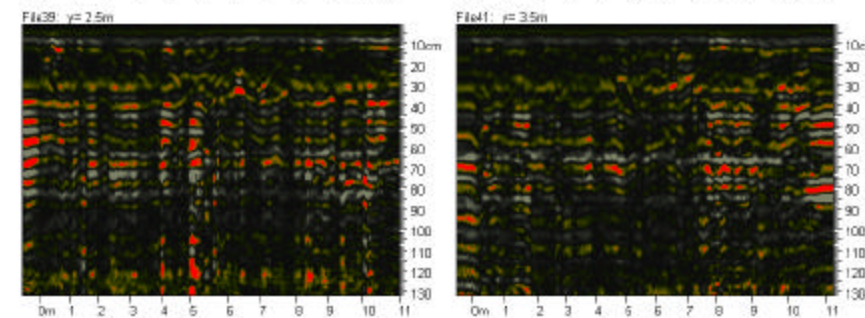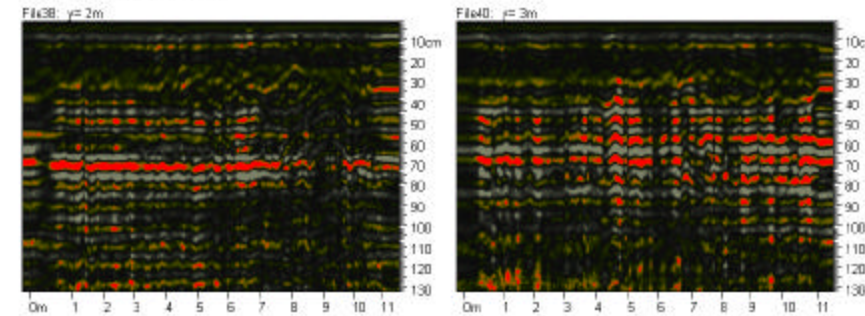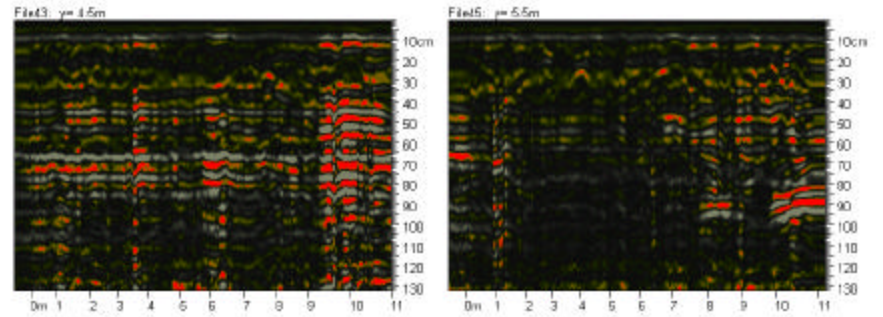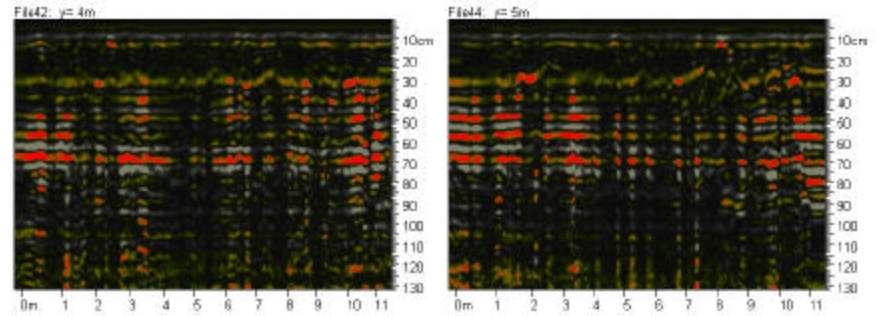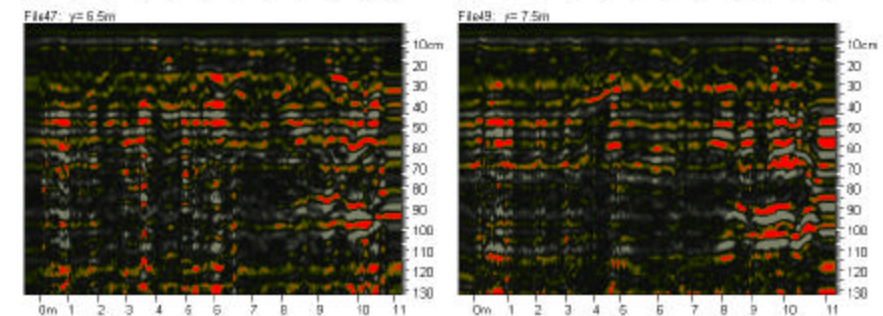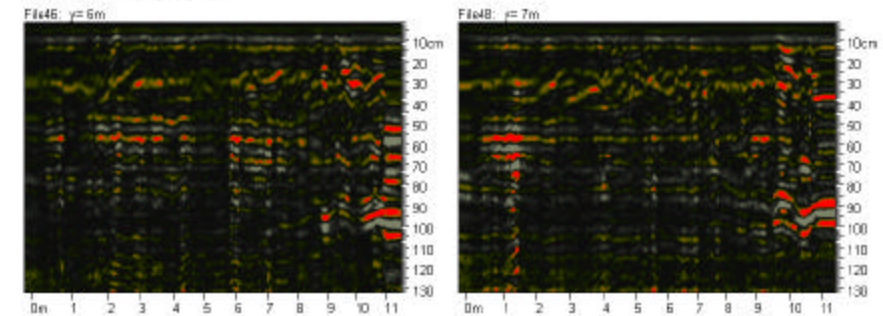
Figure B.6 Grid 1b Radargrams for Y = 8 to 15.5 m
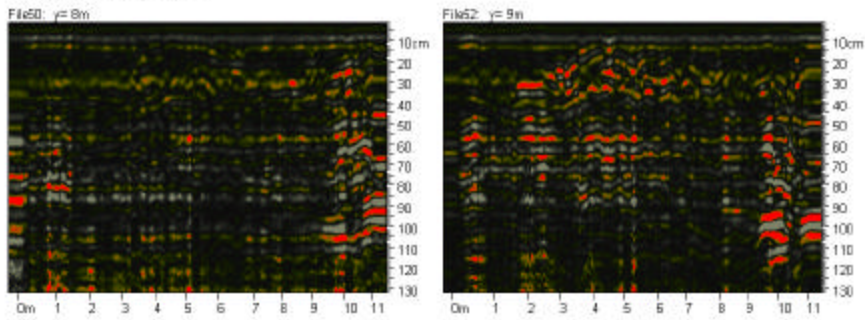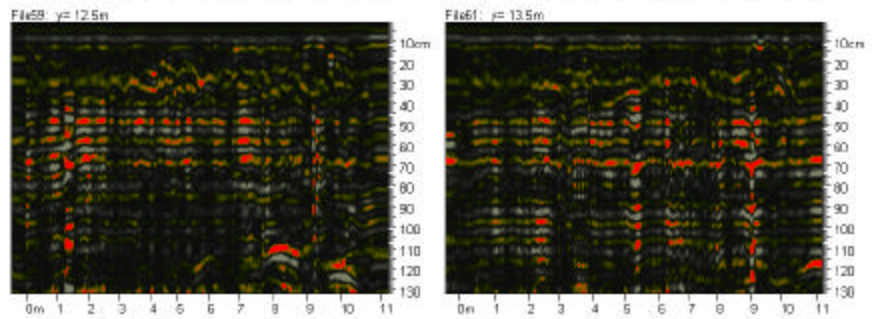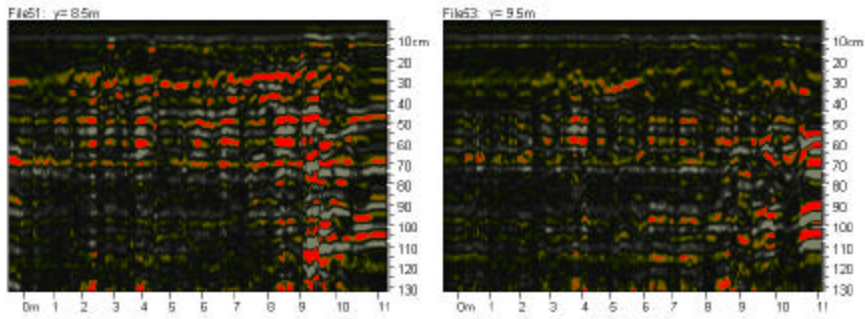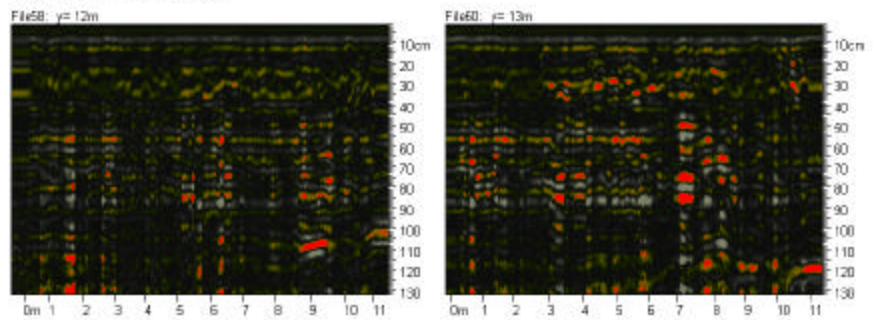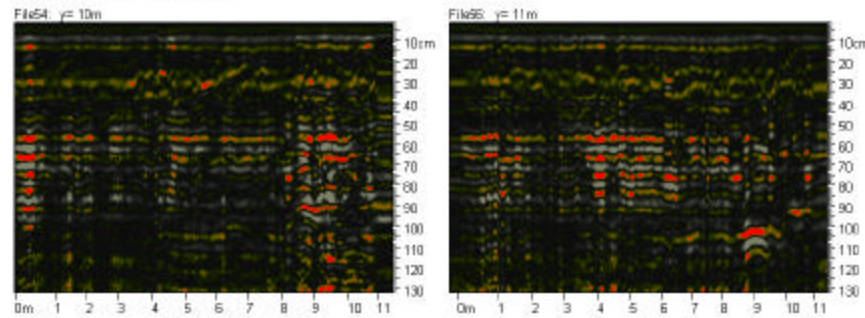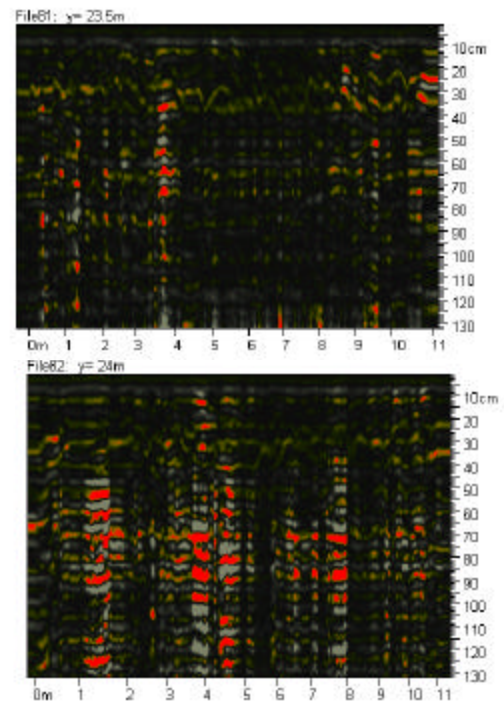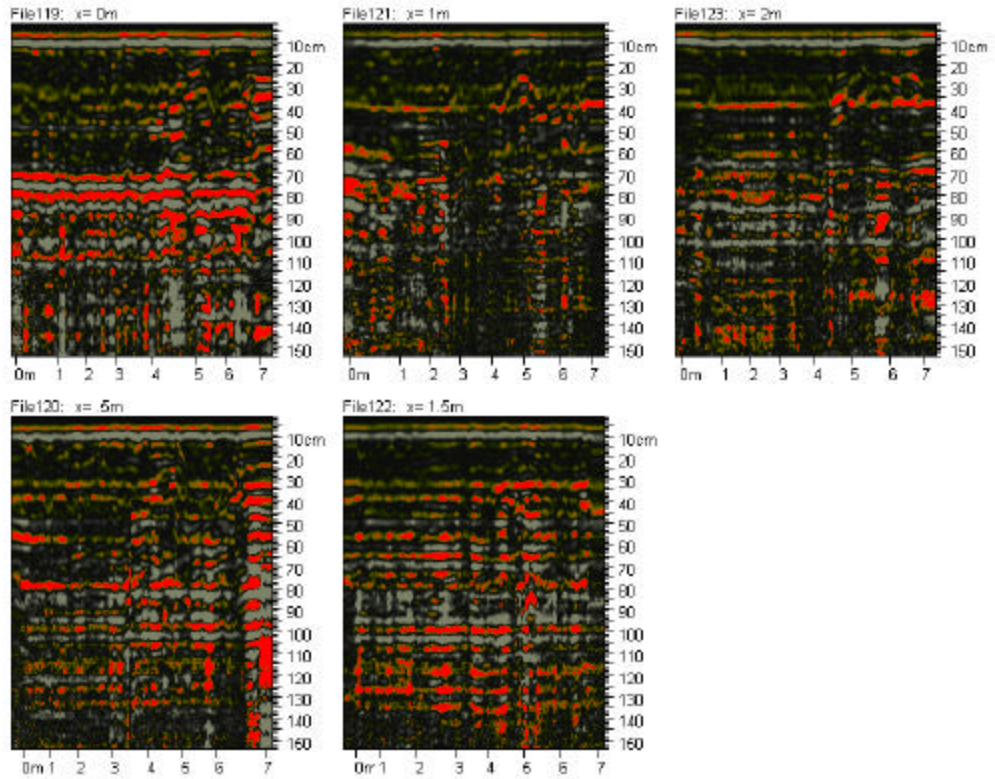
Figure B.7 Grid 1b Radargrams for Y = 16 to 23 m
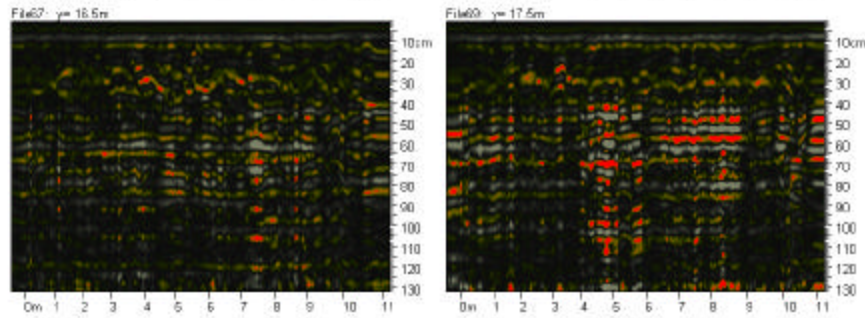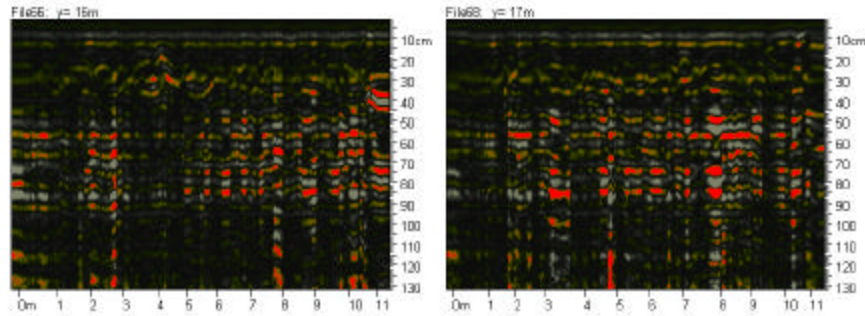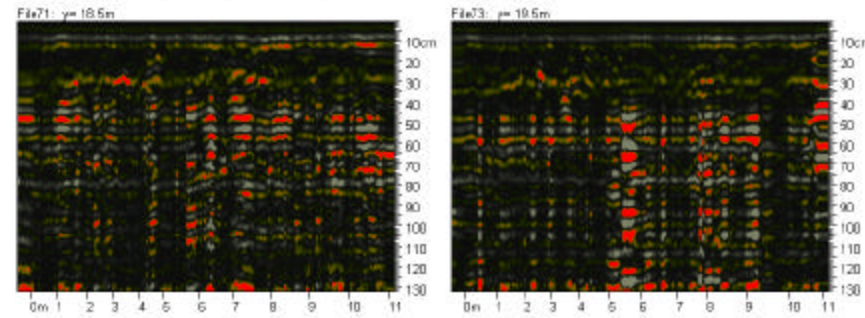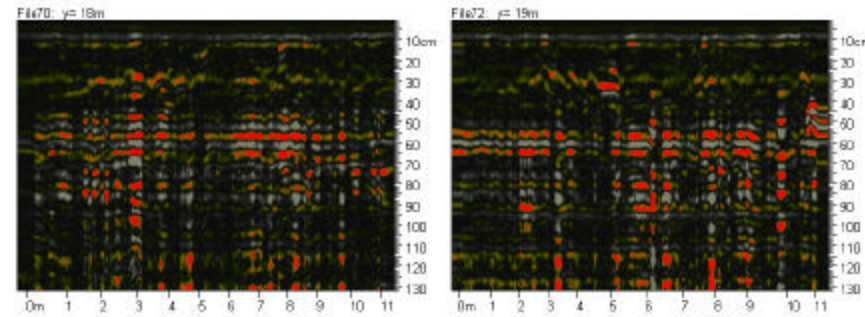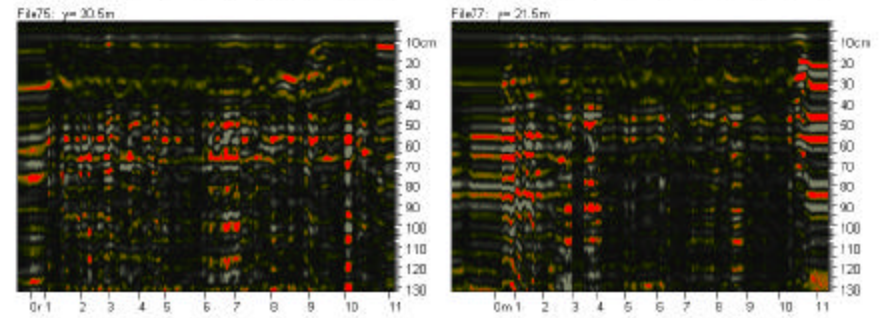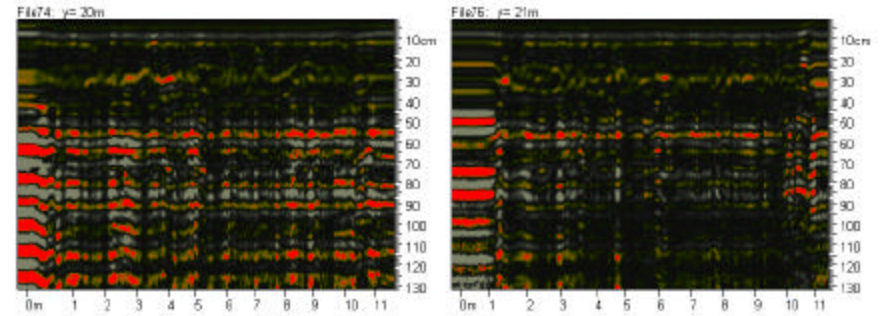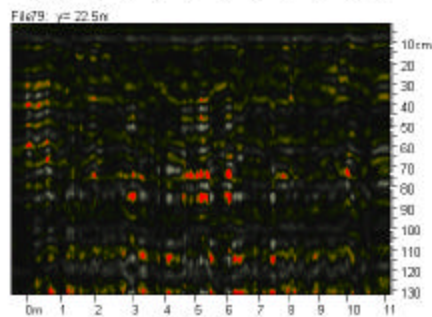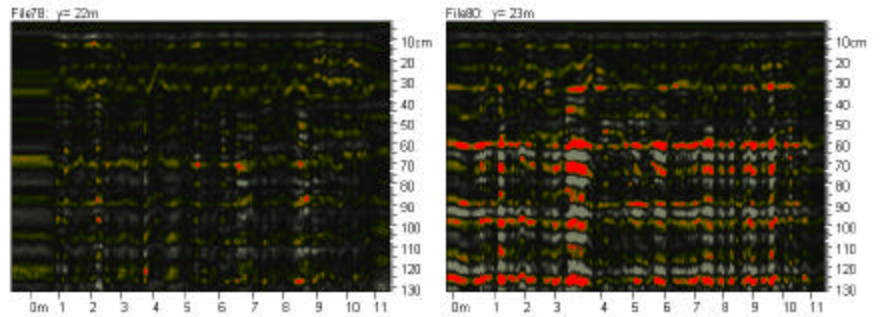
Figure B.8 Grid 1b Radargrams for Y = 23.5 to 24 m

Monte Pallano Grid2 400 MHz
Files 119-123 0 - 2m

Figure B.9 Grid 2 Radargrams Y = 0 to 4.5 m

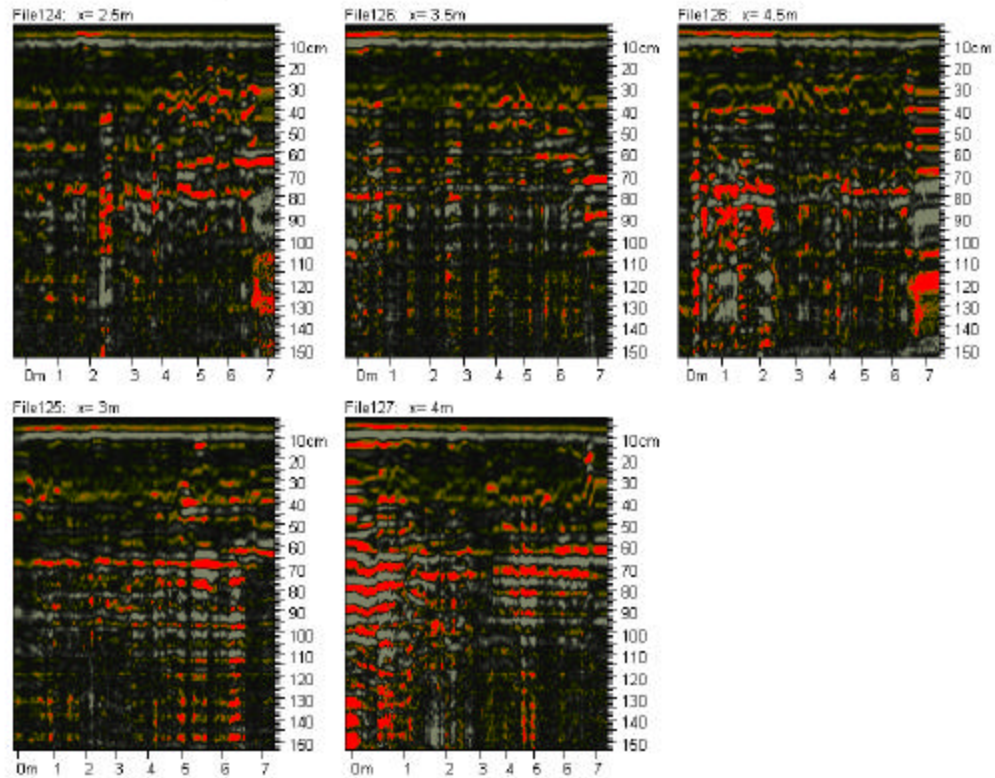Monte Pallano Grid2 400 MHz
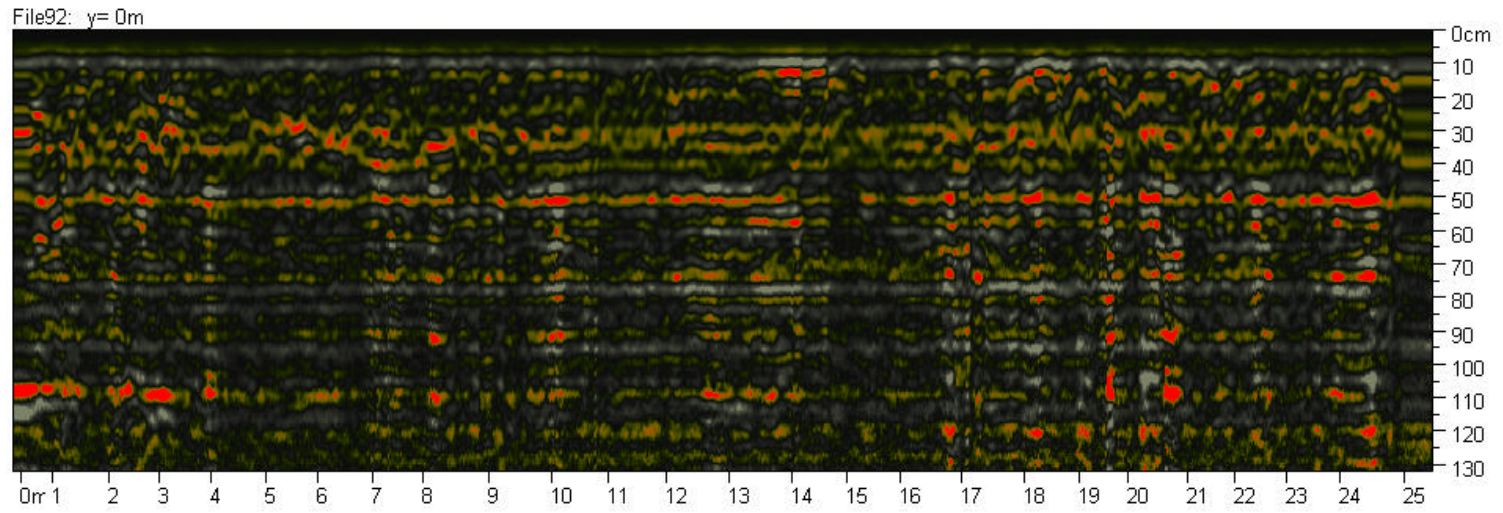Files 124-128 X = 2.5 - 4.5m Log

Figure B.10 Grid 4 Radargram

File92: y= 0m
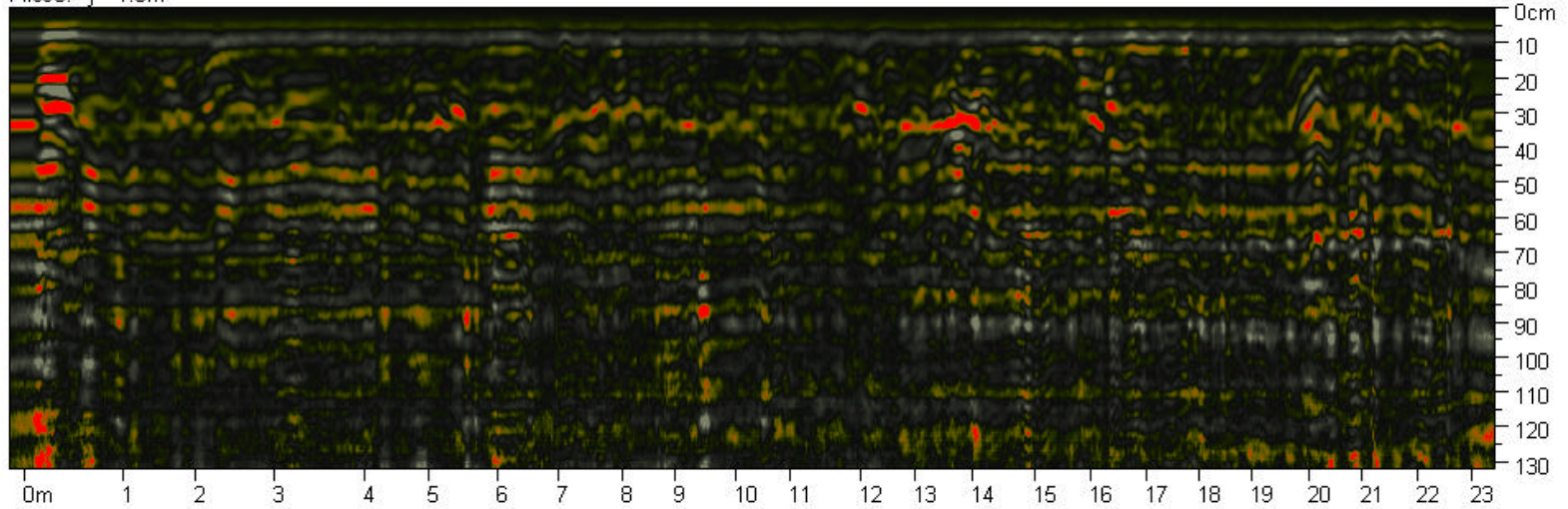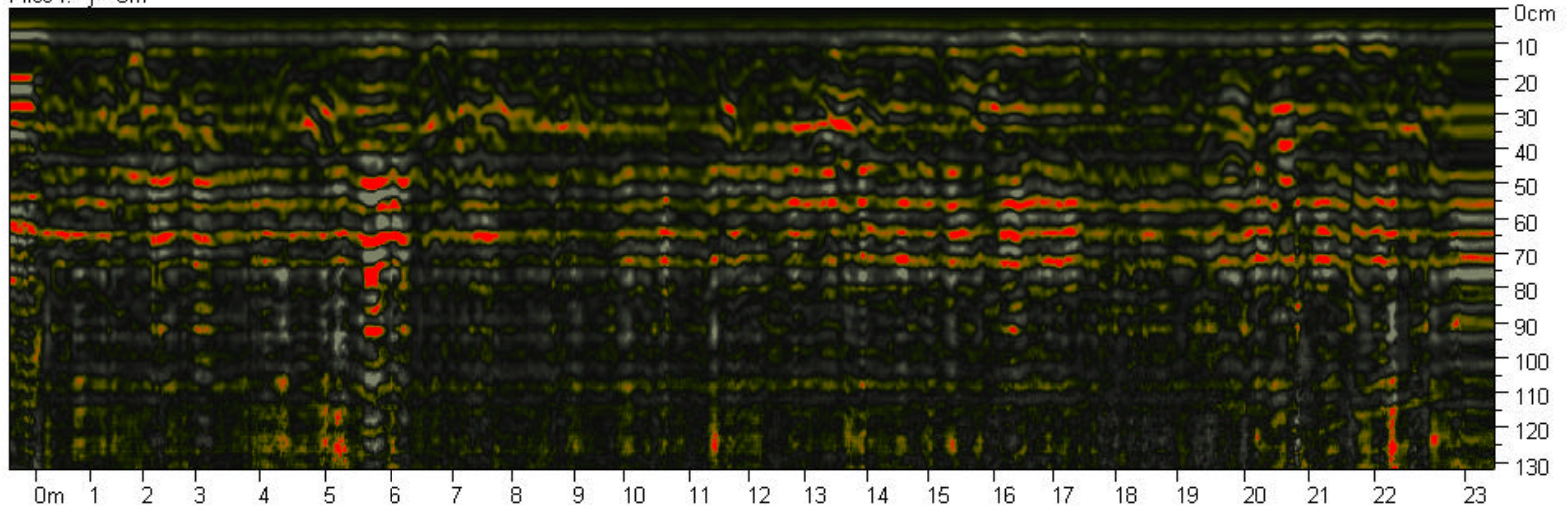
Figure B.11 Grid 5 Radargrams

Monte Pallano lines 93 - 94 Grid 5
400 MHz GPR Survey Toward the south
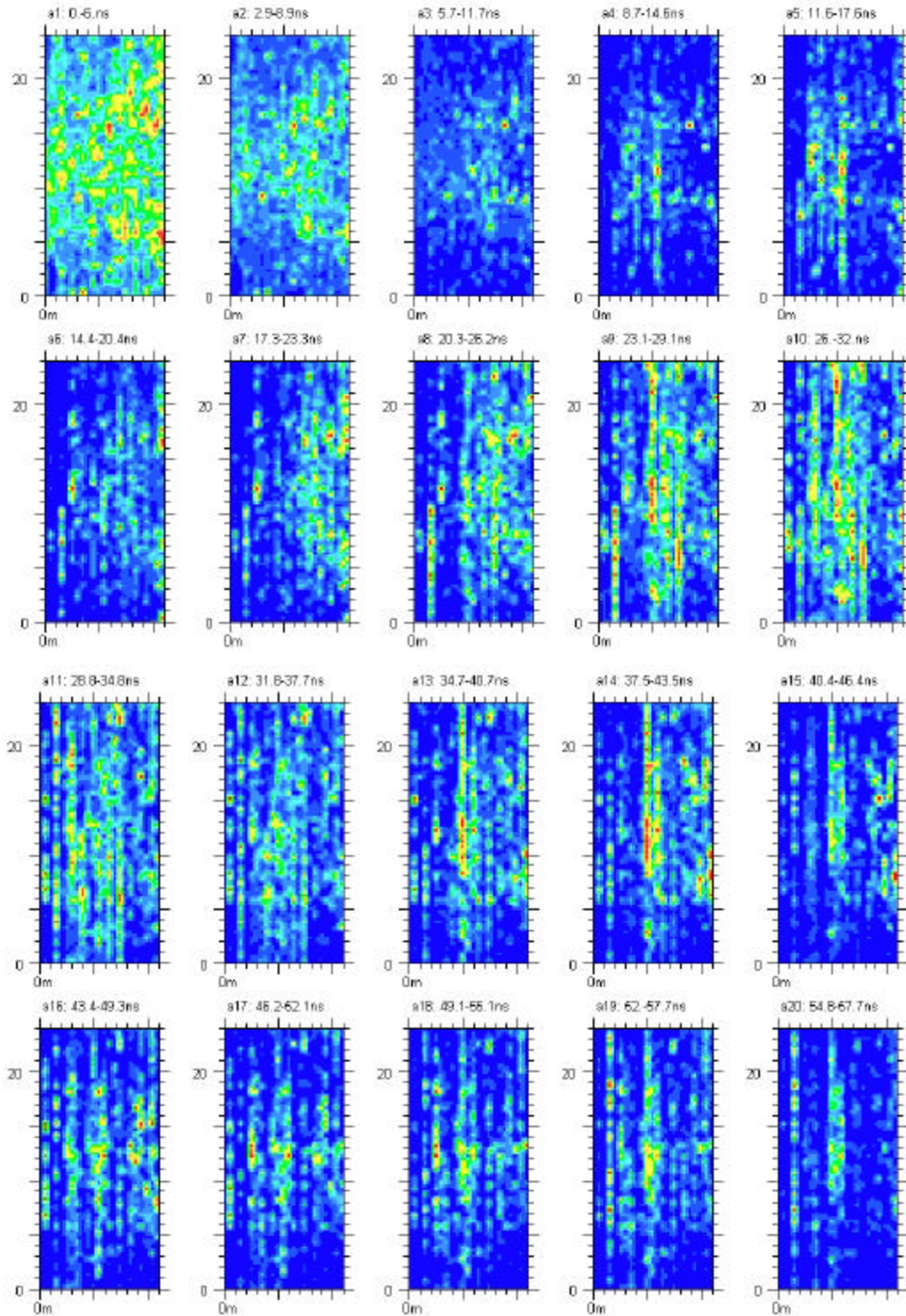
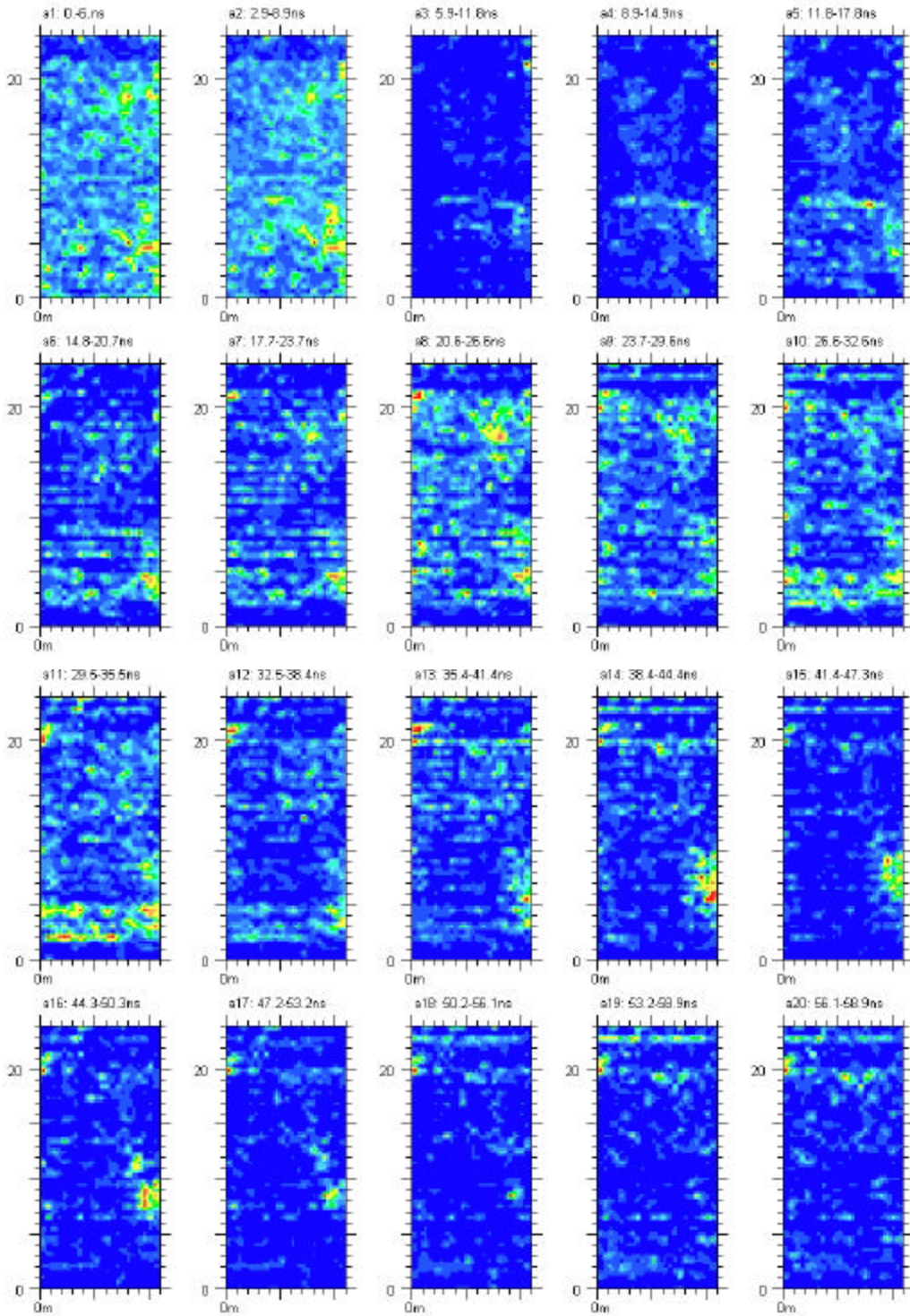Figure B.12 Grid 1a time slices with 6 ns window and 3 ns overlap

Figure B.13 Grid 1b time slices with 6 ns window and 3 ns overlap
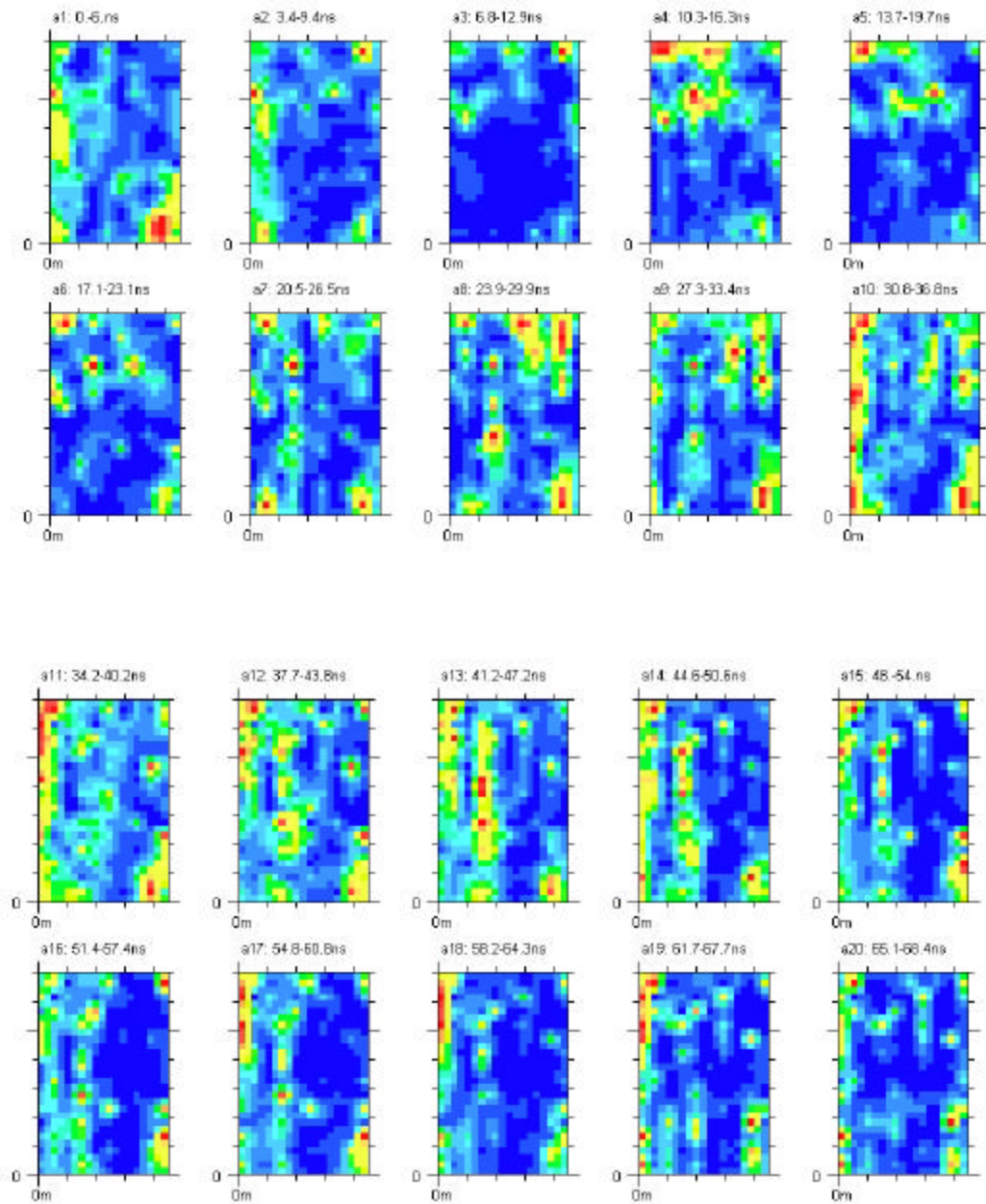
Figure B.14 Grid 2 time slices with 6 ns window and 3 ns overlap

APPENDIX C

SYNTHETIC CROSS-CORRELATION TESTS WITH MULTIPLE RANDOMLY

LOCATED ANOMALY SOURCES

Purpose

To determine the efficacy of cross-correlation for identifying the positions and
depths of anomaly sources in a profile with multiple anomaly sources at varying depths
and horizontal separation distances between sources.

Method

Several 100 m long synthetic profiles were created each with six anomaly sources
situated at random depths, integers from (1 – 5 m) and separated by random distances,
integers from (1 – 21 m) (Figure C.1). The locations and depths of the anomaly sources
from one profile are presented in Table C.1. This profile was cross-correlated with six
pilot signals for anomaly sources computed for depths of (0.5, 1, 2, 3, 4, and 5 m) with 19
samples (Figure C.2). Cross-correlations were conducted with added random noise with
S/N ratios of 20/1, 4/1 and 1/1 (Figures C.3 – C.5). The added noise was scaled based on
the greatest amplitude in the original profile, therefore the S/N ratio was actually smaller
for the lower amplitude anomaly sources.

Five of the six anomalies were visible in the profile without any added noise
(Figure C.1). Anomaly sources 5 and 6 were spaced 2 m apart and therefore their signals
were combined by superposition into a single anomaly peak. This composite peak was

located at (x) = 20 m because anomaly 6, located at (x) = 20 m, was shallower and had a much greater amplitude than anomaly 5, located at (x) = 18 m.

Results

In the absence of added noise the positions of five of the Anomaly sources (1, 2, 3, 4, and 6) were identified in the profile as well as the correlograms (Figure C.2). It was possible to determine the relative depths of the anomaly sources based on a comparison of peak amplitudes from the correlograms for all six pilot signal source depths. For example, anomaly source 3, with a depth of 4 m, had its greatest r_m value in the correlogram for a pilot signal computed for a source depth of 4 m and Anomaly sources 1 and 6, with depths of 1 m, had their greatest r_m values in the correlogram for a pilot signal computed for a source depth of 1 m.

With the addition of noise with a S/N ratio of 20/1 (Figure C.3), cross-correlation was still able to locate five of the six anomaly source locations. Anomalies 2 and 3 had their S/N ratio greatly increased as compared with the original profile in which they were indiscernible from the spurious noise peaks

With the addition of noise with a S/N ratio of 4/1 (Figure C.4) cross-correlations was only able to resolve the shallower Anomaly sources, 1, 4, and 6 with source depths of 1, 2, and 1 m respectively. Anomaly sources 2 and 3 exhibited peaks on the correlograms though they had lower r_m values than some of the spurious noise peaks.

With the addition of noise with a S/N ratio of 1/1 (Figure C.5) cross-correlation was only able to identify the location of anomaly 6 with certainty. Anomalies 1, 3, and 4 were broader and had lower r_m values from 0.21 to 0.37, though a spurious peak at (x) = 35 m had a r_m value of 0.53 and could be confused with an anomaly source.

Conclusions

       This series of tests demonstrated the ability of cross-correlation to locate anomaly sources from a profile with multiple anomaly sources at different depths and with varying spacing between sources. The deepest anomaly sources on the profile were often overshadowed if they were adjacent to a shallower greater amplitude anomaly source. Cross-correlation was able to increase the signal to noise ratio of low amplitude signals such as Anomalies 2 and 3 thereby locating anomaly sources not apparent from the raw data profile. Cross-correlation wasn't able to separate adjacent or very near anomalies, which were correlated as a single anomaly such as Anomaly 5, which was 2 m away from Anomaly 6.

Figure C.1 A synthetic F$_{at}$ profile with six anomaly sources at random depths and with random spacing distances between sources. The relative positions of the anomaly spheres are presented below the profile. A summary of the positions and depths of the anomaly sources is presented in Table C.1.
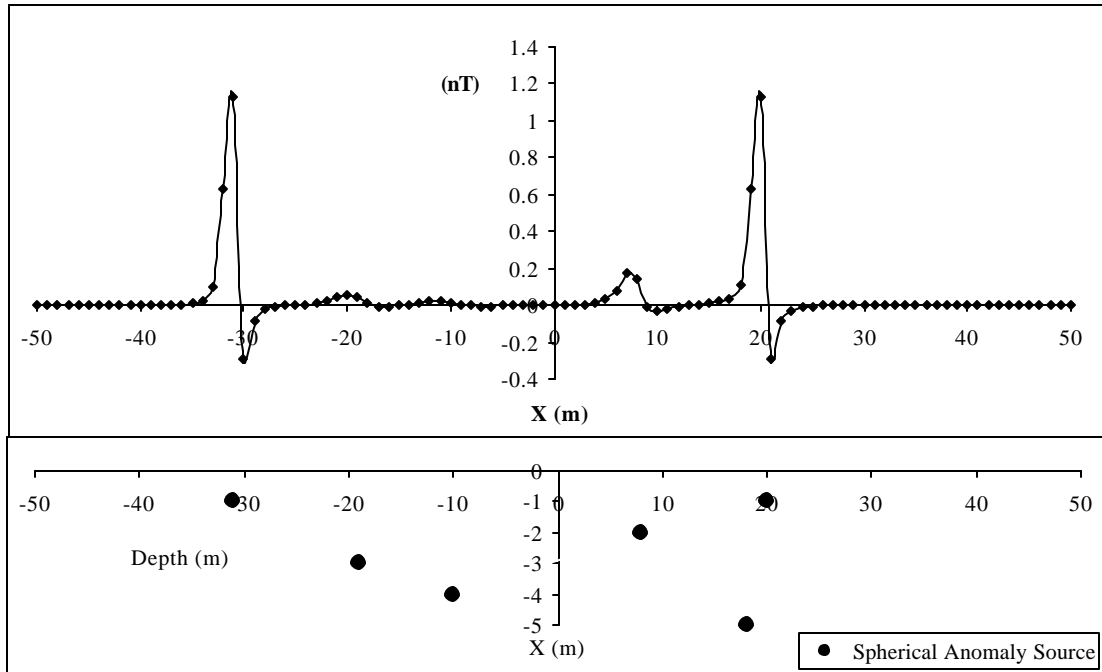

Table C.1 The positions and depths of anomaly sources

Anomaly Source	1	2	3	4	5	6
X Position (m)	-31	-19	-10	8	18	20
Depth (m)	1	3	4	2	5	1

Figure C.2 A comparison of correlograms of the cross-correlation between the random anomaly source profile (C.1) with no noise added and pilot signals computed for anomaly sources at six different depths each with 19 samples. Numbers and arrows denote the locations of anomalies from Table 1 on the correlograms with pilot signals at the same depth as the anomaly sources.
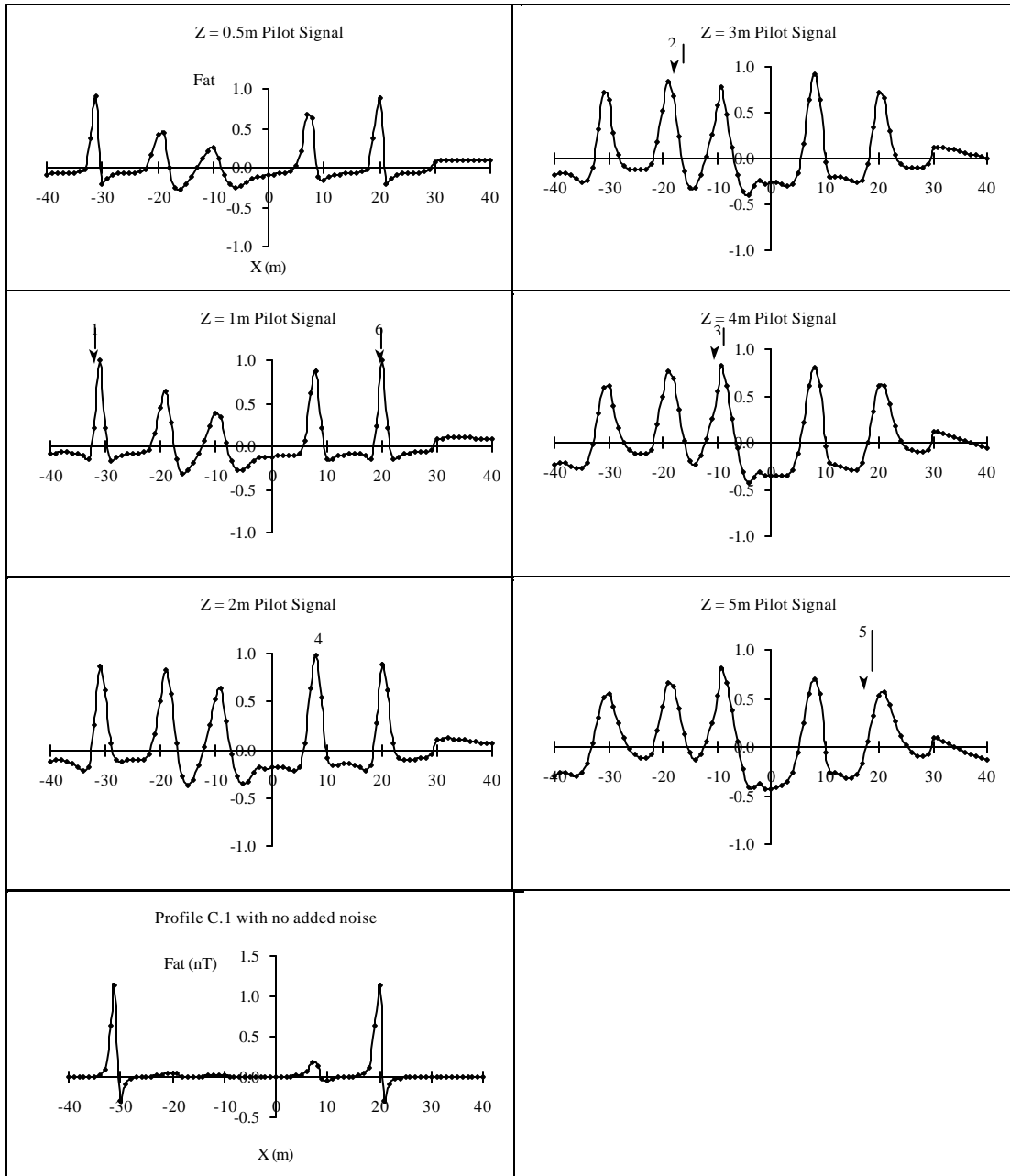
Figure C.3 A comparison of correlograms of the cross-correlation between the random anomaly source profile (C.1) with S/N of 20/1 and pilot signals computed for anomaly sources at six different depths each with 19 samples. Numbers and arrows denote the locations of anomalies from Table 1 on the correlograms with pilot signals at the same depth as the anomaly sources.
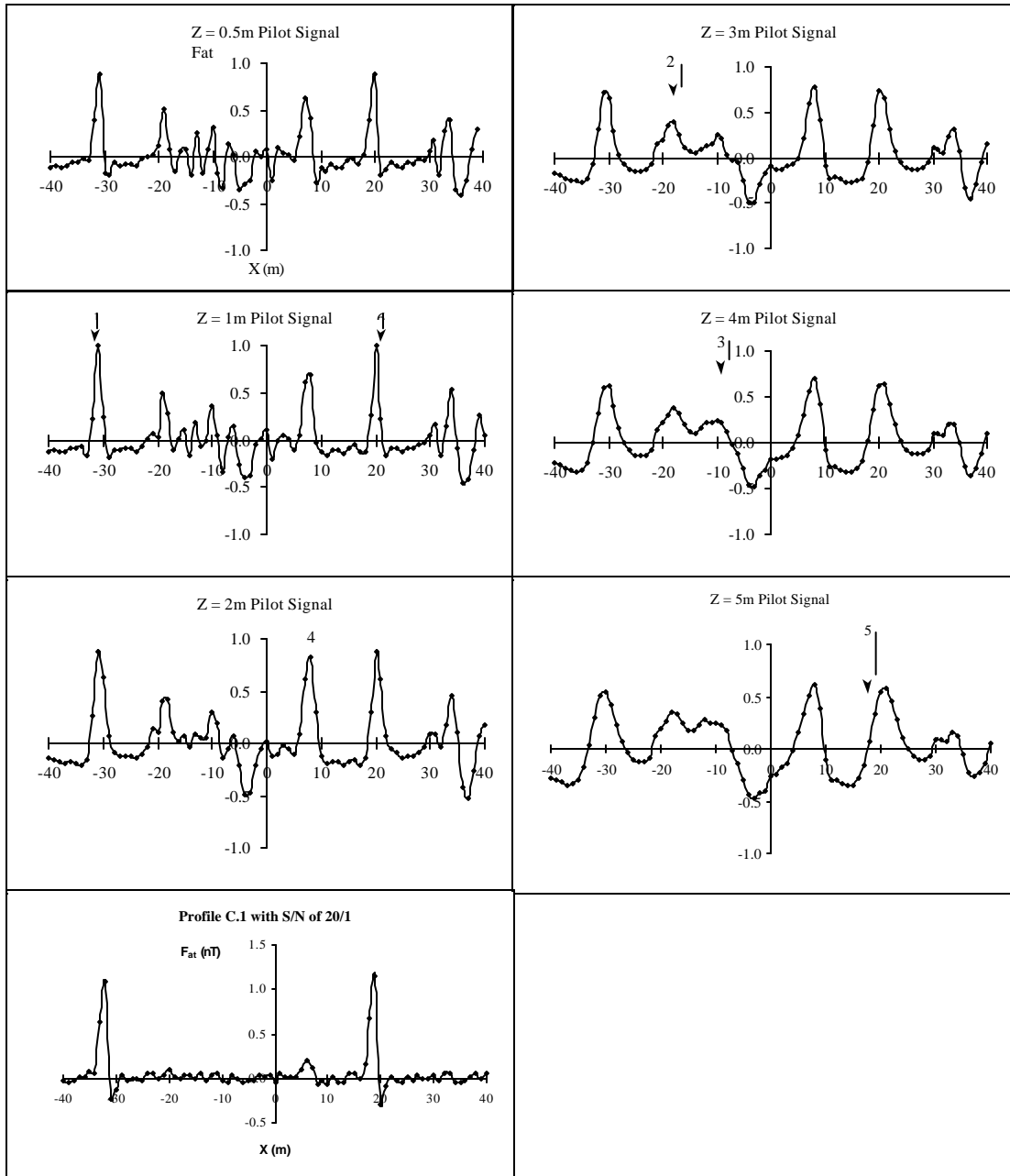
Figure C.4 A comparison of correlograms of the cross-correlation between the random anomaly source profile (C.1) with S/N of 4/1 and pilot signals computed for anomaly sources at six different depths each with 19 samples. Numbers and arrows denote the locations of anomalies from Table 1 on the correlograms with pilot signals at the same depth as the anomaly sources.
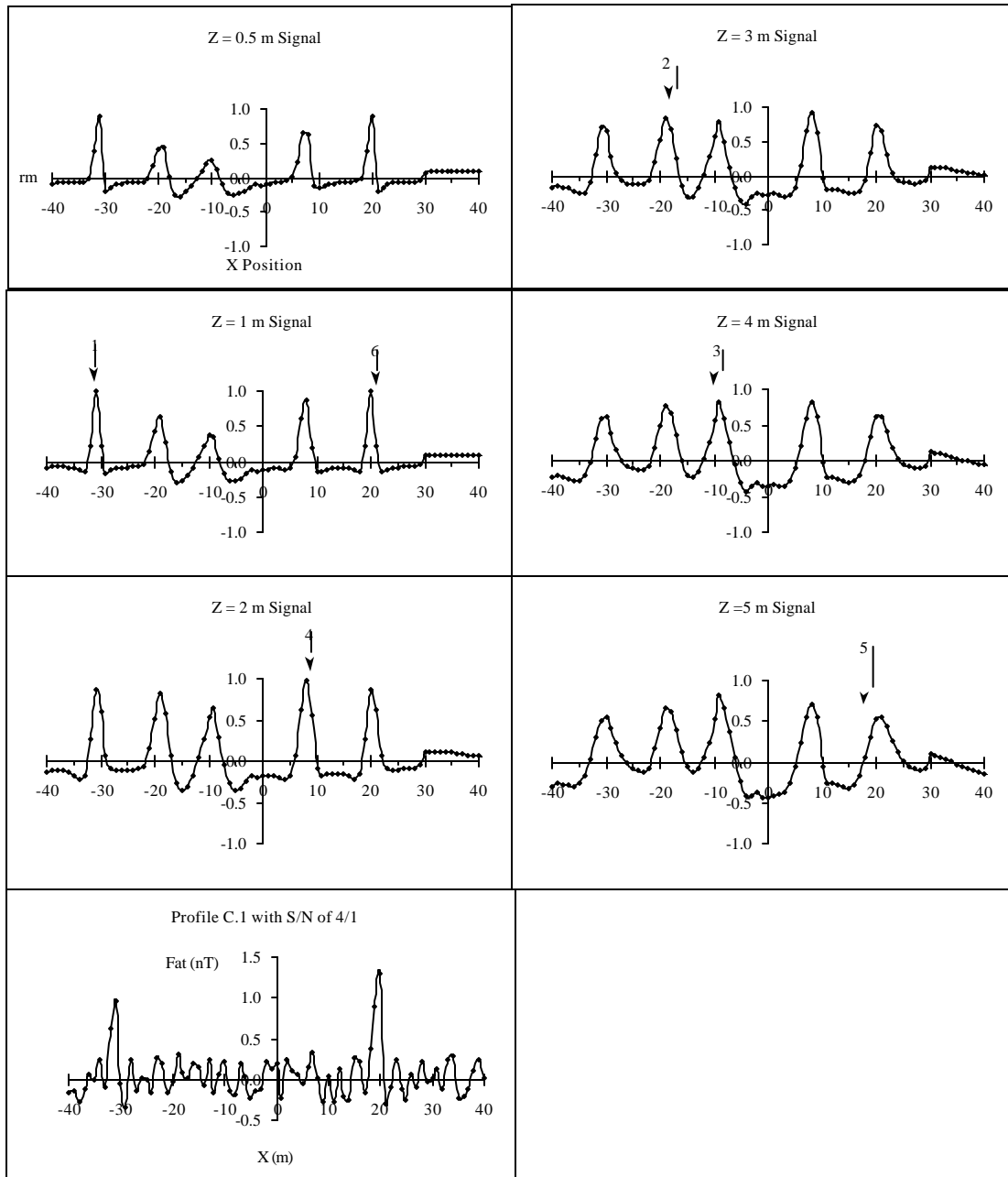
Figure C.5 A comparison of correlograms of the cross-correlation between the random anomaly source profile (C.1) with S/N of 1/1 and pilot signals computed for anomaly sources at six different depths each with 19 samples. Numbers and arrows denote the locations of anomalies from Table 1 on the correlograms with pilot signals at the same depth as the anomaly sources.